João Gabriel Alencar Caribé

Correlations in a Quantum Scalar Field on a Schwarzschild spacetime



MINISTÉRIO DA CIÊNCIA,TECNOLOGIA E INOVAÇÃO



"CORRELATIONS IN A QUANTUM SCALAR FIELD ON A SCHWARZSCHILD SPACETIME"

JOÃO GABRIEL ALENCAR CARIBÉ

Tese de Doutorado em Física apresentada no Centro Brasileiro de Pesquisas Físicas do Ministério da Ciência Tecnologia e Inovação. Fazendo parte da banca examinadora os seguintes professores:

Marc Casals Casanellas - Orientador/CBPF

Jochen Zahn – UNI-LEIPZIG

ALESSAND Firmado digitalmente por RO|FABBRI ALESSANDRO| FABBRI FABBRI

Alessandro Fabbri – UV

Documento assinado digitalmente

CARLOS AUGUSTO DOMINGUES ZARRO
Data: 21/07/2025 14:52:10-0300
Verifique em https://validar.iti.gov.br

Carlos Augusto Domingues Zarro - UFRJ

Documento assinado digitalmente

GEORGE EMANUEL AVRAAM MATSAS
Data: 22/07/2025 14:11:21-0300
Verifique em https://validar.iti.gov.br

George Emanuel Avraam Matsas – UNESP

Rio de Janeiro, 18 de julho de 2025.

João Gabriel Alencar Caribé

Correlations in a Quantum Scalar Field on a Schwarzschild spacetime

Dissertation presented to the Brazilian Center for Research in Physics in partial fulfillment of the requirements to obtain the degree of Doctor in Physics.

Dissertação apresentada ao Centro Brasileiro de Pesquisas Físicas como parte dos requisitos para obtenção do titulo de Doutor em Física.

Centro Brasileiro de Pesquisas Físicas - CBPF

Supervisor: Marc Casals Casanellas

Rio de Janeiro, RJ, Brasil 2025

D 1:					
Dearco e				o o apoio dad loutorado.	lo a m
Dearco e			lene, por tod e durante o d		$lo\ a\ m$
Dearco e					lo a m
Dearco e					lo a m
Dearco e					lo a m
Dearco e					lo a m

Acknowledgements

I would like to thank everyone who has supported me, directly and indirectly, throughout the development of this work. In particular, my family for never letting me give up, my friends for keeping me sane, my girlfriend for her partnership in the final stretch, my supervisor, Marc, for the countless meetings and rounds of proofreading and improvements to this work, the CBPF staff for always being so helpful, and my fellow harvesters Eduardo Martín-Martínez, Achim Kempf, and Robert Jonsson, with whom Marc and I worked together to produce the published work included in this thesis.

Finally, I would like to thank the Brazilian National Council for Scientific and Technological Development (CNPq) for their financial support during my PhD.

Resumo

A radiação Hawking é um fenômeno que conecta a Relatividade Geral e a Mecânica Quântica. Embora sua extrema fraqueza torne sua detecção direta desafiadora, ela tem gerado debates profundos sobre a compatibilidade entre essas duas teorias. Um exemplo é o conhecido paradoxo da perda de informação, onde um sistema quântico em um espaço-tempo de buraco negro parece evoluir de um estado puro para um estado misto, aparentemente apagando a informação inicial contida nesse sistema. Uma suspeita é que essa informação não é de fato perdida, mas sim codificada na radiação Hawking - o que motiva estudos aprofundados sobre correlações quânticas em espaços-tempo curvos.

Duas abordagens principais têm sido utilizadas para investigar campos quânticos em espaços-tempo curvos: A análise direta das funções de dois pontos do campo e o método indireto de colheita de emaranhamento (entanglement harvesting), onde pares de detectores extraem emaranhamento pré-existente do campo. Embora ambos os métodos tenham produzido resultados significativos no espaço-tempo de Schwarzschild (1+1)D - revelando assinaturas da radiação Hawking em correlações momento-momento e demonstrando a possibilidade de colheita de emaranhamento através do horizonte - resultados semelhantes em (3+1)D permanecem escassos, com exceção do nosso trabalho publicado [1].

Esta tese contribui para preencher essa lacuna através de um estudo abrangente das correlações quânticas nos vácuos de Boulware, Unruh e Hartle-Hawking de um campo escalar sem massa no espaço-tempo de Schwarzschild (3+1)D. Desenvolvemos e implementamos um esquema numérico novo para calcular funções de Wightman de forma eficiente, obtendo avanços significativos: (1) a revelação de uma estrutura de singularidade 2-fold na parte real da função de Wightman em pontos cáusticos; (2) a identificação de uma assinatura distinta (um comportamento degrau seguido de um mínimo local) que pode representar a impressão digital das correlações da radiação Hawking em (3+1)D; e (3) a descoberta de singularidades previamente desconhecidas escondidas na função de Wightman. Além disso, demonstramos que o fenômeno de colheita de emaranhamento é amplificado próximo a pontos cáusticos, permitindo que mesmo detectores separados por intervalos do tipo tempo adquiram emaranhamento predominantemente através da colheita [1] - em contraste com o caso (1+1)D. Esses resultados estabelecem ferramentas e ideias relevantes para futuros estudos de campos quânticos no espaço-tempo de Schwarzschild (3+1)D.

Palavras-chave: Radiação Hawking, Buracos negros, Relatividade Geral, Emaranhamento.

Abstract

Hawking radiation is a phenomenon linking General relativity and Quantum mechanics. While its extreme weakness makes direct detection challenging, it has sparked enduring debates about the compatibility between Quantum mechanics and General relativity. An example is the known information loss puzzle, where a quantum system on a black hole spacetime seems to evolve from a pure state into a mixed state, effectively erasing the initial information encoded in the quantum system. A suspicion is that such information is not erased, but encoded in Hawking radiation instead. This motivates a deeper study of quantum correlations in curved spacetimes.

Two principal approaches have emerged for such investigations in quantum fields on curved spacetimes: direct analysis of the field's two-point functions, and indirect probing via entanglement harvesting — where detector pairs extract preexisting entanglement from the field. While both methods have yielded significant insights in (1+1)D Schwarzschild spacetime, demonstrating Hawking radiation signatures in momentum-momentum correlators and horizon-crossing entanglement harvesting, comparable (3+1)D results remain scarce beyond our published work [1].

This thesis helps bridging this gap through a comprehensive study of quantum correlations in the Boulware, Unruh, and Hartle-Hawking vacua of a massless scalar field on (3+1)D Schwarzschild spacetime. We develop and implement a novel numerical scheme to compute Wightman functions efficiently, allowing several key advances: (1) revelation of a 2-fold singularity structure in the Wightman function's real part at caustic points, (2) identification of a distinctive step-like feature followed by a local minimum — a possible (3+1)D imprint of Hawking radiation correlations, and (3) discovery of previously unknown non-light-crossing singularities hidden in the Wightman function. Furthermore, we demonstrate that entanglement harvesting is amplified near caustics, allowing for timelike-separated detectors to acquire entanglement predominantly by harvesting from the background field [1], in constrast to the (1+1)D case. These results establish relevant tools and insights for, but not limited to, future studies of correlations in quantum fields the (3+1)D Schwarzschild spacetime.

Keywords: Hawking radiation, Black holes, General relativity, Entanglement.

List of Figures

Figure 1 –	Penrose-Carter diagram of Schwarzschild spacetime	19
Figure 2 –	EF and KS coordinate axis in the conformal diagram of Schwarzschild	
	spacetime	22
Figure 3 –	SD coordinate axis in a conformal diagram of the Schwarzschild spacetime	24
Figure 4 –	The effective potential for null geodesics	28
Figure 5 –	Upgoing modes with a relative error larger than ϵ in the Wrosnkian	55
Figure 6 –	Upgoing modes with a relative error larger than 10^{-9} in their Wrosnkians	56
Figure 7 –	Number of relative differences larger than ϵ in the tests of the amplitudes	
	as a function of ϵ	61
Figure 8 –	Number of relative differences larger than or equal to 10^{-9} in the tests	
	of the amplitudes as a function of ℓ	62
Figure 9 –	Values of ω and ℓ of the amplitudes with relative differences larger than	
	10^{-9} in tests	63
Figure 10 –	First example of interpolating $G_{\ell}^{\text{in},R;\text{in},R*}(\omega)$ and $G_{\ell}^{\text{up},R;\text{up},R*}(\omega)$ for $r=$	
	$r' \approx 6.009 M$ and $\ell = 2 \ldots \ldots \ldots \ldots \ldots$	66
Figure 11 –	Second example of interpolating $G_{\ell}^{\text{in},R;\text{in},R*}(r,r',\omega)$ and $G_{\ell}^{\text{up},R;\text{up},R*}(r,r',\omega)$	
	for $r \approx 6.009 M, r' \approx 3.9 M$ and $\ell = 2 \dots \dots \dots \dots \dots$	67
Figure 12 –	Integration of $G_{\ell}^{\text{in},R;\text{in},R*}(\omega)$ and $G_{\ell}^{\text{up},R;\text{up},R*}(\omega)$ for $r \approx 6.009M, r' \approx$	
	$3.9M$ and $\ell = 5$	68
		70
Figure 14 –	Integration of frequency-smoothed $G_{\ell}^{\text{in},R;\text{in},R*}(r,r',\omega)$ and $G_{\ell}^{\text{up},R;\text{up},R*}(r,r',\omega)$	
	for $r \approx 6.009M, r' \approx 3.9M$, and $\ell = 5.$	71
Figure 15 –	Example of terms of the ℓ -sums for $W_{\text{in}}^{B}(x;x')$ and $W_{\text{up}}^{B}(x;x')$	73
Figure 16 –	Example of the ℓ -sum process for $W_{\text{in}}^{B}(x;x')$ and $W_{\text{up}}^{B}(x;x')$	74
Figure 17 –	Sample points for evaluating $W^{B}(x;x')$ - first example	76
Figure 18 –	Wightman function $W^{B}(x;x')$ with fixed r and r' - first example	78
Figure 19 –	Wightman function $W^B(\mathbf{x};\mathbf{x}')$ with fixed r and r' with null geodesic	
	connections - first example	79
Figure 20 –	Orbiting null geodesics connecting \boldsymbol{x} and \boldsymbol{x}' with angular separation	
	$\gamma = \pi/3$	80
Figure 21 –	Wightman function $W^B(x;x')$ with fixed r and r' with null geodesic	
	connections and ℓ -smoothing - first example	81
Figure 22 –	Real part of $W^B(\mathbf{x};\mathbf{x}')$ with fixed r and r' , linear scale - first example .	82
Figure 23 –	Imaginary part of $W^{B}(\mathbf{x};\mathbf{x}')$ with fixed r and r' , linear scale - first example	83
Figure 24 –	The Retarded Green Function on caustic points at $r = r'$ on $\gamma = 0$	84

Figure 25 – The Real part of the Wightman Function on caustic points at $r=r'$ on $\gamma=0$
Figure 26 – Points for evaluating $W^B(x;x')$ with x and x' outside the horizon 87
Figure 27 – Real part of $W^B(\mathbf{x}; \mathbf{x}')$ with \mathbf{x} and \mathbf{x}' outside the horizon
Figure 28 – Imaginary part of $W^B(x;x')$ with x and x' outside the horizon 89
Figure 29 – Real part of $W^H(x;x')$ with x and x' outside the horizon 90
Figure 30 – The Wightman function $W^{\psi}(\mathbf{x}; \mathbf{x}')$ with $\mathbf{x} = (v = 0M, r \approx 6.009M, \theta =$
$0, \varphi = 0$) separated by an angle of $\gamma = \pi/3$ from all points x' at $r' \approx 2.7M$ 92
Figure 31 – The quantum relative contribution $\Delta w^{\psi}(\mathbf{x},\mathbf{x}')$ with $\mathbf{x}=(v=0M,u=0)$
$-14.8M, \ \theta = 0, \ \varphi = 0) \ \text{and} \ x' = (v', \ r' \approx 2.7M, \ \theta = 0, \ \varphi = \pi/3) \ \dots \ 94$
Figure 32 – The quantum relative contribution $\Delta w^{\psi}(x,x')$ vs the Wightman function
with $x = (v = 0M, u = -14.8M, \theta = 0, \varphi = 0)$ separated by an angle
of $\gamma = \pi/3$ from all points x' at $r' \approx 2.7M$
Figure 33 – The quantum relative contribution $\Delta w^U(x,x')$
Figure 34 – The quantum relative contribution $\Delta w^H(x,x')$
Figure 35 – ℓ -summed integrands of $W^{\psi}(x;x')$, $\psi \in \{B,U,H\}$, with $x \in II$ and $x \in I$ 98
Figure 36 – Mesh of points across the horizon with $x \in II$ and $x' \in I$
Figure 37 – $\left \operatorname{Im} \left[M^2 W^U \right] \right $ for $x \in II$ and $x' \in I$
Figure 38 – $\left \operatorname{Im} \left[M^2 W^U \right] \right $ with $x \in II$ and $x' \in I$ on a slice of constant $r' \dots 102$
Figure 39 – Singularity structure of Im M^2W^U with $x \in II$ and $x' \in I$
Figure 40 – $\left \operatorname{Re} \left[M^2 W^U \right] \right $ with $\mathbf{x} \in II$ and $\mathbf{x}' \in I$
Figure 41 – $\left \operatorname{Re} \left[M^2 W^H \right] \right $ with $x \in II$ and $x' \in I$
Figure 42 – $ \operatorname{Im} [M^2 W^U] $ with $x \in II$ and $x' \in I$ on a slice of constant $r' = 1.5$
Figure 43 – Singularity structure of Im M^2W^U with $x \in II$ and $x' \in I$
Figure 44 – Re M^2W^U with $x \in II$ and $x' \in I$ not causally connected 108
Figure 45 – Re $[M^2W^U - M^2W_{\Delta}]$ with $x \in II$ and $x' \in I$ not causally connected . 110
Figure 46 – $ W_{\Delta}(x, x') $ with x inside the horizon and x' outside
Figure 47 – Tracking the zero of $W_{\Delta}(x,x')$
Figure 48 – Tracking the zero of $W_{\Delta}(x,x')$ with $V=3$
Figure 49 – $W_{\Delta}\left(x,x'\right)$ with x inside the horizon and x' outside in a linear scale 115
Figure 50 – $W_{\Delta}\left(x,x'\right)$ with x inside the horizon and x' outside on slices of constant $r'116$
Figure 51 – $W_{\Delta}(x,x')$ with x inside the horizon and x' outside on slices of constant
r' as a function of v'
Figure 52 – Manifestation of correlations across the horizon in $M^2W^U\left(x;x'\right)$ 118
Figure 53 – Manifestation of correlations across the horizon in $M^2W^H\left(\mathbf{x};\mathbf{x}'\right)$ 119
Figure 54 – $ \text{Re}[M^2W_{\text{in,R}}] $ with $x, x' \in I$
Figure 55 – $ \text{Im}[M^2W_{\text{in,R}}] $ with $x, x' \in I$
Figure 56 – $ \text{Re}[M^2W_{\text{up,R}}] $ with $x, x' \in I$
Figure 57 – $ \text{Im}[M^2W_{\text{up,R}}] $ with $x, x' \in I$

Figure 58 –	The magnitude of the real parts of $W_{\text{in,R}}(x;x'), W_{\text{up,R}}(x;x')$ and $W^B(x;x')$ with $x,x' \in I$
Figure 50	The magnitude of the imaginary parts of $W_{\text{in,R}}(\mathbf{x};\mathbf{x}')$, $W_{\text{up,R}}(\mathbf{x};\mathbf{x}')$ and
rigure 59 –	The magnitude of the imagnary parts of $W_{\text{in,R}}(\mathbf{x},\mathbf{x})$, $W_{\text{up,R}}(\mathbf{x},\mathbf{x})$ and $W^B(\mathbf{x};\mathbf{x}')$ with $\mathbf{x},\mathbf{x}' \in I$
Figure 60	Re $[M^2W_{\text{in,R}}(x;x')]$, Re $[M^2W_{\text{up,R}}(x;x')]$ and Re $[M^2W^B(x;x')]$ with
rigure oo –	L J
D'	$\mathbf{x}, \mathbf{x}' \in I \text{ and } \Delta v > 0.$
Figure 61 –	Im $[M^2W_{\text{in,R}}(x;x')]$, Im $[M^2W_{\text{up,R}}(x;x')]$ and Im $[M^2W^B(x;x')]$ with
F:	$\mathbf{x}, \mathbf{x}' \in I \text{ and } \Delta v > 0.$
Figure 62 –	The non-light-crossing singularities in Re $[M^2W_{\rm up,R}(x;x')]$ and Im $[M^2W_{\rm up,R}(x;x')]$
D: 60	with $x, x' \in I$ and $\Delta v > 0$
Figure 63 –	Model of the behavior of the non-light-crossing singularities in the
	ingoing and upgoing sectors of the Wightman function for the Boulware
T. 64	state $\dots \dots \dots$
Figure 64 –	Magnitudes of Re $[M^2W_{\text{in,R}}(\mathbf{x};\mathbf{x}')]$, Re $[M^2W_{\text{up,R}}(\mathbf{x};\mathbf{x}')]$ and Re $[M^2W^B(\mathbf{x};\mathbf{x}')]$
T. 65	with $x, x' \in I$ and $r' = r \approx 2.1M$
Figure 65 –	Magnitudes of Im $[M^2W_{\text{in,R}}(\mathbf{x};\mathbf{x}')]$, Im $[M^2W_{\text{up,R}}(\mathbf{x};\mathbf{x}')]$ and Im $[M^2W^B(\mathbf{x};\mathbf{x}')]$
_	with $x, x' \in I$ and $r' = r \approx 2.1M$
Figure 66 –	Magnitudes of Re $[M^2W_{\text{in,R}}(x;x')]$, Re $[M^2W_{\text{up,R}}(x;x')]$ and Re $[M^2W^B(x;x')]$
_	with $x, x' \in I$ and $r' = r \approx 2.995M$
Figure 67 –	Magnitudes of Im $[M^2W_{\text{in,R}}(x;x')]$, Im $[M^2W_{\text{up,R}}(x;x')]$ and Im $[M^2W^B(x;x')]$
	with $x, x' \in I$ and $r' = r \approx 2.995M$
	Gravitational lensing of entanglement harvesting from the Boulware state 154
_	Same data as Figure 68 from a different perspective
Figure 70 –	Logarithmic plot version of Figure 69
Figure 71 –	Gravitational lensing of entanglement harvesting from the field in the
	Unruh state
Figure 72 –	Gravitational lensing of entanglement harvesting from the field in the
	Hartle-Hawking state
Figure 73 –	Relative differences between correlation terms in the Boulware state,
	and the Hartle-Hawking and Unruh states
Figure 74 –	Entanglement harvesting from the Boulware state by static detectors at
	antipodal positions close to a Schwarzschild black hole
Figure 75 –	Light propagation coordinate time between detectors in the scenario of
	Figure 74
Figure 76 –	Integrand in Equation (B.1) as a function of $M\omega$ and ℓ for the Boulware
	state
Figure 77 –	Relative difference between the integral in Equation (B.1) for the Boul-
	ware state
Figure 78 –	Summand in Equation (B.1) as a function of ℓ for the Boulware state . 175

Figure 79 –	Relative difference between the ℓ -sum in Equation (B.1) for the Boulware	
	state	175
Figure 80 –	Boulware state integrand in Equation (A.10) after rewriting the integral	
	so that it ranges from $\omega = 0$ to $M\omega = 10 \dots \dots \dots \dots \dots$	177
Figure 81 –	Relative difference in the Boulware state integral in Eq. (A.10) after	
	rewriting the integral so that it ranges from $\omega = 0$ to $\omega = \omega_{cut}$	177
Figure 82 –	Boulware state integral in Equation (A.10), after rewriting the integral	
	so that it ranges from $\omega = 0$ to $\omega = \omega_{cut}$	178
Figure 83 –	Relative difference in the Boulware state integral from Equation (A.10),	
	after rewriting the integral so that it ranges from $\omega = 0$ to $\omega = \omega_{cut}$	178

List of Tables

Table 1 –	Asymptotic infinities of the Maximally extended Schwarzschild spacetime	20
Table 2 -	Horizons and singularities of Schwarzschild spacetime	20
Table 3 -	Regions of the Schwarzschild spacetime in Kruskal-Szekeres coordinates	21
Table 4 -	Definition of the Eddington-Finkelstein coordinates in terms of Kruskal-	
	Szekeres coordinates	22
Table 5 -	Definition of the Schwarzschild coordinates in terms of Eddington-	
	Finkeltesin coordinates	23
Table 6 -	The cut-off of the Jaffé series	51
Table 7 -	Wronskian relations for the radial part of the ingoing modes	53
Table 8 -	Slow convergence of the ω -integrals of $G_{\ell}^{\text{in},R;\text{in},R*}(r,r',\omega)$ and $G_{\ell}^{\text{up},R;\text{up},R*}(r,r',\omega)$	ω) 69
Table 9 -	Convergence of the frequency-smoothed ω -integrals of $G_{\ell}^{\text{in},R;\text{in},R*}(r,r',\omega)$	
	and $G_{\ell}^{\text{up},R;\text{up},R*}(r,r',\omega)$	72
Table 10 -	Example of numerical values of $W_{\text{in}}^{B}(x;x'),W_{\text{up}}^{B}(x;x')$ and $W^{B}(x;x')$	75
Table 11 –	Numerical values of the local noise terms in the three different states	
	considered, for the scenarios in Figure 68, Figure 71 and Figure 72,	
	respectively	158

Contents

1	INTRODUCTION	14
2	THE SCHWARZSCHILD SPACETIME	18
2.1	The Maximal extension	18
2.2	The Schwarzschild-Droste (SD) and Eddington-Finkelstein (EF)	
	coordinates	21
2.3	Geodesics in Schwarzschild spacetime	24
2.3.1	The geodesic equations in Ingoing and Outgoing Eddington-Finkelstein	
	coordinates	26
2.3.1.1	Ingoing Eddington-Finkelstein (IEF) Coordinates	26
2.3.1.2	Outgoing Eddington-Finkelstein (OEF) Coordinates	26
2.3.2	The different behaviors of null geodesics	27
3	QUANTUM FIELD THEORY ON SCHWARZSCHILD SPACETIME	29
3.1	The semi-classical framework	29
3.2	Quantum scalar field	30
3.3	Field modes and quantum states	33
3.3.1	The Eddington-Finkelstein modes	34
3.3.2	The Unruh modes	35
3.3.3	The Quantum states	36
3.4	Wightman function	37
3.4.1	Singularity structure	38
3.4.2	(1+1)D	40
3.4.3	(3+1)D	42
3.4.3.1	The Boulware state	42
3.4.3.2	The Unruh state	42
3.4.3.3	The Hartle-Hawking state	45
4	NUMERICAL EVALUATION OF THE EDDINGTON-FINKELSTEIN	
	MODES	48
4.1	The radial component of the Eddington-Finkelstein modes	48
4.1.1	Ingoing modes	49
4.1.2	Upgoing modes	51
4.1.3	Inside modes	52
4.2	The Wronskian relations	5 3
4.3	Reliability of the numerical solutions to the Schrödinger-like equation	54

4.3.1	The ingoing modes
4.3.2	The inside modes
4.3.3	The upgoing modes
4.3.4	Scattering amplitudes
5	QUANTUM CORRELATIONS IN A SCALAR FIELD IN THE
	SCHWARZSCHILD SPACETIME
5.1	Outside the horizon
5.1.1	The numerical method
5.1.2	Maps of the Wightman function for the Unruh, Boulware and Hartle-Hawking
	states
5.1.3	The quantum relative contribution $W^{\psi}(x,x')$
5.2	Across the horizon
5.3	Singularities in the ingoing and upgoing sectors of the Wightman
	function
5.3.1	The ingoing and upgoing sectors of the Wightman function
5.3.2	Overview of the ingoing and upgoing sectors of the Wightman function 123
5.3.3	The structure of the light-crossing and non-light-crossing singularities 126
5.3.4	The dependence on the r -coordinate
6	LENSING OF ENTANGLEMENT HARVESTING NEAR SCHWARZSCHILD
	BLACK HOLES
6.1	Unruh-DeWitt detectors
6.2	A brief introduction to entanglement harvesting
6.3	Setting up the theoretical experiment
6.4	When is the entanglement extracted versus generated? 150
6.5	Harvesting of gravitationally lensed vacuum entanglement 152
7	CONCLUSION
Α	DENSITY MATRIX CONTRIBUTIONS
В	NUMERICAL TECHNIQUES FOR THE WIGHTMAN FUNCTION 172
B.1	$L_{ extbf{dd}}^{\psi}$ -terms
B.2	M^{ψ} -terms
	Bibliography

1 Introduction

Hawking's paper [2] can be considered as the beginning of a scientific snowball that has been rolling for the last 50 years. In it is the prediction that black holes emit thermal radiation, which still strongly echoes in the community due to its developments.

From an experimental point of view, measuring Hawking radiation is challenging due to its weakness: A Schwarzschild black hole of mass M would emit radiation equivalent to that of a black body with temperature [2]

$$T = \frac{\hbar c^3}{8\pi G M k_B},\tag{1.1}$$

where c is the speed of light in vacuum, \hbar is the reduced Planck constant, G is the gravitational constant and k_B is the Boltzmann constant. For the amusement of the reader, this expression yields a temperature of $\approx 10^{-7} K$ which is seven orders of magnitude below the cosmic microwave background temperature [3]. To the best of our knowledge Hawking radiation has not yet been measured. However there are recent experimental proposals to perform indirect measurements [4, 5]. Despite being extremely challenging, a measurement that either confirms or dispute Hawking radiation from a gravitational black hole can have far reaching consequences in the current understanding of quantum gravity. For instance, a measurement that dispute Hawking radiation would imply that the semi-classical approximation is not correct (or at least not consistent). This relates to the significance of that phenomenon from the theoretical point of view.

From that point of view, the existence of Hawking radiation provides a mechanism to subsidize the relation between black holes and thermodynamics formulated by Bekenstein [6]. That is because until the prediction of Hawking radiation there was no known phenomena to explain how black holes could emit radiation of any kind. Beyond that, Hawking radiation is a quantum phenomenon which suggests that the entropy associated to black holes is of quantum nature. Hence, in the absence of a complete quantum theory of gravity, probing Hawking radiation represents a method to obtain insights into a possible quantum nature of gravity.

An important development in that direction is the so-called information loss puzzle [7], where a seemingly inconsistency between Quantum Mechanics and General Relativity is brought into to the spotlight. It stems from the observation that on a black hole spacetime, a quantum system evolves from a pure state into a mixed state due to the thermal radiation emitted by the black hole. Hence, to advance in its understanding also provides a path to insights into a possible quantum nature of gravity. Recent reviews on this issue are available in [8] and [9].

To proceed in that direction, a possibility is to study the distribution and propagation of correlations in a given state of a quantum field on a black hole spacetime. Within the

scope of the semi-classical framework, where the gravitational field is not quantized, there are two promising approaches to that issue: A direct one where one tries to learn about these correlations from the field's 2-point functions and an indirect one, where one uses another quantum system as a probe for these correlations.

Using the first approach, [10, 11] showed that the field-field correlator (a two-point function known as the Wightman function) of a quantum scalar field on a (1+1)D Schwarzschild spacetime presents no clear signature of the correlations across the horizon. On the other hand, they conclude that there is a signature of correlations across the horizon in the form of a local maxima in the momentum-momentum correlator, that they attribute to Hawking radiation. The same kind of signature also manifests as a local maximum in the field energy density measured by freely-falling observers in opposite sides of the horizon [12]. This was experimentally verified for analogue black holes [13, 14, 15, 16, 17, 18]. Up to the publication of this thesis, there were, to the best of our knowledge, no analogous results regarding the Wightman function for the (3+1)D Schwarzschild spacetime.

Regarding the second approach, a common theoretical experiment consists in evaluating the amount of entanglement acquired by two initially uncorrelated Unruh-DeWitt detectors (2-level quantum systems) after interacting with the background quantum field in a given state. By using the criteria from [19] one can assess if the acquired entanglement results from communication between the detectors mediated by the field or from extracting preexisting entanglement from the field. The second is known as entanglement harvesting [20, 21]. Hence, by studying the configurations that allow the detectors to harvest entanglement, one can attest the existence of preexisting entanglement in the background field.

That method was used to study a massless quantum scalar field on the (1+1)D Schwarzschild spacetime [22, 23, 24] and showed that it is possible to harvest entanglement when both detectors are outside the horizon or on opposite sides of it. To the best of our knowledge, the only result about harvesting in (3+1)D Schwarzschild is our work [1], where we showed that detectors placed outside the horizon at antipodal points can acquire entanglement predominantly by harvesting from the background field, even when the detectors are timelike separated. This is in contrast to the results for (1+1)D, where the entanglement acquired by timelike separated detectors is predominantly due to causal communication through the field. This is an example that illustrates how the (3+1)D case brings with it a richer correlation structure.

In this thesis the main object of study are the correlations in a massless quantum scalar field on a (3+1)D Schwarzschild spacetime. The objective is to advance the current understanding about how correlations are distributed and propagate within that quantum field in scenarios with and without Hawking radiation. For that end, we use the semi-classical framework to computed the Wightman function of that quantum scalar field for the Boulware, Unruh and Hartle-Hawking states by using state-of-the-art numerical methods. In addition, we employ the methods developed here to study entanglement

harvesting outside the horizon of a (3+1)D Schwarzschild black hole.

This thesis is organized as follows: In Chapter 2 we provide an introduction to the Schwarzschild spacetime and the coordinate systems that will be used throughout the text. This is followed by a summary of the geodesic equations for null geodesics and an analysis of their different behaviors.

In Chapter 3 we introduce the semi-classical framework and construct the massless quantum scalar field $\hat{\phi}$ that will be used throughout this thesis using the formulation in [25]. We then construct the Boulware, Unruh and Hartle-Hawking states, which we will analyze in the course of this work. In the next step, we introduce the Wightman function and present its relations with the advanced, retarded and Feynman Green functions as well as its 4-fold singularity structure. Finally, we consider three setups: Both points outside de horizon, both points inside the horizon, and points at opposite sides of the horizon. In each of these, we present a derivation for the Wightman function in the Boulware (only in the first setup), Unruh and Hartle-Hawking states for the (1+1)D and (3+1)D Schwarzschild spacetimes.

In Chapter 4 we present the definitions of the radial Eddington-Finkelstein field modes that are used to reconstruct the Boulware, Unruh and Hartle-Hawking states. To compute them, we use the Jaffé series for the ingoing modes, the Frobenius series for the inside modes and the numerical solution to the upgoing modes implemented in the Black Hole Perturbation Toolkit [26]. With exception of the reflection amplitudes for the ingoing and upgoing modes which were computed via Wronskian relations, all other scattering amplitudes were obtained from the data of [27]. This is followed by a comprehensive study of the reliability and self-consistence of the numerical results obtained in these computations.

Chapter 5 is the largest one and contains our novel results about the Wightman function of $\hat{\phi}$ on a (3+1)D Schwarzschild spacetime. In its first part we construct the numerical method and smoothing schemes used to compute that Wightman function. In it, we also include commentaries on the limitations and possible improvements for that method. We finish this part by reproducing known results for the Retarded Green Function using our method. In the second part we present our results for the case when both points are outside the horizon. The first is the Wightman function for $\hat{\phi}$ in the Boulware, Unruh and Hartle-Hawking states, with one point x fixed outside the horizon and another point x' varying outside. The second one is the difference between the Wightman function for $\hat{\phi}$ in the Unruh and Hartle-Hawking states and the Wightman function for $\hat{\phi}$ in the Boulware state. The final result of the second part of this chapter is the Wightman function for $\hat{\phi}$ in the Unruh and Hartle-Hawking states, with one point x fixed inside and x' varying outside the horizon. In the third and last part of this chapter, we consider a decomposition of the Wightman function as a sum of two terms, one depending only on ingoing and another on upgoing modes. We then consider two points x and x' are on the same r-coordinate

outside the horizon. In that setup, we analyze how changing the value of r affects each of those terms. With that we revealed, for the first time, the singularity structure of the real part of the Wightman function for points on caustics, found a novel structure in the Wightman Function that seems to be a signature of correlations between points on opposite sides of the horizon carried by Hawking radiation and unveiled novel non-light-crossing singularities hidden within the Wightman function.

In Chapter 6 we study entanglement harvesting from $\hat{\phi}$ on the (3+1)D Schwarzschild spacetime. For that end, we consider, two initially uncorrelated and identical Unruh-DeWitt detectors positioned at antipodal points of the black-hole. To quantify the resulting entanglement between the detectors, we computed the negativity of their joint-state. To leading order, it depends, up to properties of the detectors, on an integral of the Wightman function of $\hat{\phi}$. This allowed us to apply the method from Chapter 5 to evaluate these integrals, and hence, the negativity of the joint-state of the detectors. The difference is that here the smoothing function was prescribed by the physical setup. To obtain the results, we considered detectors placed at different radial positions (always on antipodal points around the horizon) and time intervals between the moments when they are maximally turned on. The resulting work is published in [1] with my supervisor, Marc Casals, in collaboration with Robert Jonsson, Achim Kempf and Eduardo-Martín-Martínez. Our key finding here is that when placed on caustic points, the harvesting capacity of the detectors is amplified to the point where it dominates the acquired entanglement even when these detectors are timelike separated.

Unless explicitly stated otherwise, we will use geometrized units $c = G = \hbar = k_B = 1$ and assume Einstein convention for summation over repeated indices throughout the text.

2 The Schwarzschild spacetime

Throughout this chapter, general considerations about the Schwarzschild spacetime are presented to introduce notation, fix conventions, and ensure partial self-containment for this thesis. For an in-depth and mathematically rigorous exploration of this topic, see [25]; for a concise introduction with fewer technical details, [28] is recommended.

The exposition is structured as follows: Section 2.1 presents the maximally extended Schwarzschild spacetime and the Kruskal-Szekeres (KS) coordinates. Section 2.2 introduces the Schwarzschild-Droste (SD) and Eddington-Finkelstein (EF) coordinate systems. Finally, Section 2.3 derives the conserved quantities associated with motion in this spacetime and constructs the corresponding geodesic equations.

2.1 The Maximal extension

The maximally extended Schwarzschild spacetime is a 4-dimensional manifold equipped with a metric \mathbf{g} that is a vacuum solution to Einstein's equations in (3+1) dimensions. In Kruskal-Szekeres (KS) coordinates

$$(U, V, \theta, \varphi), \quad U \in \mathbb{R}, \ V \in \mathbb{R}, \ \theta \in [0, \pi], \ \varphi \in [0, 2\pi),$$
 (2.1)

it takes the form [25]

$$ds^{2} = -\frac{32M^{3}}{r}e^{-r/2M} dU dV + r^{2} \left(d\theta^{2} + \sin^{2}(\theta) d\varphi^{2}\right).$$
 (2.2)

Here, M denotes the black-hole mass, and r is implicitly defined as a function of U and V via

$$UV = \left(1 - \frac{r}{r_s}\right) e^{r/r_s},\tag{2.3}$$

where $r_s = 2M$ is the Schwarzschild radius.

As usual, a vector \vec{V} of the tangent space to \mathfrak{S} at a point $x \in \mathfrak{S}$ is classified as: timelike if $g(\vec{V}, \vec{V}) < 0$, null if $g(\vec{V}, \vec{V}) = 0$ and spacelike if $g(\vec{V}, \vec{V}) > 0$.

The conformal (Penrose-Carter) diagram of \mathfrak{S} is shown in Figure 1. Its construction is well documented, with detailed treatments available in [29, Section 5.1.3] and [25, Section 6.4]. In this diagram, \mathfrak{S} is partitioned into four causal patches (I–IV). The asymptotic regions are given by the union:

$$i_R^+ \cup i_R^- \cup i_R^0 \cup \mathscr{I}_R^+ \cup \mathscr{I}_R^- \cup i_L^+ \cup i_L^- \cup i_L^0 \cup \mathscr{I}_L^+ \cup \mathscr{I}_L^-,$$

where the components are defined in terms of Kruskal-Szekeres (KS) coordinates in Table 1.

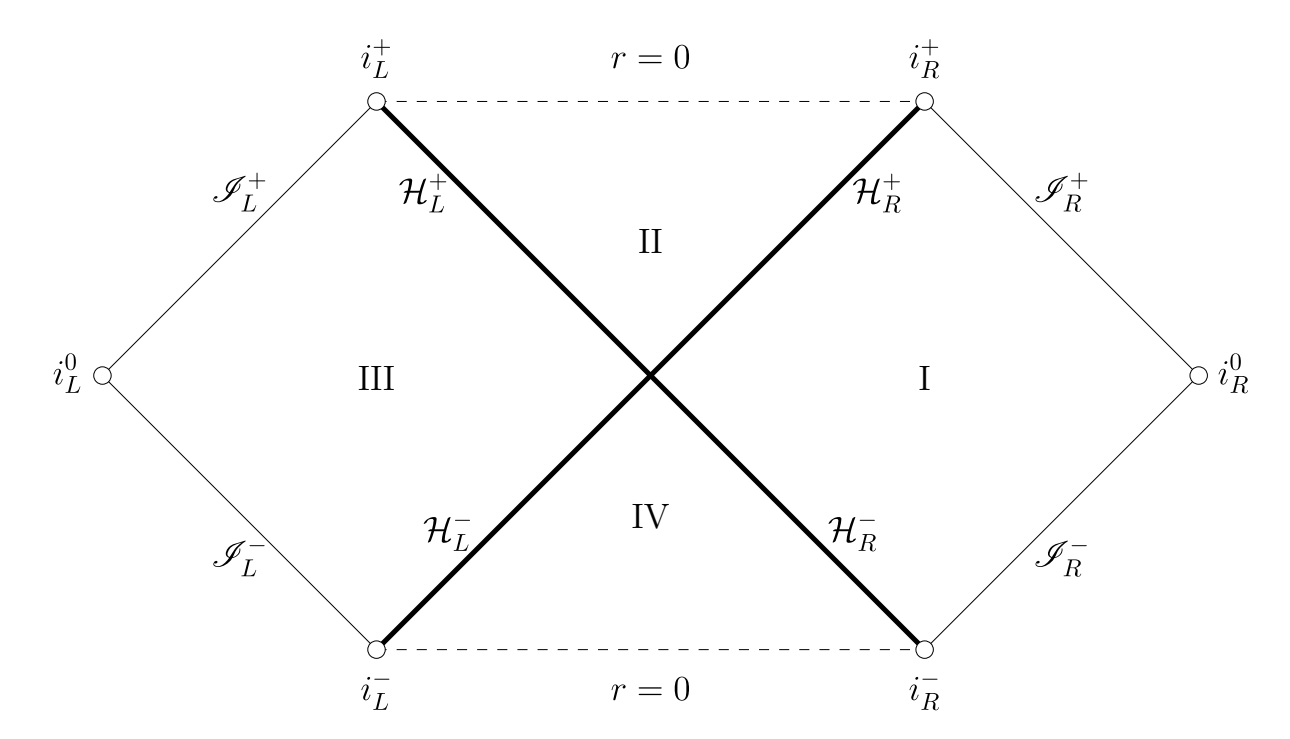


Figure 1 – Penrose-Carter conformal diagram for the maximally extended Schwarzschild spacetime. In this illustration, thin lines and circles are part of the boundary $\mathfrak S$ of the spacetime manifold while thick lines are part of the spacetime. The thin dashed horizontal lines represent the singularities at r=0, the thick lines represent the horizons $\mathcal H_{R/L}^\pm$, the thin lines represent the null infinities $\mathscr S_{R/L}^\pm$ and the circles represent the spacelike $i_{R/L}^0$ and timelike $i_{R/L}^\pm$ infinities. Regions I–IV correspond to distinct causal patches of the spacetime.

Alongside the asymptotic infinities, the horizons

$$\mathcal{H}_R^+ \cup \mathcal{H}_R^- \cup \mathcal{H}_L^+ \cup \mathcal{H}_L^-,$$

located at $r = r_s = 2M$, and the curvature singularities at r = 0 are also represented in the conformal diagram. Their definitions in terms of Kruskal-Szekeres (KS) coordinates are summarized in Table 2. For a matter of convenience, the convention adopted in this text is different from the one in [29], which refers to $\mathcal{H}_R^+ \cup \mathcal{H}_L^-$ as the event horizon \mathcal{H}^+ and to $\mathcal{H}_L^+ \cup \mathcal{H}_L^-$ as the past horizon \mathcal{H}^- .

Finally, the definition of regions I-IV, in terms of KS coordinates is presented in table 3.

While the KS coordinates are globally regular (non-singular) across \mathfrak{S} , the numerical methods developed in Chapter 4 to compute radial modes of a scalar field rely on Eddington-Finkelstein (EF) coordinates. This choice stems from the advantageous separability of the field equations in EF coordinates, as detailed in Section 4.1. To establish the basis of this framework, we introduce both EF and Schwarzschild-Droste (SD) coordinates in the following section.

Region	Name	Symbol	Set
	Future timelike infinity	i_R^+	$\{x \in \partial \mathfrak{S} ; V \to \infty, U \to 0\}$
	Future null infinity	\mathscr{I}_R^+	$\{{\bf x}\in\partial\mathfrak{S};V\to\infty,U<0\}$
I	Spacelike infinity	i_R^0	$\{{\sf x}\in\partial\mathfrak{S};V\to\infty,U=-V\}$
	Past null infinity	\mathscr{I}_R^-	$\{{\bf x}\in\partial\mathfrak{S};V>0,U\to-\infty\}$
	Past timelike infinity	i_R^-	$\{x \in \partial \mathfrak{S} ; V \to 0_+, U \to -\infty\}$
	Future timelike infinity	i_L^+	$\{x\in\partial\mathfrak{S};V\to0,U\to\infty\}$
	Future null infinity	\mathscr{I}_L^+	$\{{\bf x}\in\partial\mathfrak{S};V<0,U\to\infty\}$
III	Spacelike infinity	i_L^0	$\{{\sf x}\in\partial\mathfrak{S};V\to-\infty,U=-V\}$
	Past null infinity	\mathscr{I}_L^-	$\{{\bf x}\in\partial\mathfrak{S};V\to-\infty,U>0\}$
	Past timelike infinity	i_L^-	$\{x \in \partial \mathfrak{S} ; V \to -\infty, U \to 0_+\}$

Table 1 – The asymptotic infinities of the Schwarzschild spacetime. These are boundary surfaces in the conformal compactification (not part of $\mathfrak S$ itself), as illustrated in figure 1. Specifically, the timelike $i_{R/L}^\pm$ and spacelike $i_{R/L}^0$ infinities are 3-dimensional surfaces while the null infinities $\mathscr{I}_{R/L}^\pm$ are 3-dimensional null hypersurfaces. The definitions used here follow the conventions in [30, Section 5.1].

Region	Name	Symbol	Set
I	Future horizon	\mathcal{H}_R^+	$\{x\in\mathfrak{S};V>0,U=0\}$
1	Past horizon	\mathcal{H}_R^-	$\{\mathbf{x}\in\mathfrak{S};V=0,U<0\}$
II	Singularity	-	$\{x\in\mathfrak{S}\:;\:V>0\:,\:UV=1\}$
III	Future horizon	\mathcal{H}_L^+	$\{\mathbf{x}\in\mathfrak{S};V=0,U>0\}$
111	Past horizon	\mathcal{H}_L^-	$\{\mathbf{x}\in\mathfrak{S}\:;\:V<0\:,\:U=0\}$
\overline{IV}	Singularity	_	$\{x\in\mathfrak{S};V<0,UV=1\}$

Table 2 – The horizons and singularities of the Maximally extended Schwarzschild spacetime are presented in terms of KS-coordinates. The singularities are spacelike hypersurfaces at r=0 and the horizons are null hypersurfaces at $r=r_s$ defined by U=0 or V=0 in KS-coordinates. The definitions used here follow the conventions in [30, Section 5.1].

Region	Name	Set
\overline{I}	Universe	$\{x\in\mathfrak{S};V>0,U<0\}$
II	Black hole	$\{\mathbf{x}\in\mathfrak{S};V>0,U>0\}$
III	Parallel Universe	$\{\mathbf{x}\in\mathfrak{S};V<0,U>0\}$
IV	White hole	$\{\mathbf{x}\in\mathfrak{S};V<0,U<0\}$

Table 3 – Definitions of the universe, black hole, parallel universe and white hole regions of the maximally extended Schwarzschild spacetime in terms of KS coordinates.

2.2 The Schwarzschild-Droste (SD) and Eddington-Finkelstein (EF) coordinates

Standard general relativity textbooks (e.g., [25, 31]) typically introduce SD-coordinates first, followed by the maximal extension of the Schwarzschild spacetime using KS-coordinates, with Eddington-Finkelstein (EF) coordinates appearing as intermediate tools. However, SD and EF coordinates are not globally defined on \mathfrak{S} ; covering the entire spacetime requires four distinct coordinate patches of either system. To emphasize this limitation, this work reverses the traditional order: Section 2.1 begins with the singularity-free KS coordinates, which are globally valid. We now turn to the SD and EF-coordinates. The angular coordinates (θ , φ) are identical across KS, EF, and SD systems. For brevity, these will be omitted in subsequent equations where no ambiguity arises

From the KS coordinates (U, V), we define four coordinates $u, \bar{u}, v, \bar{v} \in \mathbb{R}$ and construct four patches of EF-coordinates that together cover \mathfrak{S} , as presented in table 4. When expressed in EF-coordinates, the line element 2.2 in region I takes the form

$$ds^{2} = -f(r) du dv + r^{2} \left(d\theta^{2} + \sin^{2}(\theta) d\varphi^{2} \right), \qquad (2.4)$$

where $f(r) = \left(1 - \frac{r_s}{r}\right)$. In regions II-IV the metric can be obtained by substituting $du \to d\bar{u}$ and $dv \to d\bar{v}$ as needed, preserving the structure of (2.4) across all patches.

To visualize the relationship between EF and KS-coordinates, Figure 2 illustrates their axes on the conformal diagram of \mathfrak{S} . This diagram clarifies how the EF coordinates extend across the horizons $(r = r_s)$ in each region. Specifically, coordinates v and \bar{v} are continuous across $I \cup II$ and $III \cup IV$, respectively; u and \bar{u} similarly span $I \cup IV$ and $II \cup III$.

We now turn to the SD-coordinates. As an accessory, we define an implicit function r_* of r(U,V) such that

$$\frac{\mathrm{d}r_*}{\mathrm{d}r} = \left(1 - \frac{r_s}{r}\right)^{-1},\tag{2.5}$$

known as the tortoise-coordinate. This equation admits two distinct solutions: One for $r > r_s$ that will be called r_* and another for $r < r_s$ which will be referred to as \bar{r}_* .

Covered region	EF coordinates	Definition
I	(u,v)	$\begin{cases} U = -e^{-u/(2r_s)} \\ V = e^{v/(2r_s)} \end{cases}$
II	(\bar{u},v)	$\begin{cases} U = e^{\bar{u}/(2r_s)} \\ V = e^{v/(2r_s)} \end{cases}$
III	$(ar{u},ar{v})$	$\begin{cases} U = e^{\bar{u}/(2r_s)} \\ V = -e^{-\bar{v}/(2r_s)} \end{cases}$
IV	$(u,ar{v})$	$\begin{cases} U = -e^{-u/(2r_s)} \\ V = -e^{-\bar{v}/(2r_s)} \end{cases}$

Table 4 – The four EF-coordinate patches covering the maximally extended Schwarzschild spacetime are defined via KS-coordinates. Regions I–IV correspond to those in the conformal diagram in Fig. 1. We adopted the same convention as [32, Section II.A] to define the EF-coordinates.

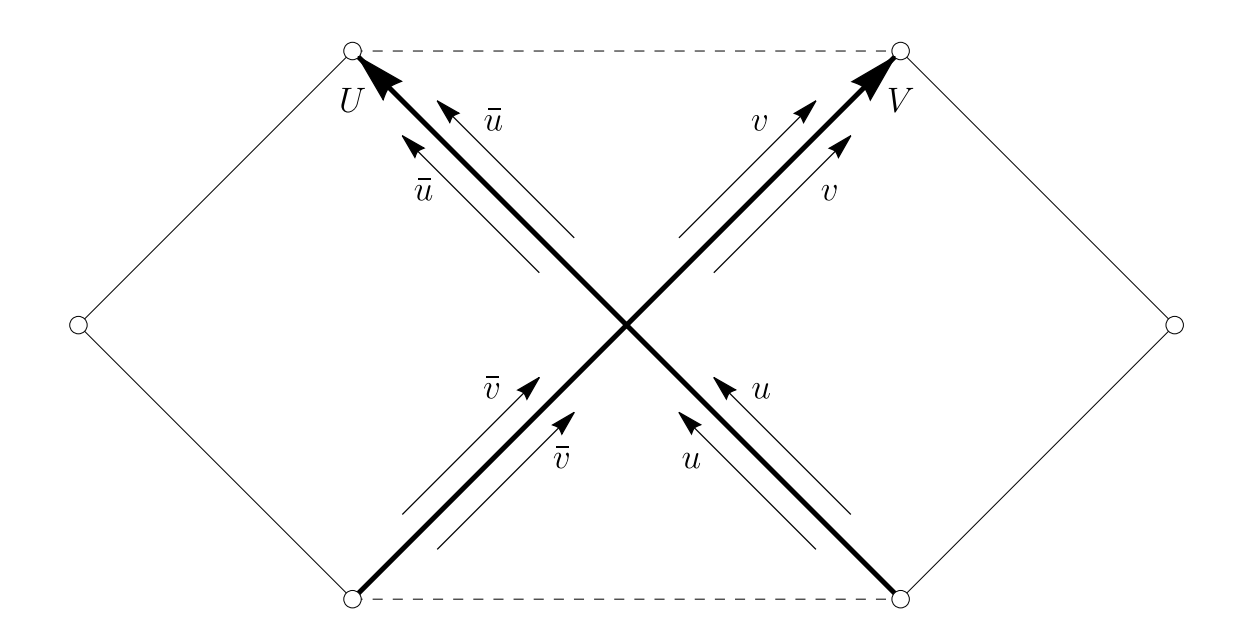


Figure 2 – Penrose-Carter conformal diagram for the maximally extended Schwarzschild spacetime, showing the coordinate axes of Kruskal-Szekeres (KS) and Eddington-Finkelstein (EF) coordinates.

Covered region	SD coordinates	Definition
I	(r_I,t_I)	$\begin{cases} u = t_I - r_{*I} \\ v = t_I + r_{*I} \end{cases}$
II	(r_{II},t_{II})	$\begin{cases} \bar{u} = t_{II} - \bar{r}_{*II} \\ v = t_{II} + \bar{r}_{*II} \end{cases}$
III	$\left(r_{III},t_{III} ight)$	$\begin{cases} \bar{u} = t_{III} - r_{*III} \\ \bar{v} = t_{III} + r_{*III} \end{cases}$
IV	(r_{IV},t_{IV})	$\begin{cases} u = t_{IV} - \bar{r}_{*IV} \\ \bar{v} = t_{IV} + \bar{r}_{*IV} \end{cases}$

Table 5 – The four patches of Schwarzschild-Droste (SD) coordinates covering \mathfrak{S} are defined in terms of Eddington-Finkelstein (EF) coordinates.

Explicitly, these solutions are

$$r_* = r + r_s \ln\left(\frac{r}{r_s} - 1\right), r > r_s \tag{2.6}$$

and

$$\bar{r}_* = r + r_s \ln \left(1 - \frac{r}{r_s} \right), \ r < r_s,$$
 (2.7)

where the integration constant has been set to zero for simplicity.

While many texts combine these cases using an absolute value inside the logarithm (e.g., $r_* = r + r_s \ln |\frac{r}{r_s} - 1|$), this convention obscures the lack of bijectivity between r_* and r. Specifically, the absolute value renders the function non-invertible: distinct r values (e.g., $r > r_s$ and $r < r_s$) map to overlapping regions of r_* , complicating coordinate transformations. By separating the solutions into r_* (exterior) and \bar{r}_* (interior), we preserve invertibility and maintain clarity in subsequent analyses.

Using the tortoise coordinate r_* (and its interior counterpart \bar{r}_* defined in (2.6)–(2.7)), we construct four SD-coordinate patches covering \mathfrak{S} . Each patch comprises a radial coordinate $r_{\alpha} \in \mathbb{R}_{\geq 0}$ and a time coordinate $t_{\alpha} \in \mathbb{R}$, where $\alpha \in \{I, II, III, IV\}$ denotes the spacetime region, together with the angular coordinates θ, φ . Specifically, $r_I, r_{III} \in (r_s, \infty)$ and $r_{II}, r_{IV} \in (0, r_s)$).

The explicit mappings between SD coordinates (t_{α}, r_{α}) and EF coordinates are summarized in Table 5, where $r_{*\alpha}$ and $\bar{r}_{*\alpha}$ are treated as functions of r_{α} , ensuring invertibility within their respective domains. In these coordinates, the line element 2.2 in region I takes the form

$$ds^{2} = -f(r_{I}) dt_{I}^{2} + f(r_{I})^{-1} dr_{I}^{2} + r_{I}^{2} (d\theta^{2} + \sin^{2}(\theta) d\varphi^{2}).$$
(2.8)

The expressions for the other regions can be obtained by substituting t_I and r_I by the t and r-coordinates of the desired region. For completeness, the lines of constant t_{α} and r_{α} , where

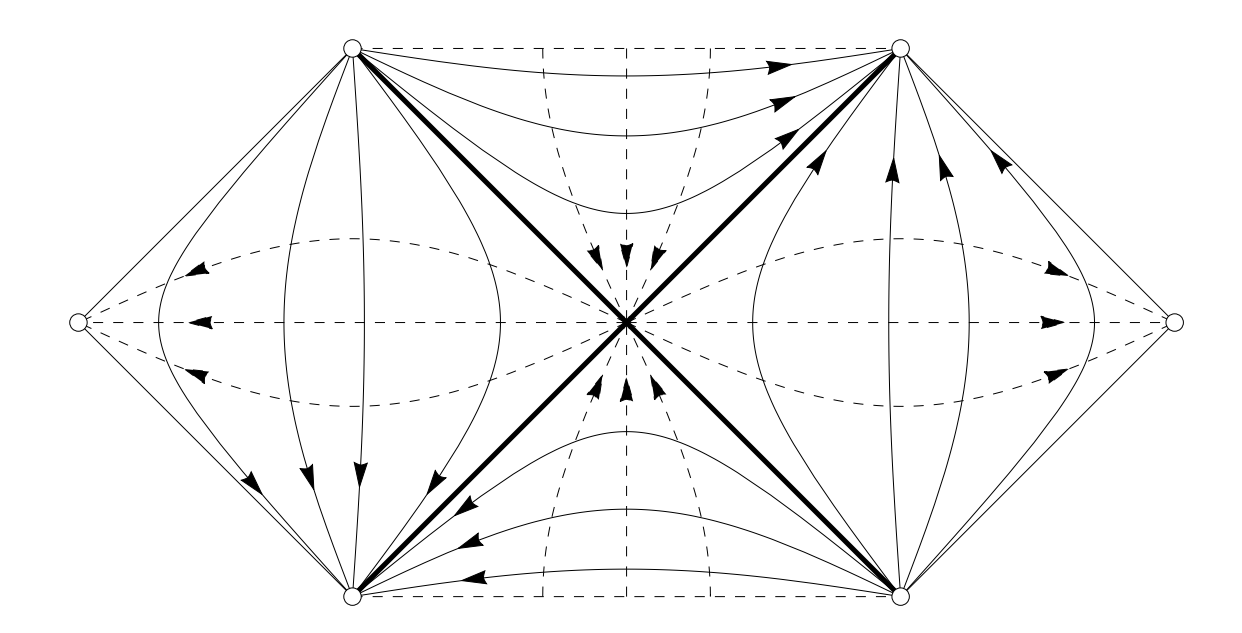


Figure 3 – Penrose-Carter conformal diagram of the Schwarzschild spacetime. The lines of constant $t_{I,II,III,IV}$ are the thin dashed lines and the arrowheads point towards increasing $r_{I,II,III,IV}$. The lines of constant $r_{I,II,III,IV}$ are the thin lines with arrowheads indicating the direction of increasing $t_{I,II,III,IV}$.

 $\alpha \in \{I, II, III, IV\}$, are represented on a conformal diagram in figure 3. Throughout the text the label indicating which region a given SD-coordinate describes will be suppressed whenever no ambiguity arises.

2.3 Geodesics in Schwarzschild spacetime

Let ∇ be a covariant derivative on \mathfrak{S} . A geodesic is defined as a curve $\gamma: \mathbb{R} \to \mathfrak{S}$, parametrized by $b \in \mathbb{R}$, such that its tangent vector $\dot{\gamma} = \frac{d\gamma}{db}$ obeys

$$\dot{\gamma}^{\mu} \nabla_{\mu} \dot{\gamma}^{\nu} = \alpha \dot{\gamma}^{\nu}, \tag{2.9}$$

for some scalar $\alpha \in \mathbb{R}$. It is always possible to re-parametrize γ by a parameter $\lambda \in \mathbb{R}$ in such a way that

$$\dot{\gamma}^{\mu} \nabla_{\mu} \dot{\gamma}^{\nu} = 0. \tag{2.10}$$

In this case, λ is called an affine-parameter. Following [25, Section 3.3], we define this expression as the geodesic equation.

In an arbitrary coordinate system $\{x^{\alpha}\}$ with $\alpha \in \{0, 1, 2, 3\}$, the components of the geodesic equation (2.10) are

$$\frac{\mathrm{d}^2 x^{\mu}}{\mathrm{d}\lambda^2} + \Gamma^{\mu}_{\alpha\beta} \frac{\mathrm{d}x^{\alpha}}{\mathrm{d}\lambda} \frac{\mathrm{d}x^{\beta}}{\mathrm{d}\lambda} = 0, \tag{2.11}$$

where $\Gamma^{\mu}_{\alpha\beta}$ are the Christoffel symbols which depend upon the choice of the covariant derivative.

By [25, Theorem 3.1.1], there exists a unique choice of covariant derivative such that

$$\nabla_{\mu} \mathbf{g}_{\alpha\beta} = 0. \tag{2.12}$$

This equation is known as the metric compatibility condition and uniquely determines the Christoffel symbols

$$\Gamma^{\mu}_{\alpha\beta} = \frac{1}{2} g^{\mu\nu} \left(\partial_{\alpha} g_{\nu\beta} + \partial_{\beta} g_{\alpha\nu} - \partial_{\nu} g_{\alpha\beta} \right), \tag{2.13}$$

where $\partial_{\alpha} = \partial/\partial x^{\alpha}$. Until the end of this thesis, this choice of covariant derivative operator is assumed.

The geodesic equations on \mathfrak{S} constitute a system of four coupled second order differential equations with solutions determined by eight boundary conditions. Due to the curvature of \mathfrak{S} the uniqueness of a geodesic connecting two points x_A and x_B of \mathfrak{S} is guaranteed only when x_B lies within x_A 's normal neighborhood $\mathcal{N}(x_A)$ - a region where every $x_B \in \mathcal{N}(x_A)$ is linked to x_A by a unique geodesic entirely contained in $\mathcal{N}(x_A)$.

The symmetries of \mathfrak{S} yield four Killing vector fields, which imply four conserved quantities along geodesics. Expressed in SD-coordinates for region I,

$$\vec{\varepsilon_t} = \partial_t, \tag{2.14}$$

is a Killing vector field that is timelike when $r > r_s$ and spacelike when $r < r_s$. It reflects the t-coordinate translation symmetry of \mathfrak{S} .

$$\vec{\varepsilon_{\varphi}} = \partial_{\varphi}, \quad \vec{\varepsilon_{a}} = \sin(\varphi)\partial_{\theta} + \cot(\theta)\cos(\varphi)\partial_{\varphi} \quad \text{and} \quad \vec{\varepsilon_{b}} = \cos(\varphi)\partial_{\theta} - \cot(\theta)\sin(\varphi)\partial_{\varphi}, \quad (2.15)$$

are spacelike Killing vector fields, which reflect the spherical symmetry of \mathfrak{S} . In the notation adopted, the subscripts t, φ, a, b label distinct Killing vectors, not tensor components. For example, the μ -component of $\vec{\varepsilon_t}$ is denoted $(\varepsilon_t)^{\mu}$.

Each Killing vector $\vec{\varepsilon}$ yields a quantity $\eta = \varepsilon^{\mu}\dot{\gamma}_{\mu}$ that is conserved along a geodesic γ affinely parametrized by $\lambda \in \mathbb{R}$. In \mathfrak{S} , they are

$$\eta_t = (\varepsilon_t)^\mu \dot{\gamma}_\mu = -f(r) \frac{\mathrm{d}t}{\mathrm{d}\lambda},$$
(2.16)

$$\eta_{\varphi} = (\varepsilon_{\varphi})^{\mu} \dot{\gamma}_{\mu} = r^2 \sin(\theta)^2 \frac{\mathrm{d}\varphi}{\mathrm{d}\lambda},$$
(2.17)

$$\eta_a = (\varepsilon_a)^{\mu} \dot{\gamma}_{\mu} = r^2 \left(\sin(\varphi) \frac{\mathrm{d}\theta}{\mathrm{d}\lambda} + \cos(\varphi) \sin(\theta) \cos(\theta) \frac{\mathrm{d}\varphi}{\mathrm{d}\lambda} \right)$$
(2.18)

and

$$\eta_b = (\varepsilon_b)^{\mu} \dot{\gamma}_{\mu} = r^2 \left(\cos(\varphi) \frac{\mathrm{d}\theta}{\mathrm{d}\lambda} - \sin(\varphi) \sin(\theta) \sin(\theta) \frac{\mathrm{d}\varphi}{\mathrm{d}\lambda} \right). \tag{2.19}$$

In addition to these quantities, by using equation (2.9) one can show that

$$\mathscr{C} = \dot{\gamma}_{\mu}\dot{\gamma}^{\mu} = -f(r)\left(\frac{\mathrm{d}t}{\mathrm{d}\lambda}\right)^{2} + f(r)^{-1}\left(\frac{\mathrm{d}r}{\mathrm{d}\lambda}\right)^{2} + r^{2}\left(\frac{\mathrm{d}\theta}{\mathrm{d}\lambda}\right)^{2} + r^{2}\sin(\theta)^{2}\left(\frac{\mathrm{d}\varphi}{\mathrm{d}\lambda}\right)^{2}$$
(2.20)

is also conserved along γ . On a timelike (spacelike) geodesic one can always choose the proper time (length) as the affine-parameter to get $\mathscr{C} = -1$ (+1). On a null geodesic $\dot{\gamma}_{\mu}$ is a null vector by definition, hence $\mathscr{C} = 0$.

2.3.1 The geodesic equations in Ingoing and Outgoing Eddington-Finkelstein coordinates

Due to the spherical symmetry of \mathfrak{S} the study of geodesics can be confined to the $\theta = \pi/2$ plane without loss of generality. Below the geodesic equations in Ingoing Eddington-Finkelstein (IEF) and Outgoing Eddington-Finkelstein (OEF) coordinates are derived, emphasizing their utility for trajectories crossing horizons.

2.3.1.1 Ingoing Eddington-Finkelstein (IEF) Coordinates

For geodesics traveling from the universe (region I) into the black hole (region II) the IEF-coordinates offer a convenient description due to its regularity across $I \cup II$. In this region, these coordinates consist in a combination of the EF-coordinate v with the SD-coordinate r. Therefore, the IEF coordinates in $I \cup II$ are (v, r, θ, φ) .

In these coordinates, the conserved quantities (2.16), (2.17) and (2.20) are

$$\eta_t = -f(r)\frac{\mathrm{d}v}{\mathrm{d}\lambda} + \frac{\mathrm{d}r}{\mathrm{d}\lambda},\tag{2.21}$$

$$\eta_{\varphi} = r^2 \frac{\mathrm{d}\varphi}{\mathrm{d}\lambda} \text{ and}$$
(2.22)

$$\mathscr{C} = -f(r) \left(\frac{\mathrm{d}v}{\mathrm{d}\lambda}\right)^2 + 2\frac{\mathrm{d}v}{\mathrm{d}\lambda}\frac{\mathrm{d}r}{\mathrm{d}\lambda} + r^2 \left(\frac{\mathrm{d}\varphi}{\mathrm{d}\lambda}\right)^2. \tag{2.23}$$

Substituting these into the geodesic equations (2.11) yields

$$\frac{\mathrm{d}^2 v}{\mathrm{d}\lambda^2} + \frac{r_s}{2r^2} \left(\frac{\mathrm{d}v}{\mathrm{d}\lambda}\right)^2 - \frac{1}{r^3} \eta_{\varphi}^2 = 0$$

$$\frac{\mathrm{d}^2 r}{\mathrm{d}\lambda^2} + \frac{r_s}{2r^2} \left(\frac{\eta_{\varphi}^2}{r^2} - \mathscr{C}\right) - f(r) \frac{\eta_{\varphi}^2}{r^3} = 0$$

$$\frac{\mathrm{d}^2 \varphi}{\mathrm{d}\lambda^2} + \frac{2}{r} \frac{\mathrm{d}r}{\mathrm{d}\lambda} \frac{\mathrm{d}\varphi}{\mathrm{d}\lambda} = 0.$$
(2.24)

2.3.1.2 Outgoing Eddington-Finkelstein (OEF) Coordinates

For geodesics traveling from the universe (region I) into the black hole (region II) the IEF-coordinates offer a convenient description due to its regularity across $I \cup II$. In this region, these coordinates consist in a combination of the EF-coordinate v with the SD-coordinate r. Therefore, the IEF coordinates in $I \cup II$ are (v, r, θ, φ) .

For geodesics escaping the white hole (region IV) into the universe (region I), the OEF-coordinates are employed due to their regularity across $IV \cup I$. In this region, it

consists in a combination of the EF-coordinate u with the SD-coordinate r. Hence, the OEF coordinates in $IV \cup I$ are (u, r, θ, φ) .

In these coordinates, the conserved quantities (2.16), (2.17) and (2.20) are

$$\eta_t = -f(r)\frac{\mathrm{d}u}{\mathrm{d}\lambda} - \frac{\mathrm{d}r}{\mathrm{d}\lambda},\tag{2.25}$$

$$\eta_{\varphi} = r^2 \frac{\mathrm{d}\varphi}{\mathrm{d}\lambda}$$
 and (2.26)

$$\mathscr{C} = -f(r) \left(\frac{\mathrm{d}u}{\mathrm{d}\lambda}\right)^2 - 2\frac{\mathrm{d}u}{\mathrm{d}\lambda}\frac{\mathrm{d}r}{\mathrm{d}\lambda} + r^2 \left(\frac{\mathrm{d}\varphi}{\mathrm{d}\lambda}\right)^2. \tag{2.27}$$

Substituting these into the geodesic equations (2.11) results in

$$\frac{\mathrm{d}^2 u}{\mathrm{d}\lambda^2} - \frac{r_s}{2r^2} \left(\frac{\mathrm{d}u}{\mathrm{d}\lambda}\right)^2 + \frac{1}{r^3} \eta_{\varphi}^2 = 0$$

$$\frac{\mathrm{d}^2 r}{\mathrm{d}\lambda^2} + \frac{r_s}{2r^2} \left(\frac{\eta_{\varphi}^2}{r^2} - \mathcal{C}\right) - f(r) \frac{\eta_{\varphi}^2}{r^3} = 0$$

$$\frac{\mathrm{d}^2 \varphi}{\mathrm{d}\lambda^2} + \frac{2}{r} \frac{\mathrm{d}r}{\mathrm{d}\lambda} \frac{\mathrm{d}\varphi}{\mathrm{d}\lambda} = 0.$$
(2.28)

2.3.2 The different behaviors of null geodesics

To characterize the behavior of the null geodesics in Schwarzschild, we use Equations (2.16), (2.17) and (2.20) as in [33, Equation (5)] to write

$$\eta_t^2 = \left(\frac{\mathrm{d}r}{\mathrm{d}\lambda}\right)^2 + \left(1 - \frac{r_s}{r}\right)\frac{\eta_\phi^2}{r^2},\tag{2.29}$$

where λ is an affine parameter. From this equation we can read the effective potential for the r-coordinate of the null geodesics as

$$V(r) = \left(1 - \frac{r_s}{r}\right) \frac{\eta_\phi^2}{r^2}.\tag{2.30}$$

A plot of this effective potential is presented in Figure 4. It has a single local maxima of $\frac{4\eta_{\phi}^2}{27r_s^2}$ at $r=3r_s/2=3M$, a region known as the photonsphere, where there exists circular null geodesics. For the sake of simplicity, we define the impact parameter $\varepsilon=\eta_{\phi}/\eta_t$.

For the purpose of this thesis, we are interested in the null geodesics that are launched from the horizon $(r=r_s)$ towards infinity $(r\to\infty)$ or from infinity towards the singularity. In both cases, equation (2.29) implies that the effective potential at these points is zero and $\frac{\mathrm{d}r}{\mathrm{d}\lambda}^2 = \eta_t^2$. We now divide the further analyses in a three sub-cases: $\frac{4\eta_\phi^2}{27r_s^2} < \eta_t^2$, $\frac{4\eta_\phi^2}{27r_s^2} = \eta_t^2$ and $\frac{4\eta_\phi^2}{27r_s^2} > \eta_t^2$.

The first case, $\frac{4\eta_{\phi}^2}{27r_s^2} < \eta_t^2$, can be re-stated in terms of the impact parameter as $\varepsilon^2 < 27r_s^2/4$. When this condition is fulfilled, the the null geodesics launched from the horizon do reach infinity and those launched from infinity ends up at the singularity. Hence, in this case there is no turning point. In Figure 4 this is depicted by the yellow region.

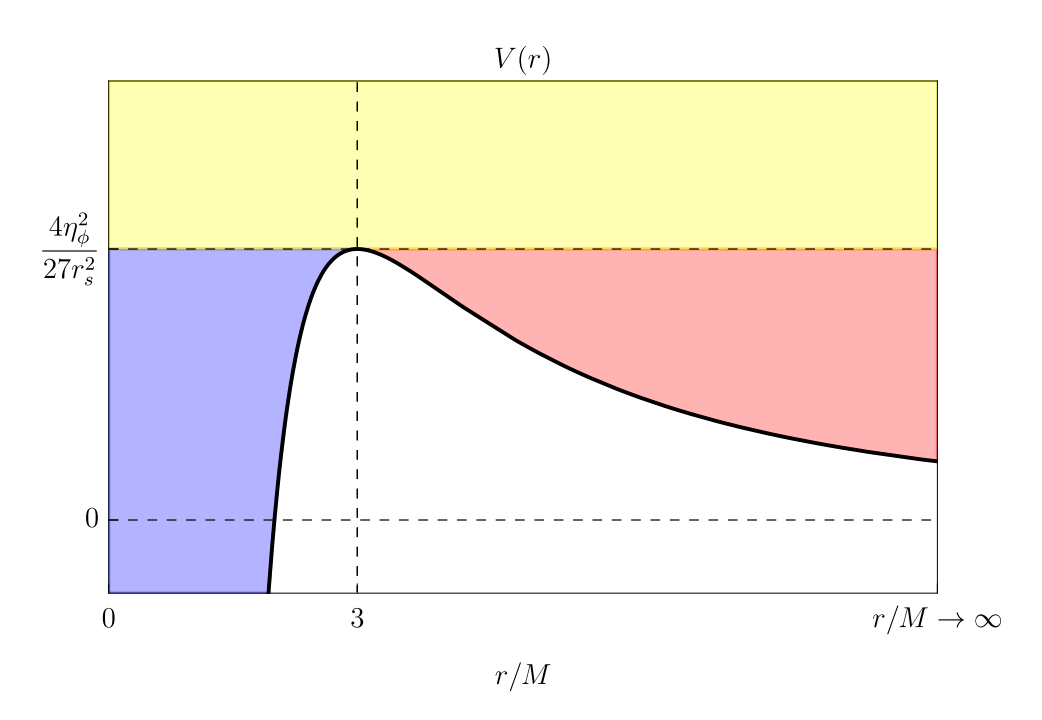


Figure 4 – The effective potential V(r) (Equation (2.30)) for the null geodesics. The value of the peak $(\frac{4\eta_{\phi}^2}{27r_s^2})$ as well as its location (r=3M) are marked by dashed lines. The effective potential is zero at the horizon $r=r_s$ and decays to zero as $r\to\infty$. Inside the horizon it decays to $-\infty$ as $r\to0$. There are three shaded regions in the plot. The yellow region is where the null geodesics launched from $r=r_s$ $(r\to\infty)$ can reach $r\to\infty$ $(r=r_s)$. In the blue region, the null geodesics launched from $r=r_s$ are confined between a turning point below the photonsphere and the singularity. Hence, these null geodesics are recaptured by the black hole. In the red region, the null geodesics launched from $r\to\infty$ are confined between a turning point above the photonsphere and $r\to\infty$, these null geodesics escape to infinity. This effective potential shows that if a null geodesic (with non-zero impact parameter) crosses the photonsphere, it will never meet a turning point.

The second case, $\frac{4\eta_{\phi}^2}{27r_s^2} = \eta_t^2$ can be re-written as $\varepsilon^2 = 27r_s^2/4$. In this the case, the null geodesics launched from the horizon and from infinity reach an unstable equilibrium point at the photonsphere and becomes trapped. In Figure 4 this is the local maximum of the effective potential.

The third case, $\frac{4\eta_{\phi}^2}{27r_s^2} > \eta_t^2$, can be cast as $\varepsilon^2 > 27r_s^2/4$. In this case the null geodesics launched from the horizon meet a turning point below the photonsphere and are deflected back to the singularity. Hence, these geodesics are trapped below the photonsphere. In Figure 4 this is depicted as a blue region. On the other hand, the null geodesics launched from infinity meet a turning point above the photonsphere and are deflected back to infinity. In contrast to the null geodesics launched from the horizon, the ones launched from infinity are trapped above the photonsphere. This is depicted by the red region in Figure 4.

3 Quantum Field Theory on Schwarzschild spacetime

This chapter develops the quantization of a massless scalar field on the Schwarzschild spacetime and the construction of the Wightman function. While this material is well-trodden in foundational texts [34, 25, 35], the presentation here is tailored to also embrace readers with less experience in quantum field theory in curved spacetimes.

This chapter is structured as follows: Section 3.1 introduces the semi-classical framework. Section ?? summarizes the process of quantization of a massless scalar field presented in [34]. Section 3.3 introduces the field modes with which we to construct the Boulware, Unruh and Hartle-Hawking vacua. Finally, Section 3.4 defines the Wightman function and derives its expression for several setups in the (1+1)D and (3+1)D versions of the Schwarzschild spacetime.

3.1 The semi-classical framework

To clarify the interplay between quantum matter and spacetime geometry, we temporarily restore dimensional constants (\hbar, G, c) in this section.

In the paradigm of Classical General Relativity (GR), the Einstein Field Equations (EFE) describe the relation between matter and the spacetime:

$$G_{\mu\nu} = \frac{8\pi G}{c^4} T_{\mu\nu},\tag{3.1}$$

where

$$G_{\mu\nu} = R_{\mu\nu} - \frac{1}{2} R g_{\mu\nu} \tag{3.2}$$

is the Einstein tensor, $R_{\mu\nu}$ is the Ricci tensor, $R=Tr(R_{\mu\nu})$ is the scalar curvature and

$$T_{\mu\nu} = \frac{-2}{\sqrt{-g}} \frac{\delta S_m}{\delta g^{\mu\nu}} \tag{3.3}$$

is the matter stress-energy tensor derived from the matter field action S_m .

In the absence of a complete quantum theory of gravity, one can resort to the semiclassical framework, where only the matter field is quantized. To implement it, $T_{\mu\nu}$ is substituted by $\langle \psi | \hat{T}_{\mu\nu} | \psi \rangle$, the expectation value of the renormalized stress-energy tensor of the quantum matter field in a quantum state $|\psi\rangle$. This yields the semi-classical EFE

$$G_{\mu\nu} = \frac{8\pi G}{c^4} \langle \psi | \hat{T}_{\mu\nu} | \psi \rangle . \tag{3.4}$$

In an ideal world, such equations would be solved self-consistently but this is a very difficult problem both from a technical and a computational perspective as pointed out

in [36, Chapter 1]. These difficulties are circumvented as follows: First, considering a fixed background spacetime, one evaluates $\langle \psi | \hat{T}_{\mu\nu} | \psi \rangle$. With that result at hand, one can find the first-order quantum corrected background metric by solving the semi-classical EFE with a fixed $\langle \psi | \hat{T}_{\mu\nu} | \psi \rangle$ that was evaluated in the previous step. This establishes the program of Quantum Field Theory on Curved Spacetimes (QFTCS), which should offer a reasonable approximation to describe quantum phenomena in regions where the curvature invariants of the spacetime are small enough, such that effects from quantum gravity are negligible. More precisely, for any curvature invariant R,

$$R \ll \frac{1}{\ell_p},\tag{3.5}$$

where $\ell_p = \sqrt{\frac{\hbar G}{c^3}} \approx 10^{-35} m$ is the Planck length. In Schwarzschild spacetime — the case of interest in this thesis — this approximation is satisfied in any region sufficiently far from the singularity at r = 0. This restriction can be understood by the r^{-6} behavior of the Krestchmann scalar, which makes it divergent at r = 0.

Even tough the semi-classical formalism is not a full quantum theory of gravity, it produces important results. Two examples of such results are [37], where it was shown that quantum effects predicted by this formalism are capable of dressing a naked singularity in the (2+1)D anti-deSitter spacetime and [38] where the authors show that quantum effects within the semi-classical framework converts the Cauchy horizon inside the Reissner-Nordstrom-deSitter black hole into a singularity, thus enforcing the strong cosmic censorship hypothesis.

This thesis focuses on the first part of the semi-classical program, specifically studying the correlations in the quantized matter field that arise from the quantization process on a fixed spacetime background.

3.2 Quantum scalar field

To define a quantum scalar field on the Schwarzschild spacetime, we follow the construction presented in [34]. We begin by considering a classical, minimally coupled free massless scalar field ϕ described by the Klein-Gordon (KG) action, which plays the role of the matter action S_m on the Schwarzschild spacetime. In an arbitrary coordinate system $\{x^{\alpha}\}$ with $\alpha \in \{0, 1, 2, 3\}$,

$$S_m = -\frac{1}{2} \int_{\mathfrak{S}} d^4 \mathbf{x} \sqrt{-g} \mathbf{g}^{\mu\nu} \nabla_{\mu} \phi \nabla_{\nu} \phi. \tag{3.6}$$

By applying the principle of least action, we obtain the usual massless KG equation

$$\nabla_{\mu}\nabla^{\mu}\phi = 0. \tag{3.7}$$

For a given set of smooth initial conditions on a Cauchy surface $\Sigma \subset \mathfrak{S}$, the uniqueness of the corresponding solution to the KG equation is guaranteed because the Schwarzschild

spacetime is globally hyperbolic [30, Section 7.4]. The set of smooth, spatially compactly supported solutions to the KG equation will be denoted by \mathfrak{s} .

Given two of its solutions $\phi_1, \phi_2 \in \mathfrak{s}$, it is straightforward to show that the quantity

$$j_{\mu}(\phi_1, \phi_2) = \phi_1^* \nabla_{\mu} \phi_2 - \phi_2 \nabla_{\mu} \phi_1^*$$
(3.8)

is such that $\nabla_{\mu}j^{\mu}=0$. Consequently, on any Cauchy surface Σ , the integral

$$\int_{\Sigma} d\Sigma^{\mu} j_{\mu} = \int_{\Sigma} d\Sigma^{\mu} \left(\phi_1^* \nabla_{\mu} \phi_2 - \phi_2 \nabla_{\mu} \phi_1^* \right), \tag{3.9}$$

where $d\Sigma^{\mu} = n^{\mu}d\Sigma$ with n^{μ} being the unit normal to Σ and $d\Sigma$ its volume element, yields the same result if j_{μ} vanishes at spatial infinity. To see that, let $\Omega \subset \mathfrak{S}$ be a compact region of the spacetime bounded by two Cauchy surfaces $\Sigma_1, \Sigma_2 \subset \mathfrak{S}$ and a timelike hypersurface Λ_{∞} at spatial infinity. Then

$$\int_{\Omega} d^4 \mathbf{x} \sqrt{-g} \nabla_{\mu} j^{\mu} = 0 \tag{3.10}$$

since $\nabla_{\mu}j^{\mu}=0$. On the other hand, by using Gauss' theorem,

$$\int_{\Omega} d^4 \mathbf{x} \sqrt{-g} \nabla_{\mu} j^{\mu} = \int_{\partial_{\Omega}} d\Omega^{\mu} j_{\mu} = \int_{\Sigma_1} d\Sigma^{\mu} j_{\mu} - \int_{\Sigma_2} d\Sigma^{\mu} j_{\mu} + \int_{\Lambda_{\infty}} d\Lambda^{\mu} j_{\mu}.$$
(3.11)

The last integral is a boundary term that is zero because j_{μ} is assumed to vanish at spatial infinity. Therefore,

$$\int_{\Omega} d^4 \mathbf{x} \sqrt{-g} \nabla_{\mu} j^{\mu} = 0 = \int_{\Sigma_1} d\Sigma^{\mu} j_{\mu} - \int_{\Sigma_2} d\Sigma^{\mu} j_{\mu}$$
 (3.12)

Hence,

$$\int_{\Sigma_1} d\Sigma^{\mu} j_{\mu} = \int_{\Sigma_2} d\Sigma^{\mu} j_{\mu}. \tag{3.13}$$

Finally, we conclude that the result of the integral (3.9) is independent of the particular choice of Cauchy surface over which it is evaluated, provided that j_{μ} vanishes at spatial infinity. This motivates the definition of the so-called KG inner product:

$$(\cdot, \cdot) : \mathfrak{s} \times \mathfrak{s} \to \mathbb{C}$$

$$(\phi_1, \phi_2) = i \int_{\Sigma} d\Sigma^{\mu} \left(\phi_1^* \nabla_{\mu} \phi_2 - \phi_2 \nabla_{\mu} \phi_1^* \right),$$
(3.14)

which is sesquilinear¹ and Hermitian². Notice that despite its name, the KG inner product is not an inner product on \mathfrak{s} because it is not positive-definite, i.e., $(\phi, \phi) \not > 0 \,\forall \, \phi \in \mathfrak{s}$.

To circumvent this difficulty and construct a Hilbert space availing the structure of \mathfrak{s} , we split it into two subspaces, \mathfrak{s}^+ and \mathfrak{s}^- such that the KG inner product is positive-definite in the first one and negative-definite in the second one³. Within this perspective, consider

¹ Antilinear in the first entry and linear in the second one.

That is, symmetric under complex conjugation: $(\phi_1, \phi_2)^* = (\phi_2, \phi_1)$.

³ It is important to remark that these subspaces are not unique.

a choice of \mathfrak{s}^+ and an orthonormal basis $\{u_j\}_j$, where j is a generic multi-index, for it. From the definition of the KG inner product (3.14) it follows that

$$(u_j^*, u_k^*) = -(u_j, u_k)^*. (3.15)$$

Hence, the set $\{u_j^*\}_j$ is an orthonormal basis of \mathfrak{s}^- . Therefore, the subspace \mathfrak{s}^- is fixed by the choice of \mathfrak{s}^+ . Moreover, every element of \mathfrak{s}^+ is orthogonal to every element of \mathfrak{s}^- with respect to the KG inner product.

The elements of \mathfrak{s}^+ and \mathfrak{s}^- are referred to as positive- and negative-frequency solutions (of the KG equation), respectively. The value of the frequency is defined with respect to some vector $\vec{\xi}$ in the following sense: A solution $\phi \in \mathfrak{s}$ is said to be of frequency ω with respect to $\vec{\xi}$ if

$$\mathcal{L}_{\vec{\xi}} \phi = -i\omega\phi, \tag{3.16}$$

where $\mathcal{L}_{\vec{\xi}}$ denotes the Lie derivative along $\vec{\xi}$. If $\omega > 0$, then ϕ is a positive-frequency solution. Conversely, if $\omega < 0$, then ϕ is a negative-frequency solution.

With this construction, the space of solutions factors as $\mathfrak{s} = \mathfrak{s}^+ \oplus \mathfrak{s}^-$ and a solution $\phi \in \mathfrak{s}$ to the KG equation can be decomposed as

$$\phi = \phi^{+} + \phi^{-} = \sum_{j} a_{j} u_{j} + b_{j} u_{j}^{*}$$
(3.17)

where $\phi^+ \in \mathfrak{s}^+$, $\phi^- \in \mathfrak{s}^-$, $a_j = (u_j, \phi)$ and $b_j = -(u_j^*, \phi)$. In particular, for real-valued solutions these coefficients satisfy $b_j = a_j^*$ and the decomposition reads

$$\phi(\mathbf{x}) = \sum_{j} a_j u_j(\mathbf{x}) + a_j^* u_j^*(\mathbf{x}). \tag{3.18}$$

With that, we quantize the real scalar field by following the canonical quantization procedure of promoting the coefficients of the expansion (3.18) to operators

$$a_j \to \hat{a}_j \text{ and } a_j^* \to \hat{a}_j^{\dagger},$$
 (3.19)

such that the canonical commutation relations

$$[\hat{a}_{i}, \hat{a}_{k}^{\dagger}] = \delta_{ik} \hat{1}, \ [\hat{a}_{i}, \hat{a}_{k}] = 0 \text{ and } [\hat{a}_{i}^{\dagger}, \hat{a}_{k}^{\dagger}] = 0$$
 (3.20)

are obeyed. As usual, we will refer to \hat{a}_j as the annihilation operator and \hat{a}_j^{\dagger} as the creation operator. The resulting field operator⁴ $\hat{\phi}$ is given by

$$\hat{\phi} = \sum_{j} \hat{a}_j u_j + \hat{a}_j^{\dagger} u_j^*. \tag{3.21}$$

The corresponding vacuum state $|0\rangle$ is defined by the condition

$$\hat{a}_i |0\rangle = 0, \forall j \tag{3.22}$$

We remark that $\hat{\phi}$ is an operator-valued distribution and not an operator in itself, i.e., it defines an operator only when smeared against a suitable test-function.

and from it, we define a single-particle state $|j\rangle$ as

$$|j\rangle = a_j^{\dagger} |0\rangle. \tag{3.23}$$

The collection of all single-particle states span the single-particle Hilbert space \mathcal{H} and from it we construct the Fock space $\mathfrak{F}(\mathcal{H})$ of the theory as

$$\mathfrak{F}(\mathcal{H}) = \mathbb{C} \oplus \mathcal{H} \oplus (\mathcal{H} \otimes \mathcal{H})_s \oplus \cdots, \tag{3.24}$$

where the sub-index s denotes symmetrization.

We remark that the field operator $\hat{\phi}$ presented in equation (3.21) is a singular object and should be understood as an operator-valued distribution since it is not a well-defined operator on $\mathfrak{F}(\mathcal{H})$. However, by smearing it against a test function f that is compactly supported on \mathfrak{F} one obtains a well-defined operator $\hat{\phi}(f)$ on $\mathfrak{F}(\mathcal{H})$ which is commonly referred to as the smeared field operator

$$\hat{\phi}(f) = \int_{\mathfrak{S}} d^4 \mathbf{x} \sqrt{-g} \,\hat{\phi}(\mathbf{x}) f(\mathbf{x}). \tag{3.25}$$

For each choice of \mathfrak{s}^+ , characterized by an orthonormal basis of positive-frequency solutions $\{u_j\}_j$, one obtains a different vacuum state. In general, there is no need for these vacuum states to be related by a unitary operator and there are many possible unitarily nonequivalent choices of vacuum, although not all of them model physically reasonable situations. This ambiguity is particularly relevant in the Schwarzschild spacetime which does not admit a global timelike Killing vector that could have been used to choose a natural \mathfrak{s}^+ and hence, construct a natural vacuum state. Given that, in this thesis we work with three vacuum states: the Boulware $|B\rangle$, Unruh $|U\rangle$ and Hartle-Hawking $|H\rangle$ states. These have different physical interpretations and are constructed through suitable choices of complete sets of positive-frequency solutions to the KG equation, as presented in what follows.

3.3 Field modes and quantum states

Throughout this section the KS 2.1, SD and EF coordinates 2.2 will be used. In any of these, the spherical symmetry of \mathfrak{S} allows a solution $f_{\omega\ell m}^{\lambda}$ to the KG equation (3.7) to be decomposed as

$$f_{\omega\ell m}^{\lambda}(\mathbf{x}) = \frac{1}{\sqrt{4\pi\omega}} Y_{\ell m}(\theta, \varphi) \frac{\tilde{f}_{\omega\ell}^{\lambda}(\mathbf{x}_{\perp})}{r}, \tag{3.26}$$

where $\omega > 0$, r is to be understood as the r-coordinate of SD-coordinates or the r-function in the EF and KS coordinates; θ and φ are the angular coordinates of x; x_{\perp} are the non-angular coordinates of x; $\lambda \in \{\text{in}, R; \text{up}, R; R; L; \text{in}, L; \text{up}, R; IN; IN; UP; UP}\}$ is a label that will be used to identify the solution and $1/\sqrt{4\pi\omega}$ is a normalization factor to ensure that

$$(f_{\omega\ell m}^{\lambda}, f_{\omega'l'm'}^{\lambda}) = \delta(\omega - \omega')\delta_{l,l'}\delta_{m,m'}. \tag{3.27}$$

In this decomposition, the multi-index i of an element u_i of the orthonormal basis of \mathfrak{s}^+ is to be understood as the combination of the three indices ω , ℓ and m, that is, $u_i \to f_{\omega\ell m}$.

With the intent to provide a better organization for the reader, the definitions of the modes are divided in the following subsections.

3.3.1 The Eddington-Finkelstein modes

These modes are defined as the ones of positive frequency with respect to the timelike Killing vector $\vec{\varepsilon_t} = \partial_t$, in SD coordinates 2.2. For the sake of organization, they are divided in 6 families: $f_{\omega\ell m}^{\text{in,R}}$, $f_{\omega\ell m}^{\text{up,R}}$, $f_{\omega\ell m}^{\text{up,L}}$, $f_{\omega\ell m}^{\text{R}}$ and $f_{\omega\ell m}^{\text{L}}$.

The ones that establish a complete set of orthonormal positive frequency solutions on region I, i.e., an orthonormal basis of \mathfrak{s}^+ on I are $f_{\omega\ell m}^{\mathrm{in,R}}$ and $f_{\omega\ell m}^{\mathrm{up,R}}$, defined by the initial conditions

$$f_{\omega\ell m}^{\rm in,R} \sim \frac{1}{r\sqrt{4\pi\omega}} Y_{\ell m}(\theta,\varphi) \times \begin{cases} 0, \, \mathsf{x} \to \mathcal{H}_R^- \cup \mathcal{H}_L^+ \cup \mathscr{I}_L^+ \\ \mathrm{e}^{-\mathrm{i}\omega v}, \, \mathsf{x} \to \mathscr{I}_R^- \end{cases}$$
(3.28)

and

$$f_{\omega\ell m}^{\mathrm{up,R}} \sim \frac{1}{r\sqrt{4\pi\omega}} Y_{\ell m}(\theta,\varphi) \times \begin{cases} 0, \, \mathsf{x} \to \mathscr{I}_{R}^{-} \cup \mathcal{H}_{L}^{+} \cup \mathscr{I}_{L}^{+} \\ \mathrm{e}^{-\mathrm{i}\omega u}, \, \mathsf{x} \to \mathcal{H}_{R}^{-}. \end{cases}$$
(3.29)

For convenience, we write below these expressions propagated to $\mathscr{I}_L^- \cup \mathcal{H}_R^- \cup \mathcal{H}_L^+ \cup \mathscr{I}_L^+$:

$$f_{\omega\ell m}^{\text{in,R}} \sim \frac{1}{r\sqrt{4\pi\omega}} Y_{\ell m}(\theta, \varphi) \times \begin{cases} 0, \, \mathsf{x} \to \mathscr{I}_{L}^{-} \cup \mathcal{H}_{L}^{-} \\ \rho_{\omega\ell}^{\text{in}} \mathrm{e}^{-\mathrm{i}\omega u}, \, \mathsf{x} \to \mathscr{I}_{R}^{+} \\ T_{\omega\ell} \mathrm{e}^{-\mathrm{i}\omega v}, \, \mathsf{x} \to \mathcal{H}_{R}^{+} \end{cases}$$
(3.30)

and

$$f_{\omega\ell m}^{\mathrm{up,R}} \sim \frac{1}{r\sqrt{4\pi\omega}} Y_{\ell m}(\theta, \varphi) \times \begin{cases} 0, \mathbf{x} \to \mathscr{I}_{L}^{-} \cup \mathcal{H}_{L}^{-} \\ T_{\omega\ell} e^{-\mathrm{i}\omega u}, \mathbf{x} \to \mathscr{I}_{R}^{+} \end{cases}$$

$$\rho_{\omega\ell}^{\mathrm{up}} e^{-\mathrm{i}\omega v}, \mathbf{x} \to \mathcal{H}_{R}^{+},$$
(3.31)

where the coefficients $T_{\omega\ell}$, $\rho_{\omega\ell}^{\rm in}$, $\rho_{\omega\ell}^{\rm up} \in \mathbb{C}$ were introduced to account for the scattering effect produced by the radial effective potential that will be introduced in Section 4.1.

With respect to these coefficients, $T_{\omega\ell}$ is the transmission amplitude across that effective potential and is the same for both $f_{\omega\ell m}^{\rm in,R}$ and $f_{\omega\ell m}^{\rm up,R}$. The coefficients $\rho_{\omega\ell}^{\rm in}$ and $\rho_{\omega\ell}^{\rm up}$ are the reflection amplitudes across the effective potential for $f_{\omega\ell m}^{\rm in,R}$ and $f_{\omega\ell m}^{\rm in,R}$, respectively. The linear independence of these modes imply several relations between the amplitudes (including the equality of the transmission amplitude for $f_{\omega\ell m}^{\rm in,R}$ and $f_{\omega\ell m}^{\rm up,R}$) that can be derived from the Wronskian relations that will be introduced in Section 4.2.

The orthonormal basis of \mathfrak{s}^+ on II is given by $f_{\omega\ell m}^{\rm R}$ and $f_{\omega\ell m}^{\rm L}$, defined by the initial conditions

$$f_{\omega\ell m}^{R} \sim \frac{1}{r\sqrt{4\pi\omega}} Y_{\ell m}(\theta, \varphi) \times \begin{cases} 0, \mathbf{x} \to \mathscr{I}_{R}^{+} \cup \mathscr{I}_{L}^{+} \\ e^{-i\omega v}, \mathbf{x} \to \mathcal{H}_{R}^{+} \\ 0, \mathbf{x} \to \mathcal{H}_{L}^{+} \end{cases}$$
(3.32)

and

$$f_{\omega\ell m}^{L} \sim \frac{1}{r\sqrt{4\pi\omega}} Y_{\ell m}(\theta, \varphi) \times \begin{cases} 0, \mathbf{x} \to \mathscr{I}_{R}^{+} \cup \mathscr{I}_{L}^{+} \\ 0, \mathbf{x} \to \mathcal{H}_{R}^{+} \\ e^{-\mathrm{i}\omega\bar{u}}, \mathbf{x} \to \mathcal{H}_{L}^{+}. \end{cases}$$
(3.33)

On III, the orthonormal basis of \mathfrak{s}^+ is given by $f_{\omega\ell m}^{\mathrm{in,L}}$ and $f_{\omega\ell m}^{\mathrm{up,L}}$, defined by the transformation

$$f_{\omega\ell m}^{\Lambda,L}(U,V,\theta,\phi) = f_{\omega\ell m}^{\Lambda,R*}(-U,-V,\theta,\phi), \tag{3.34}$$

in terms of KS coordinates, with $\Lambda \in \{in, up\}$. Explicitly, the intial conditions defining these modes are

$$f_{\omega\ell m}^{\rm in,L} \sim \frac{1}{r\sqrt{4\pi\omega}} Y_{\ell m}(\theta,\varphi) \times \begin{cases} 0, \, \mathsf{x} \to \mathscr{I}_R^- \cup \mathcal{H}_R^- \cup \mathcal{H}_L^+ \\ \mathrm{e}^{-\mathrm{i}\omega\bar{v}}, \, \mathsf{x} \to \mathscr{I}_L^+ \end{cases}$$
(3.35)

and

$$f_{\omega\ell m}^{\mathrm{up,L}} \sim \frac{1}{r\sqrt{4\pi\omega}} Y_{\ell m}(\theta,\varphi) \times \begin{cases} 0, \, \mathsf{x} \to \mathscr{I}_{R}^{-} \cup \mathcal{H}_{R}^{-} \cup \mathscr{I}_{L}^{+} \\ \mathrm{e}^{-\mathrm{i}\omega\bar{u}}, \, \mathsf{x} \to \mathcal{H}_{L}^{+}. \end{cases}$$
(3.36)

These modes have no support on region I. This can be understood as follows: Both $f_{\omega\ell m}^{\mathrm{in,L}}$ and $f_{\omega\ell m}^{\mathrm{up,L}}$ are zero on $\mathscr{I}_R^- \cup \mathcal{H}_R^-$, which is the past domain of dependence of region I. Therefore, both these modes are also zero inside this region.

More specifically, as will be important in Section 3.4.3,the $f_{\omega\ell m}^{\text{in,L}}$ modes have no support on region II. This is a consequence of being zero on \mathcal{H}_R^+ (inherited from having no support on region I) and \mathcal{H}_L^+ (from its initial conditions). Since $\mathcal{H}_L^+ \cup \mathcal{H}_R^+$ is the past domain of dependence of II, being zero on this hypersurface implies being zero everywhere inside this region.

In this work we will not explore region IV and for this reason, no basis of \mathfrak{s}^+ on this region will be provided.

3.3.2 The Unruh modes

Originally constructed by Unruh in [39], these modes are summarized in what follows. For organization, they are divided in 4 families: $f_{\omega\ell m}^{\rm IN}$, $f_{\omega\ell m}^{\rm UP}$, $f_{\omega\ell m}^{\rm UP}$, $f_{\omega\ell m}^{\rm UP}$. The first two are composed by modes of positive frequency with respect to ∂_V on $\mathcal{H}_L^- \cup \mathcal{H}_R^+$ defined by the relations

$$f_{\omega\ell m}^{\rm IN}(\mathsf{x}) = \frac{\mathrm{e}^{\pi r_s \omega}}{\sqrt{2\sinh(2\pi r_s \omega)}} \Big(f_{\omega\ell m}^{\rm in,R}(\mathsf{x}) + \mathrm{e}^{-2\pi r_s \omega} f_{\omega\ell m}^{\rm in,L*}(\mathsf{x}) \Big)$$
(3.37)

and

$$f_{\omega\ell m}^{\bar{\text{IN}}}(\mathsf{x}) = \frac{\mathrm{e}^{\pi r_s \omega}}{\sqrt{2 \sinh(2\pi r_s \omega)}} \Big(f_{\omega\ell m}^{\text{in,L}}(\mathsf{x}) + \mathrm{e}^{-2\pi r_s \omega} f_{\omega\ell m}^{\text{in,R*}}(\mathsf{x}) \Big). \tag{3.38}$$

The last two are composed by modes of positive frequency with respect to ∂_U on $\mathcal{H}_R^- \cup \mathcal{H}_L^+$ defined by

$$f_{\omega\ell m}^{\rm UP}(\mathsf{x}) = \frac{\mathrm{e}^{\pi r_s \omega}}{\sqrt{2\sinh(2\pi r_s \omega)}} \Big(f_{\omega\ell m}^{\rm up,R}(\mathsf{x}) + \mathrm{e}^{-2\pi r_s \omega} f_{\omega\ell m}^{\rm up,L*}(\mathsf{x}) \Big)$$
(3.39)

and

$$f_{\omega\ell m}^{\bar{\text{UP}}}(\mathsf{x}) = \frac{e^{\pi r_s \omega}}{\sqrt{2\sinh(2\pi r_s \omega)}} \Big(f_{\omega\ell m}^{\text{up,L}}(\mathsf{x}) + e^{-2\pi r_s \omega} f_{\omega\ell m}^{\text{up,R*}}(\mathsf{x}) \Big). \tag{3.40}$$

The collection of all Unruh modes compose an orthonormal basis of \mathfrak{s}^+ on the whole⁵ spacetime \mathfrak{S} . As a note that will be used in the next section, notice that one can also construct different orthonormal basis of \mathfrak{s}^+ by combining Unruh and Eddington-Finkelstein modes.

3.3.3 The Quantum states

As pointed in the end of section ??, we are concerned about the Boulware $|B\rangle$, Unruh $|U\rangle$ and Hartle-Hawking $|H\rangle$ vacuum states. Each of these have a different physical interpretation and are obtained by different choices of basis of \mathfrak{s}^+ .

The Boulware state [40] $|B\rangle$ can be understood as a model of the vacuum around a spherically symmetric non-rotating object such as a star or a black hole, a setup known as cold star. This state is defined by using suitable Eddington-Finkelstein modes as the basis of \mathfrak{s}^+ in the region of interest. As a concrete example, the expression for the field $\hat{\phi}$ in region I in terms of these modes is given by

$$\hat{\phi}(\mathbf{x}) = \sum_{\ell=0}^{\infty} \sum_{m=-\ell}^{\ell} \int_{0}^{\infty} d\omega \left(f_{\omega\ell m}^{\mathrm{in,R}}(\mathbf{x}) \hat{a}_{\omega\ell m}^{\mathrm{in,R}} + f_{\omega\ell m}^{\mathrm{up,R}}(\mathbf{x}) \hat{a}_{\omega\ell m}^{\mathrm{up,R}} + \boldsymbol{h.c.} \right), \, \mathbf{x} \in I,$$
 (3.41)

where **h.c.** is a short notation for hermitian conjugate. The Boulware state is known to be irregular on the black hole and white hole horizons [41, Section 3] (see [34, Section 8.4] for a textbook reference).

The Unruh state [39] $|U\rangle$ models a spherically symmetric, non-rotating black hole emitting thermal radiation. It is defined in region $I \cup II$ by combining the Eddington-Finkelstein modes $f_{\omega\ell m}^{\mathrm{in,R}}$ and $f_{\omega\ell m}^{\mathrm{in,L}}$ with the Unruh modes $f_{\omega\ell m}^{\mathrm{UP}}$ and $f_{\omega\ell m}^{\mathrm{UP}}$ as the orthonormal basis of \mathfrak{s}^+ . The field operator in this region is

$$\hat{\phi}(\mathbf{x}) = \sum_{\ell=0}^{\infty} \sum_{m=-\ell}^{\ell} \int_{0}^{\infty} d\omega \left(f_{\omega\ell m}^{\mathrm{in,R}}(\mathbf{x}) \hat{a}_{\omega\ell m}^{\mathrm{in,R}} + f_{\omega\ell m}^{\mathrm{in,L}}(\mathbf{x}) \hat{a}_{\omega\ell m}^{\mathrm{in,L}} + f_{\omega\ell m}^{\mathrm{UP}}(\mathbf{x}) \hat{a}_{\omega\ell m}^{\mathrm{UP}} + f_{\omega\ell m}^{\mathrm{UP}}(\mathbf{x}) \hat{a}_{\omega\ell m}^{\mathrm{UP}} + f_{\omega\ell m}^{\mathrm{UP}}(\mathbf{x}) \hat{a}_{\omega\ell m}^{\mathrm{UP}} + h.c. \right), \mathbf{x} \in I \cup II.$$
(3.42)

Provided that the $f_{\omega\ell m}^{{\rm in/up},R/L}({\sf x})$ modes are suitably extended into the $r < r_s$ region.

In contrast to the Boulware state, the Unruh state is regular [41] across the black-hole horizon but still irregular across the white-hole horizon.

Finally, the Hartle-Hawking state [42] $|H\rangle$ models a black hole in thermal equilibrium with the surrounding environment. It is defined in all of the spacetime \mathfrak{S} by using the Unruh modes as the orthonormal basis of \mathfrak{s}^+ . In particular, the expression for $\hat{\phi}$ in the whole spacetime is

$$\hat{\phi}(\mathbf{x}) = \sum_{\ell=0}^{\infty} \sum_{m=-\ell}^{\ell} \int_{0}^{\infty} d\omega \left(f_{\omega\ell m}^{\mathrm{UP}}(\mathbf{x}) \hat{a}_{\omega\ell m}^{\mathrm{UP}} + f_{\omega\ell m}^{\bar{\mathrm{UP}}}(\mathbf{x}) \hat{a}_{\omega\ell m}^{\bar{\mathrm{UP}}} + f_{\omega\ell m}^{\mathrm{IN}}(\mathbf{x}) \hat{a}_{\omega\ell m}^{\mathrm{IN}} + \mathbf{h.c.} \right), \mathbf{x} \in \mathfrak{S}.$$
(3.43)

This state is regular through both the black hole and white hole horizons.

3.4 Wightman function

The Wightman function W^{ψ} of the field $\hat{\phi}$ in a quantum state $|\psi\rangle$ is defined as

$$W^{\psi}(\mathbf{x}; \mathbf{x}') = \langle \psi | \hat{\phi}(\mathbf{x}) \hat{\phi}(\mathbf{x}') | \psi \rangle \quad \mathbf{x}, \mathbf{x}' \in \mathcal{Q} \subseteq \mathfrak{S}, \tag{3.44}$$

where \mathcal{Q} denotes the subset of the spacetime manifold \mathfrak{S} over which the state $|\psi\rangle$ is defined. Specifically, for the Boulware state, $\mathcal{Q} = I$; for the Unruh state, $\mathcal{Q} = I \cup II$; and for the Hartle-Hawking state, $\mathcal{Q} = \mathfrak{S}$.

The Wightman function encodes both classical and quantum correlations in the field for a given state. Assuming that $|\psi\rangle$ is a vacuum state, we substitute the mode expansion (3.21) into this definition to obtain the mode-sum expansion

$$W^{\psi}(\mathbf{x}; \mathbf{x}') = \sum_{i} u_i(\mathbf{x}) u_i^*(\mathbf{x}'), \tag{3.45}$$

where u_i is an element of the set of positive frequency orthonormal modes that form a basis of \mathfrak{s}^+ . From the mode-sum expression it readily follows that

$$W^{\psi}(x';x) = W^{\psi*}(x;x').$$
 (3.46)

Using this property it is straightforward to derive a relation between the expectation value of the field commutator and the imaginary part of the Wightman

$$\langle \psi | [\hat{\phi}(\mathsf{x})\hat{\phi}(\mathsf{x}')] | \psi \rangle = W^{\psi}(\mathsf{x};\mathsf{x}') - W^{\psi*}(\mathsf{x};\mathsf{x}') = 2\mathrm{i}\mathrm{Im}[W^{\psi}(\mathsf{x};\mathsf{x}')]$$
(3.47)

and a relation between the expectation value of the field anti-commutator and the real part of the Wightman function

$$\langle \psi | \{ \hat{\phi}(\mathsf{x}) \hat{\phi}(\mathsf{x}') \} | \psi \rangle = W^{\psi}(\mathsf{x}; \mathsf{x}') + W^{\psi*}(\mathsf{x}; \mathsf{x}') = 2 \text{Re}[W^{\psi}(\mathsf{x}; \mathsf{x}')].$$
 (3.48)

From this relations, it becomes evident that any correlations in the field between two causally disconnected points should be encoded in the real part of the Wightman, since the field commutator is expected to vanish at spacelike connected points.

All Green functions of $\hat{\phi}$ can be derived from the Wightman function using the relations provided in [35, Equation 4.9]. Thus, the Wightman function fully characterizes all two-point correlation functions of $\hat{\phi}$ in the state $|\psi\rangle$. In particular, the Feynman Green Function (FGF), the retarded Green Function (RGF) and the advanced Green Function (AGF) are expressed as

$$G_{F}^{\Psi}(\mathbf{x}, \mathbf{x}') = iW^{\psi}(\mathbf{x}; \mathbf{x}') \Theta(t - t') - iW^{\psi*}(\mathbf{x}; \mathbf{x}') \Theta(t' - t), \tag{3.49}$$

$$G_{\text{ret}}^{\Psi}(\mathsf{x}, \mathsf{x}') = -2\text{Im}[W^{\psi}(\mathsf{x}; \mathsf{x}')]\Theta(t - t'), \tag{3.50}$$

and

$$G_{\text{adv}}^{\Psi}(\mathbf{x}, \mathbf{x}') = 2\text{Im}[W^{\Psi}(\mathbf{x}; \mathbf{x}')]\Theta(t' - t), \tag{3.51}$$

respectively, where Θ denotes the Heaviside step function. These expressions will play a key hole in Chapter 5.

In the next subsection, we analyze the singularity structure of the Wightman function. This discussion is followed by two subsections detailing the mode-sum expressions of the Wightman function for the states $|B\rangle$, $|U\rangle$ and $|H\rangle$ in both (1+1)-dimensional and (3+1)-dimensional Schwarzschild spacetime. For the (1+1)-dimensional case, these results are well established [43]; we briefly review them here for completeness. The novel contributions of this part of this work are the explicit expressions for the (3+1)-dimensional case where one point lies inside the black hole and the other outside. A detailed derivation of these new results is provided.

3.4.1 Singularity structure

Despite the generality of the definition of the Wightman function in Equation (3.44), its local behavior is well-known [44, Chapter 2] for a class of states called Hadamard states, which $|B\rangle$, $|U\rangle$, $|H\rangle$ are part of. For states of this class, the Wightman function $W^{\psi}(\mathbf{x}; \mathbf{x}')$ with $\psi \in \{B, U, H\}$ in a normal neighborhood $\mathcal{N}(\mathbf{x})$ of \mathbf{x} is given by

$$W^{\psi}(\mathbf{x}; \mathbf{x}') = \lim_{\epsilon \to 0^{+}} \frac{1}{4\pi^{2}} \left[\frac{U}{\sigma + i\epsilon \Delta t} - V \ln(\sigma + i\epsilon \Delta t) + w^{\psi} \right], \tag{3.52}$$

where $U=U(\mathsf{x},\mathsf{x}'),\,V=V(\mathsf{x},\mathsf{x}')$ and $w^\psi=w^\psi(\mathsf{x},\mathsf{x}')$ are regular, real-valued bi-scalars. The bi-scalar $\sigma=\sigma(\mathsf{x},\mathsf{x}')$ is the Synge's world function, defined as one-half of the square of the distance between x and x' on the unique geodesic connecting them⁶. Consequently, it is positive/zero/negative whenever that geodesic is spacelike/null/timelike. The bi-scalars $U(\mathsf{x},\mathsf{x}')$ and $V(\mathsf{x},\mathsf{x}')$ are uniquely determined by the geometry of the underlying spacetime. On the other hand $w^\psi(\mathsf{x},\mathsf{x}')$ is not uniquely fixed by that geometry and depends on

⁶ Since $x' \in \mathcal{N}(x)$, there is only one geodesic connecting x and x' that is entirely within $\mathcal{N}(x)$.

the quantum state in question. Therefore, it is this last term that encodes information particular to each quantum state.

By applying the distributional limits

$$\lim_{\epsilon \to 0^+} \frac{1}{\sigma \pm i\epsilon} = \text{P.V.} \left(\frac{1}{\sigma}\right) \mp i\pi\delta(\sigma) \quad \text{and} \quad \lim_{\epsilon \to 0^+} \ln(\sigma \pm i\epsilon) = \ln|\sigma| \pm i\pi\Theta(-\sigma), \quad (3.53)$$

where P.V. is the principal value distribution, to the Wightman function from Equation (3.52), we get

$$W^{\psi}\left(\mathbf{x};\mathbf{x}'\right) = \frac{1}{4\pi^{2}} \left\{ U\left[P.V.\left(\frac{1}{\sigma}\right) - i\pi\delta(\sigma)\right] - V\left[\ln|\sigma| + i\pi\Theta(-\sigma)\right] + w^{\psi} \right\}. \tag{3.54}$$

This form exposes the local singularity structure of the Wightman function: Whenever $\sigma = 0$ (i.e., when x and x' are connected by a null geodesic) the real part of the Wightman function is dominated by the P.V. $\left(\frac{1}{\sigma}\right)$ singularity with a $-\ln|\sigma|$ tail while its imaginary part is dominated by a $-\delta(\sigma)$ singularity. The $\Theta(-\sigma)$ tail only contributes to the imaginary part when $\sigma = -1$ (i.e., when x and x' are connected by a timelike geodesic).

Despite the local validity of these expressions, it is known [45, 46] that the Wightman function diverges whenever x and x' are connected by a null geodesic, even if x' is not within a normal neighborhood of x. In particular, the global singularity structure of the Wightman function in the Schwarzschild spacetime was calculated for the first time in [27]⁷. It presents a four-fold structure where the singularity changes its character whenever it crosses a caustic point, with the dominant divergences in its real and imaginary parts following the patterns⁸

$$\operatorname{Re}[W^{\psi}(\mathsf{x};\mathsf{x}')]: \operatorname{P.V.}\left(\frac{1}{\sigma}\right) \to -\delta(\sigma) \to -\operatorname{P.V.}\left(\frac{1}{\sigma}\right) \to \delta(\sigma) \to \operatorname{P.V.}\left(\frac{1}{\sigma}\right) \to \cdots$$
 (3.55)

and

$$\operatorname{Im}[W^{\psi}(\mathsf{x};\mathsf{x}')] : -\delta(\sigma) \to -\operatorname{P.V.}\left(\frac{1}{\sigma}\right) \to \delta(\sigma) \to \operatorname{P.V.}\left(\frac{1}{\sigma}\right) \to -\delta(\sigma) \to \cdots, \quad (3.56)$$

respectively. In these expression, Synge's world is used in a global sense and $x' \notin \mathcal{N}(x)$. To make it well-posed in this scenario, it is necessary to indicate what is the geodesic on which it is being evaluated, as constructed in [47].

For completeness, we mention that this reference also showed that the sub-leading singularity structure of the imaginary part of the Wightman function is four-fold and follows

$$-\Theta(-\sigma) \to \ln |\sigma| \to \Theta(-\sigma) \to -\ln |\sigma| \to -\Theta(-\sigma) \to \cdots$$
 (3.57)

and conjectured that for the real part it is also four-fold and follows

$$-\ln|\sigma| \to -\Theta(-\sigma) \to \ln|\sigma| \to \Theta(-\sigma) \to -\ln|\sigma| \to \cdots. \tag{3.58}$$

This reference calculated the FGF from which the Wightman function readily follows by using Equation (3.49).

Except at the caustic points, where the singularities are stronger and the structure is two-fold (see [47, Chapter V]).

3.4.2 (1+1)D

The (1+1)D Schwarzschild spacetime is geometrically distinct from its (3+1)D counterpart and we will refer to the former as \mathfrak{S}_2 . Its metric can be formally read directly from equation (2.2) by setting $d\theta = 0 = d\phi$. The definitions of the EF, KS and SD coordinates presented in sections 2.1 and 2.2 are still valid but without the angular coordinates.

A massless scalar field ϕ on \mathfrak{S}_2 described by the Klein-Gordon action (3.6) will also obey the K-G equation (3.7). The crucial difference with \mathfrak{S} is that on \mathfrak{S}_2 , the K-G equation is just a free wave equation: In EF coordinates it reads

$$\partial_u \partial_v \phi = 0 \tag{3.59}$$

and in KS coordinates, it is

$$\partial_U \partial_V \phi = 0. (3.60)$$

In (1+1)D, the solutions to the K-G equation can be decomposed as

$$f_{\omega}^{\lambda}(\mathbf{x}) = \frac{1}{\sqrt{4\pi|\omega|}} \tilde{f}_{\omega}^{\lambda}(\mathbf{x}), \tag{3.61}$$

in a similar way to that was done in (3+1)D (Equation (3.26)): The only formal difference is that one has to remove the spherical harmonics and the r^{-1} factor.

The corresponding EF and Unruh modes in (1+1)D are defined by initial conditions analogous to the ones for the (3+1)D case, presented in sections 3.3.1 and 3.3.2. To obtain the (1+1)D initial conditions, one has to remove the spherical harmonics and the r^{-1} factor from the (3+1)D initial conditions and consider $T_{\omega\ell} = 1$ and $\rho_{\omega\ell}^{\rm in} = 0 = \rho_{\omega\ell}^{\rm up}$, because in (1+1)D the modes propagate as free waves.

Despite the similarities, there is a remarkable difference between the massless scalar field in these two cases: In (1+1)D its Wightman function is infra-red divergent, as will be shown in what follows, while in (3+1)D it is not.

To construct the Wightman function of $\hat{\phi}$ for the Boulware state we apply the (1+1)D EF-modes in the mode-sum expansion (3.45) to obtain

$$W_2^B(\mathbf{x}; \mathbf{x}') = \frac{1}{4\pi} \int_{\lambda}^{\infty} \frac{d\omega}{\omega} \left(f_{\omega}^{\text{in,R}}(\mathbf{x}) f_{\omega}^{\text{in,R}*}(\mathbf{x}') + f_{\omega}^{\text{up,R}}(\mathbf{x}) f_{\omega}^{\text{up,R}*}(\mathbf{x}') \right), \quad \mathbf{x}, \mathbf{x}' \in I.$$
 (3.62)

where $\lambda > 0$ is a cutoff frequency to regulate the infra-red divergence of this correlator. Since the modes are free waves,

$$W_2^B(\mathbf{x}; \mathbf{x}') = \frac{1}{4\pi} \int_{\lambda}^{\infty} \frac{d\omega}{\omega} \left(e^{-i\omega(v - v')} + e^{-i\omega(u - u')} \right), \quad \mathbf{x}, \mathbf{x}' \in I.$$
 (3.63)

In terms of exponential integrals $E_1(y)$ [48, Equation 6.2.1] this equation can be written as

$$W_2^B(\mathbf{x}; \mathbf{x}') = \frac{1}{4\pi} \left[E_1(i\lambda \Delta v) + E_1(i\lambda \Delta u) \right], \tag{3.64}$$

where $\Delta v = v - v'$ and $\Delta u = u - u'$. Expanding around small λ using [49, Equation 5.1.11] results in

$$W_2^B(\mathbf{x}; \mathbf{x}') = \frac{-1}{4\pi} \left[2\gamma_E + \ln(\mathrm{i}\lambda\Delta v) + \ln(\mathrm{i}\Delta u) \right] + O(\lambda), \tag{3.65}$$

where γ_E is the Euler-Mascheroni constant. Notice that in the principal branch $\arg(i\lambda\Delta v)$ is $\pi/2$ if $\Delta v > 0$ and $-\pi/2$ if $\Delta v < 0$, since $\lambda > 0$. Therefore,

$$\ln(\mathrm{i}\lambda\Delta v) = \ln(\lambda) + \ln(|\Delta v|) + \frac{\mathrm{i}\pi}{2}(\Theta(\Delta v) - \Theta(-\Delta v)). \tag{3.66}$$

By performing an analogous analysis on $\arg(i\lambda\Delta u)$, we can write the Wightman function as

$$W_2^B(\mathbf{x}; \mathbf{x}') = \frac{-1}{4\pi} \left[2\gamma_E + \ln(|\Delta v \Delta u|) + 2\ln(\lambda) + \frac{\mathrm{i}\pi}{2} \left(\Theta(\Delta v) + \Theta(\Delta u) - \Theta(-\Delta v) - \Theta(-\Delta u) \right) \right] + O(\lambda).$$
(3.67)

This expression is already known and more details about its properties are provided in [36, Chapter 4].

To write the Wightman functions for the Unruh and Hartle-Hawking states, we remark that $W_2^B(\mathbf{x};\mathbf{x}')$ is a solution to the homogeneous wave equation (3.59), that is,

$$\partial_u \partial_v W_2^B(\mathbf{x}; \mathbf{x}') = 0. \tag{3.68}$$

On the other hand the Wightman functions for the Unruh and Hartle-Hawking states are solutions to, respectively,

$$\partial_U \partial_v W_2^U(\mathbf{x}; \mathbf{x}') = 0 \tag{3.69}$$

and

$$\partial_U \partial_V W_2^H(\mathbf{x}; \mathbf{x}') = 0. (3.70)$$

Since all these equations are of the same form, one can infer that their solutions will also be of the same form, therefore,

$$W_2^U(\mathbf{x}; \mathbf{x}') = \frac{-1}{4\pi} \left[2\gamma_E + \ln(|\Delta v \Delta U|) + 2\ln(\lambda) + \frac{\mathrm{i}\pi}{2} \left(\Theta(\Delta v) + \Theta(\Delta U) - \Theta(-\Delta v) - \Theta(-\Delta U) \right) \right] + O(\lambda).$$
(3.71)

and

$$W_2^H(\mathbf{x}; \mathbf{x}') = \frac{-1}{4\pi} \left[2\gamma_E + \ln(|\Delta V \Delta U|) + 2\ln(\lambda) + \frac{\mathrm{i}\pi}{2} \left(\Theta(\Delta V) + \Theta(\Delta U) - \Theta(-\Delta V) - \Theta(-\Delta U) \right) \right] + O(\lambda).$$
(3.72)

3.4.3 (3+1)D

In the (3+1)D Schwarzschild spacetime, the mode-sum expressions for the Wightman function are known in the $|B\rangle$ [40], $|U\rangle$ [39] and $|H\rangle$ [42] states when both points are either outside or inside the black hole. These expressions can be derived from the results about the field commutator, also known as the Hadamard elementary function, presented in [32]. In what follows we present an alternative derivation of these expressions, in the aforementioned quantum states, based on the Unruh modes defined in Section 3.3.2, extending the mode-sum expressions for the Wightman function to the case where one of the points is inside and another outside the black hole.

3.4.3.1 The Boulware state

To obtain the expression of the Wightman function for the Boulware state one can substitute the Eddington-Finkelstein modes from Section 3.3.1 into the generic mode-sum expression from Equation (3.45) and use the decomposition from Equation (3.26). This yields

$$W^{B}(\mathbf{x};\mathbf{x}') = \frac{1}{4\pi r r'} \sum_{\ell=0}^{\infty} \sum_{m=-\ell}^{\ell} Y_{\ell m}(\theta,\varphi) Y_{\ell m}^{*}(\theta',\varphi') \int_{0}^{\infty} \frac{d\omega}{\omega} \left(\tilde{f}_{\omega\ell}^{\mathrm{in,R}}(\mathbf{x}_{\perp}) \tilde{f}_{\omega\ell}^{\mathrm{in,R*}}(\mathbf{x}'_{\perp}) + \tilde{f}_{\omega\ell}^{\mathrm{up,R}}(\mathbf{x}_{\perp}) \tilde{f}_{\omega\ell}^{\mathrm{up,R*}}(\mathbf{x}'_{\perp}) \right)$$

$$(3.73)$$

with $x, x' \in I$ and x_{\perp} are the non-angular coordinates of x (an analogous notation is used for x'). Using the spherical harmonics addition theorem [50, Equation 16.57],

$$W^{B}(\mathbf{x}; \mathbf{x}') = \frac{1}{(4\pi)^{2}rr'} \sum_{\ell=0}^{\infty} (2\ell+1) P_{\ell}(\cos(\gamma)) \int_{0}^{\infty} \frac{d\omega}{\omega} \left(\tilde{f}_{\omega\ell}^{\text{in,R}}(\mathbf{x}_{\perp}) \tilde{f}_{\omega\ell}^{\text{in,R}*}(\mathbf{x}'_{\perp}) + \tilde{f}_{\omega\ell}^{\text{up,R}}(\mathbf{x}_{\perp}) \tilde{f}_{\omega\ell}^{\text{up,R}*}(\mathbf{x}'_{\perp}) \right), \tag{3.74}$$

where $\gamma \in [0, \pi]$ is the angular separation between x and x'.

Despite being formally similar to its (1+1)D counterpart $W_2^B(\mathbf{x};\mathbf{x}')$, the expression that was just derived is regular as $\omega \to 0$ since in that limit, each term in the integrand tends to a finite value, as demonstrated in Figures 10, 11, 12 and 14.

Region II is also of interest for this thesis but the Boulware state is not regular across \mathcal{H}_R^+ , therefore the Wightman function for the Boulware state with points in that region does not reflect a physically reasonable situation and for that reason, is not included in this text.

3.4.3.2 The Unruh state

To obtain the expression of the Wightman function for the Unruh state we use the generic mode-sum expression form Equation (3.45) with a suitable combination of Eddington-Finkelstein modes from Section 3.3.1 and Unruh modes from Section 3.3.2, as prescribed in Section 3.3.3, together with the decomposition from Equation (3.26). After using the

spherical harmonics addition theorem the Wightman function for the Unruh state reads

$$W^{U}(\mathbf{x}; \mathbf{x}') = \frac{1}{(4\pi)^{2}rr'} \sum_{\ell=0}^{\infty} (2\ell+1) P_{\ell}(\cos(\gamma)) \int_{0}^{\infty} \frac{d\omega}{\omega} \left(\tilde{f}_{\omega\ell}^{\text{in,R}}(\mathbf{x}_{\perp}) \tilde{f}_{\omega\ell}^{\text{in,R*}}(\mathbf{x}'_{\perp}) + \tilde{f}_{\omega\ell}^{\text{in,L}}(\mathbf{x}_{\perp}) \tilde{f}_{\omega\ell}^{\text{in,L*}}(\mathbf{x}'_{\perp}) + \tilde{f}_{\omega\ell}^{\text{UP}}(\mathbf{x}_{\perp}) \tilde{f}_{\omega\ell}^{\text{UP}}(\mathbf{x}_{\perp}) \tilde{f}_{\omega\ell}^{\text{UP}}(\mathbf{x}_{\perp}) \right), \quad \mathbf{x}, \mathbf{x}' \in I \cup II.$$

$$(3.75)$$

Using the expressions from Section 3.3.2 to write the Unruh modes in terms of the Eddington-Finkelstein modes,

$$W^{U}(\mathbf{x};\mathbf{x}') = \frac{1}{(4\pi)^{2}rr'} \sum_{\ell=0}^{\infty} (2\ell+1) P_{\ell}(\cos(\gamma)) \int_{0}^{\infty} \frac{d\omega}{\omega} \left[\tilde{\mathbf{f}}_{\omega\ell}^{\text{in,R}}(\mathbf{x}_{\perp}) \tilde{\mathbf{f}}_{\omega\ell}^{\text{in,R}*}(\mathbf{x}') + \tilde{\mathbf{f}}_{\omega\ell}^{\text{in,L}}(\mathbf{x}_{\perp}) \tilde{\mathbf{f}}_{\omega\ell}^{\text{in,L}*}(\mathbf{x}') \right]$$

$$+ \frac{1}{2 \sinh(2\pi r_{s}\omega)} \left(e^{2\pi r_{s}\omega} \tilde{\mathbf{f}}_{\omega\ell}^{\text{up,R}}(\mathbf{x}_{\perp}) \tilde{\mathbf{f}}_{\omega\ell}^{\text{up,R}*}(\mathbf{x}'_{\perp}) + e^{-2\pi r_{s}\omega} \tilde{\mathbf{f}}_{\omega\ell}^{\text{up,R}*}(\mathbf{x}_{\perp}) \tilde{\mathbf{f}}_{\omega\ell}^{\text{up,R}}(\mathbf{x}'_{\perp}) \right)$$

$$+ \frac{1}{2 \sinh(2\pi r_{s}\omega)} \left(e^{2\pi r_{s}\omega} \tilde{\mathbf{f}}_{\omega\ell}^{\text{up,L}}(\mathbf{x}_{\perp}) \tilde{\mathbf{f}}_{\omega\ell}^{\text{up,L}*}(\mathbf{x}'_{\perp}) + e^{-2\pi r_{s}\omega} \tilde{\mathbf{f}}_{\omega\ell}^{\text{up,L}*}(\mathbf{x}_{\perp}) \tilde{\mathbf{f}}_{\omega\ell}^{\text{up,L}}(\mathbf{x}'_{\perp}) \right)$$

$$+ \frac{1}{\sinh(2\pi r_{s}\omega)} \operatorname{Re} \left[\tilde{\mathbf{f}}_{\omega\ell}^{\text{up,R}}(\mathbf{x}_{\perp}) \tilde{\mathbf{f}}_{\omega\ell}^{\text{up,L}}(\mathbf{x}'_{\perp}) + \tilde{\mathbf{f}}_{\omega\ell}^{\text{up,L}}(\mathbf{x}_{\perp}) \tilde{\mathbf{f}}_{\omega\ell}^{\text{up,R}}(\mathbf{x}'_{\perp}) \right], \quad \mathbf{x}, \mathbf{x}' \in I \cup II$$

$$(3.76)$$

When $x, x' \in I$, the modes $\tilde{f}_{\omega}^{\text{in,L}}$ and $\tilde{f}_{\omega}^{\text{up,L}}$ have no support and the result is

$$W^{U}(\mathbf{x}; \mathbf{x}') = \frac{1}{(4\pi)^{2}rr'} \sum_{\ell=0}^{\infty} (2\ell+1) P_{\ell}(\cos(\gamma)) \int_{0}^{\infty} \frac{d\omega}{\omega} \left(\tilde{\mathbf{f}}_{\omega\ell}^{\text{in,R}}(\mathbf{x}_{\perp}) \tilde{\mathbf{f}}_{\omega\ell}^{\text{in,R}*}(\mathbf{x}'_{\perp}) + \frac{e^{2\pi r_{s}\omega}}{2\sinh(2\pi r_{s}\omega)} \tilde{\mathbf{f}}_{\omega\ell}^{\text{up,R}}(\mathbf{x}_{\perp}) \tilde{\mathbf{f}}_{\omega\ell}^{\text{up,R}*}(\mathbf{x}'_{\perp}) + \frac{e^{-2\pi r_{s}\omega}}{2\sinh(2\pi r_{s}\omega)} \tilde{\mathbf{f}}_{\omega\ell}^{\text{up,R}*}(\mathbf{x}_{\perp}) \tilde{\mathbf{f}}_{\omega\ell}^{\text{up,R}}(\mathbf{x}'_{\perp}) \right), \, \mathbf{x}, \mathbf{x}' \in I$$

$$(3.77)$$

For the case $x, x' \in II$, the $f_{\omega \ell}^{\text{in,L}}$ modes have no support (see Section 3.3.1) and the Wightman is

$$W^{U}(\mathbf{x};\mathbf{x}') = \frac{1}{(4\pi)^{2}rr'} \sum_{\ell=0}^{\infty} (2\ell+1) P_{\ell}(\cos(\gamma)) \int_{0}^{\infty} \frac{d\omega}{\omega} \left[\tilde{\mathbf{f}}_{\omega\ell}^{\text{in,R}}(\mathbf{x}_{\perp}) \tilde{\mathbf{f}}_{\omega\ell}^{\text{in,R}*}(\mathbf{x}'_{\perp}) + \frac{1}{2\sinh(2\pi r_{s}\omega)} \left(e^{2\pi r_{s}\omega} \tilde{\mathbf{f}}_{\omega\ell}^{\text{up,R}}(\mathbf{x}_{\perp}) \tilde{\mathbf{f}}_{\omega\ell}^{\text{up,R}*}(\mathbf{x}'_{\perp}) + e^{-2\pi r_{s}\omega} \tilde{\mathbf{f}}_{\omega\ell}^{\text{up,R}*}(\mathbf{x}_{\perp}) \tilde{\mathbf{f}}_{\omega\ell}^{\text{up,R}}(\mathbf{x}'_{\perp}) \right) + \frac{1}{2\sinh(2\pi r_{s}\omega)} \left(e^{2\pi r_{s}\omega} \tilde{\mathbf{f}}_{\omega\ell}^{\text{up,L}}(\mathbf{x}_{\perp}) \tilde{\mathbf{f}}_{\omega\ell}^{\text{up,L}*}(\mathbf{x}'_{\perp}) + e^{-2\pi r_{s}\omega} \tilde{\mathbf{f}}_{\omega\ell}^{\text{up,L}*}(\mathbf{x}_{\perp}) \tilde{\mathbf{f}}_{\omega\ell}^{\text{up,L}}(\mathbf{x}'_{\perp}) \right) + \frac{1}{\sinh(2\pi r_{s}\omega)} \operatorname{Re} \left[\tilde{\mathbf{f}}_{\omega\ell}^{\text{up,R}}(\mathbf{x}_{\perp}) \tilde{\mathbf{f}}_{\omega\ell}^{\text{up,L}}(\mathbf{x}'_{\perp}) + \tilde{\mathbf{f}}_{\omega\ell}^{\text{up,L}}(\mathbf{x}_{\perp}) \tilde{\mathbf{f}}_{\omega\ell}^{\text{up,R}}(\mathbf{x}'_{\perp}) \right] \right], \mathbf{x}, \mathbf{x}' \in II.$$

$$(3.78)$$

For future convenience it is useful to write $\tilde{f}^{\text{in,R}}_{\omega\ell}$, $\tilde{f}^{\text{up,R}}_{\omega\ell}$, $\tilde{f}^{\text{in,L}}_{\omega\ell}$ and $\tilde{f}^{\text{up,L}}_{\omega\ell}$ in terms of $\tilde{f}^{\text{R}}_{\omega\ell}$ and $\tilde{f}^{\text{L}}_{\omega\ell}$ when considering points inside the black hole. This can be done by comparing the initial conditions of these modes on $\mathcal{H}^+_R \cup \mathcal{H}^+_L$. Since region II can be understood

as the future domain of dependence of that hypersurface, the intial conditions set on it completely determine the modes in this region.

By definition, $\tilde{\mathbf{f}}_{\omega\ell}^{\text{in,R}}$ is zero on \mathcal{H}_L^+ which makes it independent of $\tilde{\mathbf{f}}_{\omega\ell}^L$. On the other hand, comparing the initial conditions of $\tilde{\mathbf{f}}_{\omega\ell}^{\text{in,R}}$ and $\tilde{\mathbf{f}}_{\omega\ell}^{\text{R}}$ at $\mathcal{H}_R^+ \cup \mathcal{H}_L^+$ yields

$$\tilde{\mathbf{f}}_{\omega\ell}^{\mathrm{in,R}}(\mathbf{x}_{\perp}) = T_{\omega\ell}\tilde{\mathbf{f}}_{\omega\ell}^{\mathrm{R}}(\mathbf{x}_{\perp}), \, \mathbf{x} \in II.$$
 (3.79)

Similarly, $\tilde{\mathbf{f}}_{\omega\ell}^{\mathrm{up,R}}$ is zero on \mathcal{H}_L^+ and consequently, independent of $\tilde{\mathbf{f}}_{\omega\ell}^{\mathrm{L}}$. By comparing its initial conditions with the ones of $\tilde{\mathbf{f}}_{\omega\ell}^{\mathrm{R}}$ at \mathcal{H}_R^+ , we obtain

$$\tilde{\mathbf{f}}_{\omega\ell}^{\mathrm{up,R}}(\mathbf{x}_{\perp}) = \rho_{\omega\ell}^{\mathrm{up}} \tilde{\mathbf{f}}_{\omega\ell}^{\mathrm{R}}(\mathbf{x}_{\perp}), \, \mathbf{x} \in II.$$
(3.80)

As mentioned before, the $\tilde{\mathbf{f}}^{\text{in,L}}_{\omega\ell}$ modes are zero on II (see Section 3.3.1). Finally, the $\tilde{\mathbf{f}}^{\text{up,L}}_{\omega\ell}$ are independent of $\tilde{\mathbf{f}}^{\text{R}}_{\omega\ell}$ because the former are zero on \mathcal{H}^+_R by definition. Comparing the initial conditions of $\tilde{\mathbf{f}}^{\text{up,L}}_{\omega\ell}$ and $\tilde{\mathbf{f}}^{\text{L}}_{\omega\ell}$ at $\mathcal{H}^+_R \cup \mathcal{H}^+_L$ results in

$$\tilde{\mathbf{f}}_{\omega\ell}^{\mathrm{up,L}}(\mathbf{x}_{\perp}) = \tilde{\mathbf{f}}_{\omega\ell}^{\mathrm{L}}(\mathbf{x}_{\perp}), \, \mathbf{x} \in II. \tag{3.81}$$

Considering these expressions, one can rewrite the previous expression of the Wightman function as

$$W^{U}(\mathbf{x};\mathbf{x}') = \frac{1}{(4\pi)^{2}rr'} \sum_{\ell=0}^{\infty} (2\ell+1) P_{\ell}(\cos(\gamma)) \int_{0}^{\infty} \frac{d\omega}{\omega} \left\{ |T_{\omega\ell}|^{2} \tilde{\mathbf{f}}_{\omega\ell}^{R}(\mathbf{x}_{\perp}) \tilde{\mathbf{f}}_{\omega\ell}^{R*}(\mathbf{x}'_{\perp}) + \frac{\left|\rho^{\mathrm{up,ref}}\right|^{2}}{2 \sinh(2\pi r_{s}\omega)} \left(e^{2\pi r_{s}\omega} \tilde{\mathbf{f}}_{\omega\ell}^{R}(\mathbf{x}_{\perp}) \tilde{\mathbf{f}}_{\omega\ell}^{R*}(\mathbf{x}'_{\perp}) + e^{-2\pi r_{s}\omega} \tilde{\mathbf{f}}_{\omega\ell}^{R*}(\mathbf{x}_{\perp}) \tilde{\mathbf{f}}_{\omega\ell}^{R}(\mathbf{x}'_{\perp}) \right) + \frac{1}{2 \sinh(2\pi r_{s}\omega)} \left(e^{2\pi r_{s}\omega} \tilde{\mathbf{f}}_{\omega\ell}^{L}(\mathbf{x}_{\perp}) \tilde{\mathbf{f}}_{\omega\ell}^{L*}(\mathbf{x}'_{\perp}) + e^{-2\pi r_{s}\omega} \tilde{\mathbf{f}}_{\omega\ell}^{L*}(\mathbf{x}_{\perp}) \tilde{\mathbf{f}}_{\omega\ell}^{L}(\mathbf{x}'_{\perp}) \right) + \frac{1}{\sinh(2\pi r_{s}\omega)} \operatorname{Re} \left[\rho_{\omega\ell}^{\mathrm{up}} \left(\tilde{\mathbf{f}}_{\omega\ell}^{R}(\mathbf{x}_{\perp}) \tilde{\mathbf{f}}_{\omega\ell}^{L}(\mathbf{x}'_{\perp}) + \tilde{\mathbf{f}}_{\omega\ell}^{L}(\mathbf{x}_{\perp}) \tilde{\mathbf{f}}_{\omega\ell}^{R}(\mathbf{x}'_{\perp}) \right) \right] \right\} \mathbf{x}, \mathbf{x}' \in II,$$

$$(3.82)$$

which agrees with [32, Equation 3.11].

Finally, to obtain an expression for the case $x \in I$, $x' \in II$ we begin by using Equation (3.76) and the previously derived properties

$$\tilde{\mathbf{f}}_{\omega\ell}^{\mathrm{in,L}}(\mathbf{x}_{\perp}) = 0, \, \forall \, \mathbf{x} \in I \cup II \quad \text{and} \quad \tilde{\mathbf{f}}_{\omega\ell}^{\mathrm{up,L}}(\mathbf{x}_{\perp}) = 0, \, \forall \, \mathbf{x} \in I$$
 (3.83)

to obtain

$$W^{U}(\mathbf{x}; \mathbf{x}') = \frac{1}{(4\pi)^{2} r r'} \sum_{\ell=0}^{\infty} (2\ell+1) P_{\ell}(\cos(\gamma)) \int_{0}^{\infty} \frac{d\omega}{\omega} \left[\tilde{\mathbf{f}}_{\omega\ell}^{\text{in,R}}(\mathbf{x}_{\perp}) \tilde{\mathbf{f}}_{\omega\ell}^{\text{in,R}*}(\mathbf{x}'_{\perp}) + \frac{1}{2 \sinh(2\pi r_{s}\omega)} \left(e^{2\pi r_{s}\omega} \tilde{\mathbf{f}}_{\omega\ell}^{\text{up,R}}(\mathbf{x}_{\perp}) \tilde{\mathbf{f}}_{\omega\ell}^{\text{up,R}*}(\mathbf{x}'_{\perp}) + e^{-2\pi r_{s}\omega} \tilde{\mathbf{f}}_{\omega\ell}^{\text{up,R}*}(\mathbf{x}) \tilde{\mathbf{f}}_{\omega\ell}^{\text{up,R}}(\mathbf{x}'_{\perp}) \right) + \frac{1}{\sinh(2\pi r_{s}\omega)} \text{Re} \left[\tilde{\mathbf{f}}_{\omega\ell}^{\text{L}}(\mathbf{x}_{\perp}) \tilde{\mathbf{f}}_{\omega\ell}^{\text{up,R}}(\mathbf{x}'_{\perp}) \right] \right], \quad \mathbf{x} \in II, \mathbf{x}' \in I$$

$$(3.84)$$

In the next step we use Equations (3.79), (3.80) and (3.81) to write the Eddington-Finkelstein modes inside the horizon in terms of $\tilde{f}_{\omega\ell}^L$ and $\tilde{f}_{\omega\ell}^R$. This results in

$$W^{U}(\mathbf{x}; \mathbf{x}') = \frac{1}{(4\pi)^{2}rr'} \sum_{\ell=0}^{\infty} (2\ell+1) P_{\ell}(\cos(\gamma)) \int_{0}^{\infty} \frac{d\omega}{\omega} \left[T_{\omega\ell} \tilde{\mathbf{f}}_{\omega\ell}^{R}(\mathbf{x}_{\perp}) \tilde{\mathbf{f}}_{\omega\ell}^{in,R*}(\mathbf{x}'_{\perp}) + \frac{1}{2\sinh(2\pi r_{s}\omega)} \left(e^{2\pi r_{s}\omega} \rho_{\omega\ell}^{up} \tilde{\mathbf{f}}_{\omega\ell}^{R}(\mathbf{x}_{\perp}) \tilde{\mathbf{f}}_{\omega\ell}^{up,R*}(\mathbf{x}'_{\perp}) + e^{-2\pi r_{s}\omega} \rho_{\omega\ell}^{up*} \tilde{\mathbf{f}}_{\omega\ell}^{R*}(\mathbf{x}_{\perp}) \tilde{\mathbf{f}}_{\omega\ell}^{up,R}(\mathbf{x}'_{\perp}) \right) + \frac{1}{\sinh(2\pi r_{s}\omega)} \operatorname{Re} \left[\tilde{\mathbf{f}}_{\omega\ell}^{L}(\mathbf{x}_{\perp}) \tilde{\mathbf{f}}_{\omega\ell}^{up,R}(\mathbf{x}'_{\perp}) \right], \quad \mathbf{x} \in II, \mathbf{x}' \in I.$$

$$(3.85)$$

3.4.3.3 The Hartle-Hawking state

To write the mode-sum expression of the Wightman function for the Hartle-Hawking state we apply the Unruh modes from Section 3.3.2, as prescribed in Section 3.3.3, in the generic mode-sum expression from Equation (3.45) and use the decomposition from Equation (3.26). After using the spherical harmonics addition theorem the resulting expression is

$$W^{H}(\mathbf{x}; \mathbf{x}') = \frac{1}{(4\pi)^{2}rr'} \sum_{\ell=0}^{\infty} (2\ell+1) P_{\ell}(\cos(\gamma)) \int_{0}^{\infty} \frac{d\omega}{\omega} \left(\tilde{\mathbf{f}}_{\omega}^{\mathrm{IN}}(\mathbf{x}_{\perp}) \tilde{\mathbf{f}}_{\omega}^{\mathrm{IN*}}(\mathbf{x}'_{\perp}) + \tilde{\mathbf{f}}_{\omega}^{\mathrm{I}\bar{\mathrm{N}}}(\mathbf{x}_{\perp}) \tilde{\mathbf{f}}_{\omega}^{\mathrm{I}\bar{\mathrm{N}}*}(\mathbf{x}'_{\perp}) + \tilde{\mathbf{f}}_{\omega}^{\mathrm{UP}}(\mathbf{x}_{\perp}) \tilde{\mathbf{f}}_{\omega}^{\mathrm{UP}*}(\mathbf{x}'_{\perp}) \right), \quad \mathbf{x}, \mathbf{x}' \in \mathfrak{S}.$$

$$(3.86)$$

Writing the Unruh modes in terms of Eddington-Finkelstein modes yields

$$W^{H}(\mathbf{x};\mathbf{x}') = \frac{1}{(4\pi)^{2}rr'} \sum_{\ell=0}^{\infty} (2\ell+1) P_{\ell}(\cos(\gamma)) \int_{0}^{\infty} \frac{d\omega}{\omega} \left[\frac{1}{2\sinh(2\pi r_{s}\omega)} \left(e^{2\pi r_{s}\omega} \tilde{\mathbf{f}}_{\omega\ell}^{\mathrm{in,R}}(\mathbf{x}_{\perp}) \tilde{\mathbf{f}}_{\omega\ell}^{\mathrm{in,R}*}(\mathbf{x}'_{\perp}) + e^{-2\pi r_{s}\omega} \tilde{\mathbf{f}}_{\omega\ell}^{\mathrm{in,R}*}(\mathbf{x}_{\perp}) \tilde{\mathbf{f}}_{\omega\ell}^{\mathrm{in,R}}(\mathbf{x}'_{\perp}) \right) \right. \\ + \frac{1}{2\sinh(2\pi r_{s}\omega)} \left(e^{2\pi r_{s}\omega} \tilde{\mathbf{f}}_{\omega\ell}^{\mathrm{in,L}}(\mathbf{x}_{\perp}) \tilde{\mathbf{f}}_{\omega\ell}^{\mathrm{in,L}*}(\mathbf{x}'_{\perp}) + e^{-2\pi r_{s}\omega} \tilde{\mathbf{f}}_{\omega\ell}^{\mathrm{in,L}*}(\mathbf{x}_{\perp}) \tilde{\mathbf{f}}_{\omega\ell}^{\mathrm{in,L}}(\mathbf{x}'_{\perp}) \right) \right. \\ + \frac{1}{2\sinh(2\pi r_{s}\omega)} \left(e^{2\pi r_{s}\omega} \tilde{\mathbf{f}}_{\omega\ell}^{\mathrm{up,R}}(\mathbf{x}_{\perp}) \tilde{\mathbf{f}}_{\omega\ell}^{\mathrm{up,R}*}(\mathbf{x}'_{\perp}) + e^{-2\pi r_{s}\omega} \tilde{\mathbf{f}}_{\omega\ell}^{\mathrm{up,R}*}(\mathbf{x}_{\perp}) \tilde{\mathbf{f}}_{\omega\ell}^{\mathrm{up,R}}(\mathbf{x}'_{\perp}) \right) \right. \\ + \frac{1}{2\sinh(2\pi r_{s}\omega)} \left(e^{2\pi r_{s}\omega} \tilde{\mathbf{f}}_{\omega\ell}^{\mathrm{up,L}}(\mathbf{x}_{\perp}) \tilde{\mathbf{f}}_{\omega\ell}^{\mathrm{up,L}*}(\mathbf{x}'_{\perp}) + e^{-2\pi r_{s}\omega} \tilde{\mathbf{f}}_{\omega\ell}^{\mathrm{up,L}*}(\mathbf{x}_{\perp}) \tilde{\mathbf{f}}_{\omega\ell}^{\mathrm{up,L}}(\mathbf{x}'_{\perp}) \right. \\ + \frac{1}{\sinh(2\pi r_{s}\omega)} \operatorname{Re} \left[\tilde{\mathbf{f}}_{\omega\ell}^{\mathrm{up,R}}(\mathbf{x}_{\perp}) \tilde{\mathbf{f}}_{\omega\ell}^{\mathrm{up,L}}(\mathbf{x}'_{\perp}) + \tilde{\mathbf{f}}_{\omega\ell}^{\mathrm{up,L}}(\mathbf{x}_{\perp}) \tilde{\mathbf{f}}_{\omega\ell}^{\mathrm{up,R}}(\mathbf{x}'_{\perp}) \right] \\ + \frac{1}{\sinh(2\pi r_{s}\omega)} \operatorname{Re} \left[\tilde{\mathbf{f}}_{\omega\ell}^{\mathrm{in,R}}(\mathbf{x}_{\perp}) \tilde{\mathbf{f}}_{\omega\ell}^{\mathrm{in,L}}(\mathbf{x}'_{\perp}) + \tilde{\mathbf{f}}_{\omega\ell}^{\mathrm{in,L}}(\mathbf{x}_{\perp}) \tilde{\mathbf{f}}_{\omega\ell}^{\mathrm{in,R}}(\mathbf{x}'_{\perp}) \right] \right], \quad \mathbf{x}, \mathbf{x}' \in \mathfrak{S}.$$

When both points are in region $I \cup II$, the modes $\tilde{\mathbf{f}}_{\omega\ell}^{\mathrm{in,L}}(\mathbf{x}_{\perp}) = 0$ and the Wightman function simplifies to

$$W^{H}(\mathbf{x};\mathbf{x}') = \frac{1}{(4\pi)^{2}rr'} \sum_{\ell=0}^{\infty} (2\ell+1) P_{\ell}(\cos(\gamma)) \int_{0}^{\infty} \frac{d\omega}{\omega} \left[\frac{1}{2\sinh(2\pi r_{s}\omega)} \left(e^{2\pi r_{s}\omega} \tilde{\mathbf{f}}_{\omega\ell}^{\mathrm{in,R}}(\mathbf{x}_{\perp}) \tilde{\mathbf{f}}_{\omega\ell}^{\mathrm{in,R}*}(\mathbf{x}'_{\perp}) + e^{-2\pi r_{s}\omega} \tilde{\mathbf{f}}_{\omega\ell}^{\mathrm{in,R}*}(\mathbf{x}_{\perp}) \tilde{\mathbf{f}}_{\omega\ell}^{\mathrm{in,R}}(\mathbf{x}'_{\perp}) \right) \right. \\ \left. + \frac{1}{2\sinh(2\pi r_{s}\omega)} \left(e^{2\pi r_{s}\omega} \tilde{\mathbf{f}}_{\omega\ell}^{\mathrm{up,R}}(\mathbf{x}_{\perp}) \tilde{\mathbf{f}}_{\omega\ell}^{\mathrm{up,R}*}(\mathbf{x}'_{\perp}) + e^{-2\pi r_{s}\omega} \tilde{\mathbf{f}}_{\omega\ell}^{\mathrm{up,R}*}(\mathbf{x}_{\perp}) \tilde{\mathbf{f}}_{\omega\ell}^{\mathrm{up,R}}(\mathbf{x}'_{\perp}) \right) \right. \\ \left. + \frac{1}{2\sinh(2\pi r_{s}\omega)} \left(e^{2\pi r_{s}\omega} \tilde{\mathbf{f}}_{\omega\ell}^{\mathrm{up,L}}(\mathbf{x}_{\perp}) \tilde{\mathbf{f}}_{\omega\ell}^{\mathrm{up,L}*}(\mathbf{x}'_{\perp}) + e^{-2\pi r_{s}\omega} \tilde{\mathbf{f}}_{\omega\ell}^{\mathrm{up,L}*}(\mathbf{x}_{\perp}) \tilde{\mathbf{f}}_{\omega\ell}^{\mathrm{up,L}}(\mathbf{x}'_{\perp}) \right. \\ \left. + \frac{1}{\sinh(2\pi r_{s}\omega)} \operatorname{Re} \left[\tilde{\mathbf{f}}_{\omega\ell}^{\mathrm{up,R}}(\mathbf{x}_{\perp}) \tilde{\mathbf{f}}_{\omega\ell}^{\mathrm{up,L}}(\mathbf{x}'_{\perp}) + \tilde{\mathbf{f}}_{\omega\ell}^{\mathrm{up,L}}(\mathbf{x}_{\perp}) \tilde{\mathbf{f}}_{\omega\ell}^{\mathrm{up,R}}(\mathbf{x}'_{\perp}) \right] \right], \quad \mathbf{x}, \mathbf{x}' \in I \cup II.$$

$$(3.88)$$

Specializing this expression to the case where both points are in region I (outside the black hole) the modes $\tilde{\mathbf{f}}_{\omega\ell}^{\mathrm{in/up,L}}(\mathbf{x}_{\perp}) = 0$ and the Wightman function becomes

$$W^{H}(\mathbf{x}; \mathbf{x}') = \frac{1}{(4\pi)^{2}rr'} \sum_{\ell=0}^{\infty} (2\ell+1) P_{\ell}(\cos(\gamma)) \int_{0}^{\infty} \frac{\mathrm{d}\omega}{\omega} \left[\frac{1}{2\sinh(2\pi r_{s}\omega)} \left(e^{2\pi r_{s}\omega} \tilde{\mathbf{f}}_{\omega\ell}^{\mathrm{in,R}}(\mathbf{x}_{\perp}) \tilde{\mathbf{f}}_{\omega\ell}^{\mathrm{in,R*}}(\mathbf{x}'_{\perp}) + e^{-2\pi r_{s}\omega} \tilde{\mathbf{f}}_{\omega\ell}^{\mathrm{in,R*}}(\mathbf{x}_{\perp}) \tilde{\mathbf{f}}_{\omega\ell}^{\mathrm{in,R}}(\mathbf{x}'_{\perp}) \right) + \frac{1}{2\sinh(2\pi r_{s}\omega)} \left(e^{2\pi r_{s}\omega} \tilde{\mathbf{f}}_{\omega\ell}^{\mathrm{up,R}}(\mathbf{x}_{\perp}) \tilde{\mathbf{f}}_{\omega\ell}^{\mathrm{up,R*}}(\mathbf{x}'_{\perp}) + e^{-2\pi r_{s}\omega} \tilde{\mathbf{f}}_{\omega\ell}^{\mathrm{up,R*}}(\mathbf{x}_{\perp}) \tilde{\mathbf{f}}_{\omega\ell}^{\mathrm{up,R}}(\mathbf{x}'_{\perp}) \right) \right], \quad \mathbf{x}, \mathbf{x}' \in I.$$

$$(3.89)$$

On the other hand, when both points are in region II, we use expressions (3.79), (3.80) and (3.81) to write the Eddington-Finkelstein modes inside the horizon in terms of $\tilde{\mathbf{f}}_{\omega\ell}^{\mathbf{L}}$ and $\tilde{\mathbf{f}}_{\omega\ell}^{\mathbf{R}}$, which results in

$$W^{H}(\mathbf{x};\mathbf{x}') = \frac{1}{(4\pi)^{2}rr'} \sum_{\ell=0}^{\infty} (2\ell+1) P_{\ell}(\cos(\gamma)) \int_{0}^{\infty} \frac{d\omega}{\omega} \left[\frac{|T_{\omega\ell}|^{2}}{2\sinh(2\pi r_{s}\omega)} \left(e^{2\pi r_{s}\omega} \tilde{\mathbf{f}}_{\omega\ell}^{R}(\mathbf{x}_{\perp}) \tilde{\mathbf{f}}_{\omega\ell}^{R*}(\mathbf{x}'_{\perp}) + e^{-2\pi r_{s}\omega} \tilde{\mathbf{f}}_{\omega\ell}^{R*}(\mathbf{x}_{\perp}) \tilde{\mathbf{f}}_{\omega\ell}^{R}(\mathbf{x}'_{\perp}) \right) + \frac{|\rho_{\omega\ell}^{\mathrm{up}}|^{2}}{2\sinh(2\pi r_{s}\omega)} \left(e^{2\pi r_{s}\omega} \tilde{\mathbf{f}}_{\omega\ell}^{R}(\mathbf{x}_{\perp}) \tilde{\mathbf{f}}_{\omega\ell}^{R*}(\mathbf{x}'_{\perp}) + e^{-2\pi r_{s}\omega} \tilde{\mathbf{f}}_{\omega\ell}^{R*}(\mathbf{x}_{\perp}) \tilde{\mathbf{f}}_{\omega\ell}^{R}(\mathbf{x}'_{\perp}) \right) + \frac{1}{2\sinh(2\pi r_{s}\omega)} \left(e^{2\pi r_{s}\omega} \tilde{\mathbf{f}}_{\omega\ell}^{L}(\mathbf{x}_{\perp}) \tilde{\mathbf{f}}_{\omega\ell}^{L*}(\mathbf{x}'_{\perp}) + e^{-2\pi r_{s}\omega} \tilde{\mathbf{f}}_{\omega\ell}^{L*}(\mathbf{x}_{\perp}) \tilde{\mathbf{f}}_{\omega\ell}^{L}(\mathbf{x}'_{\perp}) \right) + \frac{1}{\sinh(2\pi r_{s}\omega)} \operatorname{Re} \left[\rho_{\omega\ell}^{\mathrm{up}} \left(\tilde{\mathbf{f}}_{\omega\ell}^{R}(\mathbf{x}_{\perp}) \tilde{\mathbf{f}}_{\omega\ell}^{L}(\mathbf{x}'_{\perp}) + \tilde{\mathbf{f}}_{\omega\ell}^{L}(\mathbf{x}_{\perp}) \tilde{\mathbf{f}}_{\omega\ell}^{R}(\mathbf{x}'_{\perp}) \right) \right] \right], \quad \mathbf{x}, \mathbf{x}' \in II.$$

$$(3.90)$$

As a consequence of the Wronskian relations that will be introduced in Section 4.2,

 $\left|T_{\omega\ell}\right|^2+\left|
ho_{\omega\ell}^{\mathrm{up}}\right|^2=1$ and this expression is further simplified to

$$W^{H}(\mathbf{x}; \mathbf{x}') = \frac{1}{(4\pi)^{2}rr'} \sum_{\ell=0}^{\infty} (2\ell+1) P_{\ell}(\cos(\gamma)) \int_{0}^{\infty} \frac{d\omega}{\omega} \left[\frac{1}{2\sinh(2\pi r_{s}\omega)} \left(e^{2\pi r_{s}\omega} \tilde{\mathbf{f}}_{\omega\ell}^{R}(\mathbf{x}_{\perp}) \tilde{\mathbf{f}}_{\omega\ell}^{R*}(\mathbf{x}'_{\perp}) + e^{-2\pi r_{s}\omega} \tilde{\mathbf{f}}_{\omega\ell}^{R*}(\mathbf{x}_{\perp}) \tilde{\mathbf{f}}_{\omega\ell}^{R}(\mathbf{x}'_{\perp}) \right) + \frac{1}{2\sinh(2\pi r_{s}\omega)} \left(e^{2\pi r_{s}\omega} \tilde{\mathbf{f}}_{\omega\ell}^{L}(\mathbf{x}_{\perp}) \tilde{\mathbf{f}}_{\omega\ell}^{L*}(\mathbf{x}'_{\perp}) + e^{-2\pi r_{s}\omega} \tilde{\mathbf{f}}_{\omega\ell}^{L*}(\mathbf{x}_{\perp}) \tilde{\mathbf{f}}_{\omega\ell}^{L}(\mathbf{x}'_{\perp}) \right) + \frac{1}{\sinh(2\pi r_{s}\omega)} \operatorname{Re} \left[\rho_{\omega\ell}^{\mathrm{up}} \left(\tilde{\mathbf{f}}_{\omega\ell}^{R}(\mathbf{x}_{\perp}) \tilde{\mathbf{f}}_{\omega\ell}^{L}(\mathbf{x}'_{\perp}) + \tilde{\mathbf{f}}_{\omega\ell}^{L}(\mathbf{x}_{\perp}) \tilde{\mathbf{f}}_{\omega\ell}^{R}(\mathbf{x}'_{\perp}) \right) \right] \right], \quad \mathbf{x}, \mathbf{x}' \in II.$$

$$(3.91)$$

Finally, we specialize (3.88) to the case where one point is inside and another outside the black hole ($x \in I$ and $x' \in II$). For that, we use the property $\tilde{f}_{\omega\ell}^{up,L}(x) = 0 \,\forall x \in I$ then apply expressions (3.79), (3.80) and (3.81) to write the Eddington-Finkelstein modes inside the horizon in terms of $\tilde{f}_{\omega\ell}^L$ and $\tilde{f}_{\omega\ell}^R$. This procedure results in

$$W^{H}(\mathbf{x};\mathbf{x}') = \frac{1}{(4\pi)^{2}rr'} \sum_{\ell=0}^{\infty} (2\ell+1) P_{\ell}(\cos(\gamma)) \int_{0}^{\infty} \frac{d\omega}{\omega} \left[\frac{1}{2\sinh(2\pi r_{s}\omega)} \left(e^{2\pi r_{s}\omega} T_{\omega\ell} \tilde{\mathbf{f}}_{\omega\ell}^{R}(\mathbf{x}_{\perp}) \tilde{\mathbf{f}}_{\omega\ell}^{in,R*}(\mathbf{x}'_{\perp}) + e^{-2\pi r_{s}\omega} T_{\omega\ell}^{*} \tilde{\mathbf{f}}_{\omega\ell}^{R*}(\mathbf{x}_{\perp}) \tilde{\mathbf{f}}_{\omega\ell}^{in,R}(\mathbf{x}'_{\perp}) \right) \right. \\ \left. + \frac{1}{2\sinh(2\pi r_{s}\omega)} \left(e^{2\pi r_{s}\omega} \rho_{\omega\ell}^{up} \tilde{\mathbf{f}}_{\omega\ell}^{R}(\mathbf{x}_{\perp}) \tilde{\mathbf{f}}_{\omega\ell}^{up,R*}(\mathbf{x}'_{\perp}) + e^{-2\pi r_{s}\omega} \rho_{\omega\ell}^{up*} \tilde{\mathbf{f}}_{\omega\ell}^{R*}(\mathbf{x}_{\perp}) \tilde{\mathbf{f}}_{\omega\ell}^{up,R}(\mathbf{x}'_{\perp}) \right) \right. \\ \left. + \frac{1}{\sinh(2\pi r_{s}\omega)} \operatorname{Re} \left[\tilde{\mathbf{f}}_{\omega\ell}^{up,L}(\mathbf{x}_{\perp}) \tilde{\mathbf{f}}_{\omega\ell}^{up,R}(\mathbf{x}'_{\perp}) \right] \right], \quad \mathbf{x} \in II, \mathbf{x}' \in I$$

$$(3.92)$$

4 Numerical evaluation of the Eddington-Finkelstein modes

A number of challenges is involved in evaluating the Wightman function, as can be anticipated from the expressions presented in Section 3.4. The absence of exact solutions to the KG equation in the Schwarzschild spacetime implies that the field modes embroiled in the quantization process must be determined through numerical methods. On top of that, to evaluate the Wightman function $W^{\psi}(\mathbf{x};\mathbf{x}')$ of the quantum scalar field $\hat{\phi}$ in a quantum state $|\psi\rangle$ for a single pair of points $\mathbf{x},\mathbf{x}'\in\mathfrak{S}$, one has to numerically perform an integral over $\omega\in\mathbb{R}_{>0}$ and a sum over $\ell\in\mathbb{N}_{\geq 0}$, using sensible cut-offs in both operations. Achieving a reasonable precision in these procedures requires a large amount of data to produce a single result, i.e., the numerical value of $W^{\Psi}(\mathbf{x};\mathbf{x}')$. Furthermore, even with sufficient data available, the process of summing over ℓ and integrating over ω is computationally intensive.

These difficulties may explain why only a few prior works apply a similar procedure, although in different setups and with different objectives. For example, in [27] the Feynman Green function is evaluated with x' fixed outside the black hole and x following a circular timelike geodesic at $r = 3r_s$. In [51] the response function, which is essentially the Wightman function smeared against a smooth function, is evaluated along the world-line of an Unruh-DeWitt detector (see Section 6.1) freely falling to the horizon. Finally, [1] evaluates a measure of entanglement called negativity (see Chapter 6) for a system of two static Unruh-DeWitt detectors placed at antipodal points around the horizon.

This chapter introduces the techniques used to compute the field modes and the scattering amplitudes, together with an analysis of the results. This exposition is structured as follows: Section 4.1 presents the radial component of the EF modes from Subsection 3.3.1 and the details of the numerical methods used to compute them. Section 4.2 introduces the Wronskian relations and Section 4.3 presents the analysis of the reliability of the numerical data for the field modes and scattering amplitudes.

4.1 The radial component of the Eddington-Finkelstein modes

The mode-sum expressions of the Wightman function in Section 3.4 are written in terms of EF modes because these are convenient to compute numerically. The reason is that the modes $\tilde{f}_{\omega\ell m}^{\Lambda}$ (with $\Lambda \in \{\text{in}, R; \text{up}, R; R; L\}$) from the decomposition in Equation (3.26), can be factored out as

$$\tilde{f}_{\omega\ell m}^{\Lambda}(\mathbf{x}_{\perp}) = e^{\pm i\omega t} \psi_{\omega\ell}^{\Lambda}(r), \tag{4.1}$$

where the sign in the exponential is defined by the boundary conditions of $\tilde{f}_{\omega\ell m}^{\Lambda}$ and x_{\perp} are the non-angular coordinates of x . Substituting this expression into (3.26) and applying the result in the KG equation (3.7) leads to a Schrödinger-like equation for $\psi_{\omega\ell}^{\Lambda}$:

$$\frac{\mathrm{d}^2 \psi_{\omega \ell}^{\Lambda}}{\mathrm{d}r_*^2} + \left(\omega^2 - V_{\ell}^{\mathrm{eff}}(r)\right) \psi_{\omega \ell}^{\Lambda} = 0, \tag{4.2}$$

where the effective potential is

$$V_{\ell}^{\text{eff}}(r) = \left(1 - \frac{r_s}{r}\right) \left(\frac{\ell(\ell+1)}{r^2} + \frac{r_s}{r^3}\right).$$
 (4.3)

This equation is structurally identical to the well-known Regge-Wheeler equation from black hole perturbation theory (See [52, Section 3.1] for a brief review) which can be conveniently solved through the numerical methods that will be presented.

The boundary conditions defining each $\psi_{\omega\ell}^{\Lambda}$ are inherited from those of $\hat{f}_{\omega\ell m}^{\Lambda}$ and will be detailed in subsequent sections. All solutions were computed for $M\omega \in [10^{-3}, 10]$ in steps of 10^{-3} and $\ell \in [0, 100]$ in steps of 1. For future convenience these sets of values for ω and ℓ will be referred to as \mathbf{w} and \mathbf{l} , respectively. This frequency range enables capturing both low- and high-energy contributions, while the fine step size ensures sufficient sampling density for accurate numerical integration over the frequencies (ω -integral) when computing the Wightman function. The upper bound of $\ell = 100$ in angular momentum has two objectives: The first is to ensure the convergence of the sum over angular momentum (ℓ -sum) when computing the Wightman function at two points that are out of coincidence and not connected by null geodesics, i.e., where it is not expected to diverge. The second is to smoothen the divergences that appear due to the ℓ -sum when computing the Wightman function at two points connected by a null geodesic, where divergences are expected. We do not expect this method to be able to resolve the Wightman function near coincidence or close to it since a very similar approach, used in [27] was not able to do it.

Outside the horizon the $\psi_{\omega\ell}^{\Lambda}$ modes and their derivatives were evaluated for $r_* \in [-4M, 24.4M]$ in increments of 0.2M; inside the horizon, we sampled $\bar{r}_* \in [-14M, -0.1M]$ with the same step size. For future convenience, these sets of values of r_* will be referred to as \mathfrak{r}_* and $\bar{\mathfrak{r}}_*$, respectively. This computational effort generates approximately 720 million data points, spanning the parameter space of ω , ℓ , and r_* .

4.1.1 Ingoing modes

Applying the decomposition from Equation (4.1) to $\tilde{f}_{\omega\ell m}^{\rm in,R}$ yields

$$\tilde{f}_{\omega\ell m}^{\text{in,R}}(\mathbf{x}) = e^{-i\omega t} \psi_{\omega\ell}^{\text{in,R}}(r), \tag{4.4}$$

where $\psi_{\omega\ell}^{\text{in,R}}$ is defined by asymptotic boundary conditions near the horizon $(r_* \to -\infty)$ and at infinity $(r_* \to \infty)$

$$\psi_{\omega\ell}^{\text{in,R}} \sim \begin{cases} T_{\omega\ell} e^{-i\omega r_*}, & r_* \to -\infty \\ e^{-i\omega r_*} + \rho_{\omega\ell}^{\text{in}} e^{i\omega r_*}, & r_* \to \infty. \end{cases}$$

$$(4.5)$$

For computational convenience, we define re-scaled modes satisfying

$$\bar{\psi}_{\omega\ell}^{\text{in,R}} = \frac{\psi_{\omega\ell}^{\text{in,R}}}{T_{\omega\ell}} \sim \begin{cases} e^{-i\omega r_*}, & r_* \to -\infty\\ \bar{I}_{\omega\ell}e^{-i\omega r_*} + \bar{\rho}_{\omega\ell}^{\text{in}}e^{i\omega r_*}, & r_* \to \infty, \end{cases}$$
(4.6)

where $\bar{I}_{\omega\ell} = T_{\omega\ell}^{-1}$ and $\bar{\rho}_{\omega\ell}^{\rm in} = T_{\omega\ell}^{-1} \rho_{\omega\ell}^{\rm in}$. Throughout this text any mode re-scaled by $T_{\omega\ell}^{-1}$ will be classified as transmission-normalized; for example, $\bar{\psi}_{\omega\ell}^{\rm in,R}$ is transmission-normalized.

For $r > r_s$, the $\bar{\psi}_{\omega\ell}^{\text{in,R}}(r)$ solution to Equation (4.2) is expressed via the Jaffé series [53, Section IV.A]

$$\bar{\psi}_{\omega\ell}^{\text{in,R}}(r) = e^{i\omega r} \left(\frac{r}{r_s} - 1\right)^{-i\omega r_s} \left(\frac{r}{r_s}\right)^{2i\omega r_s} \sum_{n=0}^{\infty} a_{n\omega\ell} \left(1 - \frac{r_s}{r}\right)^n, \tag{4.7}$$

where the coefficients $a_{n\omega\ell}$ obey the recurrence relation

$$a_{n\omega\ell} = -\left(\frac{\beta_{(n-1)\omega\ell}a_{(n-1)\omega\ell} + \gamma_{(n-1)\omega}a_{(n-2)\omega\ell}}{\alpha_{(n-1)\omega}}\right),\tag{4.8}$$

with initial conditions $a_{0\omega\ell}=\mathrm{e}^{-2\mathrm{i}\omega r_s},\;a_{n\omega\ell}=0$ for n<0, and coefficients

$$\alpha_{n\omega} = (n+1)(n+1-2i\omega r_s),$$

$$\beta_{n\omega\ell} = 8(\omega r_s)^2 + 8in\omega r_s + 4i\omega - \ell(\ell+1) - 2n(n+1) - 1,$$

$$\gamma_{n\omega} = (n-2i\omega r_s)^2.$$
(4.9)

The choice $a_{0\omega\ell}=\mathrm{e}^{-2\mathrm{i}\omega r_s}$ ensures that

$$\bar{\psi}_{\omega\ell}^{\text{in,R}}(r) \sim e^{-i\omega r_*}, \quad r_* \to -\infty.$$
 (4.10)

Had we chosen $a_{0\omega\ell}=1$, the solution would instead behave as $\mathrm{e}^{-\mathrm{i}\omega(r_*-2r_s)}$ in that limit.

The series is absolutely convergent for $r \in [r_s, \infty)$, and the convergence becomes slower as r increases. A series representation for the derivative $\bar{\psi}_{\omega\ell}^{\text{in,R}}(r)$ of $\bar{\psi}_{\omega\ell}^{\text{in,R}}(r)$ is readily obtained by differentiating Equation (4.7) with respect to r.

In practice, a numerical implementation truncates the series at $n = n_{\text{cut}}$ which introduces a relative error in the real (δ_{Re}^J) and imaginary (δ_{Im}^J) parts of $\bar{\psi}_{\omega\ell}^{\text{in,R}}(r)$ estimated by

$$\delta_{\text{Re/Im}}^{J} = \frac{\left| \text{Re/Im} \left[a_{(n_{\text{cut}}+1)\omega\ell} \left(1 - \frac{r_s}{r} \right)^{n_{\text{cut}}+1} \right] \right|}{\left| \text{Re/Im} \left[\sum_{n=0}^{n_{\text{cut}}} a_{n\omega\ell} \left(1 - \frac{r_s}{r} \right)^{n} \right] \right|}.$$
(4.11)

An analogous error estimation is applied to the series representation of $\bar{\psi}^{\text{in,R}}_{\omega\ell}(r)$.

To determine $n_{\rm cut}$ for $r_* \in [-4M, 13M]$, we evaluated the slowest-converging case $r_* = 13M$ with $\ell = 0$ and $M\omega = 10$, dynamically increasing $n_{\rm cut}$ until $\delta_{\rm Re}^J < 10^{-22}$ and $\delta_{\rm Im}^J < 10^{-22}$ for both $\bar{\psi}_{\omega\ell}^{\rm in,R}$ and $\bar{\psi}_{\omega\ell}^{\rm in,R}$. A safety margin of two orders of magnitude was applied to the convergence criteria (targeting 20 significant digits, enforcing 22). The same procedure established $n_{\rm cut}$ for $r_* \in [13.2M, 24.4M]$, with stricter thresholds of $\delta_{\rm Re/Im}^J < 10^{-66}$ to safeguard 64-digit precision. Results are presented in Table 6.

r_*	n_{cut}	$\psi_{10M^{-1},0}^{ ext{in,R}}(r_*)$	Execution time (s)
$\overline{13M}$	2298	$-0.3784442763432927 + 0.9256281869513429\mathrm{i}$	$0.05\mathrm{s}$
$\overline{24.4M}$	10183	$0.4918333004999262 + 0.8706900301763171 \mathrm{i}$	$0.25\mathrm{s}$

Table 6 – Dynamically determined cutoff $n_{\rm cut}$ and computed modes $\psi_{\omega\ell}^{\rm in,R}(r_*)$ at the slowestconverging points in each interval. Tabulated values are truncated to 8 significant digits; full precision was retained in calculations.

For the actual computation, we implemented these series in Mathematica using a fixed $n_{\rm cut} = 5000$ to ensure at least 20 significant digits for $r_* \in [-4M, 13M]$ and a fixed $n_{\rm cut} = 11000$ for 64 significant digits for $r_* \in [13.2M, 24.4M]$. These distinct precision levels reflect computational priorities at different stages of the project. The fixed number of terms in the series reduces the small computational overhead caused by computing $\delta_{\rm Re}^J$ and δ_{Im}^{J} , which would be necessary to dynamically update n_{cut} .

4.1.2 Upgoing modes

Similar to the treatment of the ingoing modes, applying the decomposition from Equation (4.1) to $\tilde{f}_{\omega\ell m}^{\mathrm{up,R}}$ yields

$$\tilde{f}_{\omega\ell m}^{\text{up,R}}(\mathbf{x}) = e^{-i\omega t} \psi_{\omega\ell}^{\text{up,R}}(r), \tag{4.12}$$

where $\psi_{\omega\ell}^{\text{up,R}}$ is defined by asymptotic boundary conditions near the horizon $(r_* \to -\infty)$ and at infinity $(r_* \to \infty)$

$$\psi_{\omega\ell}^{\text{up,R}} \sim \begin{cases} e^{i\omega r_*} + \rho_{\omega\ell}^{\text{up}} e^{-i\omega r_*}, & r_* \to -\infty \\ T_{\omega\ell} e^{i\omega r_*}, & r_* \to \infty. \end{cases}$$
(4.13)

For computational convenience we define the transmission-normalized version of these modes which satisfy

$$\bar{\psi}_{\omega\ell}^{\text{up,R}} \sim \begin{cases} \bar{I}_{\omega\ell} e^{i\omega r_*} + \bar{\rho}_{\omega\ell}^{\text{up}} e^{-i\omega r_*}, & r_* \to -\infty \\ e^{i\omega r_*}, & r_* \to \infty, \end{cases}$$
(4.14)

where $\bar{I}_{\omega\ell} = T_{\omega\ell}^{-1}$ and $\bar{\rho}_{\omega\ell}^{\rm up} = T_{\omega\ell}^{-1} \rho_{\omega\ell}^{\rm up}$. To compute $\bar{\psi}_{\omega\ell}^{\rm up,R}$ and $\bar{\psi}_{\omega\ell}^{\rm up,R}$ numerically, we employed the NDSolve-based method implemented in the ReggeWheeler Mathematica package from the Black Hole Perturbation Toolkit (BHPToolkit)[26]. Specifically, the ReggeWheelerRadial command was executed with 23 significant digits for ω and r_* in the interval $r_* \in [-4M, 13M]$, and 32 significant digits for these parameters in the interval $r_* \in [13.2M, 24.4M]$.

Unlike the Jaffé series method used for the ingoing modes—where truncation errors are explicitly controlled via the cutoff n_{cut} —the NDSolve-based approach relies on adaptive algorithms. Consequently, the precision in the resulting solutions and its derivatives can only be coarsely estimated before evaluation. Therefore, post-testing is necessary to verify the number of consistent significant digits. A summary of these tests and their results is presented in Section 4.3.

4.1.3 Inside modes

Similar to the treatment of the ingoing and upgoing modes, applying the decomposition from Equation (4.1) to $\tilde{f}_{\omega\ell m}^{\rm R}$ and $\tilde{f}_{\omega\ell m}^{\rm L}$ yields

$$\tilde{f}_{\omega\ell m}^{\mathrm{R}}(\mathsf{x}) = \mathrm{e}^{-\mathrm{i}\omega t} \psi_{\omega\ell}^{\mathrm{ins}}(r) \quad \text{and} \quad \tilde{f}_{\omega\ell m}^{\mathrm{L}}(\mathsf{x}) = \mathrm{e}^{\mathrm{i}\omega t} \psi_{\omega\ell}^{\mathrm{ins}}(r),$$
 (4.15)

where $\psi_{\omega\ell}^{\rm ins}$ is defined by the asymptotic boundary condition near the horizon (from inside, $\bar{r}_* \to -\infty$)

$$\psi_{\omega\ell}^{\rm ins}(r) \sim e^{-i\omega\bar{r}_*}, \quad \bar{r}_* \to -\infty.$$
 (4.16)

Unlike the ingoing $\tilde{f}^{\text{in},R}_{\omega\ell m}$ and upgoing $\tilde{f}^{\text{up},R}_{\omega\ell m}$ modes, $\tilde{f}^{\text{R}}_{\omega\ell m}$ and $\tilde{f}^{\text{L}}_{\omega\ell m}$ share the same radial dependence through $\psi^{\text{ins}}_{\omega\ell}$. This arises from the timelike nature of the interior tortoise coordinate \bar{r}_* , which causes hypersurfaces of constant \bar{r}_* to become spacelike. Specifically, the limit $\bar{r}_* \to -\infty$ defines a hypersurface whose future domain of dependence is region II (black hole interior). Therefore, data on it uniquely determines $\psi^{\text{ins}}_{\omega\ell}$ inside the black hole.

For $r \in (0, r_s)$, the solution $\psi_{\omega\ell}^{\text{ins}}$ to Equation 4.2 is expressed via the Frobenius series:

$$\psi_{\omega\ell}^{\text{ins}}(r) = e^{-i\omega\bar{r}_*} \sum_{n=0}^{\infty} b_{n\omega\ell} (r - r_s)^n, \qquad (4.17)$$

where the coefficients $b_{n\omega\ell}$ obey the recurrence relation

$$b_{n\omega\ell} = \frac{2i(n-3)\omega}{n(n-2i\omega r_s)(r_s)^2} a_{(n-3)\omega\ell} + \frac{\ell(\ell+1) - (n-2)(n-3-6i\omega r_s)}{n(n-2i\omega r_s)(r_s)^2} a_{(n-2)\omega\ell} + \frac{\ell(\ell+1) - 5 - (2n+1)(n-3) + (n-1)6i\omega r_s}{n(n-2i\omega r_s)r_s} a_{(n-1)\omega\ell},$$
(4.18)

with initial conditions $a_{0\omega\ell} = 1$ and $a_{n\omega\ell} = 0$ for all n < 0. A series representation of $\psi_{\omega\ell}^{\text{ins'}}(r)$ is straightforwardly obtained by taking the r-derivative of Equation (4.17).

While the Frobenius series can, in principle, be extended beyond the horizon, its radius of convergence restricts its validity to $0 < r < 2r_s$. The full derivation of the series is presented in great detail in [54, Section 4.3].

Similarly to the Jaffé series for the ingoing modes, the Frobenius series is truncated at $n = n_{\rm cut}$ in numerical computations, introducing a relative error in the real $(\delta_{\rm Re}^F)$ and imaginary $(\delta_{\rm Im}^F)$ parts of the solution. These are estimated by

$$\delta_{\text{Re/Im}}^{F} = \frac{\left| \text{Re/Im} \left[b_{(n_{\text{cut}}+1)\omega\ell} \left(r - r_{s} \right)^{n_{\text{cut}}+1} \right] \right|}{\left| \text{Re/Im} \left[\sum_{n=0}^{n_{\text{cut}}} b_{n\omega\ell} \left(r - r_{s} \right)^{n} \right] \right|}.$$
(4.19)

$r_* \to -\infty$	Wronskian	$r_* \to \infty$
$2i\omega$	$W\left[\bar{\psi}_{\omega\ell}^{\mathrm{in,R}}, \bar{\psi}_{\omega\ell}^{\mathrm{in,R*}}\right]$	$i2\omega \left(\left \bar{I}_{\omega\ell} \right ^2 - \left \bar{\rho}_{\omega\ell}^{\rm in} \right ^2 \right)$
$-$ 2 $\mathrm{i}\omegaar{I}_{\omega\ell}$	$W\left[\bar{\psi}_{\omega\ell}^{\mathrm{in,R}},\psi_{\omega\ell}^{\mathrm{up,R}}\right]$	$2\mathrm{i}\omegaar{I}_{\omega\ell}$
$-2\mathrm{i}\omega\left(\left \bar{I}_{\omega\ell}\right ^2 - \left \bar{\rho}_{\omega\ell}^{\mathrm{up}}\right ^2\right)$	$W\left[\bar{\psi}_{\omega\ell}^{\mathrm{up,R}}, \bar{\psi}_{\omega\ell}^{\mathrm{up,R*}}\right]$	$-2i\omega$
$2\mathrm{i}\omegaar ho_{\omega\ell}^{\mathrm{up}}$	$W\left[\bar{\psi}_{\omega\ell}^{\text{up,R}}, \bar{\psi}_{\omega\ell}^{\text{in,R*}}\right]$	$-2\mathrm{i}\omega\bar{\rho}_{\omega\ell}^{\mathrm{in}*}$

Table 7 – The Wronskian between combinations of $\bar{\psi}_{\omega\ell}^{\text{in,R}}$, $\bar{\psi}_{\omega\ell}^{\text{up,R}}$ and their complex conjugates in the limits $r_* \to \pm \infty$ are presented.

An analogous approach was adopted for the error estimate in $\psi_{\omega\ell}^{\text{ins'}}(r)$.

We implemented this series in Mathematica, dynamically increasing $n_{\rm cut}$ until $\delta_{\rm Re} < 10^{-18}$ and $\delta_{\rm Im} < 10^{-18}$ for all computations. A safety margin of two orders of magnitude was applied to the convergence criteria (targeting 16 significant digits, enforcing 18).

4.2 The Wronskian relations

The Wronskian of two solutions ψ_1 and ψ_2 to the Schrödinger-like equation (4.2) is

$$W[\psi_1, \psi_2] = \psi_1 \frac{d\psi_2}{dr_*} - \psi_2 \frac{d\psi_1}{dr_*}.$$
 (4.20)

Since that equation has no first derivative term, Abel's theorem [55, Theorem 3.2.7] guarantees that $W[\psi_1, \psi_2]$ is independent of r_* . Leveraging this r_* -independence, we evaluate the Wronskians

$$W[\bar{\psi}_{\omega\ell}^{\rm in,R},\bar{\psi}_{\omega\ell}^{\rm in,R*}], \quad W[\bar{\psi}_{\omega\ell}^{\rm in,R},\bar{\psi}_{\omega\ell}^{\rm up,R}], \quad W[\bar{\psi}_{\omega\ell}^{\rm up,R},\bar{\psi}_{\omega\ell}^{\rm up,R*}] \quad \text{and} \quad W[\bar{\psi}_{\omega\ell}^{\rm up,R},\bar{\psi}_{\omega\ell}^{\rm in,R*}]$$

at the asymptotic boundaries $r_* \to \infty$ and $r_* \to -\infty$, using the boundary conditions of the modes from Equations (4.6) and (4.14). The results are summarized in Table 7. Additionally, we evaluated $W[\bar{\psi}_{\omega\ell}^{\rm ins}, \bar{\psi}_{\omega\ell}^{\rm ins*}]$ at $\bar{r}_* \to -\infty$ using its boundary condition from Equation (4.16) to obtain

$$W[\bar{\psi}_{\omega\ell}^{\text{ins}}, \bar{\psi}_{\omega\ell}^{\text{ins}*}] = 2i\omega. \tag{4.21}$$

The so-called Wronskian relations are derived by equating the Wronskian at $r_* \to -\infty$ and $r_* \to \infty$. These are summarized below:

$$1 = \left| \bar{I}_{\omega\ell} \right|^2 - \left| \bar{\rho}_{\omega\ell}^{\text{in}} \right|^2, \tag{4.22}$$

$$1 = \left| \bar{I}_{\omega \ell} \right|^2 - \left| \bar{\rho}_{\omega \ell}^{\text{up}} \right|^2, \tag{4.23}$$

$$\bar{\rho}_{\omega\ell}^{\rm up} = -\bar{\rho}_{\omega\ell}^{\rm in*}.\tag{4.24}$$

4.3 Reliability of the numerical solutions to the Schrödinger-like equation

In this section the results obtained through the numerical procedures outlined in Section 4.1 are presented. For a matter of organization, we divided this exposition in four subsections, each dedicated to a single group of results.

4.3.1 The ingoing modes

The $\bar{\psi}_{\omega\ell}^{\text{in,R}}$ modes and their derivatives were evaluated through a numerical implementation of the Jaffé series with convergence controlled by an estimate of its remainder. To test these results we computed the left-hand side (l.h.s.) of (see the first line of Table 7)

$$W\left[\bar{\psi}_{\omega\ell}^{\text{in,R}}, \bar{\psi}_{\omega\ell}^{\text{in,R*}}\right] = 2i\omega \tag{4.25}$$

and compared with the right-hand side (r.h.s.). The largest relative error obtained in this test was 10^{-20} , hence, these modes and derivatives are consistent to 20 digits, as originally targeted.

4.3.2 The inside modes

Similarly to the $\bar{\psi}_{\omega\ell}^{\text{in,R}}$ modes analyzed in the previous subsection, the $\bar{\psi}_{\omega\ell}^{\text{ins}}$ modes and their derivatives were computed by a numerical implementation of the Frobenius series from Equation (4.17) with precision controlled by an estimate of its remainder. To verify the outcome of these numerical computations, we evaluated the l.h.s. of (see Equation (4.21))

$$W\left[\bar{\psi}_{\omega\ell}^{\text{ins}}, \bar{\psi}_{\omega\ell}^{\text{ins}*}\right] = 2i\omega \tag{4.26}$$

and compared with its r.h.s. . The largest relative error obtained in this test was 10^{-16} , hence, the computed modes and derivatives are consistent to 16 digits, as originally targeted.

4.3.3 The upgoing modes

In contrast to the ingoing and inside modes, the $\bar{\psi}^{\text{up},R}_{\omega\ell}$ modes and their derivatives were not computed via series expansions. Instead, they were obtained by solving Equation (4.2) using the ReggeWheelerRadial command, which employs an NDSolve-based algorithm from the ReggeWheeler Mathematica package of the BHPToolkit [26]. This method introduces a challenge in controlling output precision, as the number of correct significant digits in the results can only be estimated after the computation is complete. More precisely, the number of significant digits in the output as given by the command Precision[] is generally larger than the number of correct significant digits as estimated by the self-consistency tests that

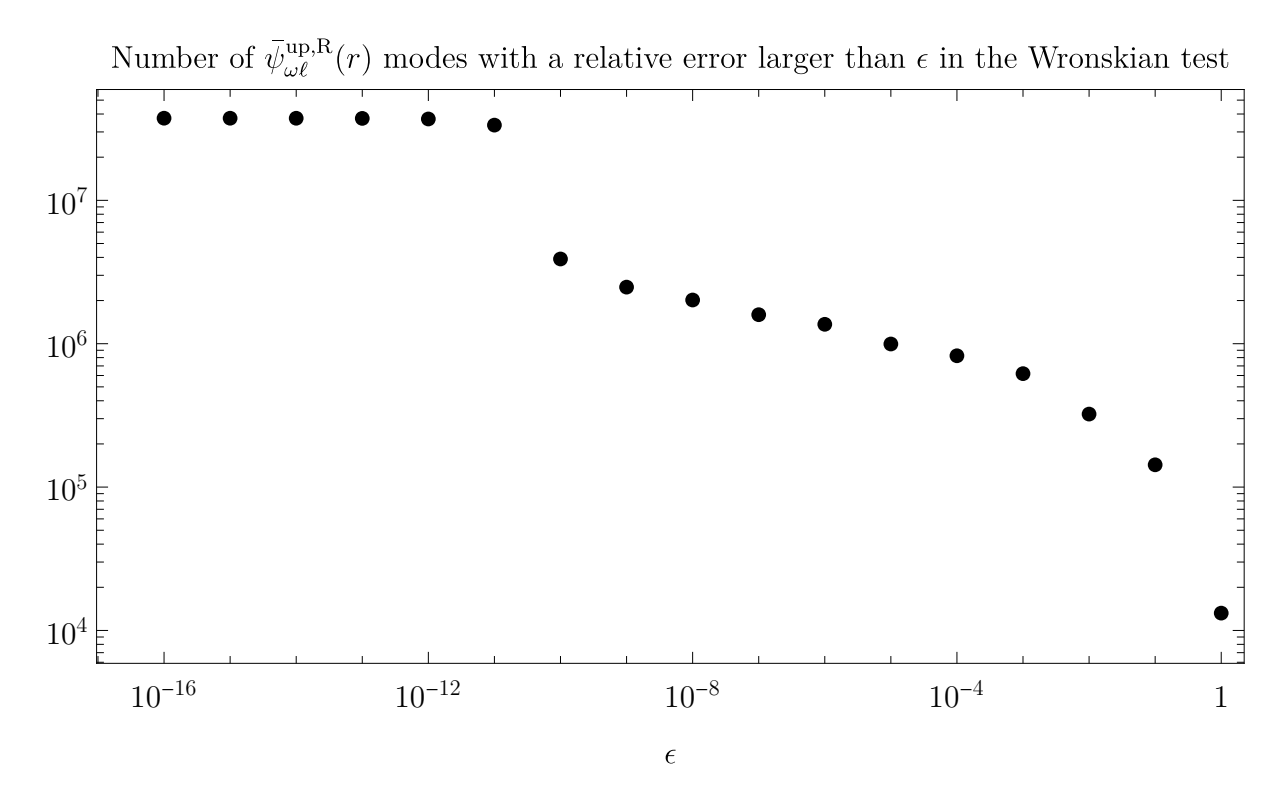


Figure 5 – The number of upgoing modes with a relative error larger than ϵ in the Wronskian test is plotted as a function of ϵ .

will be described. Consequently, achieving the upgoing modes at a target precision while ensuring self-consistency necessitates an iterative refinement process.

In the first step, we computed the upgoing modes and their derivatives using 23 significant digits for the input to ReggeWheelerRadial over the range $r_* \in [-4M, 13M]$, and 32 significant digits for $r_* \in [13.2M, 24.4M]$. In both cases, our intention was to obtain approximately 16 correct significant digits in the results. To test them, we evaluated the left-hand side (l.h.s.) of (see the third line of Table 7)

$$W\left[\bar{\psi}_{\omega\ell}^{\mathrm{up,R}},\bar{\psi}_{\omega\ell}^{\mathrm{up,R*}}\right]=-2\mathrm{i}\omega$$

and compared it with the right-hand side (r.h.s.).

For $r_* \in [13.2M, 24.4M]$, the largest relative error in the Wronskians up to $\ell = 88$ was $\approx 10^{-12}$. For $\ell > 88$, the largest relative error reached 10^0 . However, as will be argued in Section 5.1.1, modes with $\ell > 12$ are exponentially damped by the smoothing function adopted to regulate the ℓ -sum.

For $r_* \in [13.2M, 24.4M]$, an initial analysis is illustrated in Figure 5, which shows the number of Wronskians with a relative error greater than ϵ , plotted as a function of ϵ . Specifically, we found that $\approx 39\%$ of the Wronskians had a relative error exceeding 10^{-11} , whereas only $\approx 3\%$ exceeded 10^{-9} . The values of ω and ℓ for these cases are shown in Figure 6, where we see that the number of such cases increases with ω and ℓ , rising more rapidly for $\ell \gtrsim 70$.

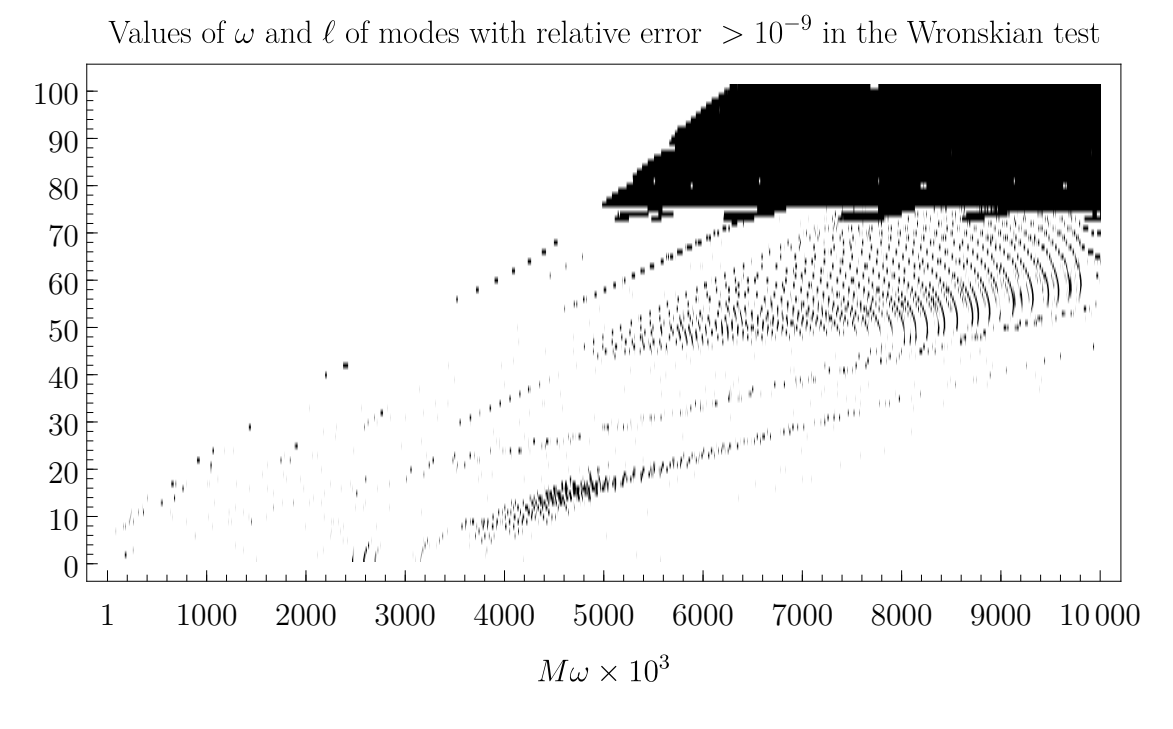


Figure 6 – The values of ω and ℓ of the upgoing modes with a relative error greater than 10^{-9} in the Wronskian test are represented by small black rectangles.

To reduce the relative error of a given mode $\bar{\psi}_{\omega\ell}^{\text{up,R}}(r)$ and its derivative in the Wronskian test, it is crucial to estimate the minimum number of significant digits required in these quantities to ensure a Wronskian with at least n significant digits. This can be reasoned as follows:

Let $\bar{\psi}_{\omega\ell}^{\mathrm{up,R}}(r)$ and its derivative be of order 10^{α} and 10^{β} , respectively. The Wronskian involves subtracting two terms, each formed by the product of the mode and its derivative (i.e., of order $10^{\alpha+\beta}$). Considering the exact expression for the Wronskian (see Table 7) and the frequency range $M\omega \in [10^{-3}, 10]$ in our dataset, the smallest Wronskian across all frequencies is of order 10^{-3} . To obtain a result of this magnitude from the subtraction of two terms of order $10^{\alpha+\beta}$, a cancellation of $\alpha + \beta + 3$ digits is expected. Therefore, ensuring that $\bar{\psi}_{\omega\ell}^{\mathrm{up,R}}(r)$ and its derivative have more than $\alpha + \beta + 3$ significant digits would yield a Wronskian with at least one significant digit across all r_* , ω , and ℓ in our dataset.

Adopting a more conservative approach, we consider $2 \max \left[\alpha, \beta\right] + 3$ instead of $\alpha + \beta + 3$ as the estimated number of significant digits in $\bar{\psi}_{\omega\ell}^{\text{up,R}}(r)$ and its derivative, such that it produces a Wronskian with at least one significant digit across all r_* , ω , and ℓ in our dataset. This results in a higher estimate whenever $\alpha \neq \beta$. This adjustment serves the practical purpose of mitigating precision degradation, as the ReggeWheelerRadial command typically outputs solutions with fewer significant digits than the input. By overestimating the required input precision (through $2 \max \left[\alpha, \beta\right] + 3$), we create a safety margin to help counteract this loss of precision. Furthermore, to guarantee at least n significant digits in the Wronskian test we add n to this conservative estimate.

Finally, to ensure that a given $\bar{\psi}_{\omega\ell}^{\mathrm{up,R}}(r)$ and its derivative produce a Wronskian with a relative error of at most 10^{-n} — which is ensured to happen, provided that this Wronskian have at least n significant digits— we estimate, based on the arguments presented in the previous paragraph, the required number of significant digits for the input to ReggeWheelerRadial as

$$\operatorname{prec}(\omega, \ell, r, n) = \left[2 \max \left[\log_{10} \left| \bar{\psi}_{\omega\ell}^{\operatorname{up,R}}(r) \right|, \log_{10} \left| \bar{\psi}_{\omega\ell}^{\operatorname{up,R}}(r) \right| \right] + 3 + n \right], \tag{4.27}$$

where the ceiling function guarantees that the estimated number of significant digits is an integer value.

With this estimate at hand, consider the set of upgoing modes and their derivatives

$$\left\{ \bar{\psi}_{\omega\ell}^{\mathrm{up,R}}(r) , \, \bar{\psi}_{\omega\ell}^{\mathrm{up,R}}(r) \, | \, r_*(r) \in [-4M, 13M] \subset \mathfrak{r}_* \, , \, \omega \in \mathfrak{w} \, , \, \ell \in \mathfrak{l} \right\}$$

$$(4.28)$$

previously evaluated with m = 23 significant digits in the input to ReggeWheelerRadial. The refinement process to ensure these modes pass the Wronskian test with a relative error of order 10^{-n} proceeds as follows:

- 1. Let $\ell_0 \in \mathfrak{l}$ be a given value of ℓ .
- 2. For each ω , let $A(\omega) = \sup \{\operatorname{prec}(\omega, \ell_0, r, n) \mid r_*(r) \in \mathfrak{r}_*\}$ be the largest estimated number of significant digits across all r.
- 3. Since the current set of modes was produced by providing m significant digits in the input to ReggeWheelerRadial, only modes where $\operatorname{prec}(\omega, \ell, r, n) > m$ need refinement. The set of such modes for ℓ_0 is

$$B(\ell_0) = \left\{ \bar{\psi}^{\mathrm{up,R}}_{\omega \ell_0}(r) \, | \, \mathrm{prec}(\omega, \ell_0, r, n) > m \, , \, r_*(r) \in [-4M, 13M] \subset \mathfrak{r}_* \, , \, \omega \in \mathfrak{w} \right\}.$$

- 4. For each $\bar{\psi}_{\omega\ell_0}^{\mathrm{up,R}}(r) \in B(\ell_0)$, recompute the mode and its derivative using $A(\omega)$ significant digits for ω and $\mathrm{prec}(\omega, \ell_0, r, n)$ digits for r.
- 5. Repeat for all other values of $\ell_0 \in \mathfrak{l}$.

In principle, we could select any value of n and refine the existing results (initially computed with m=23 significant digits in the input to ReggeWheelerRadial). However, this is impractical due to two constraints: The number of modes that should be re-evaluated (i.e., the size of B) and the time required to re-evaluate each mode and its derivative increase with n. On top of that, refining the modes with $\ell \gtrsim 12$ offers a diminishing return, since these are exponentially suppressed by the smoothing function introduced in the ℓ -sum (See 5.1.1). A pragmatic choice based on the Wronskian test results is n=9 as this would require re-evaluating at most $\approx 3\%$ of the modes. To incorporate a safety margin, we added 6 additional orders of magnitude, resulting in n=15. However, refining all modes up to $\ell=100$ would demand a prohibitively long computational time. Consequently, we

restricted the refinement process to modes with $\ell \leq 29$, the highest feasible value given our computational resources and time constraints.

Prior to refinement, 2, 481, 065 ($\approx 3\%$) Wronskians exhibited a relative error greater than 10^{-9} . Among these, 9, 489 corresponded to modes with $\ell \leq 29$. By executing the refinement process with n=15, a total of 4,864,549 modes with $\ell \leq 29$ were re-evaluated using input precisions ranging from 24 to 280 significant digits. While the primary goal was to correct the 9,489 modes, the conservative error margin of 6 additional digits (n=9+6) necessitated refining 4,864,549 modes. After this process, all refined modes and their derivatives produced Wronskians with relative errors below 10^{-9} .

In the next step, we re-ran the Wronskian test exclusively for the $\ell \leq 29$ upgoing modes and their derivatives of the complete dataset. We observed that 3,364 Wronskians still exhibited a relative error greater than 10^{-9} . These modes were not addressed during the refinement process because their estimated required input precision (≤ 23 significant digits) fell within the original 23-digit precision already used. We fixed these 3,364 modes by re-evaluating them with 64 significant digits in the input — despite the estimated requirement $\operatorname{prec}(2.001M^{-1}, 7, -0.6M, 15) = 23$ — which reduced their relative error in the Wronskian's relative error to below 10^{-30} for them.

Summarizing, all the radial upgoing modes and their derivatives yield a relative error of at most 10^{-9} within $\ell \in \{0, 29\}$ and $\forall \omega \in \mathfrak{w}$ (the relevant regime for the numerical method that will be presented in Section 5.1.1).

4.3.4 Scattering amplitudes

To evaluate the incidence amplitudes $\bar{I}_{\omega\ell}$ we used data from [27] which was produced through an implementation of the Mano-Suzuki-Takasugi (MST) method [56], where the EF modes obey a normalization different from the ones we used up to now. Specifically, in Section 3.3.1 we defined the incidence-normalized modes and in Sections 4.1.1 and 4.1.2 we introduced the transmission-normalized modes. The radial part of the EF modes in [27] obeys the following boundary conditions

$$\bar{\bar{\psi}}_{\omega\ell}^{\text{in,R}} \sim \begin{cases} \bar{\bar{T}}_{\omega\ell}^{\text{in}} e^{-i\omega r_*}, & r_* \to -\infty \\ \bar{\bar{I}}_{\omega\ell}^{\text{in}} e^{-i\omega r_*} + \bar{\bar{\rho}}_{\omega\ell}^{\text{in}} e^{i\omega r_*}, & r_* \to \infty, \end{cases}$$
(4.29)

and

$$\bar{\psi}_{\omega\ell}^{\text{up,R}} \sim \begin{cases}
\bar{\bar{I}}_{\omega\ell}^{\text{up}} e^{i\omega r_*} + \bar{\bar{\rho}}_{\omega\ell}^{\text{up}} e^{-i\omega r_*}, & r_* \to -\infty \\
\bar{\bar{T}}_{\omega\ell}^{\text{up}} e^{i\omega r_*}, & r_* \to \infty.
\end{cases}$$
(4.30)

From the modes in this data, the transmission-normalized incidence amplitude $\bar{I}_{\omega\ell}$ was calculated in two independent ways:

$$\bar{I}_{\omega\ell}^{\rm in} = \frac{\bar{\bar{I}}_{\omega\ell}^{\rm in}}{\bar{\bar{T}}_{\omega\ell}^{\rm in}} \tag{4.31}$$

and

$$\bar{I}_{\omega\ell}^{\rm up} = \frac{\bar{I}_{\omega\ell}^{\rm up}}{\bar{\bar{T}}_{\omega\ell}^{\rm up}},\tag{4.32}$$

which ideally produces equal results since the transmission-normalized modes share the same incidence amplitude, i.e., $\bar{I}_{\omega\ell} = \bar{I}^{\rm in}_{\omega\ell} = \bar{I}^{\rm up}_{\omega\ell}$. For clarity, throughout this (and only this) sub-subsection, the labels "in" and "up" will be included as superscripts in the transmission-normalized incidence amplitudes to indicate whether they were evaluated using Equation (4.31) or (4.32). Everywhere else in this text, these amplitudes will continue to be denoted as $\bar{I}_{\omega\ell}$.

The dataset from [27] did not include the values of $\bar{\rho}_{\omega\ell}^{\text{up}}$ or $\bar{\rho}_{\omega\ell}^{\text{in}}$. Therefore, we evaluated $\bar{\rho}_{\omega\ell}^{\text{up}}$ using the fourth line of Table 7, expressing it as

$$\bar{\rho}_{\omega\ell}^{\rm up} = \frac{W\left[\bar{\psi}_{\omega\ell}^{\rm up,R}, \bar{\psi}_{\omega\ell}^{\rm in,R*}\right]}{2i\omega}.$$
(4.33)

We computed this using the $\bar{\psi}_{\omega\ell}^{\text{in,R}}$ and $\bar{\psi}_{\omega\ell}^{\text{up,R}}$ modes (and their derivatives) from our data at $r_* = 13M$ as this is the farthest point from the horizon covered by our data^{1,2}.

Finally, the $\bar{\rho}_{\omega\ell}^{\text{in}}$ amplitudes were derived from $\bar{\rho}_{\omega\ell}^{\text{up}}$ via the Wronskian relation in Equation (4.24):

$$\bar{\rho}_{\omega\ell}^{\rm in} = -\bar{\rho}_{\omega\ell}^{\rm up*}.\tag{4.34}$$

Consequently, we expect $\bar{\rho}_{\omega\ell}^{\text{in}}$ and $\bar{\rho}_{\omega\ell}^{\text{up}}$ to share the same number of correct significant digits. To test $\bar{I}_{\omega\ell}^{\text{in}}$ and $\bar{I}_{\omega\ell}^{\text{up}}$ we used the fact that they should be equal:

$$\bar{I}_{\omega\ell}^{\rm in} = \bar{I}_{\omega\ell}^{\rm up}.\tag{4.35}$$

Hence, the relative difference between the l.h.s. and the r.h.s. of this equation provides an estimate of the number of correct significant digits in these amplitudes. For the reflection amplitudes, we performed two tests based on the Wronskian relations in Equations (4.22) and (4.23). These tests consisted in evaluating the relative difference between the l.h.s. and r.h.s. of

$$\left|\bar{I}_{\omega\ell}^{\rm up}\right|^2 = 1 + \left|\bar{\rho}_{\omega\ell}^{\rm up}\right|^2 \tag{4.36}$$

and

$$\left|\bar{I}_{\omega\ell}^{\rm in}\right|^2 = 1 + \left|\bar{\rho}_{\omega\ell}^{\rm in}\right|^2. \tag{4.37}$$

Across all ω and ℓ values in our dataset, the largest relative differences obtained when testing $\bar{I}^{\rm in}_{\omega\ell}$ and $\bar{I}^{\rm up}_{\omega\ell}$ were $\approx 10^{-9}$. For $\bar{\rho}^{\rm up}_{\omega\ell}$ and $\bar{\rho}^{\rm in}_{\omega\ell}$, the largest relative differences were

Unfortunately, it was only after evaluating these amplitudes that we extended our data up to $r_* = 24.4M$. We verified that re-evaluating these amplitudes using these extended would potentially increase the precision of the amplitudes up to three more orders of magnitude.

precision of the amplitudes up to three more orders of magnitude.

Due to the technique used when computing the $\bar{\psi}^{\text{up},R}_{\omega\ell}$ modes and their derivatives, it is expected that their number of correct significant digits increases with r_* because it results in solutions closer to where the boundary conditions are set.

 $\approx 10^{1}$. In all cases, the smallest relative difference was $\approx 10^{-25}$. A detailed visualization of the distribution of relative differences is shown in Figure 7.

The influence of ℓ on the frequency of relative errors $\geq 10^{-9}$ in these tests is shown in Figure 8. From this figure, we infer that most errors occur for $\ell \gtrsim 75$, with a smaller cluster near $\ell \approx 20$.

Finally, Figure 9 highlights the ω and ℓ values where the relative difference in the tests exceeds 10^{-9} . It reveals that the errors near $\ell \gtrsim 20$ occur at large $M\omega \approx 10$, while those for $\ell \gtrsim 75$ are distributed across all $M\omega$ values.

Summarizing, the ingoing and upgoing incidence amplitudes in our data are self-consistent to a relative difference of at most 10^{-9} in the Wronskian test across the span of ω and ℓ in our data. The ingoing and upgoing reflection amplitudes are self-consistent to a relative difference of at most 10^{-9} in the Wronskian test for $\ell \lesssim 75$ and $M\omega \lesssim 9.3M$, which covers more than enough the regime that is relevant for the numerical method that will be presented in Section 5.1.1.

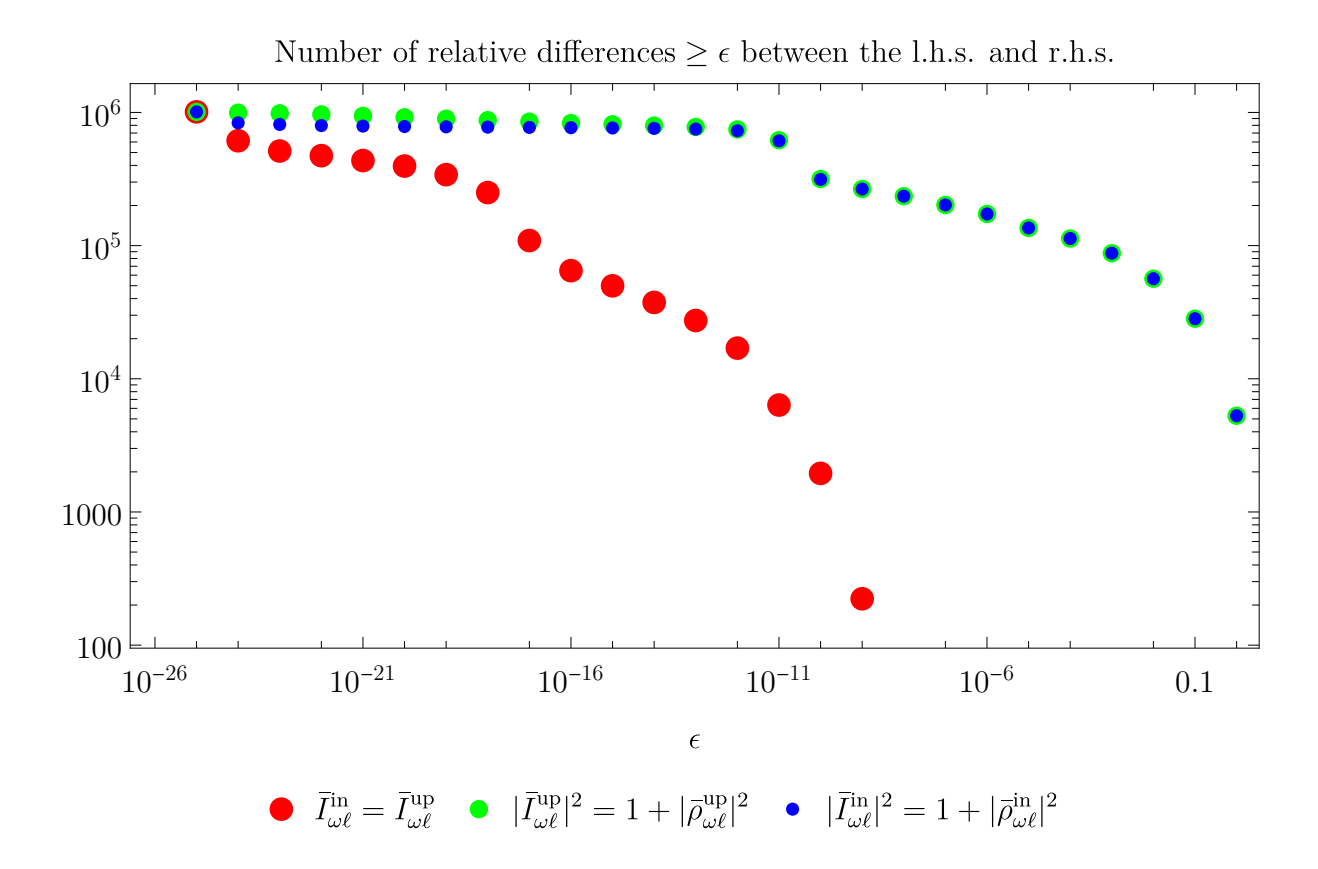


Figure 7 – The number of relative differences larger than or equal to ϵ in the tests of the amplitudes is plotted as a function of ϵ . The red dots refer to the ingoing and upgoing incidence amplitudes; the green dots refer to the ingoing and reflection upgoing amplitudes; the blue dots refer to the incidence and reflection ingoing amplitudes. In order to provide a better visualization of overlapping data, we plotted the points with different sizes. Across the span of ω and ℓ in our data, the smallest relative difference for all amplitudes is $\approx 10^{-25}$. For the incidence amplitudes, largest one is $\approx 10^{-9}$ and for the reflection amplitudes it is $\approx 10^1$.

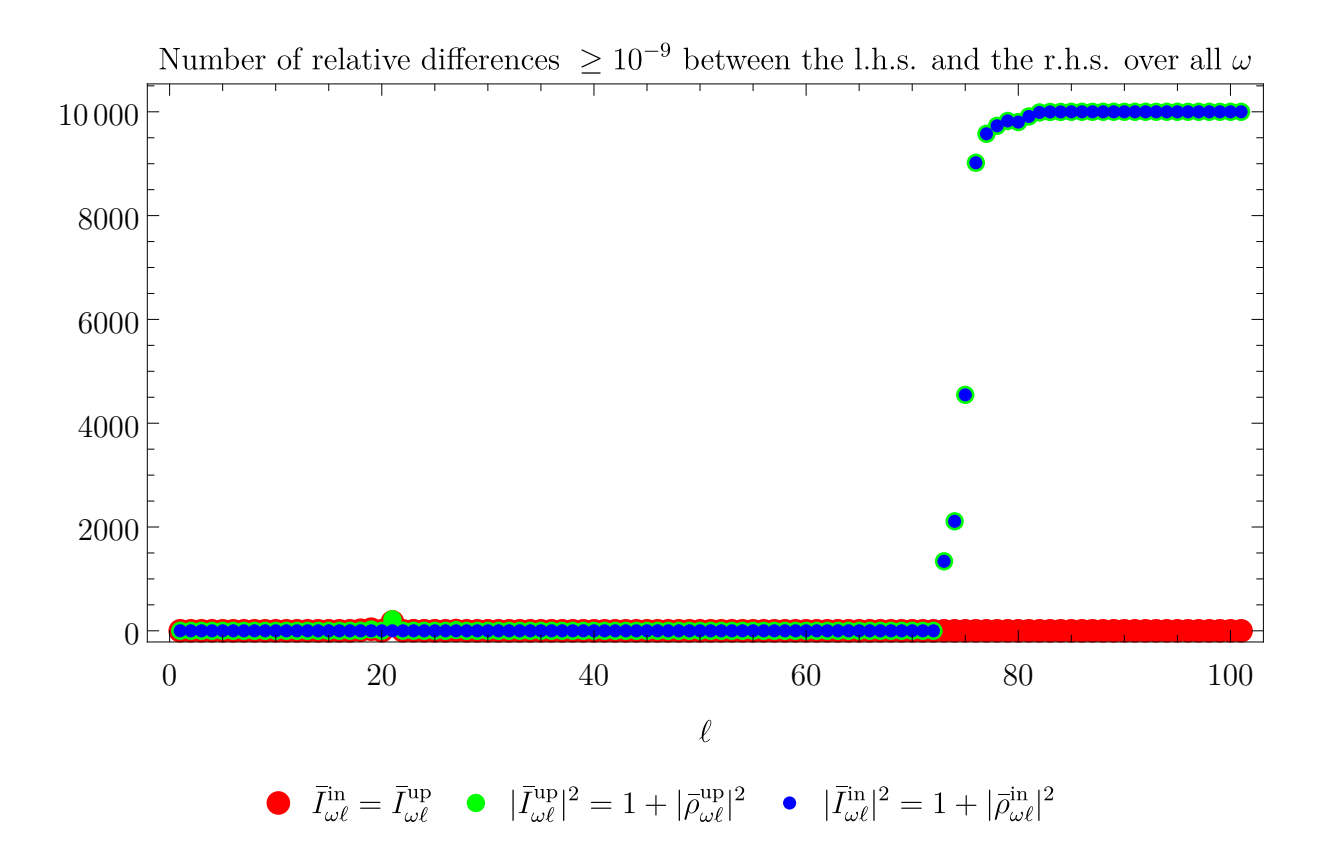


Figure 8 – The number relative differences larger than or equal to 10^{-9} in the tests of the amplitudes over all ω is plotted as a function of ℓ . The red dots refer to the ingoing and upgoing incidence amplitudes; the green dots refer to the ingoing and reflection upgoing amplitudes; the blue dots refer to the incidence and reflection ingoing amplitudes. In order to provide a better visualization of overlapping data, we plotted the points with different sizes. It can be seen that most occurrences are localized in the region $\ell \gtrsim 75$ with a smaller cluster near $\ell \approx 20$.

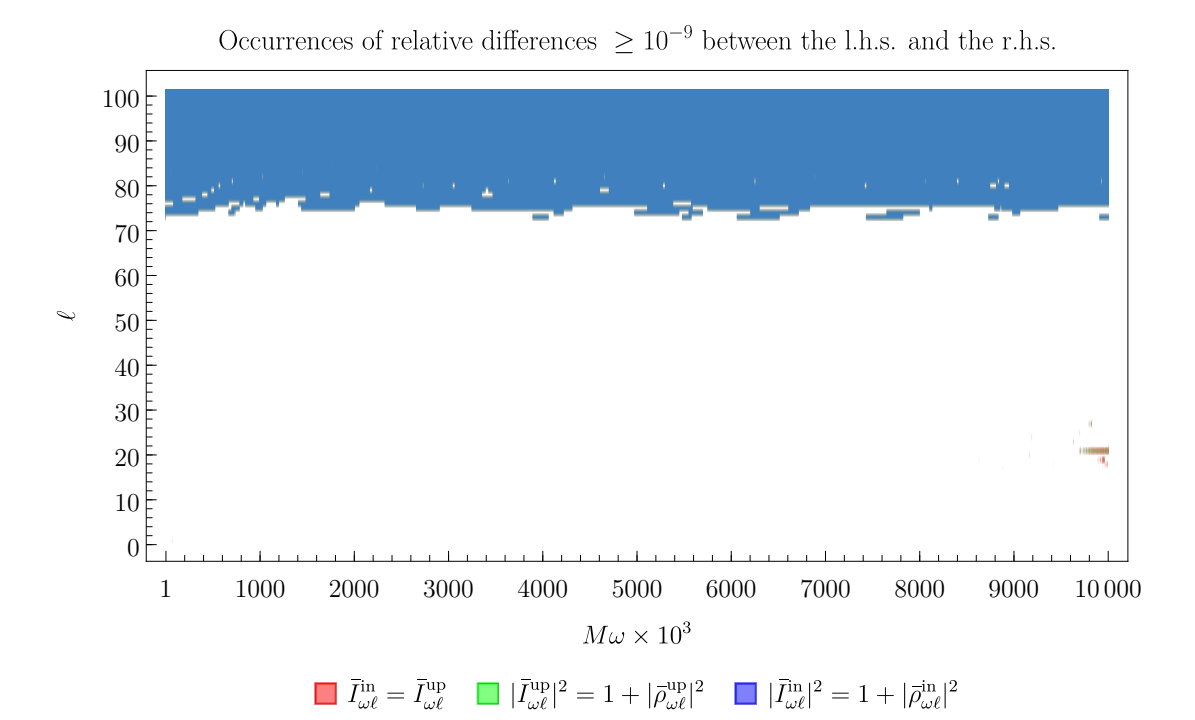


Figure 9 – The values of ω and ℓ of the amplitudes that presented a relative difference larger than or equal to 10^{-9} in the tests is presented. The red dots (mixed with the green ones in the bottom right corner) refer to the ingoing and upgoing incidence amplitudes; the green dots refer to the ingoing and reflection upgoing amplitudes; the purple dots refer to the incidence and reflection ingoing amplitudes. The color of overlapping dots is combined. This plot shows that the occurrences around $\ell \approx 20$ happen only for large $M\omega \approx 10$.

5 Quantum correlations in a scalar field in the Schwarzschild spacetime

In this chapter, we will apply the expressions of the Wightman function that were derived for several setups in Section 3.4. Throughout, we will always consider $x \in \mathfrak{S}$ to be a fixed point.

5.1 Outside the horizon

In this section, we consider both points to be outside the horizon, i.e., $x, x' \in I$.

5.1.1 The numerical method

To illustrate and justify the procedure we will use to compute the Wightman function in the $|B\rangle$ (Boulware), $|U\rangle$ (Unruh) and $|H\rangle$ (Hartle-Hawking) states, we present a construction of the computational method using $|B\rangle$ as an example.

In terms of the radial modes defined in Section 4.1, the Wightman function from Equation (3.74) is expressed as

$$W^{B}(\mathbf{x};\mathbf{x}') = \frac{1}{(4\pi)^{2}rr'} \sum_{\ell=0}^{\infty} (2\ell+1) P_{\ell}(\cos(\gamma)) \int_{0}^{\infty} \frac{d\omega}{\omega} \frac{e^{-i\omega\Delta t}}{\left|\bar{I}_{\omega\ell}\right|^{2}} \left(\bar{\psi}_{\omega\ell}^{\mathrm{in,R}}(r)\bar{\psi}_{\omega\ell}^{\mathrm{in,R*}}(r') + \bar{\psi}_{\omega\ell}^{\mathrm{up,R}}(r)\bar{\psi}_{\omega\ell}^{\mathrm{up,R*}}(r')\right),$$

$$(5.1)$$

where $\Delta t = t - t'$.

To evaluate this expression we split it in two parts: One involving ingoing modes,

$$W_{\rm in}^B(\mathbf{x};\mathbf{x}') = \frac{1}{(4\pi)^2 r r'} \sum_{\ell=0}^{\infty} (2\ell+1) P_{\ell}(\cos(\gamma)) \int_0^{\infty} \frac{\mathrm{d}\omega}{\omega} \frac{\mathrm{e}^{-\mathrm{i}\omega\Delta t}}{\left|\bar{I}_{\omega\ell}\right|^2} \bar{\psi}_{\omega\ell}^{\mathrm{in,R}}(r) \bar{\psi}_{\omega\ell}^{\mathrm{in,R}*}(r'), \tag{5.2}$$

and another involving upgoing modes,

$$W_{\rm up}^B(\mathsf{x};\mathsf{x}') = \frac{1}{(4\pi)^2 r r'} \sum_{\ell=0}^{\infty} (2\ell+1) P_{\ell}(\cos(\gamma)) \int_0^{\infty} \frac{\mathrm{d}\omega}{\omega} \frac{\mathrm{e}^{-\mathrm{i}\omega\Delta t}}{\left|\bar{I}_{\omega\ell}\right|^2} \bar{\psi}_{\omega\ell}^{\mathrm{up,R}}(r) \bar{\psi}_{\omega\ell}^{\mathrm{up,R*}}(r'). \tag{5.3}$$

The full Wightman function is obtained by evaluating and summing these contributions:

$$W^{B}(\mathbf{x}; \mathbf{x}') = W_{\text{in}}^{B}(\mathbf{x}; \mathbf{x}') + W_{\text{up}}^{B}(\mathbf{x}; \mathbf{x}'). \tag{5.4}$$

To simplify the description of the numerical implementation we define the auxiliary functions:

$$G_{\ell}^{\text{in,R};\text{in,R*}}(r,r',\omega) = \frac{1}{\omega \left| \bar{I}_{\omega\ell} \right|^2} \bar{\psi}_{\omega\ell}^{\text{in,R}}(r) \bar{\psi}_{\omega\ell}^{\text{in,R*}}(r')$$
(5.5)

and

$$G_{\ell}^{\text{up,R;up,R*}}(r,r',\omega) = \frac{1}{\omega |\bar{I}_{\omega\ell}|^2} \bar{\psi}_{\omega\ell}^{\text{up,R}}(r) \bar{\psi}_{\omega\ell}^{\text{up,R*}}(r').$$
 (5.6)

For given values of ℓ , r and r', these functions are evaluated for all $\omega \in \mathbf{w}$. Then, the results are interpolated to obtain smooth functions over the domain $M\omega \in [10^{-3}, 10]$. Throughout this process we use the Mathematica option InterpolationOrder $\to 8$.

When selecting the interpolation order, it is critical to avoid extremes. Too small an order fails to capture smooth variations between data points, while too large an order introduces spurious oscillations near the interpolation limits due to Runge's phenomenon because our data points are evenly spaced in ω . Both scenarios can propagate errors during subsequent integration steps and should be carefully mitigated.

As a first example, Figure 10 shows the interpolation results for $r=r'\approx 6.009M$ and $\ell=2$ using interpolation orders 8 and 45. Spurious oscillations are evident near the lower limit $M\omega=10^{-3}$ for the larger interpolation order. The reader might argue that this case is special because both $G_{\ell}^{\text{in},R;\text{in},R*}(r,r',\omega)$ and $G_{\ell}^{\text{up},R;\text{up},R*}(r,r',\omega)$ are real-valued due to r=r'. For this reason we present a second example with $r\approx 6.009M, r'\approx 3.9M$, and $\ell=2$ in Figure 11. In this example we observe that for the larger interpolation order the spurious oscillations near $M\omega=10^{-3}$ persist even for $r\neq r'$.

In addition to illustrating Runge's phenomenon, these figures provide insight into the convergence properties of the ω -integral. As the low-frequency regime $M\omega \to 0$ is approached, we verify that both terms decay at least linearly with ω for all cases in Figures 10 and 11. At the other end, in the high-frequency regime $M\omega \to \infty$, we confirm that the magnitude of both $G_{\ell}^{\text{in},R;\text{in},R*}(r,r',\omega)$ and $G_{\ell}^{\text{up},R;\text{up},R*}(r,r',\omega)$ decays as ω^{-1} , as expected: In this limit, the effective potential in Equation (4.2) becomes negligible for all $r > r_s$ implying that the $\bar{\psi}_{\omega\ell}^{\text{in},R/\text{up},R}(r)$ modes behave as free waves and the decay of the integrands is dictated by their oscillatory behavior with amplitude decaying as ω^{-1} . These two properties ensure the convergence of the ω -integrals in Equations (5.2) and (5.3) whenever $\Delta t \neq 0$ or $\Delta t = 0$ with $r \neq r'$. The case $\Delta t = 0$ with r = r' is more pathological because in the high-frequency limit, the integrand scales as ω^{-1} without the oscillations from $e^{-i\Delta t}$, causing the integral to diverge as $\ln(\omega)$ and some regularization technique should be employed.

From a numerical perspective, there is a critical caveat regarding the convergence of these integrals: accurate results require the cutoff frequency $M\omega_{\rm cut}$ (set to 10 in this work) up to which the ω -integral ranges to be sufficiently large for the integrand to reach the high-frequency asymptotic regime. The reason is that this regime marks the onset of the oscillatory decay of the integrand (in the aforementioned cases). Once it is reached, the integral presents residual oscillations that slowly diminishes towards its true value as $M\omega_{\rm cut}$ increases. This behavior is illustrated in Figure 12, where we integrate $G_\ell^{\rm in,R;in,R*}(r,r',\omega)$ and $G_\ell^{\rm up,R;up,R*}(r,r',\omega)$ for $\Delta t=0, \ell=5, r\approx 6.009M, r'\approx 3.9M$ up to varying values of

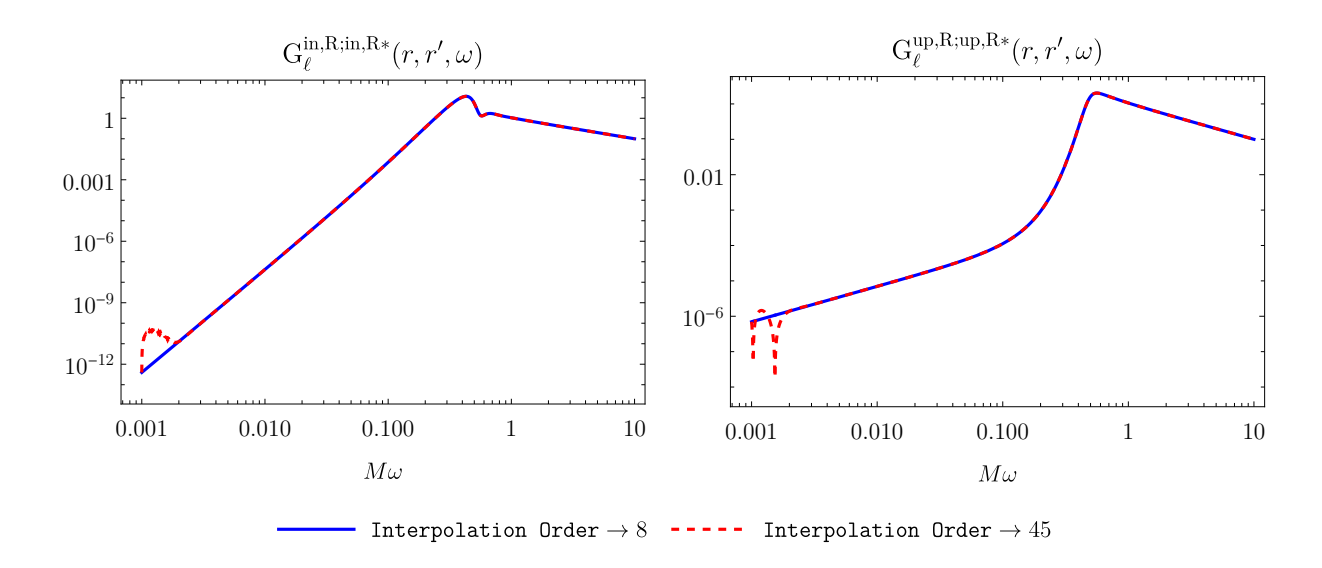


Figure 10 – The interpolated functions $G_{\ell}^{\text{in},R;\text{in},R*}(r,r',\omega)$ (left) and $G_{\ell}^{\text{up},R;\text{up},R*}(r,r',\omega)$ (right) for $r=r'\approx 6.009M$ and $\ell=2$, with interpolation orders 8 (blue) and 45 (red-dashed). Oscillations near $M\omega=10^{-3}$ in the high-order (45) interpolation are a classic manifestation of Runge's phenomenon.

 $M\omega_{\rm cut}$.

In this figure, we observe that the integrals begin to converge — oscillating around their correct values — only after the high-frequency regime is reached. This regime initiates once $(M\omega)^2$ exceeds the peak value of the effective potential defined in Equation (4.2). Since this peak is always located near $3r_s/2$, a coarse estimate for the frequency $M\omega_{\infty}$ marking the onset of the high-frequency regime is

$$M\omega_{\infty} \approx \sqrt{V_{\ell}^{\text{eff}}(3r_s/2)} = \frac{\sqrt{8 + 12\ell(\ell+1)}}{9r_s}.$$
 (5.7)

For $\ell = 5$, used to produce Figure 12, this estimate yields $M\omega_{\infty} \approx 1$, consistent with the plots in this figure.

It is important to remark that for $\ell \geq 52$ the onset of the high-frequency regime happens at frequencies larger than our cutoff frequency $(M\omega_{\infty} > M\omega_{\rm cut} = 10)$. As a consequence, the ω -integrals are not expected to converge accurately for $\ell \geq 52$. This issue will be addressed during the ℓ -summation and we defer its resolution until the summation process is discussed. Conversely, Figure 12 reveals another important issue: The ω -integral converges visually very slowly even when $M\omega_{\infty}$ (in this figure, $M\omega_{\infty} \approx 1$) is an order of magnitude smaller than $M\omega_{\rm cut}$. This is quantified in Table 8, where the values of the ω -integrals are tabulated against $M\omega_{\rm cut}$. The convergence is so sluggish that no consistent significant figure can be reliably determined from the results.

To address the slow convergence, we multiply the integrands of Equations (5.2) and (5.3) by a frequency-smoothing function $\eta(\omega, \omega_0)$ during the numerical integration process. While these integrals are formally convergent without it, the frequency smoothing makes it faster

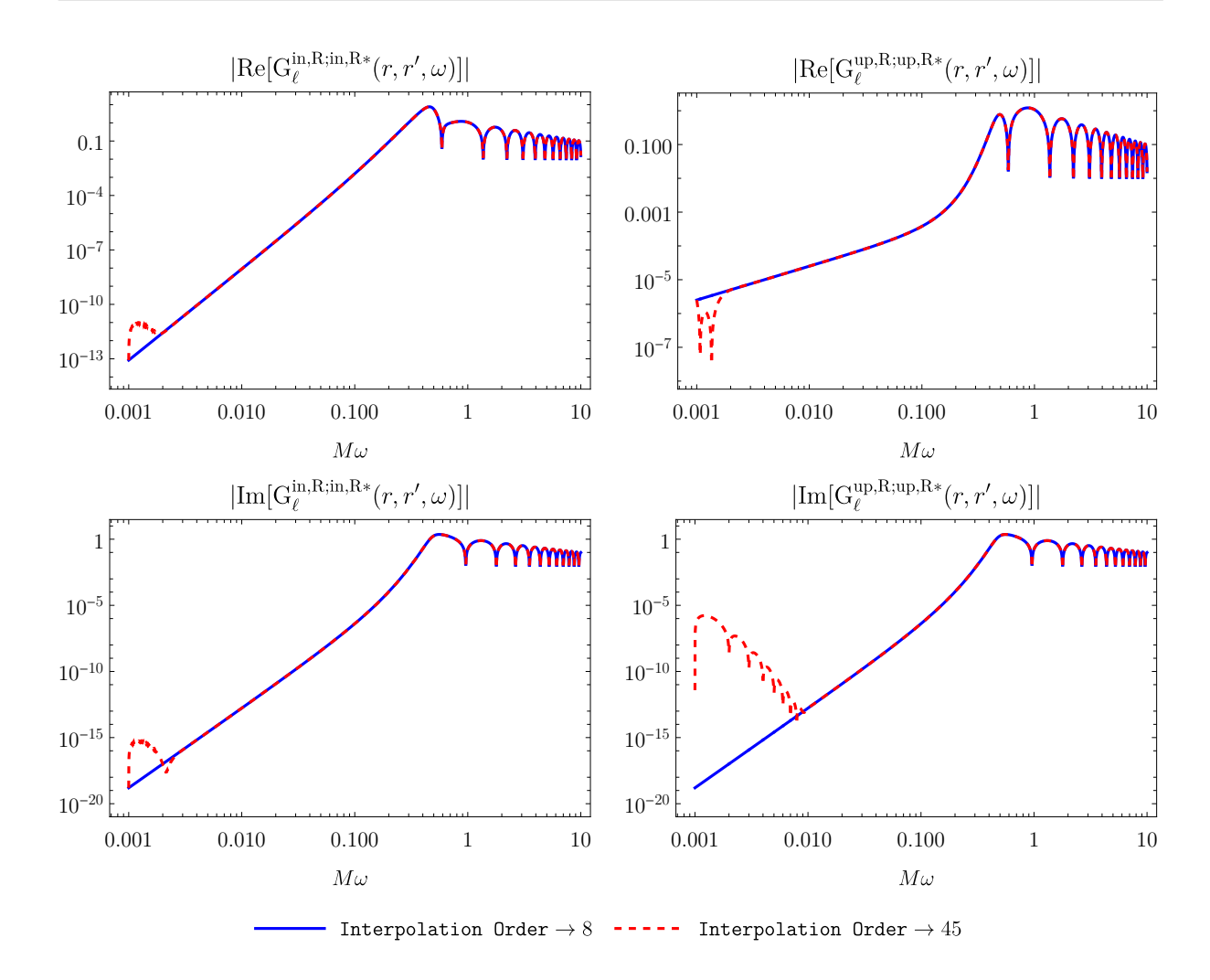


Figure 11 – Real (top row) and imaginary (bottom row) parts of the interpolated functions $G_{\ell}^{\text{in,R};\text{in,R*}}(r,r',\omega)$ (left column) and $G_{\ell}^{\text{up,R};\text{up,R*}}(r,r',\omega)$ (right column) for $r \approx 6.009M, r' \approx 3.9M$ and $\ell = 2$. Blue solid and red dashed lines correspond to interpolation orders 8 and 45, respectively. Spurious oscillations near $M\omega = 10^{-3}$ persist in both components when using an interpolation order of 45.

by suppressing high-frequency ($\omega > \omega_0$) contributions, effectively acting as a window function to accelerate numerical convergence.

While introducing $\eta(\omega, \omega_0)$ may appear ad-hoc, its use is physically motivated: the Wightman function is a bi-distribution and must be smeared with a test function to yield a physically meaningful quantity. This smearing reflects the finite resolution of measurable quantities in realistic setups. For example, in models of point-like two-level quantum systems (known as Unruh-DeWitt detectors), the temporal and spatial profile of the interaction with the background quantum field inherently defines a test function $\eta(\omega, \omega_0)$, which ensures faster integral convergence. A concrete example is seen in [1], which we will analyze in detail in the next chapter.

To maximize the fidelity (i.e., how much of the original bi-distribution behavior is preserved) of the Wightman function evaluation across $M\omega \in [10^{-3}, 10]$, the frequency-

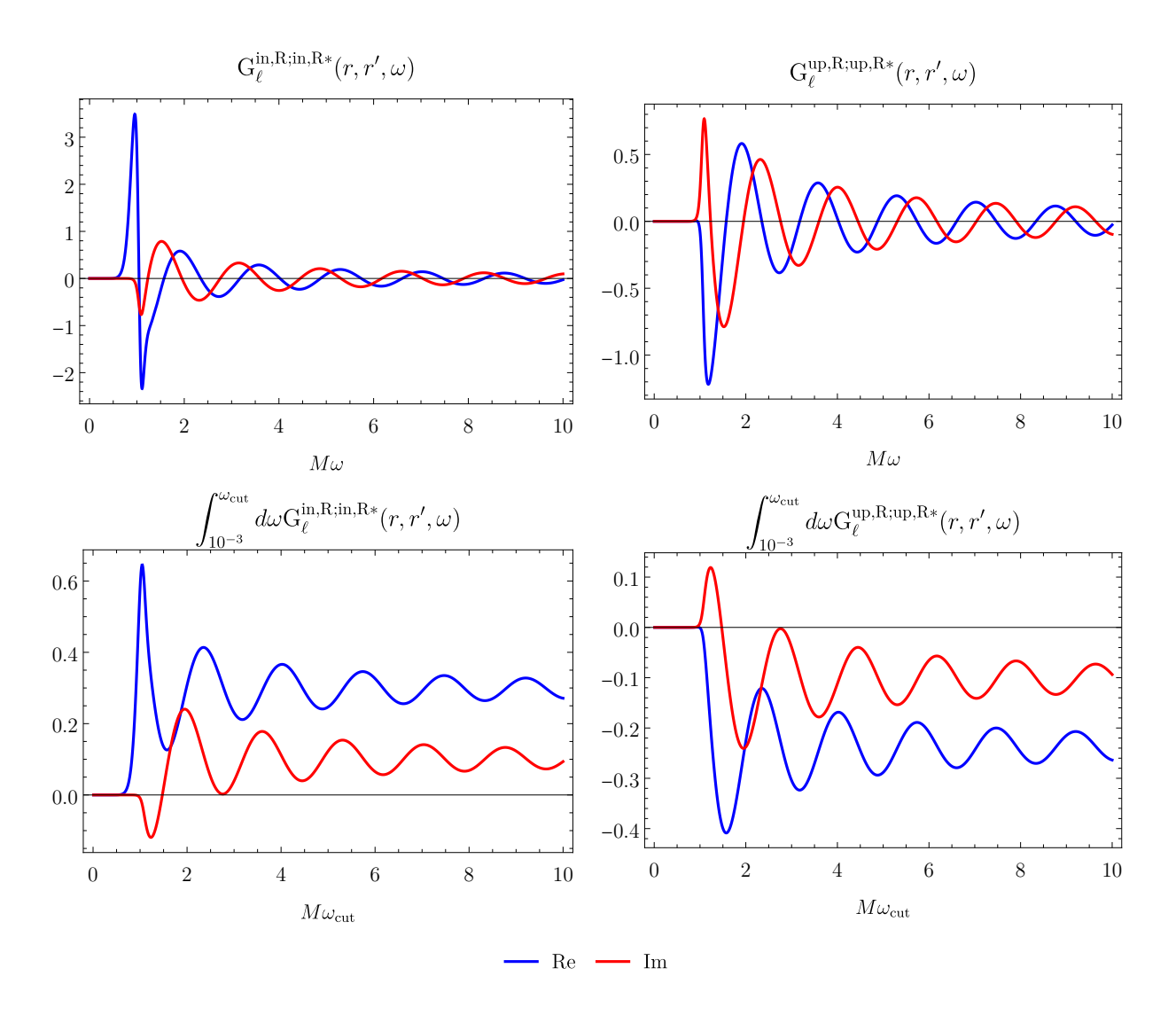


Figure 12 – First row: Auxiliary functions $G_{\ell}^{\text{in,R};\text{in,R*}}(r,r',\omega)$ (left) and $G_{\ell}^{\text{up,R};\text{up,R*}}(r,r',\omega)$ (right) for $r\approx 6.009M, r'\approx 3.9M$ and $\ell=5$, plotted as functions of $M\omega$. Second row: Their ω -integrals as functions of the cutoff frequency $M\omega_{\text{cut}}$. Oscillations around the value towards which the integrals converge begin for $M\omega_{\text{cut}} \gtrsim \sqrt{V_{\ell}^{\text{eff}}(3r_s/2)} \approx 1$, coinciding with the onset of the high-frequency asymptotic regime as predicted by Equation (5.7).

$M\omega_{\mathrm{cut}}$	$\int_{10^{-3}}^{\omega_{\text{cut}}} G_{\ell}^{\text{in,R;in,R*}}(r,r',\omega) d\omega$	$\int_{10^{-3}}^{\omega_{\text{cut}}} G_{\ell}^{\text{up,R;up,R*}}(r,r',\omega) d\omega$
10^{-2}	4.14×10^{-26}	3.44×10^{-13}
10^{-1}	7.03×10^{-14}	4.07×10^{-11}
1	0.580 - 0.009i	-0.001 + 0.009i
2	0.308 + 0.238i	-0.227 - 0.238i
3	0.231 + 0.039i	-0.304 - 0.039i
4	0.366 + 0.112i	-0.169 - 0.112i
5	0.247. + 0.123i	-0.289 - 0.123i
6	0.326 + 0.065i	-0.209 - 0.065i
7	0.295 + 0.141i	-0.244 - 0.0141i
8	0.287 + 0.069i	-0.249 - 0.069i
9	0.320 + 0.123i	-0.215 - 0.123i
10	0.271 + 0.094i	-0.264 - 0.094i

Table 8 – Numerical values of the ω -integrals of $G_{\ell}^{\text{in,R;in,R*}}(r,r',\omega)$ and $G_{\ell}^{\text{up,R;up,R*}}(r,r',\omega)$ from $M\omega = 10^{-3}$ to $M\omega_{\text{cut}}$ for $r \approx 6.009 M, r' \approx 3.9 M$ and $\ell = 5$. Despite the early (compared to $M\omega_{\text{cut}} = 10$) onset of the high-frequency regime $M\omega_{\infty} = 1$, convergence is extremely slow, with no consistent significant figures obtainable.

smoothing function $\eta(\omega, \omega_0)$ should suppress high-frequency contributions while retaining lower frequencies. Following [27], we adopt

$$\eta(\omega, \omega_0) = \frac{1 - \operatorname{erf}(2(M\omega - M\omega_0))}{2},\tag{5.8}$$

where erf is the error function [48, Equation 7.2.1], and set $M\omega_0 = 8.5$. This smoothing profile is illustrated in Figure 13. This choice suppresses frequencies $M\omega \gtrsim 8.5$, effectively acting as a soft cutoff for larger frequencies. Consequently, the ω -integrals for $\ell \geq 44$ (where $M\omega_{\infty} > 8.5$) are not expected to converge accurately. This is because up to $M\omega = 8.5$ their integrands have not yet entered the asymptotic $M\omega \gtrsim M\omega_{\infty}$ regime, where the magnitude of the oscillatory integrand decays as ω^{-1} and the integral begins to converge by oscillating around its correct value.

For completeness, Figure 14 replicates the analysis of Figure 12 but incorporates the frequency-smoothing function from Equation (5.8). Notably, the amplitude of the oscillations around the value towards which the integral is converging decays rapidly for $M\omega_{\rm cut}\gtrsim 8.5$. As summarized in Table 9, this allows us to extract results with three significant figures for $\ell=5$.

We further verified that for $\ell = 44$, the integrals converge to at least one significant figure within the current settings. Since the convergence of the ω -integrals slows down

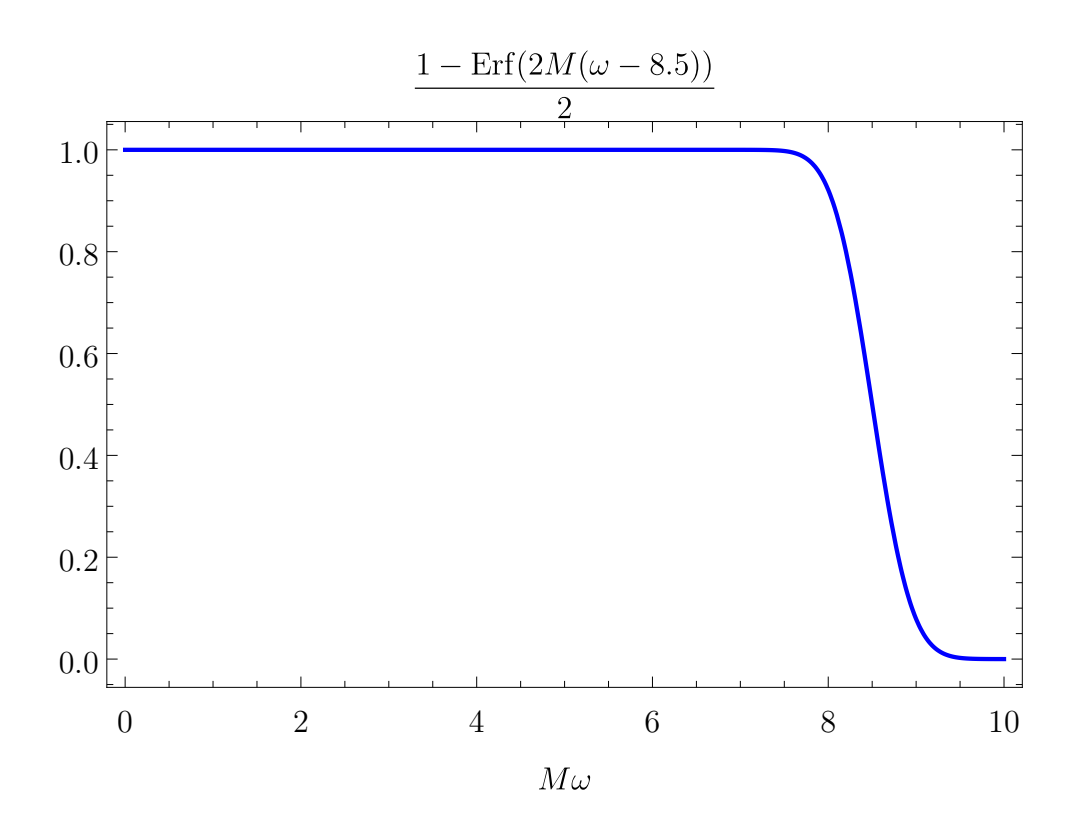


Figure 13 – Profile of the smoothing function defined in Equation (5.8). For $M\omega \lesssim 8$, the function is nearly unity ($\eta \approx 1$), making it transparent to lower frequencies. For $M\omega \gtrsim 8.5$, contributions are sharply suppressed. The transition region (8 < $M\omega < 8.5$) is governed by the steepness of the error function in Equation (5.8).

with increasing ℓ (due to delayed onset of the ω^{-1} decay regime), we conservatively assert that all integrals for $\ell \leq 44$ converge to at least one significant figure, with up to three achievable for lower ℓ .

It is important to emphasize the inherent trade-off of the frequency-smoothing technique we are using: lowering $M\omega_0$ improves the precision (more significant figures) of the ω -integrals for the ℓ -modes where $M\omega_{\infty} < M\omega_0$, but reduces the maximum ℓ for which results remain correct to at least one significant figure, as $M\omega_{\infty}$ increases with ℓ . Conversely, increasing $M\omega_0$ extends the range of ℓ -modes that converge to at least one significant figure, but sacrifices precision (fewer significant figures) for lower ℓ . For our choice $M\omega_0 = 8.5$, we balance these competing effects: ensuring integrals for $\ell \leq 42$ converge to at least one significant figure while retaining up to three figures for lower ℓ .

We remark, however, that an increasing (finite) number of ℓ -modes does not guarantee better results in the ℓ -sum: Excessively many ℓ -modes amplify the Gibbs phenomenon near the singularities of the Wightman function, manifesting as spurious oscillations around them. Examples of this behavior will be provided during the discussion of the ℓ -sum process.

When performing the numerical integration in Mathematica, we allow the software to automatically select its integration strategy based on the integrand's structure. To optimize

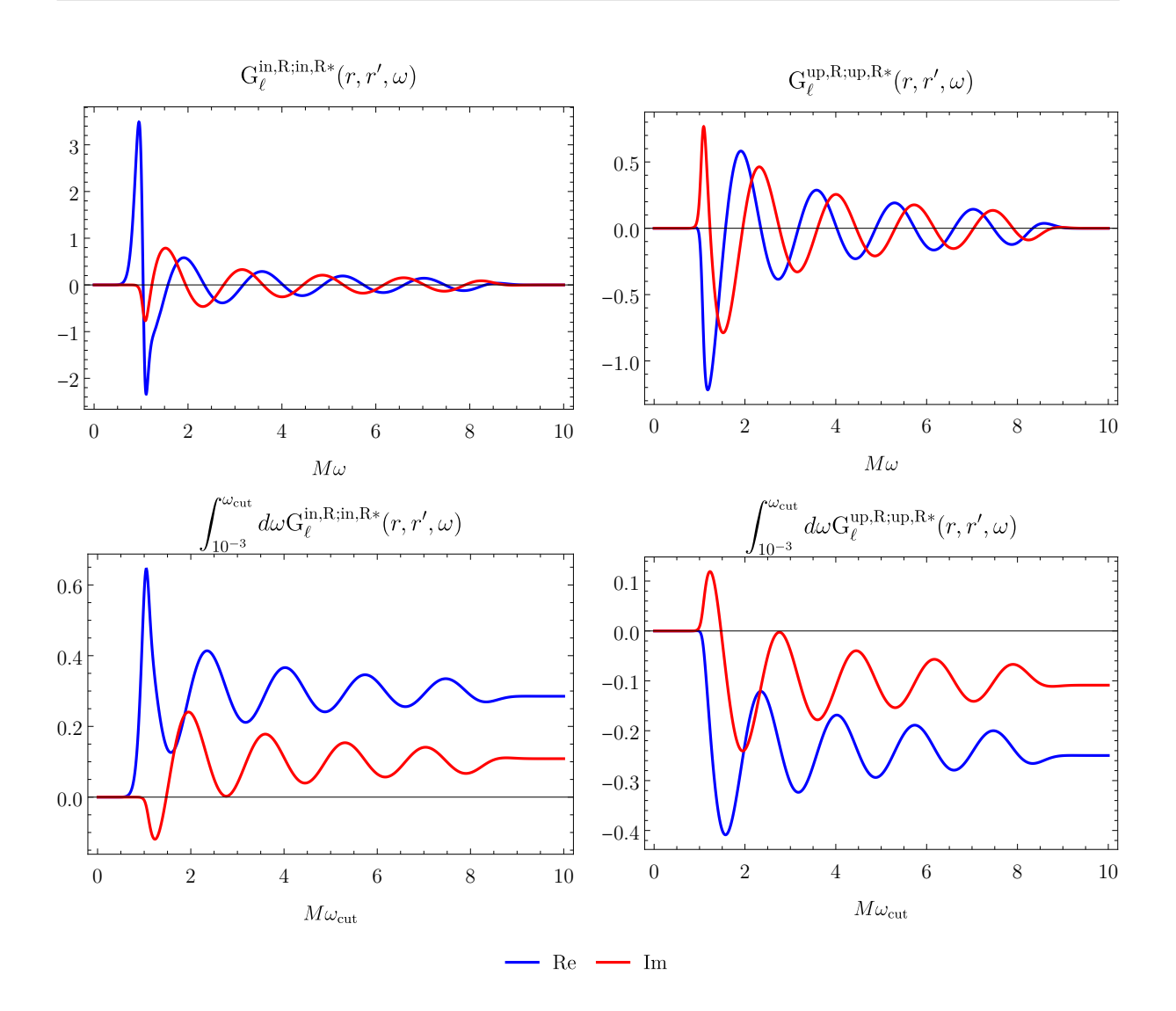


Figure 14 – First row: Functions $G_{\ell}^{\text{in,R};\text{in,R*}}(r,r',\omega)$ (left) and $G_{\ell}^{\text{up,R};\text{up,R*}}(r,r',\omega)$ (right) for $r \approx 6.009M, r' \approx 3.9M$ and $\ell = 5$, with frequency-smoothing (Equation (5.8)), plotted as functions of $M\omega$. Second row: Their ω -integrals as a function of the cutoff frequency $M\omega_{\text{cut}}$. Due to the frequency-smoothing with $M\omega_0 = 8.5$, the integrals converge rapidly for $M\omega_{\text{cut}} \gtrsim 8.5$.

computational speed, we set SymbolicProcessing to 0: generating Table 9 takes $\approx 0.5s$ with this setting versus $\approx 11s$ without it. Furthermore, we configure PrecisionGoal to 10 and AccuracyGoal to ∞ , instructing Mathematica to target a relative error of 10^{-10} during integrations.

However, Mathematica's internal error estimate does not reflect the actual relative error in the final result. As shown in Table 9, only three consistent significant figures are achieved, despite the stringent precision settings. This discrepancy arises from unaccounted systematic errors due to the residual oscillations in the integrand for $M\omega \gtrsim 8.5$. As previously commented, these could be ameliorated by reducing $M\omega_0$ (which also produces the aforementioned side-effects). An alternative that would be free of these side-effects would be to increase the values of $M\omega$ in our data which would allow for a larger $M\omega_{\rm cut}$.

$M\omega_{\mathrm{cut}}$	$\int_{10^{-3}}^{\omega_{\text{cut}}} G_{\ell}^{\text{in,R;in,R*}}(r,r',\omega) d\omega$	$\int_{10^{-3}}^{\omega_{\text{cut}}} G_{\ell}^{\text{up,R;up,R*}}(r,r',\omega) d\omega$
10^{-2}	4.14×10^{-26}	3.44×10^{-13}
10^{-1}	7.03×10^{-14}	4.07×10^{-11}
1	0.580 - 0.009i	-0.001 + 0.009i
2	0.308 + 0.238i	-0.227 - 0.238i
3	0.231 + 0.039i	-0.304 - 0.039i
4	0.366 + 0.112i	-0.169 - 0.112i
5	0.247. + 0.123i	-0.289 - 0.123i
6	0.326 + 0.065i	-0.209 - 0.065i
7	0.291 + 0.141i	-0.244 - 0.0141i
8	0.288 + 0.069i	-0.247 - 0.069i
9	0.285 + 0.110i	-0.250 - 0.110i
10	0.285 + 0.109i	-0.250 - 0.109i

Table 9 – Numerical values of the frequency-smoothed (Equation (5.8)) ω -integrals of $G_{\ell}^{\text{in},R;\text{in},R*}(r,r',\omega)$ and $G_{\ell}^{\text{up},R;\text{up},R*}(r,r',\omega)$ from $M\omega=10^{-3}$ to $M\omega_{\text{cut}}=10$ for $r\approx 6.009M,r'\approx 3.9M$ and $\ell=5$. With frequency-smoothing, the integrals stabilize to three significant figures for $M\omega_{\text{cut}}>8$.

This integration protocol will be adopted throughout all calculations when both points x and x' are outside the black hole $(r, r' > r_s)$ and a very similar procedure will be used in the other cases.

The final step involves performing the ℓ -sum to evaluate both contributions $W_{\rm in}^B(\mathbf{x};\mathbf{x}')$ and $W_{\rm up}^B(\mathbf{x};\mathbf{x}')$, which are then combined to reconstruct the Wightman function $W^B(\mathbf{x};\mathbf{x}')$. As an initial test case, we evaluated the ℓ -sum terms considering an angular separation of $\gamma = \pi/3$ between \mathbf{x} and \mathbf{x}' . The results are plotted as a function of ℓ in Figure 15. These terms exhibit an oscillatory behavior with a slow decay in amplitude for $\ell \lesssim 44$, followed by a much sharper decay for larger values of ℓ .

This transition in the decay rate arises because $M\omega_{\infty}$ — the frequency scale marking the onset of the asymptotic ω^{-1} decay of the amplitudes of the oscillations in the integrand — exceeds the smoothing threshold $M\omega_0 = 8.5$ for $\ell \gtrsim 44$. Beyond this point, the ω -integrals are systematically underestimated because they fail to resolve the local extreme at $M\omega \approx M\omega_{\infty}$ that happens before the onset of the asymptotic ω^{-1} decaying regime. Consequently, the frequency smoothing with $M\omega_0 = 8.5$ inherently imposes a corresponding cutoff in the ℓ -sum at $\ell \approx 44$.

With that, we proceed to evaluate the ℓ -sum up to $\ell_{\rm cut} = 100$ (the largest value of ℓ in our dataset). The results are tabulated in Table 10 and illustrated in Figure 16. The

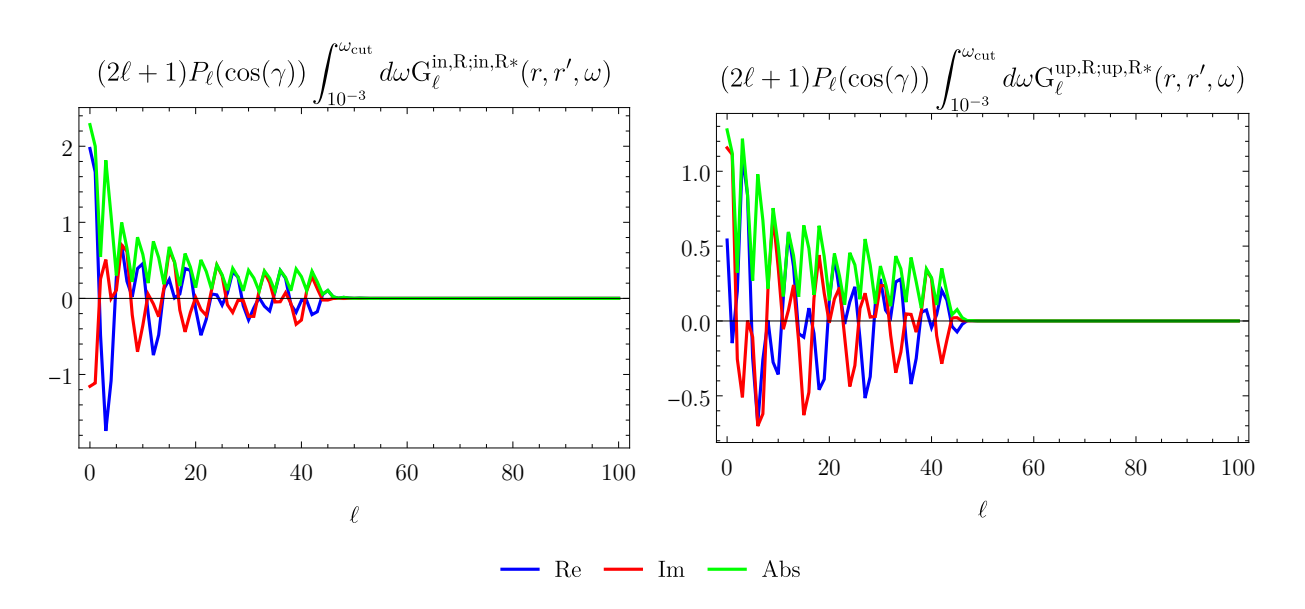


Figure 15 – Real part (blue), imaginary part (red), and magnitude (green) of the ℓ -sum terms for $W_{\rm in}^B$ (x;x') (left) and $W_{\rm up}^B$ (x;x') (right), computed for $r\approx 6.009M$, $r'\approx 3.9M$ and angular separation $\gamma=\pi/3$. The abrupt decay for $\ell\gtrsim 44$ reflects the frequency smoothing with $M\omega\gtrsim M\omega_0=8.5$ (Equation (5.8)). For the ℓ -modes with $\ell\gtrsim 44$ the onset of the high-frequency decaying behavior is not achieved because $M\omega_\infty>M\omega_0=8.5$, resulting in systematically underestimated ω -integrals.

summation exhibits an oscillatory behavior, with amplitude decaying as $\ell_{\rm cut}$ increases. This decay accelerates sharply beyond the soft cutoff (inherited from the frequency-smoothing) at $\ell \approx 44$, consistent with the behavior of the summand shown in Figure 15.

To estimate the relative error introduced by truncating the ℓ -sum at $\ell_{\rm cut}$, we compute the relative difference between successive partial sums (at $\ell_{\rm cut}$ and $\ell_{\rm cut}+1$). This error oscillates around 10^{-1} for $\ell_{\rm cut}\lesssim 44$, then decays rapidly for larger $\ell_{\rm cut}$. However, this decay is misleading: for $\ell_{\rm cut}\gtrsim 44$ the ω -integrals themselves lose accuracy (they are accurate to at least one significant figure for $\ell \leq 44$), rendering the error estimates unreliable on this interval. The relative error approaching zero at large $\ell_{\rm cut}$ reflects numerical underestimation of contributions from $\ell \gtrsim 44$ rather than true convergence.

Thus, with the current technique, the ℓ -sum should be trusted only to one significant figure, given the 10^{-1} estimated relative error in the non-underestimated contributions to the ℓ -sum ($\ell \leq 44$).

Given these caveats, we proceed to evaluate the Wightman function. To optimize efficiency, we reverse the computational order: instead of first computing the ω -integrals and then performing the ℓ -sums, we first perform the ℓ -sum and subsequently compute the ω -integral over the summed result. For the current example, this reordering yields results identical to those in Table 10, validating the consistency of the approach.

This reordering provides a substantial computational speedup: for each pair of points x and x', evaluating the Wightman function now requires only a single ω -integral over the

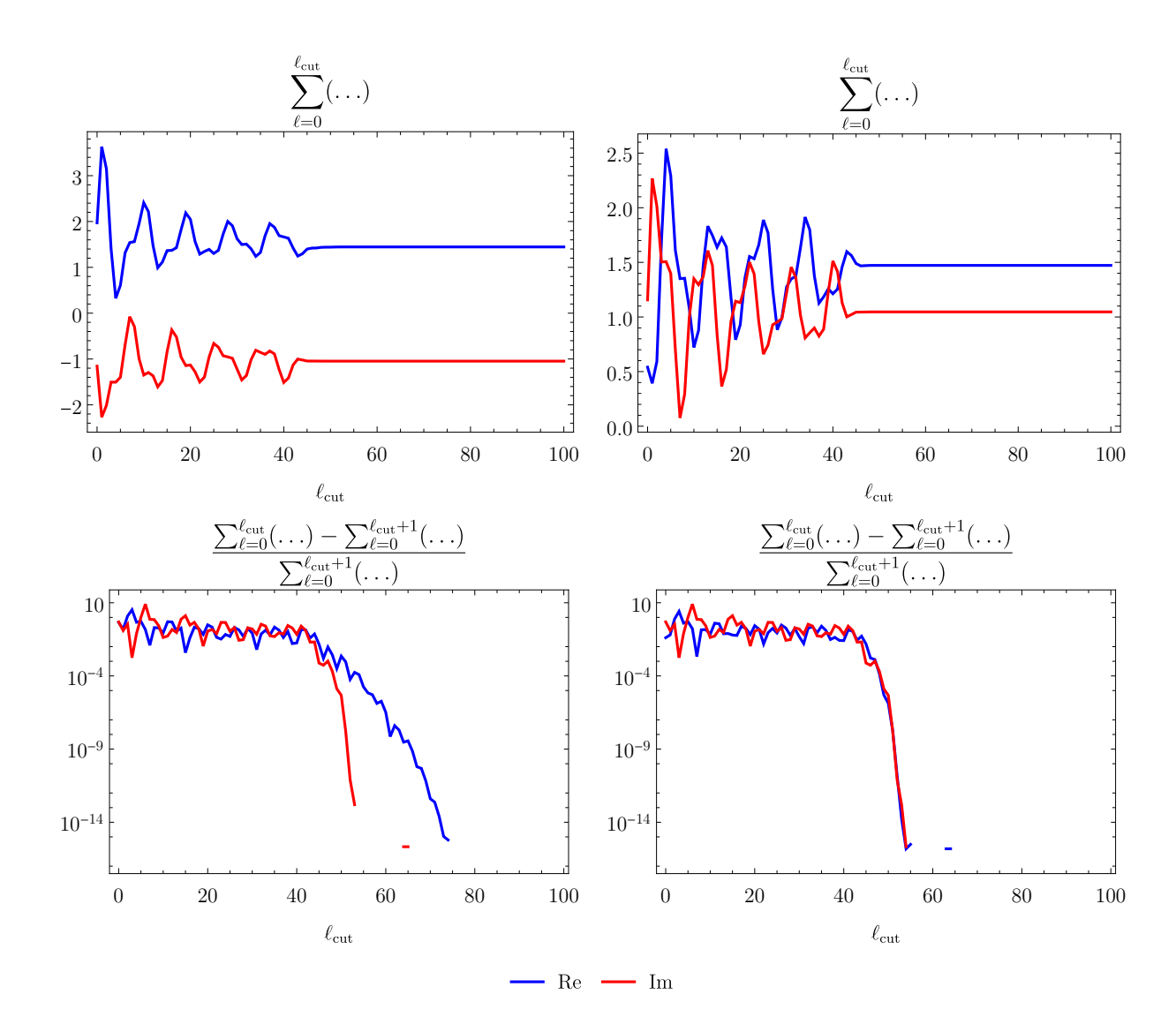


Figure 16 – First row: Real (blue) and imaginary (red) parts of the ℓ -sums for $W_{\rm in}^B(\mathbf{x};\mathbf{x}')$ (left) and $W_{\rm up}^B(\mathbf{x};\mathbf{x}')$ (right), computed for $r\approx 6.009M$, $r'\approx 3.9M$ and $\gamma=\pi/3$. Second row: Estimated relative errors in the ℓ -sums (real part in blue, imaginary part in red). As could be anticipated from Figure 15, the relative errors decay rapidly for $\ell_{\rm cut}\gtrsim 44$, aligning with the frequency-smoothing with $M\omega_0=8.5$. Discontinuities in the error curves arise from numerical cancellation of all significant digits at large $\ell_{\rm cut}$. Crucially, the ω -integrals are accurate to at least a significant figure only for $\ell\lesssim 44$. Beyond this, the apparent decay in relative error reflects a systematic underestimation of the ω -integrals, not true convergence. Thus, the ℓ -sum for $\ell_{\rm cut}=100$ should be interpreted as accurate to a single significant figure, since the estimated relative error in this sum oscillates around 10^{-1} up to $\ell_{\rm cut}=44$, where the ω -integrals are accurate.

$W_{ ext{in}}^{B}\left(x;x' ight)$	$W_{\mathrm{up}}^{B}\left(x;x'\right)$	$W^{B}\left(x;x^{\prime}\right)$
0.000390 - 0.000283i	0.000398 + 0.000283i	0.000788

Table 10 – Numerical values of $W_{\rm in}^B({\sf x};{\sf x}')$, $W_{\rm up}^B({\sf x};{\sf x}')$, and $W^B({\sf x};{\sf x}')$ for $r\approx 6.009 M$, $r'\approx 3.9 M$ and angular separation $\gamma=\pi/3$. Results are truncated to three significant figures — Although they should be trusted only to a single significant figure, as the ℓ -sum converges to a relative error of 10^{-1} when summing up to $\ell=44$ (the largest value of ℓ with at least a significant figure after ω-integration). The absolute error introduced by the integration process is $\sim 10^{-13}$, corresponding to a relative error of $\sim 10^{-10}$. Despite the high internal precision, systematic errors due to underestimation of the ω-integrals for $\ell \gtrsim 44$ restrict the results a single significant figure.

 ℓ -summed integrand, rather than 100 separate integrals (one per ℓ -mode). This reduces both runtime and numerical complexity while preserving accuracy within the established error bounds.

Following the outlined method, we proceed to evaluate $W^{B}(\mathbf{x}; \mathbf{x}')$ for the points

$$\mathbf{x} = (t = -7.4M, r_* = 7.4M, \theta = 0, \varphi = 0) \tag{5.9}$$

and

$$\mathbf{x}' = (t', r'_* = 3.8M, \theta' = 0, \varphi' = \pi/3),$$
 (5.10)

where t' varies from -147.4M up to 132.6M, resulting in a time separation $\Delta t = t - t'$ spanning $-140M \le \Delta t \le 140M$. The parameter t' is sampled in increments of 0.1M, yielding 2,801 data points.

These points are visualized in Figure 17, shown in both Eddington-Finkelstein and Penrose diagrams.

The computation required 2 minutes to perform the interpolations and approximately 48 minutes to evaluate all 2,801 distinct ω -integrals. The results, shown in Figure 18, reveal several key features. First, the magnitude of the Wightman function exhibits an overall decaying trend as $|\Delta t/M|$ increases, reflecting the intuitive expectation that correlations diminish with increasing spacetime separation between x and x'. Superimposed on this decay are localized structures: sharp peaks and valleys (zeroes in the Wightman function, emphasized by the logarithmic scale), surrounded by an oscillatory behavior.

The localized structures in the Wightman function likely arise from its singularities, which are smeared by the combined effect of the frequency-smoothing and the hard cutoffs ($M\omega_{\rm cut} = 10$ for the ω -integral and $\ell_{\rm cut} = 100$ for the ℓ -sum) procedures. These singularities occur when $\sigma(x, x') = 0^1$, i.e., when x and x' are connected by a null geodesic (See Subsection 3.4.1). To confirm this, we computed the null geodesics connecting x and

Here we refer to an extension of Synge's world function beyond a normal neighborhood $\mathcal{N}(x)$ of x, as constructed in [47].

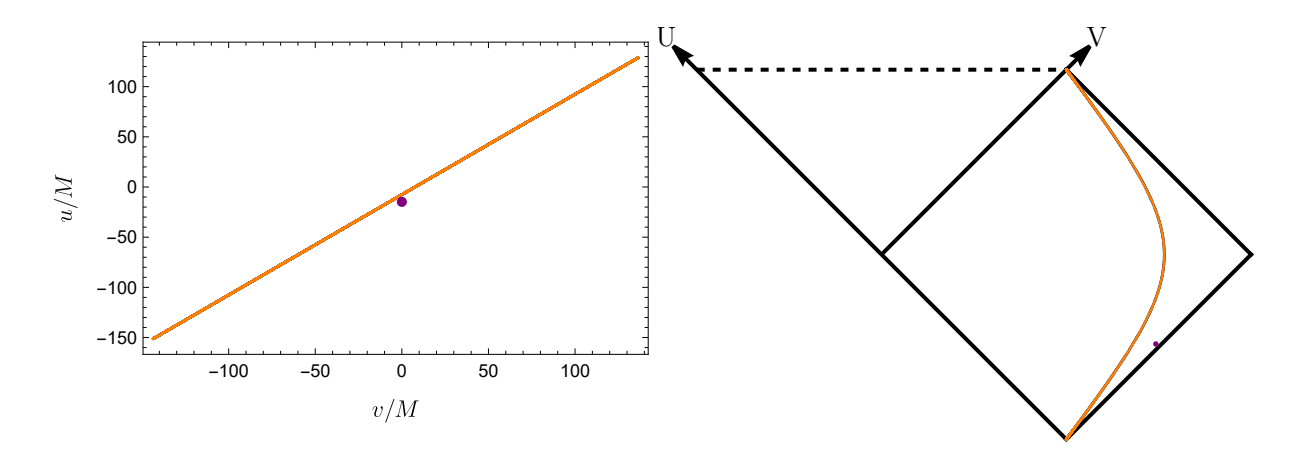


Figure 17 – Spacetime points used to evaluate $W^B(\mathbf{x}; \mathbf{x}')$ in the first numerical example. Left: Eddington-Finkelstein diagram. Right: Penrose diagram. Purple dot: Fixed point $\mathbf{x} = (t = -7.4M, r_* = 7.4M, \theta = 0, \varphi = 0)$. Orange dots: $\mathbf{x}' = (t', r'_* = 3.8M, \theta' = 0, \varphi' = \pi/3)$, where t' varies from -147.4M to 132.6M in steps of 0.1M. The points \mathbf{x} and \mathbf{x}' lie on distinct azimuthal planes $(\varphi = 0 \text{ vs. } \varphi' = \pi/3)$, hence, no radial null geodesic connects them.

x' at an angular separation $\gamma = 3\pi$ after $N \in \mathbb{N}$ half-orbits (with N = 0, 1, ..., 8) by numerically solving the geodesic equations (2.24). The first five of these null geodesics are depicted in Figure 20 and connect x and x' at different values of coordinate time separation $\Delta t = t - t'$.

By overlaying these Δt values as vertical lines on the Wightman function we produced Figure 19, where we observe alignment between Δt on the computed null geodesics and the localized structures (except zeroes). This offers an evidence that these structures are the smeared singularities of $W^B(\mathbf{x}; \mathbf{x}')$, predicted to happen when \mathbf{x} and \mathbf{x}' are light-like connected (See 3.4.1).

If the aforementioned sharply localized structures in the Wightman function correspond to its singularities, then the oscillatory behavior around them is expected: these singularities cause discontinuities in the unsmeared Wightman function (and steep variations in the smeared version). Such features are encoded in arbitrarily high- ℓ modes of the spherical harmonics expansion of the unsmeared Wightman function (or modes with large-but-finite ℓ in the smeared version). However, the soft cutoff in the ℓ -sum at $\ell=42$, induced by the ω -smoothing procedure, effectively dampens the contribution from arbitrarily high- ℓ modes, preventing these features near the singularities to be resolved. This introduces spurious oscillations around the smoothed singularities, analogous to the Gibbs phenomenon in Fourier analysis.

While the results remain mathematically consistent, these oscillations obscure the precise nature of the singularities (and the behavior of the Wightman function around them). For example, it becomes challenging to distinguish whether a sharp peak corresponds to a delta-function singularity $(\delta(\sigma))$, a principal value distribution (P.V. $(\frac{1}{\sigma})$) or another

functional form.

These spurious oscillations can be mitigated by introducing an explicit soft cutoff in the ℓ -sum. Specifically, we dampen high- ℓ modes by multiplying the summand with a Gaussian window function:

$$\iota(\ell, \ell_0) = e^{-\ell^2/(2\ell_0^2)},\tag{5.11}$$

where $\ell_0 = 12$, following the methodology of [27]. This suppresses such oscillations while preserving the localized structures associated with singularities. The results, shown in Figure 21, clearly demonstrate reduced noise and clearer resolution of the behavior near the smoothed singularities.

However, this approach introduces another trade-off: the overall magnitude of W^B (x;x') is slightly reduced, and its localized structures are blurred over broader intervals. This loss of sharpness reflects the inherent tension between numerical stability and resolving singular features in truncated mode sums. In short, increasing ℓ_0 improves the sharpness of the singularities at the cost of including spurious oscillations due to Gibbs phenomena.

On the other hand, the onset frequency of the asymptotic decay of the integrand is $M\omega_{\infty}\approx 2.4M$ for $\ell=12$, implying that the most relevant contributions to the ℓ -sum will come from more accurate ω -integrals when using $\ell_0=12$. That is, decreasing ℓ_0 improves the overall convergence, increasing the number of consistent significant digits available after the ℓ -sum. Specifically, for $\ell=12$, the ω -integrals converge to two significant figures in the case where $\Delta t=0$ (this takes x and x' closer to coincidence and is likely to converge slower). Therefore, in this approach it is reasonable to conservatively assume that the results for the ℓ -sum are correct to two significant figures.

While the logarithmic scale in Figure 21 enhances the visibility of localized structures after ℓ -smoothing, it obscures the sign of the real and imaginary parts of $W^B(\mathbf{x};\mathbf{x}')$ —crucial information for verifying whether these structures correspond to the light-crossing.

To address this issue, we generated linear-scale plots with adjusted ranges to resolve behavior near each localized structure. The results for the real and imaginary parts of $W^B(\mathbf{x};\mathbf{x}')$ are shown in Figures 22 and 23, respectively. These plots reveal a behavior consistent with the predicted singularity structures in Equations (3.55) and (3.56). Both the location and functional form of the structures align with expectations, strongly suggesting that they represent the smoothed singularities of the Wightman function. Given these evidences, we find it reasonable to assume that this is the case from now on.

It is interesting to notice the distinct behaviors (away from the singularities) in the Real and Imaginary parts of the Wightman, which become clear for $\Delta t/M \gtrsim 110$: The imaginary part is linearly decreasing with $\Delta t/M$ (and its magnitude is also decreasing, as it asymptotes to zero) while the real part linearly increases with $\Delta t/M$ (and its magnitude also decreases, since it is a negative number that is asymptoting to zero).

To finish this exposition we remark that despite the complications related to caustics for angular separations $\gamma = 0$ and $\gamma = \pi$, where the numerical evaluation of the mode-sum

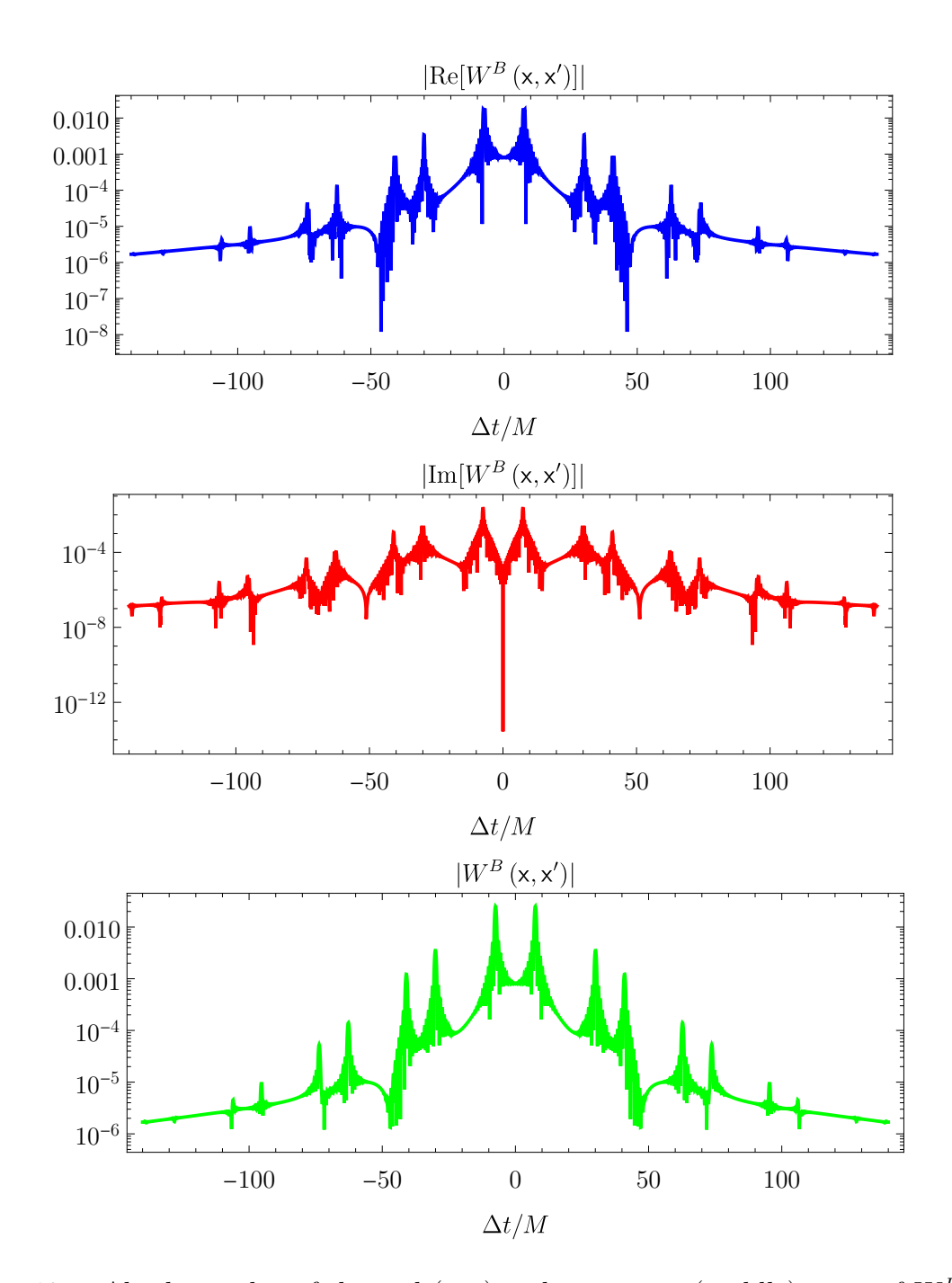


Figure 18 – Absolute value of the real (top) and imaginary (middle) parts of $W^B(\mathsf{x};\mathsf{x}')$ for $\mathsf{x} = (t = -7.4M, \, r_* = 7.4M, \, \theta = 0, \, \varphi = 0)$ and $\mathsf{x}' = (t', \, r_*' = 3.8M, \, \theta' = 0, \, \varphi' = \pi/3)$, plotted as a function of $\Delta t = t - t'$. Bottom: Magnitude of $W^B(\mathsf{x};\mathsf{x}')$. The decay with increasing $|\Delta t/M|$ reflects diminishing quantum correlations with increasing spacetime separations. The sharp peaks align with light-like connections between x and x' (see Figure 19), as discussed in Section 3.4.1.

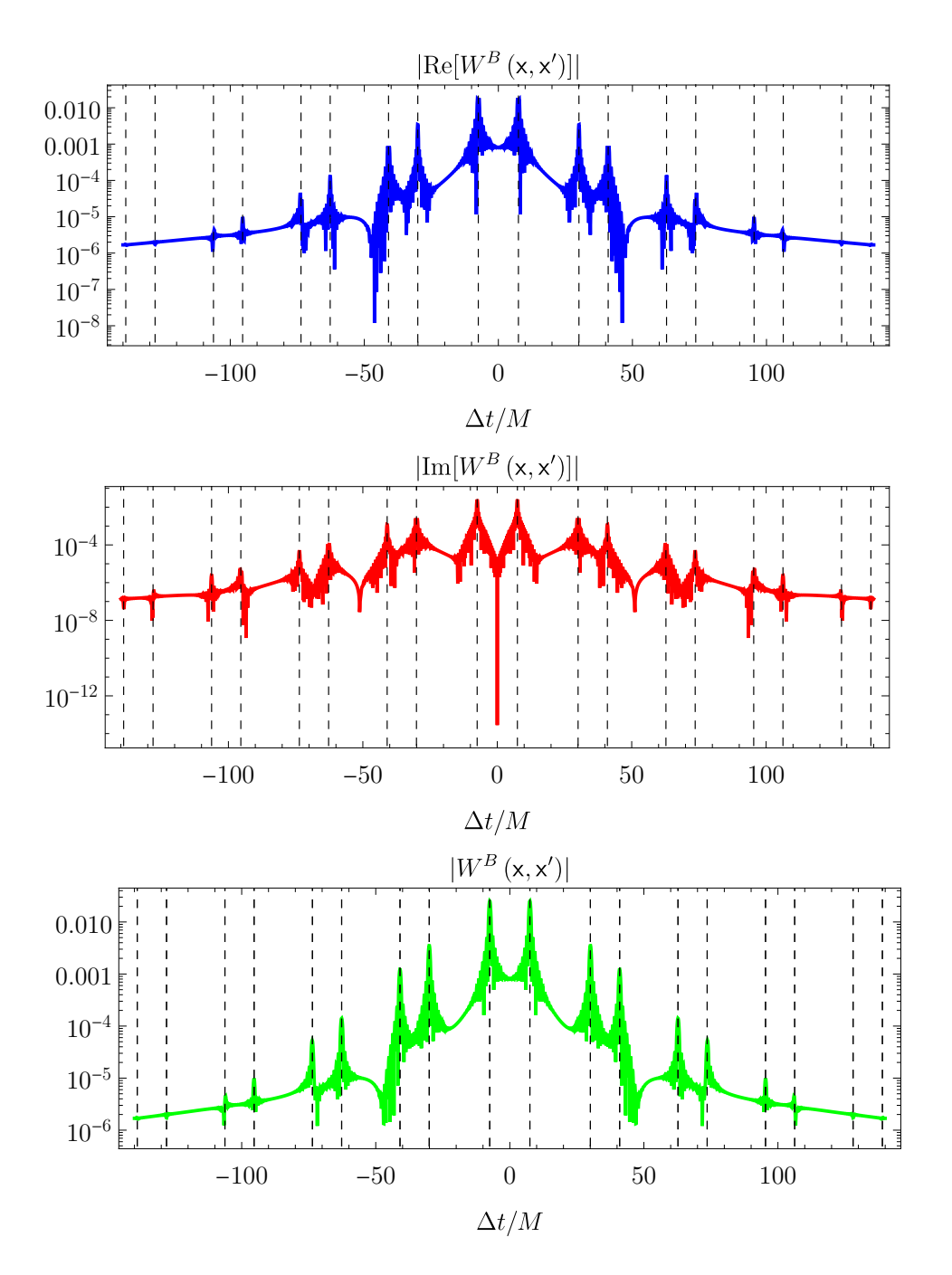


Figure 19 – The plots from Figure 18 overlapped with dashed vertical lines marking the values of Δt where x and x' are connected by null geodesics. These align with the sharp structures in the Wightman function plots, reflecting its singularity structure (Section 3.4.1).

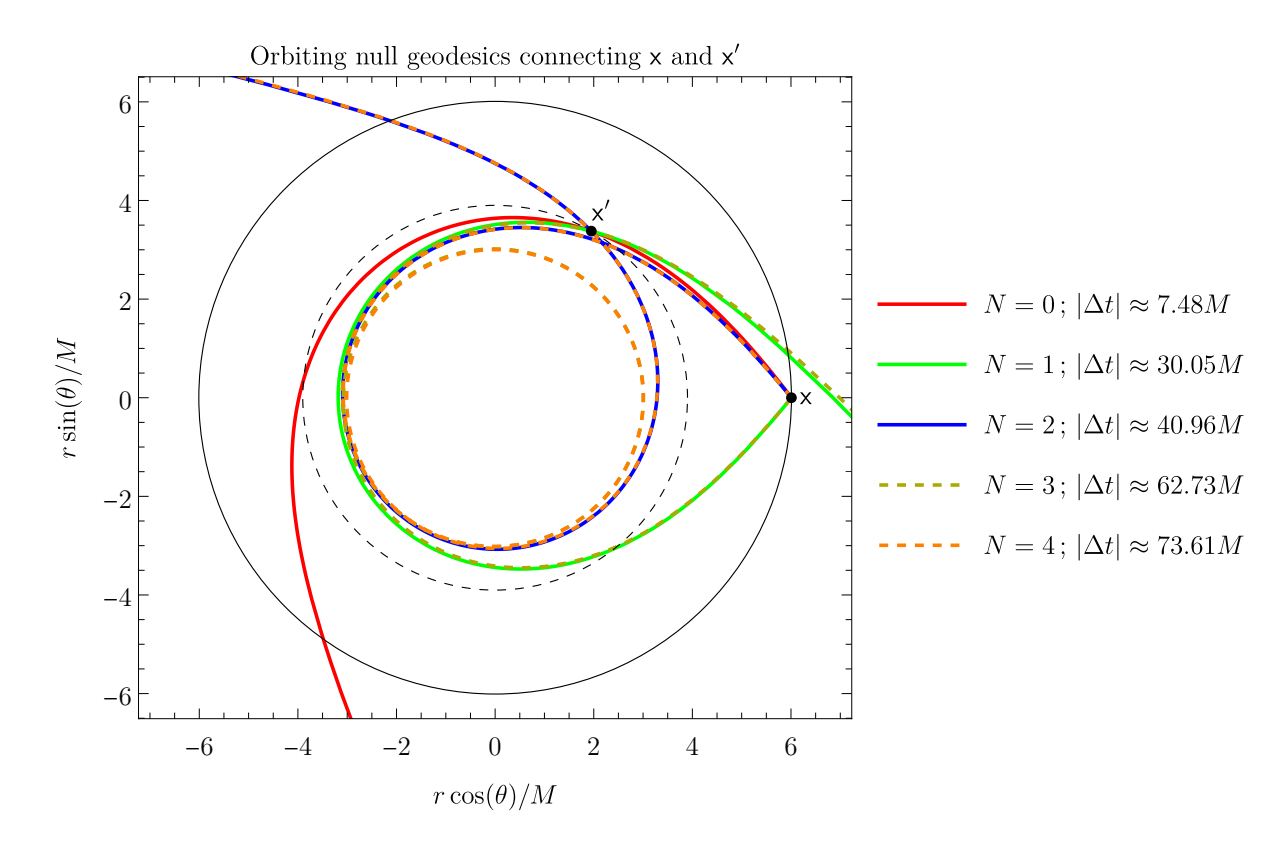


Figure 20 – Orbiting null geodesics (colored curves) connecting x at $r \approx 6.009M$ (solid black circle) to x' at $r' \approx 3.9M$ (dashed black circle) at an angular separation of $\gamma = \pi/3$. The black dots represent the points x and x'. Each geodesic completes $N \in \mathbb{N}$ half-orbits around the black hole before connecting x and x'. Legend shows $|\Delta t| = |t - t'|$ for each geodesic. These values align with the localized structures in Figure 19. Including larger values of N would crowd the plot without adding insight on the behavior of these null geodesics. For this reason we decided not to include them (N = 5, 6, 7, 8) here.

expansion of the Wightman function is not expected to behave well due to enhanced singularities (See [47]), we were able to reproduce the results for these angular separations presented in Figure 13 of [57]. Our results are presented in Figure 24. Slight differences between our results and those of [57] are expected because they use r = 6M with a gaussian source while we use $r \approx 6.009M$ with a delta source. Our method is not able to resolve the behavior near $\Delta t/M = 0$, which is expected since this implies that we are trying to take the coincidence limit $\mathbf{x}' \to \mathbf{x}$, where the mode-sum expression we use diverges.

Despite being done as an example of the method, this calculation is already interesting: To the best of our knowledge, this is the first time that the two-fold singularity structure of the real part of the Wightman function is exposed for points on caustics. In [57] only the Retarded Green Function (which depends only on the imaginary part of the Wightman function, see Equation (3.50)) was evaluated. The shape of the singularities in the real part are mirrored images of the shape of the singularities in the imaginary part. For instance, in the first singularity, the imaginary part presents a shallow minima followed by a larger

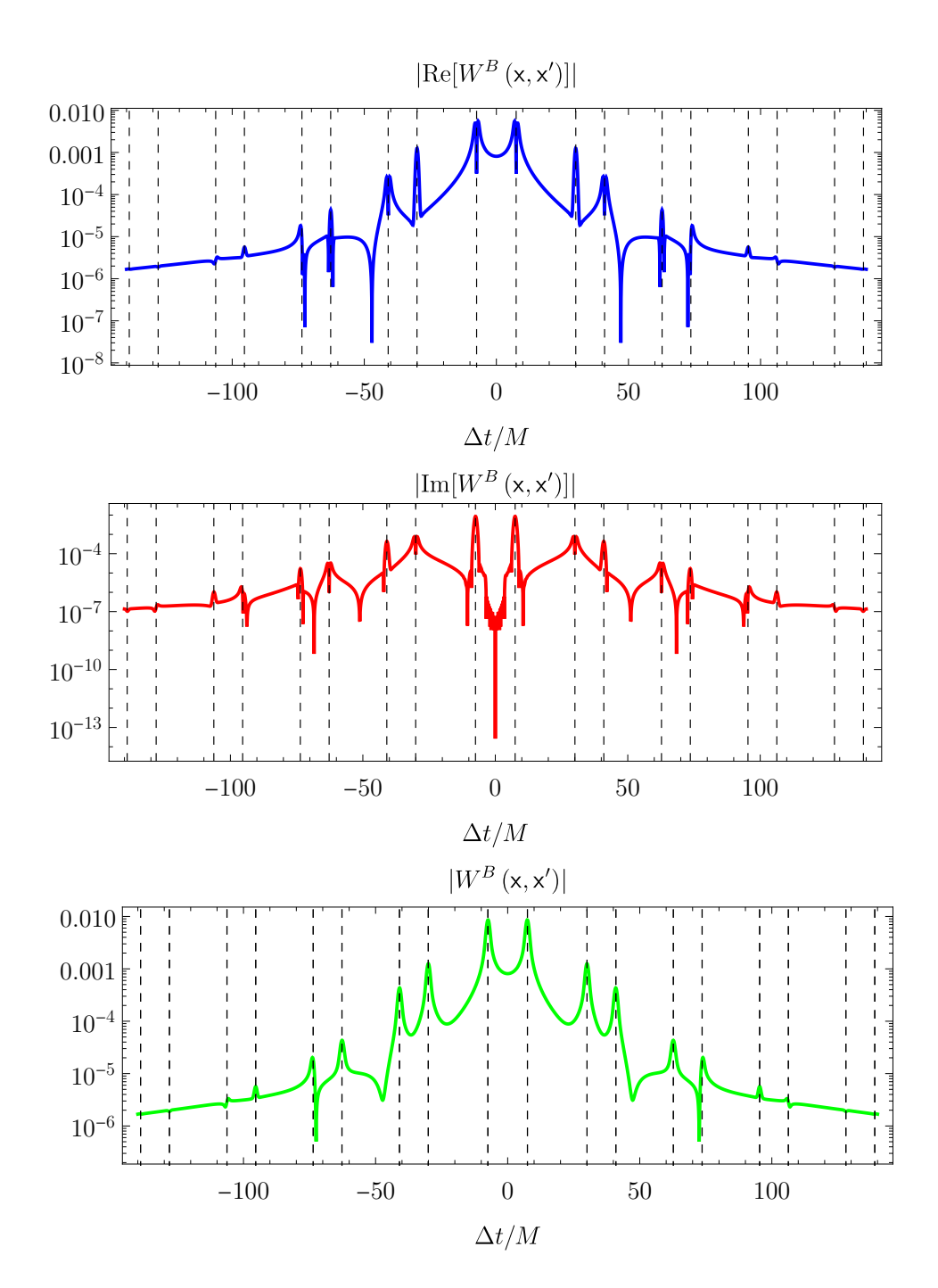


Figure 21 – Absolute value of the real (top) and imaginary (middle) parts of W^B (x; x') for x = (-7.4M, 7.4M, 0, 0) and x' = (t', 3.8M, 0, π /3), plotted as a function of $\Delta t = t - t'$. Bottom: Magnitude of W^B (x; x'). These plots were produced using the ℓ -sum smoothing function from Equation (5.11). Dashed vertical lines mark the values of Δt where x and x' are connected by null geodesics. These align with sharp structures (except zeroes) in the Wightman function, reflecting its singularity structure (See Section 3.4.1). Compared to Figure 19, we are now able to see the behavior of the singularities without spurious oscillations contaminating its surroundings.

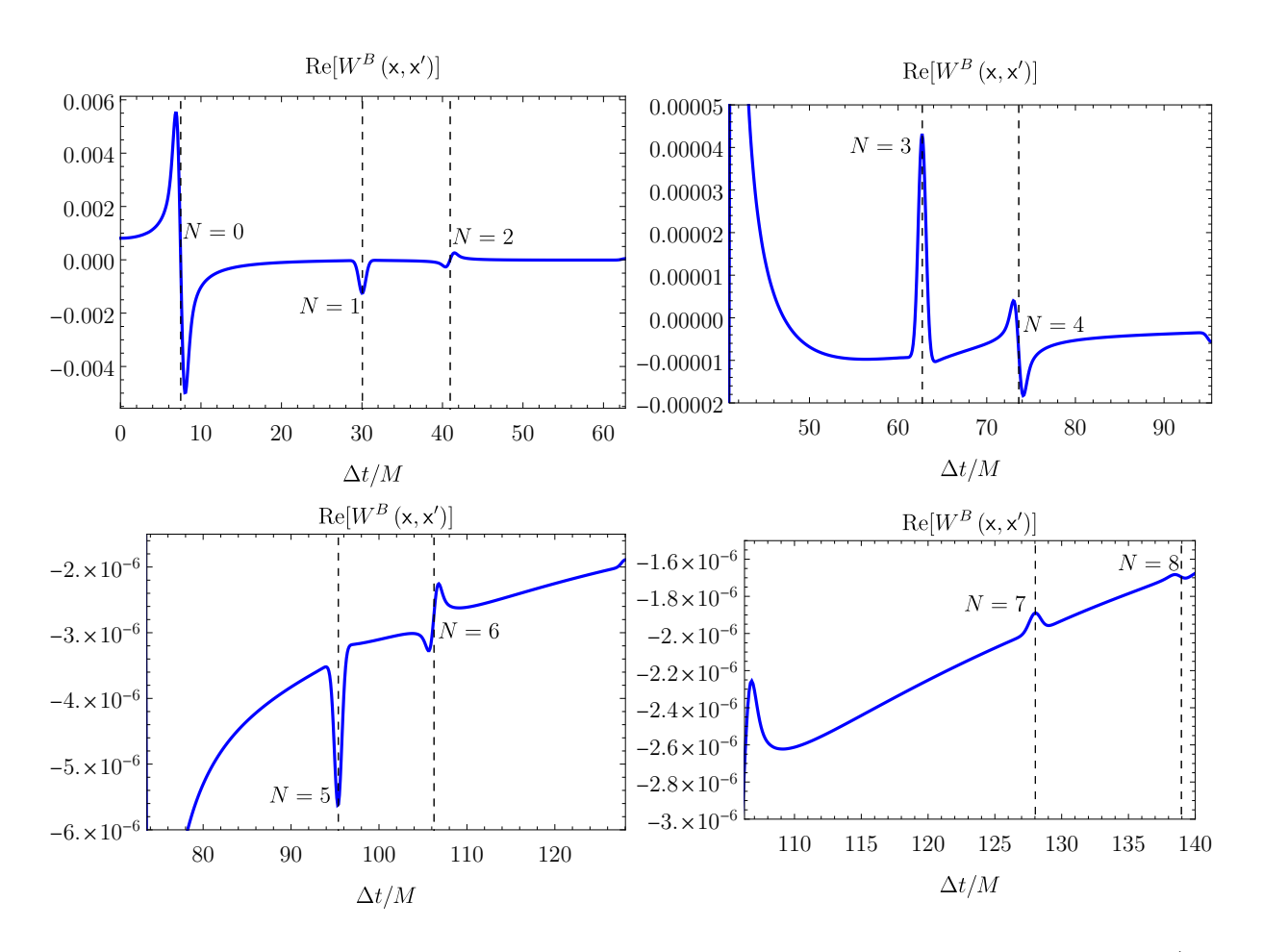


Figure 22 – The Real part of the Wightman function is plotted as a function of $\Delta t/M$ from $\Delta t/M = 0$ to $\Delta t/M = 140$. In each of the plots, vertical lines mark the value of $\Delta t/M$ for which a null geodesic connects x to x' after N half-orbits around the horizon. Notice how the singularities agree with the singularity structure described in Equation (3.55). It is also interesting to notice the roughly linear behavior for large $\Delta t/M$ ($\gtrsim 110$) in our case.

maxima while the real part presents a deep maxima followed by a smaller minima. This relation holds for the next singularities in the plots.

However, given the complications related to the singularities at caustics, further investigation is necessary to tighten the mathematical background of this result. Such study is relegated to future works.

The method developed in this section will be used, with minor adjustments(to be mentioned as needed), throughout all calculations of the Wightman function and related quantities.

5.1.2 Maps of the Wightman function for the Unruh, Boulware and Hartle-Hawking states

The expression of the Wightman function for Boulware state in terms of the radial modes defined in Section 4.1 was already presented in Equation (5.1). Performing a similar

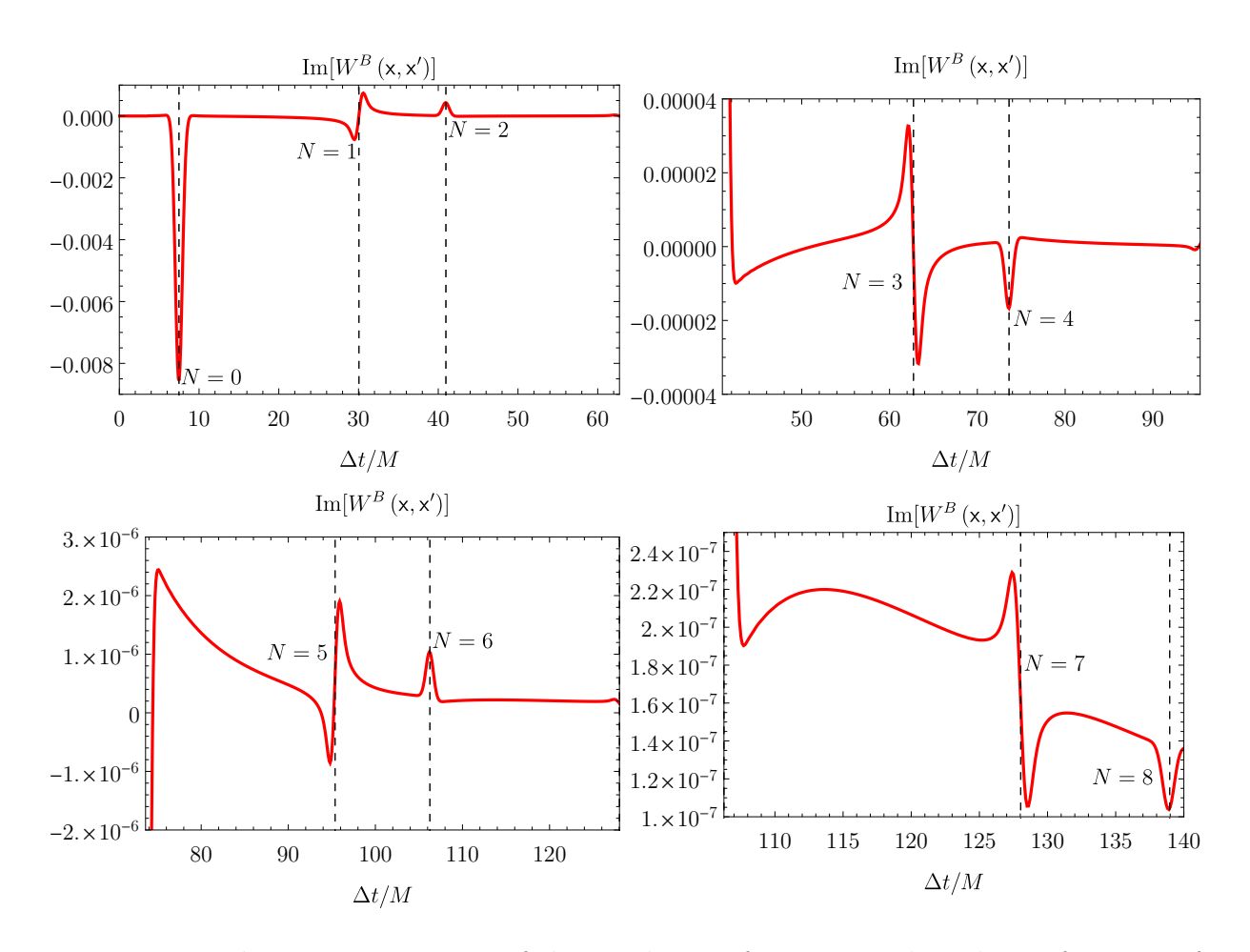


Figure 23 – The Imparinary part of the Wightman function is plotted as a function of $\Delta t/M$ from $\Delta t/M=0$ to $\Delta t/M=140$. In each of the plots, vertical lines mark the value of $\Delta t/M$ for which a null geodesic connects x to x' after N half-orbits around the horizon. Notice how the singularities agree with the singularity structure described in Equation (3.55). It is also interesting to notice the roughly linear behavior for large $\Delta t/M$ ($\gtrsim 110$) in our case.

calculation for the Wightman function of the Unruh (Equation (3.77)) and Hartle-Hawking (Equation (3.89)) states, we obtain

$$W^{U}(\mathbf{x};\mathbf{x}') = \frac{1}{(4\pi)^{2}rr'} \sum_{\ell=0}^{\infty} (2\ell+1) P_{\ell}(\cos(\gamma)) \int_{0}^{\infty} \frac{\mathrm{d}\omega}{\omega} \frac{1}{\left|\bar{I}_{\omega\ell}\right|^{2}} \left[e^{-\mathrm{i}\omega\Delta t} \bar{\psi}_{\omega\ell}^{\mathrm{in,R}}(r) \bar{\psi}_{\omega\ell}^{\mathrm{in,R*}}(r') + \frac{1}{2\sinh(2\pi\omega r_{s})} \left(e^{-\mathrm{i}\omega\Delta t} e^{2\pi\omega r_{s}} \bar{\psi}_{\omega\ell}^{\mathrm{up,R}}(r) \bar{\psi}_{\omega\ell}^{\mathrm{up,R*}}(r') + e^{\mathrm{i}\omega\Delta t} e^{-2\pi\omega r_{s}} \bar{\psi}_{\omega\ell}^{\mathrm{up,R*}}(r) \bar{\psi}_{\omega\ell}^{\mathrm{up,R}}(r') \right) \right]$$

$$(5.12)$$

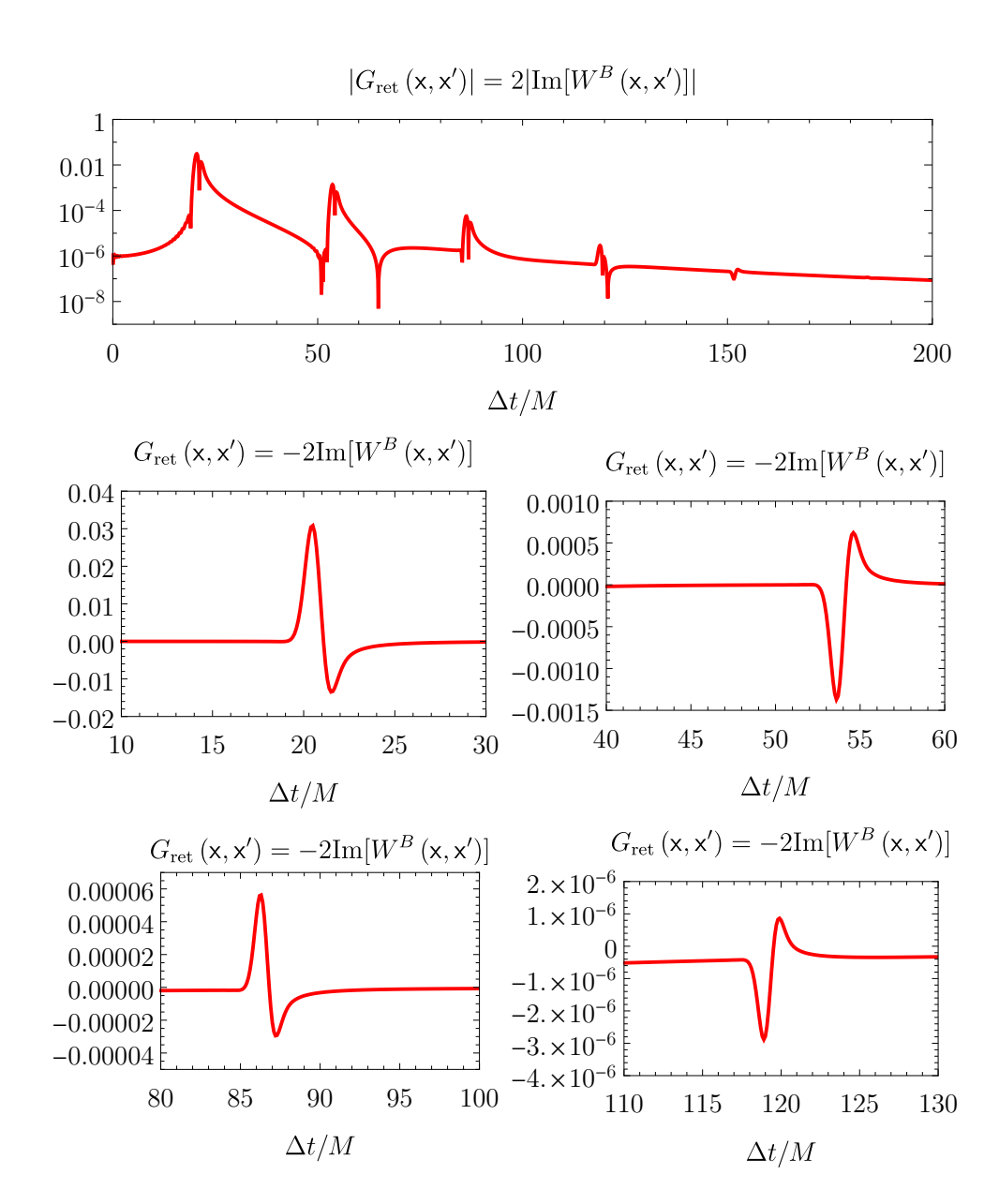


Figure 24 – The Retarded Green Function on caustic points at r=r' on $\gamma=\pi$. First row: A log-scale plot of the absolute value of the RGF as a function of $\Delta t/M$. Second row: The first and second (N=0 and N=1) singularities. Third row: The third and fourth (N=2 and N=3) singularities. The plot in the first row presents the same behavior of its equivalent in the first row of Figure 12 in [57]. The plots in the second row also match their equivalents, in the third row of Figure 12 in [57].

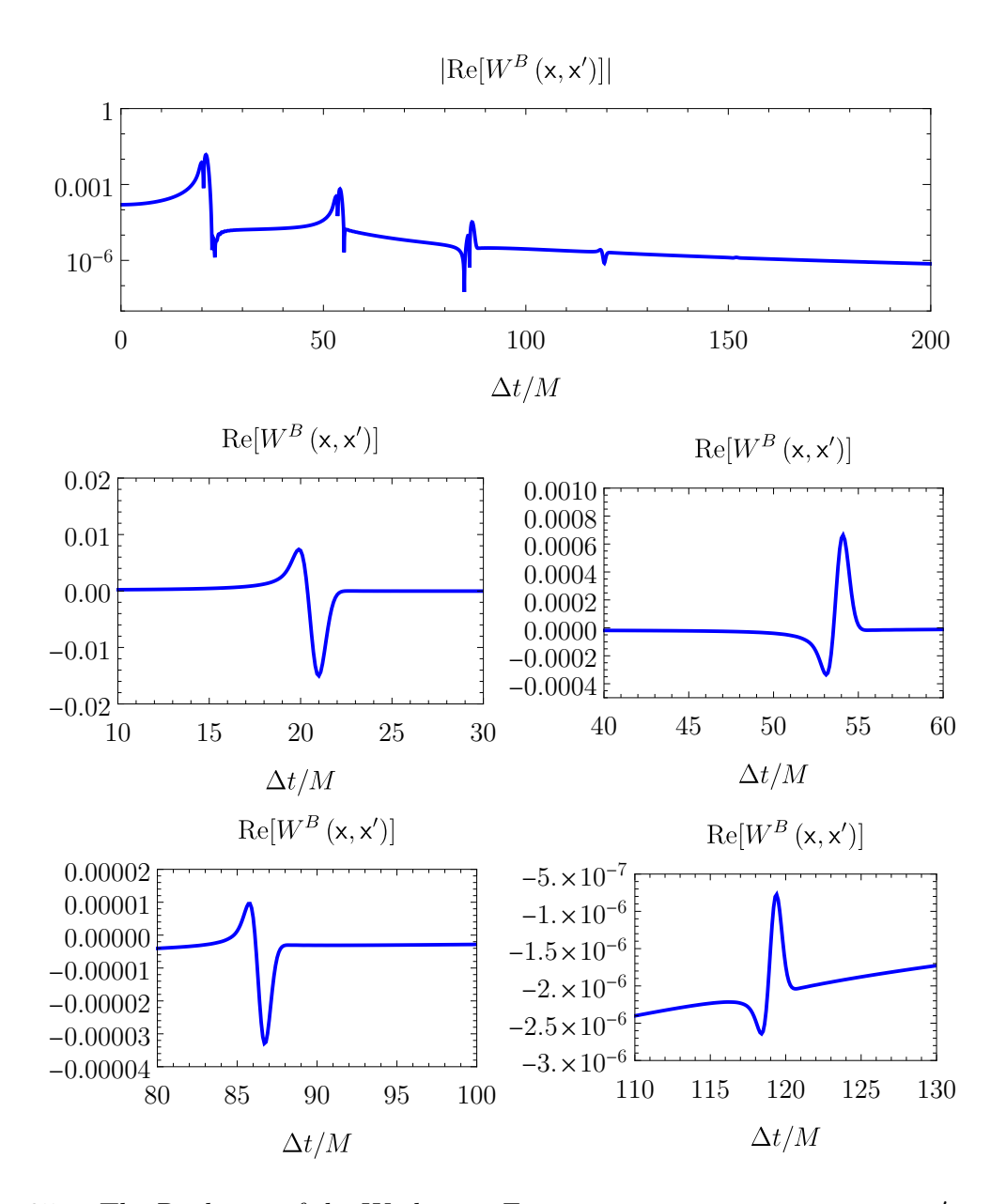


Figure 25 – The Real part of the Wightman Function on caustic points at r=r' on $\gamma=\pi$. First row: A log-scale plot of the absolute value of the Wightman function as a function of $\Delta t/M$. Second row: The first and second caustic echoes. Third row: The third and fourth caustic echoes. To the best of our knowledge, this is the first time that these singularities on the Real part of the Wightman function are exposed for caustic points.

and

$$W^{H}(\mathbf{x};\mathbf{x}') = \frac{1}{(4\pi)^{2}rr'} \sum_{\ell=0}^{\infty} (2\ell+1) P_{\ell}(\cos(\gamma)) \int_{0}^{\infty} \frac{d\omega}{\omega} \frac{1}{\left|\bar{I}_{\omega\ell}\right|^{2}} \frac{1}{2\sinh(2\pi\omega r_{s})}$$

$$\times \left[\left(e^{2\pi\omega r_{s}} e^{-i\omega\Delta t} \bar{\psi}_{\omega\ell}^{\mathrm{in,R}}(r) \bar{\psi}_{\omega\ell}^{\mathrm{in,R*}}(r') + e^{-2\pi\omega r_{s}} e^{i\omega\Delta t} \bar{\psi}_{\omega\ell}^{\mathrm{in,R}}(r) \bar{\psi}_{\omega\ell}^{\mathrm{in,R*}}(r') \right) + \left(e^{2\pi\omega r_{s}} e^{-i\omega\Delta t} \bar{\psi}_{\omega\ell}^{\mathrm{up,R*}}(r) \bar{\psi}_{\omega\ell}^{\mathrm{up,R*}}(r') + e^{-2\pi\omega r_{s}} e^{i\omega\Delta t} \bar{\psi}_{\omega\ell}^{\mathrm{up,R*}}(r) \bar{\psi}_{\omega\ell}^{\mathrm{up,R}}(r') \right) \right].$$

$$(5.13)$$

All terms in these integrals are similar to the ones in the expression for the Boulware state. Consequently, these integrals converge at least as fast as the ones for the Boulware state in the large-frequency limit. To understand why, notice that

$$\lim_{\omega \to \infty} \frac{e^{-2\pi\omega r_s}}{2\sinh(2\pi\omega r_s)} = 0,$$
(5.14)

which cause the terms it multiplies to decay faster than those of the Boulware state, and

$$\lim_{\omega \to \infty} \frac{e^{2\pi\omega r_s}}{2\sinh(2\pi\omega r_s)} = 1,$$
(5.15)

producing no effect with respect to the convergence of the integrals in the large-frequency limit. Hence, the integrals for the Unruh and Hartle-Hawking states converge at least as fast as those one of the Boulware state in this limit.

On the other end, in the low-frequency limit

$$\frac{e^{\pm 2\pi\omega r_s}}{2\sinh(2\pi\omega r_s)} = \frac{1}{4\pi r_s\omega} + \mathcal{O}(\omega^0).$$
 (5.16)

At first sight it might seem to be a problem due to the diverging ω^{-1} behavior as $\omega \to 0$. However, the integrals remain regular in this limit because they consist of $G_\ell^{\text{in},R;\text{in},R*}(\omega)$ and $G_\ell^{\text{up},R;\text{up},R*}(\omega)$ (both of these scale at least as ω^1 in the low-frequency limit, as can be seen, for instance, in Figure 11) multiplied by this factor. Therefore, the integrals for the Unruh and Hartle-Hawking states Wightman functions have the same convergence properties as the one for the Boulware state. We remark that this convergence analysis holds as long as x and x' are not connected by a null geodesic (a case where a singularity is known to appear) or at coincidence, where the large-frequency behavior is pathological.

With that, we proceed to evaluate the Wightman function for these states on several surfaces of constant v'-coordinate to obtain a picture of the correlations across different regions of the spacetime. Specifically, we fix the base point $\mathbf{x}=(v=0M\,,u=-14.8M,\,\theta=0,\,\varphi=0)$ and consider points \mathbf{x}' at an angular separation of $\gamma=\pi/3$ with respect to \mathbf{x} . We vary the EF-coordinates v' and u' of \mathbf{x}' from v'=-100M up to v'=100M in steps of $\Delta v'=1M$. For each v', we vary $u'=v'-2r'_*$ using all values of r'_* in our dataset. The result is the mesh of 28,743 points, represented in both an Eddington-Finkelstein and a Penrose diagram in Figure 26.

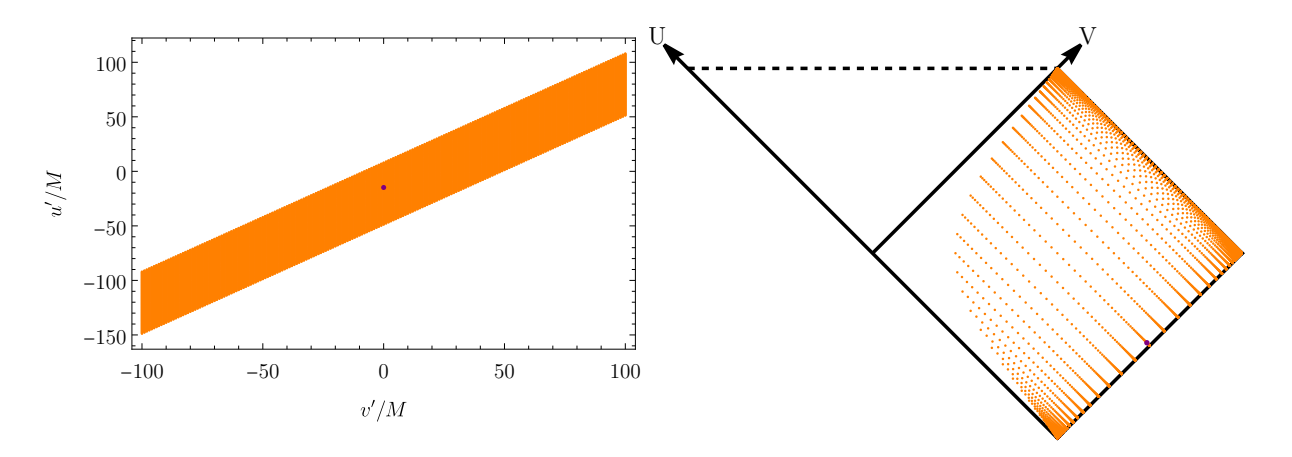


Figure 26 – Points where we will evaluate $W^B(\mathbf{x};\mathbf{x}')$. Left: Eddington-Finkelstein diagram. Right: Penrose diagram. Purple dot: Fixed point $\mathbf{x}=(v=0M,\,u=-14.8M,\,\theta=0,\,\varphi=0)$. Orange dots: The points \mathbf{x}' with varying v' and u'. For each v', we vary $u'=v'-2r'_*$ to cover all values of r'_* in our dataset. All \mathbf{x}' are separated from \mathbf{x} by an angle $\gamma=\pi/3$, hence, no radial null geodesic connects them.

For each state, the complete computation takes approximately 1 hour and 45 minutes using 6 parallel Mathematica kernels. The results for the Boulware state are presented in Figures 27 and 28, where we see, respectively, the real and imaginary parts of the Wightman function across the several x' included in the evaluations. The plot of the real part of the Wightman function for the Hartle-Hawking state is presented in Figure 29. We omit this plot for the Unruh state because it is visually identical to that of the Boulware state (only visually, as will be shown). We also omit the plots of the imaginary part of the Wightman function for the Unruh and Hartle-Hawking states because they are visually identical to that of the Boulware state. This is expected because the imaginary part of the Wightman function can be written in terms of the Advanced and Retarded Green Functions (see Equation (3.50)) which depend only on the geometry of the spacetime.

In all cases, we see the light-crossing manifesting whenever \mathbf{x}' is connected to \mathbf{x} by a null geodesic. There is also the interesting manifestation of the property that the commutator is zero whenever \mathbf{x}' is spacelike connected to \mathbf{x} , which shows as a steep decay in the magnitude of the imaginary part of the Wightman function in the region between the singularities that appear before a complete half-orbit (N=0). These results, although interesting are not something new, since these singularities and their locations are long known. Up to now, the novelty is the possibility to evaluate the Wightman function on a massive amount of spacetime points in a reasonably short time.

To illustrate the difference between the Wightman function in the three quantum states, we calculated them on the $r'\approx 2.7M$ strip of the mesh in Figure 26 (visually very close to the photonsphere represented in Figure 28), varying v'=-100M up to v'=100M in steps of $\Delta v'=0.1M$ for a finer grid. The result is presented in Figure 30. The imaginary

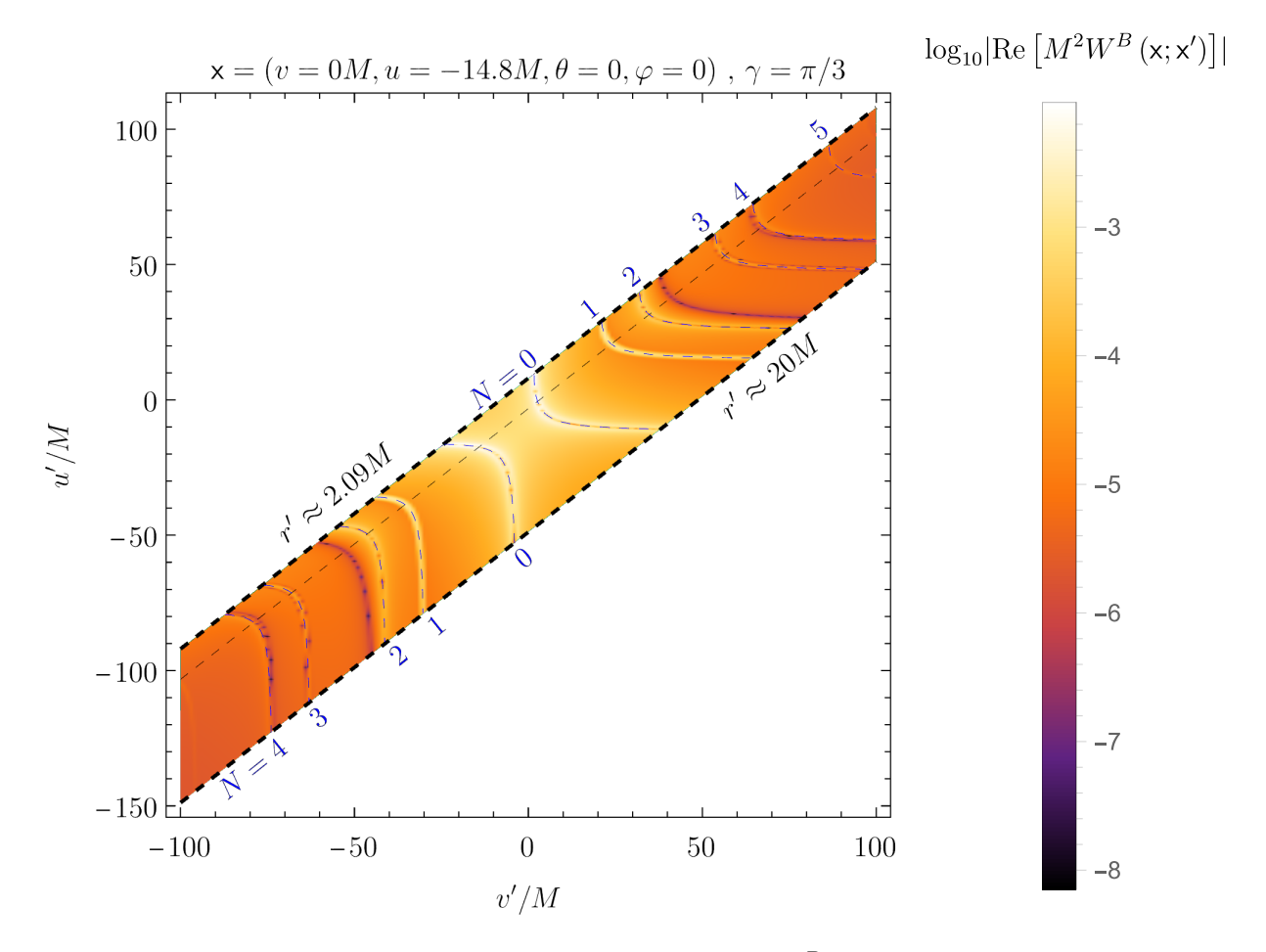


Figure 27 – The real part of the Wightman function W^B (x;x') with x = (v = 0M, u = -14.8M, $\theta = 0$, $\varphi = 0$) ($r \approx 6.009M$) separated by an angle of $\gamma = \pi/3$ from all points x' of Figure 26. The thin black-dashed line is r' = 3M, the photonsphere. The thin blue-dashed lines are the points x' connected to x by null geodesics that complete N half-orbits around the black hole. Overall, the magnitude of the real part of the Wightman function decays with increasing $|\Delta t'/M| = |(\Delta u + \Delta v)/2M|$, where $\Delta u = u - u'$ and $\Delta v = v - v'$, in line with what is seen in Figure 21 which is the $r' \approx 3.9M$ slice of this plot. The localized maxima are the manifestations of the singularities that appear when x and x' are light-like connected, i.e., on the thin blue-dashed lines. The overall structure of the plot do not change by choosing the fixed point x below the photonsphere (r < 3M).

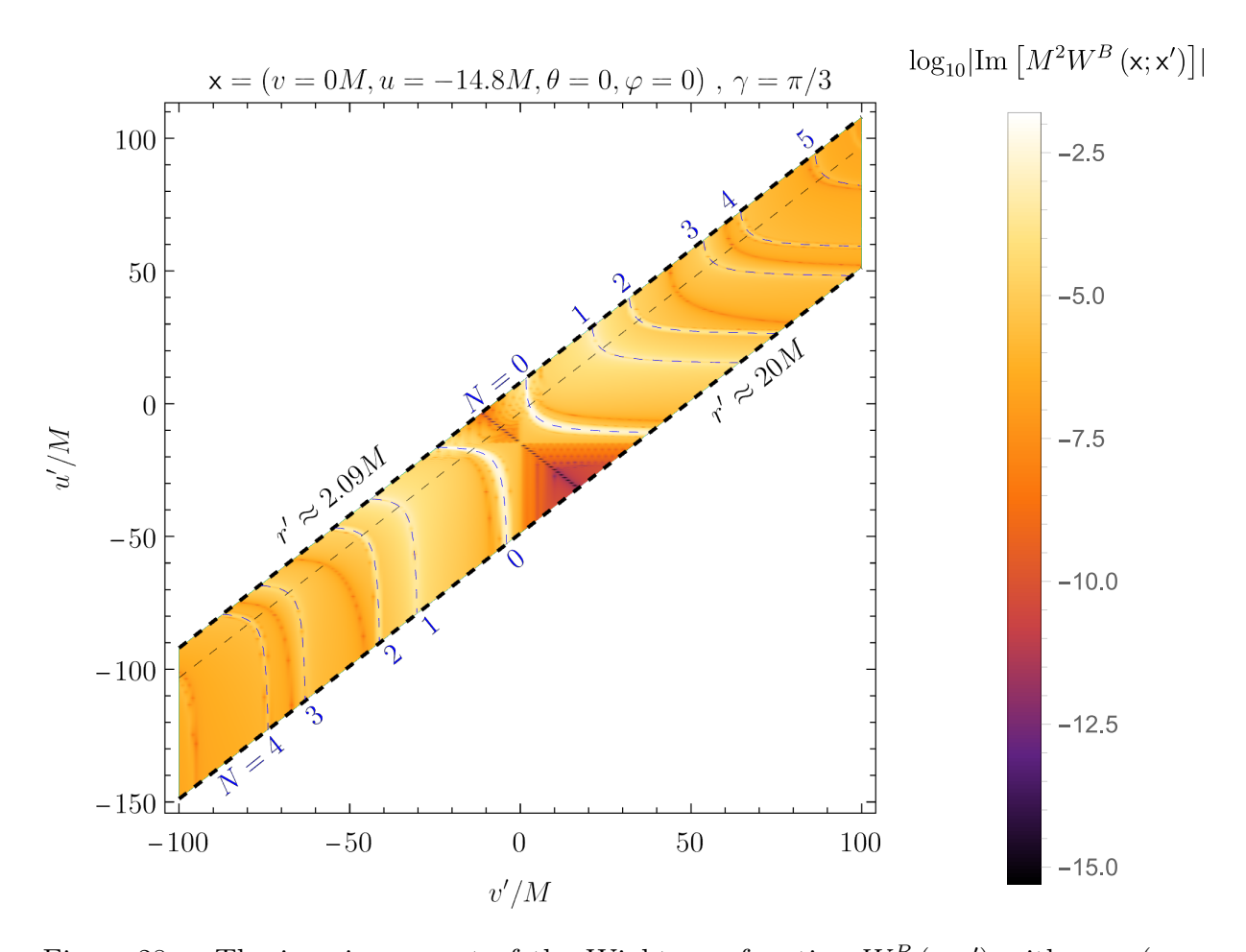


Figure 28 – The imaginary part of the Wightman function W^B (x; x') with x = (v = 0M, u = -14.8M, $\theta = 0$, $\varphi = 0$) ($r \approx 6.009M$) separated by an angle of $\gamma = \pi/3$ all points x' from Figure 26. The thin black-dashed line is r' = 3M, the photonsphere. The thin blue-dashed lines are the points x' connected to x by a null geodesic that completes N half-orbits around the black hole. Overall, the magnitude of the imaginary part of the Wightman function decays with increasing |t'| = |(u' + v')/2|, in line with what is seen in Figure 21 which is the $r' \approx 3.9M$ slice of this plot. The localized maxima are the manifestations of the singularities that appear when x and x' are light-like connected, i.e., on the thin blue-dashed lines.

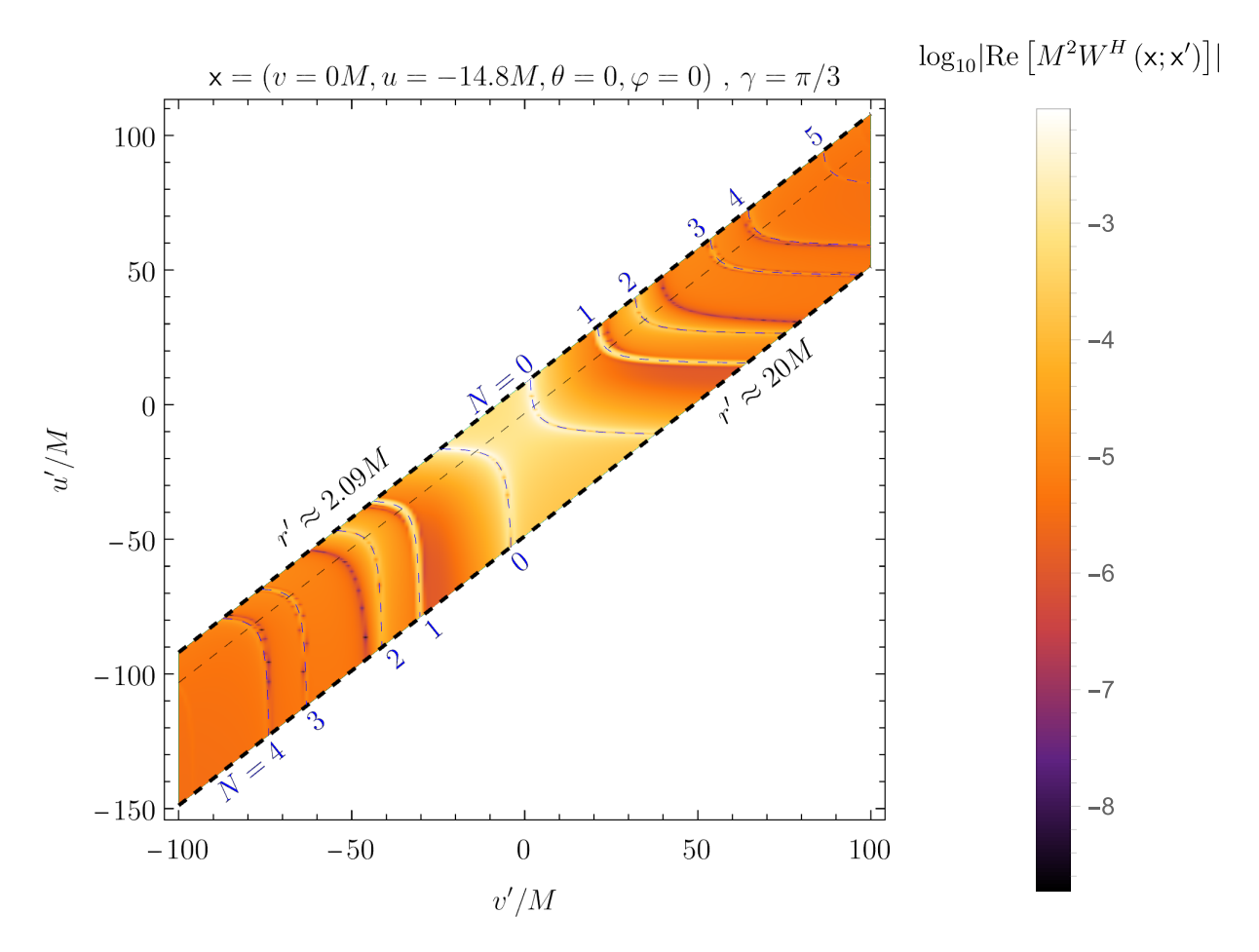


Figure 29 – The real part of the Wightman function $W^H(\mathsf{x};\mathsf{x}')$ with $\mathsf{x} = (v = 0M, u = -14.8M, \theta = 0, \varphi = 0)$ separated by an angle of $\gamma = \pi/3$ from all points x' of Figure 26. The thin black-dashed line is r' = 3M, the photonsphere. The thin blue-dashed lines are the points x' connected to x by a null geodesic that completes N half-orbits around the black hole. Overall, the magnitude of the real part of the Wightman function decays with increasing $|\Delta t'/M| = |(\Delta u + \Delta v)/2M|$, where $\Delta u = u - u'$ and $\Delta v = v - v'$, in line with what is seen in Figure 21 which is the $r' \approx 3.9M$ slice of this plot. The localized maxima are the manifestations of the singularities that appear when x and x' are light-like connected, i.e., on the thin blue-dashed lines.

part of the Wightman function across all three quantum states agree to a relative error of at most 10^{-3} when $\Delta t/M = 0$ and 10^{-8} everywhere else. The oscillations seen near $\Delta t/M = 0$ are likely explained by the fact that this point is closer to coincidence (x' = x) than our method can currently resolve.

On the other hand, the real part of the Wightman function is overall different across the three quantum states, except when it comes to the location of the singularities (as expected, since these singularities are purely geometrical and happen whenever x and x' are light-like related). Moreover we see that, except at the singularities or large |v'/M| (where low-frequencies become increasingly important), $|\text{Re}[W^B(\mathbf{x};\mathbf{x}')]| > |\text{Re}[W^U(\mathbf{x};\mathbf{x}')]| > |\text{Re}[W^H(\mathbf{x};\mathbf{x}')]|$. This is a manifestation of the nature of these quantum states: The Boulware state models a cold star and contains no thermal radiation. The Unruh state models a black hole emitting thermal radiation and the Hartle-Hawking state models a black hole in thermal equilibrium with its environment. Since thermal radiation implies less quantum correlations, it is sensible to expect that $|\text{Re}[W^B(\mathbf{x};\mathbf{x}')]| > |\text{Re}[W^U(\mathbf{x};\mathbf{x}')]| > |\text{Re}[W^U(\mathbf{x};\mathbf{x}')]|$

5.1.3 The quantum relative contribution $W^{\psi}(\mathbf{x}, \mathbf{x}')$

To the best of our knowledge, there are no known methods to explicitly evaluate the quantum state contribution that comes from the bi-scalar $w^{\psi}(\mathbf{x}, \mathbf{x}')$ of the Wightman function in Equation (3.52). While we are also not able to evaluate $w^{\psi}(\mathbf{x}, \mathbf{x}')$ for each state, we managed to calculate the overall behavior of the differences

$$W^{\psi-B}(\mathbf{x}, \mathbf{x}') = W^{\psi}(\mathbf{x}, \mathbf{x}') - W^{B}(\mathbf{x}, \mathbf{x}')$$

$$(5.17)$$

between the state $|\psi\rangle$ and the Boulware state $|B\rangle$, which we take as the reference. We will refer to this quantity as the quantum relative contribution. It has the property that

$$W^{\psi - B}(\mathbf{x}, \mathbf{x}') = w^{\psi}(\mathbf{x}, \mathbf{x}') - w^{B}(\mathbf{x}, \mathbf{x}'), \, \mathbf{x}' \in \mathcal{N}(\mathbf{x}). \tag{5.18}$$

Which can be understood as a consequence of the fact the geometry-dependent terms are the same for all quantum states. Such property allows to obtain information about the relative behavior of the bi-scalar $w^{\psi}(\mathbf{x}, \mathbf{x}')$ with respect to $w^{B}(\mathbf{x}, \mathbf{x}')$.

In terms of mode-sum expansions, it is straightforward to use Equations (5.1), (5.12) and (5.13) to write

$$W^{U-B}(\mathbf{x}, \mathbf{x}') = \frac{1}{(4\pi)^2 r r'} \sum_{\ell=0}^{\infty} (2\ell+1) P_{\ell}(\cos(\gamma))$$

$$\times \int_{0}^{\infty} \frac{d\omega}{\omega} \frac{e^{-2\pi\omega r_s}}{\sinh(2\pi\omega r_s)} \operatorname{Re} \left[\frac{e^{-i\omega\Delta t} \bar{\psi}_{\omega\ell}^{\text{up,R}}(r) \bar{\psi}_{\omega\ell}^{\text{up,R*}}(r')}{\left|\bar{I}_{\omega\ell}\right|^2} \right]$$
(5.19)

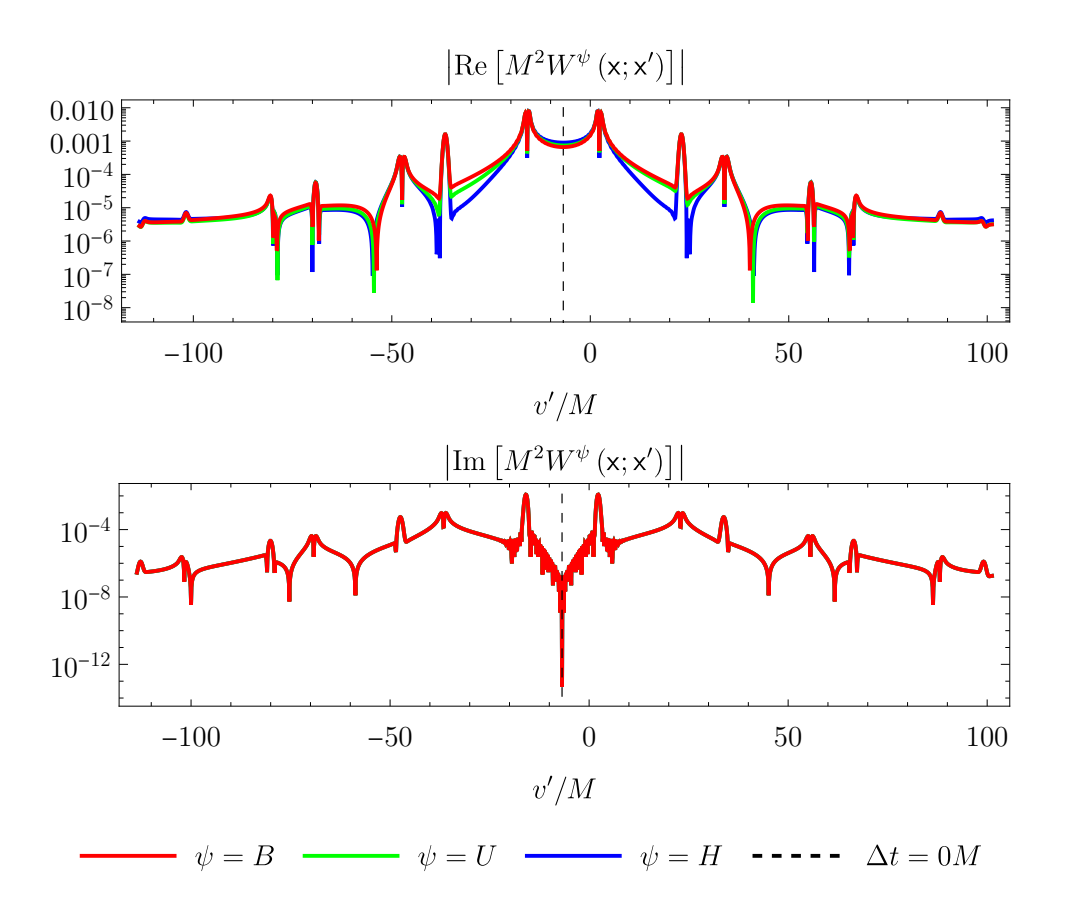


Figure 30 – The magnitudes of the real (first row) and imaginary (second row) parts of the Wightman function $W^{\psi}(\mathbf{x};\mathbf{x}')$ are presented for the Boulware (red), Unruh (green) and Hartle-Hawking states (blue) as a function of v'/M. Here we fixed $x = (v = 0M, r \approx 6.009M, \theta = 0, \varphi = 0)$ and varied $x' = (v', r' \approx$ $2.7M, \theta = 0, \varphi = \pi/3$) with v'/M spanning the range [-100, 100] in steps of 0.1M. The thin black-dashed line represents $\Delta t/M = 0$. In the imaginary part, all curves overlap perfectly, as expected since this part depends only on the spacetime geometry. At the numerical level, the relative difference between $\text{Im}[W^U(\mathbf{x};\mathbf{x}')]$ and $\text{Im}[W^B(\mathbf{x};\mathbf{x}')]$ peaks at $\approx 10^{-4}$ when $\Delta t = 0M$ $(v'=r'_*-r_*=-6.8M)$ and is smaller than 10^{-7} everywhere else. This is also the case for the relative difference between $\text{Im}[W^H(\mathsf{x};\mathsf{x}')]$ and $\text{Im}[W^B(\mathsf{x};\mathsf{x}')]$. The locations of the divergences are the same on all states, as expected, since they depend only on the spacetime geometry. Notice that between two successive singularities (except near $\Delta t/M = 0$ and large |v'/M|), it holds that $\left| \operatorname{Re}[W^B(\mathsf{x};\mathsf{x}')] \right| > \left| \operatorname{Re}[W^U(\mathsf{x};\mathsf{x}')] \right| > \left| \operatorname{Re}[W^H(\mathsf{x};\mathsf{x}')] \right|$. Heuristically, this means that the Boulware state contains overall more correlations than the Unruh state, which in turn, contains overall more correlations than the Hartle-Hawking states. This is justified by the fact the Boulware state models a cold star, hence, contains no thermal radiation. On the other hand, the Unruh state represents a black hole that emits thermal radiation, hence, it should contain less correlations than the Boulware state (as we see) due to the thermal radiation. Finally, the Hartle-Hawking state models a black hole in thermal equilibrium with its environment, which implies a situation where there is more thermal radiation than in the Unruh state, explaining why there are less correlations in this state.

and

$$W^{H-B}(\mathbf{x}, \mathbf{x}') = \frac{1}{(4\pi)^2 r r'} \sum_{\ell=0}^{\infty} (2\ell+1) P_{\ell}(\cos(\gamma))$$

$$\times \int_{0}^{\infty} \frac{d\omega}{\omega} \frac{e^{-2\pi\omega r_{s}}}{\sinh(2\pi\omega r_{s})} \operatorname{Re} \left[\frac{e^{-i\omega\Delta t} \bar{\psi}_{\omega\ell}^{\text{up,R}}(r) \bar{\psi}_{\omega\ell}^{\text{up,R*}}(r')}{\left|\bar{I}_{\omega\ell}\right|^{2}} + \frac{e^{-i\omega\Delta t} \bar{\psi}_{\omega\ell}^{\text{in,R}}(r) \bar{\psi}_{\omega\ell}^{\text{in,R*}}(r')}{\left|\bar{I}_{\omega\ell}\right|^{2}} \right], \tag{5.20}$$

where we assumed that $x, x' \in I$.

By performing this subtraction we were able to evaluate $W^{\psi-B}(\mathbf{x};\mathbf{x}')$, which can be understood as the difference between the quantum content of the states $|\psi\rangle$ and $|B\rangle$. We have done this for $\mathbf{x}=(v=0M,\,r\approx6.009M,\,\theta=0,\,\varphi=0)$ and $\mathbf{x}'=(v',\,r'\approx2.7M,\,\theta=0,\,\varphi=\pi/3)$, with v'/M spanning the range [-100,100] in steps of 0.1M. The results are presented in Figure 31.

As seen in that figure, $W^{\psi-B}(\mathbf{x};\mathbf{x}')$ presents a local maxima at $v'_{\text{max}}=-6.8M$ for $|H\rangle$ and $v'_{\text{max}}=-11.8M$ for $|U\rangle$, being symmetric around such local maxima for $|H\rangle$. The locus of the local maxima of $W^{H-B}(\mathbf{x};\mathbf{x}')$ can be understood as the point \mathbf{x}' where $\Delta t/M=0$. For $W^{U-B}(\mathbf{x};\mathbf{x}')$, we have not been able to figure out what sets the location of the maxima from this analysis. However, we suspect that being displaced from $\Delta t/M=0$ is a consequence of the asymmetry in the contributions from $\bar{\psi}^{\text{in,R}}_{\omega\ell}$ and $\bar{\psi}^{\text{up,R}}_{\omega\ell}$ (and their complex conjugates) in the mode-sum expansion of the Wightman function (5.12), i.e., there is no thermal factor multiplying the contribution from the $\bar{\psi}^{\text{in,R}}_{\omega\ell}$ (and its complex conjugate). Consequently, $W^{U-B}(\mathbf{x};\mathbf{x}')$ depends only on $\bar{\psi}^{\text{up,R}}_{\omega\ell}$ (and its complex conjugate). We suspect this displaces the axes of symmetry of $W^{U-B}(\mathbf{x};\mathbf{x}')$ from $\Delta t/M=0$ to the points where the integrand in Equation (5.19) interferes constructively.

Overall, $W^{\psi-B}(\mathbf{x};\mathbf{x}')$ behaves in a very similar way for these quantum states: As $|\Delta v'/M|$, where $\Delta v' = v' - v'_{\text{max}}$, increases there is an exponential decay which transitions into a polynomial decay as $|\Delta v'/M|^{-2}$ once $|\Delta v'/M|$ is large enough. The location of this transition seems to be roughly given by the arrival of null geodesic that connects \mathbf{x} and \mathbf{x}' after a complete orbit, as observed in Figure 32, where we overlap these plots with the real part of the Wightman function for each of the states in question. While a more careful analysis is important to confirm if it holds for other choices of γ and r', we conjecture that this transition occurs around the boundary of the normal neighborhood $\mathcal{N}(\mathbf{x})$ of \mathbf{x} .

The reader might wonder how these local maxima in the quantum relative contribution propagate as one changes r'. To answer this question, we evaluated a heat-map of this quantity on the mesh of points presented in Figure 26 and tracked the local maxima on each surface of constant r'. The results for the Unruh and Hartle-Hawking states are presented in Figures 33 and 34, respectively.

In the Hartle-Hawking state, the local maxima tracks the line of $\Delta t/M = 0$. In the Unruh state, on the other hand, we found that for $\Delta t > 0$, the local maxima remains close to u = u' as v' increases, slowly bending towards u < u' with increasing Δt and for

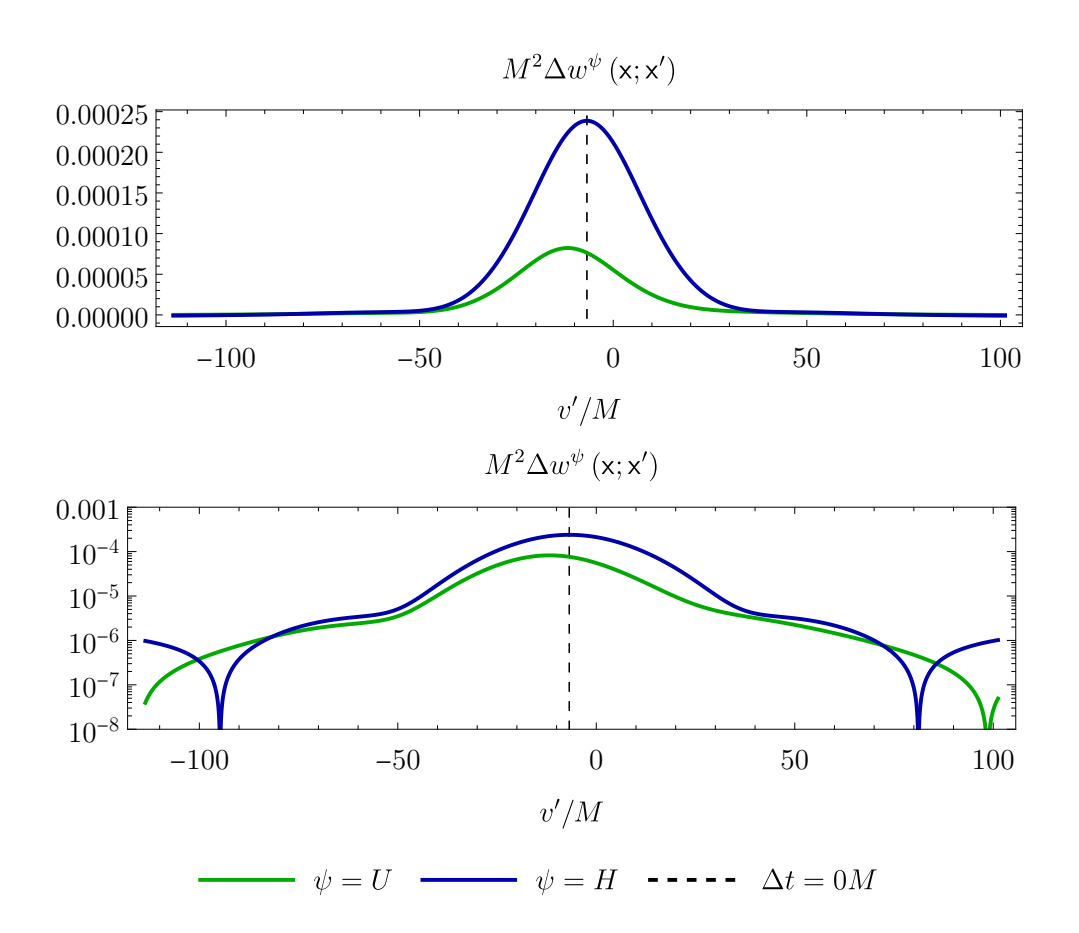


Figure 31 – The quantum relative contribution $W^{\psi-B}(\mathbf{x};\mathbf{x}')$ is presented for the Unruh (dark green) and Hartle-Hawking state (dark blue) states as a function of v'/M in a linear plot (top) and a log-plot (bottom). Here we fixed $\mathbf{x}=(v=0M,\,r\approx6.009M,\,\theta=0,\,\varphi=0)$ and varied $\mathbf{x}'=(v',\,r'\approx2.7M,\,\theta=0,\,\varphi=\pi/3)$ with v'/M spanning the range [-100,100] in steps of 0.1M. The thin black-dashed line represents $\Delta t/M=0$. Despite having the largest magnitude, the real part of the Wightman function is a negative number, implying that the quantum relative contributions are positive in the region $-95\lesssim v'/M\lesssim80$. For both states, $\Delta w^{\psi}(\mathbf{x},\mathbf{x}')$ presents a local maxima, which is located at $v'_{\rm max}/M=-6.8$ and $v'_{\rm max}/M=-11.8$ for the Hartle-Hawking and Unruh states, respectively. In both cases, as one moves away from the local maxima, i.e., increasing $|\Delta v'/M|$, where $\Delta v'=v'-v'_{\rm max}$, the quantum relative contribution decays exponentially and transitions into a polynomial decay of $|\Delta v'/M|^{-2}$ once $|\Delta v'/M|$ becomes large enough.

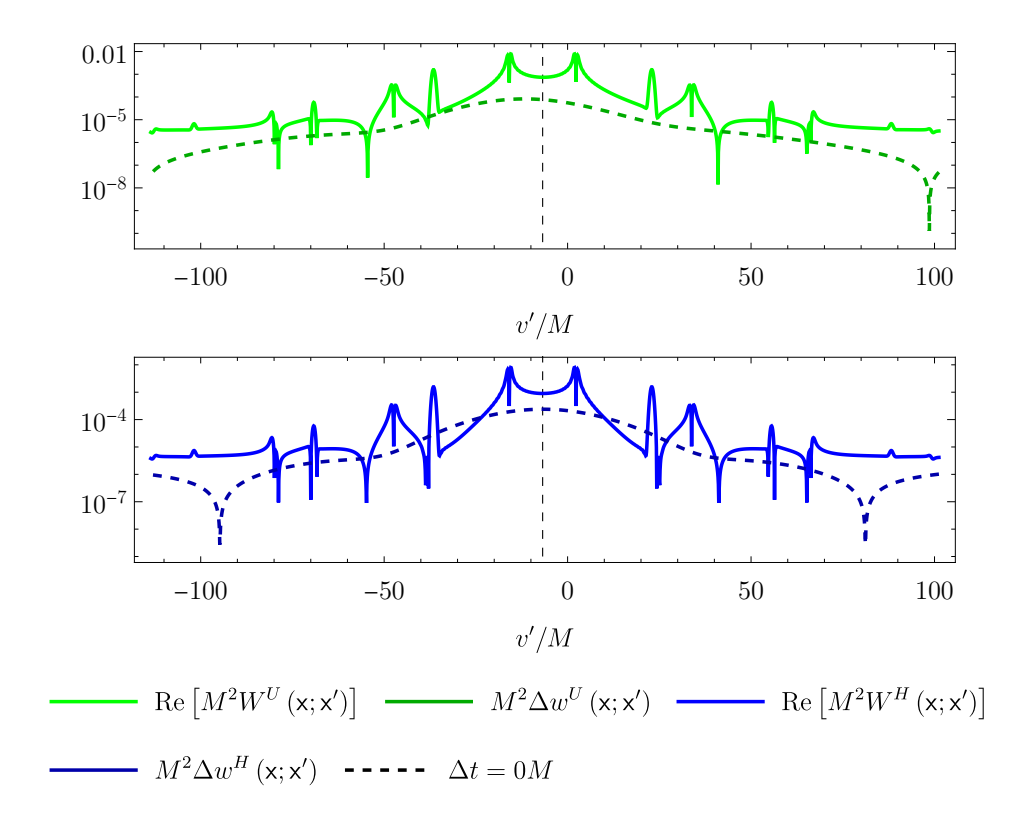


Figure 32 – The plots from Figure 31 overlapped with the quantum relative contribution $W^{\psi-B}(\mathbf{x};\mathbf{x}')$. Notice how the transition in decay of $W^{\psi-B}(\mathbf{x};\mathbf{x}')$ from exponential to polynomial roughly agrees with the location of the N=2 singularity, which marks the arrival of the null geodesic connecting \mathbf{x} and \mathbf{x}' after a complete orbit around the horizon.

 $\Delta t < 0$ it bends away from this line, in a noticeable faster fashion, towards u' > u as Δt decreases. We also found that it intersects the local maxima of the Hartle-Hawking state at $\mathbf{x}' = (v = 0M, u = -14.8M, \theta = 0, \varphi = \pi/3)$, i.e., at the point \mathbf{x}' with the same u and v coordinates of \mathbf{x} . Heuristically, these local maxima are produced by constructive interference in the integrand of (5.19). It is also interesting to notice that even for large $|\Delta v'/M|$, the quantum relative contribution persists in a region extending from the horizon up to the photonsphere.

5.2 Across the horizon

We now turn to the scenario where one point lies inside the horizon and the other is outside. Specifically, we consider $x \in II$ and $x' \in I$ and employ the numerical method developed in the previous section to compute the Wightman function.

We begin by substituting the radial modes defined in Section 4.1 into the equations of Wightman function for the Unruh (3.85) and Hartle-Hawking (3.92) states. This allows us to express the Wightman functions for all these states in terms of the radial modes n our

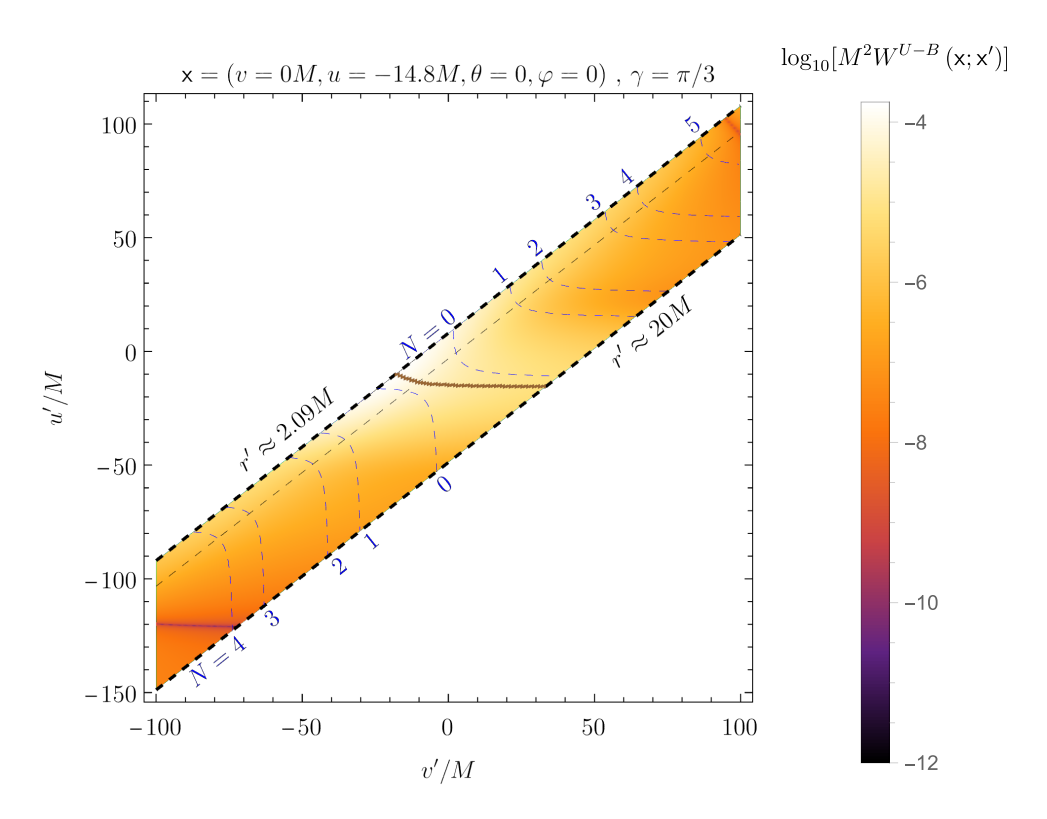


Figure 33 – The logarithm of the absolute value of the quantum relative contribution $W^{U-B}(\mathbf{x};\mathbf{x}')$ is presented as a function of v'/M and u'/M. Here we fixed $\mathbf{x}=(v=0M,\,r\approx 6.009M,\,\theta=0,\,\varphi=0)$ and varied $\mathbf{x}'=(v',\,u',\,\theta=0,\,\varphi=\pi/3)$ across all points of the mesh in Figure 26. The thin black-dashed line is r'=3M, the photonsphere. The thin blue-dashed lines are the points \mathbf{x}' connected to \mathbf{x} by a null geodesic that completes N half-orbits around the black hole. The brown line tracks the local maxima and is obtained by joining the points where it happens for each r' in our data. Above the photonsphere, it moves closer to u'=u as r' increases.

dataset. The resulting expressions are as follows:

$$W^{U}(\mathsf{x};\mathsf{x}') = \frac{1}{(4\pi)^{2}rr'} \sum_{\ell=0}^{\infty} (2\ell+1) P_{\ell}(\cos(\gamma)) \int_{0}^{\infty} \frac{\mathrm{d}\omega}{\omega} \left[e^{-\mathrm{i}\omega\Delta t} \frac{\psi_{\omega\ell}^{\mathrm{ins}}(r) \bar{\psi}_{\omega\ell}^{\mathrm{in,R*}}(r')}{\left| \bar{I}_{\omega\ell} \right|^{2}} + \frac{1}{2\sinh(2\pi r_{s}\omega)} \left(e^{-\mathrm{i}\omega\Delta t} e^{2\pi r_{s}\omega} \bar{\rho}_{\omega\ell}^{\mathrm{up}} \frac{\psi_{\omega\ell}^{\mathrm{ins}}(r) \bar{\psi}_{\omega\ell}^{\mathrm{up,R*}}(r')}{\left| \bar{I}_{\omega\ell} \right|^{2}} + e^{\mathrm{i}\omega\Delta t} e^{-2\pi r_{s}\omega} \bar{\rho}_{\omega\ell}^{\mathrm{up*}} \frac{\psi_{\omega\ell}^{\mathrm{ins*}}(r) \bar{\psi}_{\omega\ell}^{\mathrm{up,R}}(r')}{\left| \bar{I}_{\omega\ell} \right|^{2}} + \frac{1}{\sinh(2\pi r_{s}\omega)} \operatorname{Re} \left[e^{\mathrm{i}\omega\Delta t} \frac{\psi_{\omega\ell}^{\mathrm{ins}}(r) \bar{\psi}_{\omega\ell}^{\mathrm{up,R}}(r')}{\bar{I}_{\omega\ell}} \right] \right], \quad \mathsf{x} \in II, \mathsf{x}' \in I$$

$$(5.21)$$

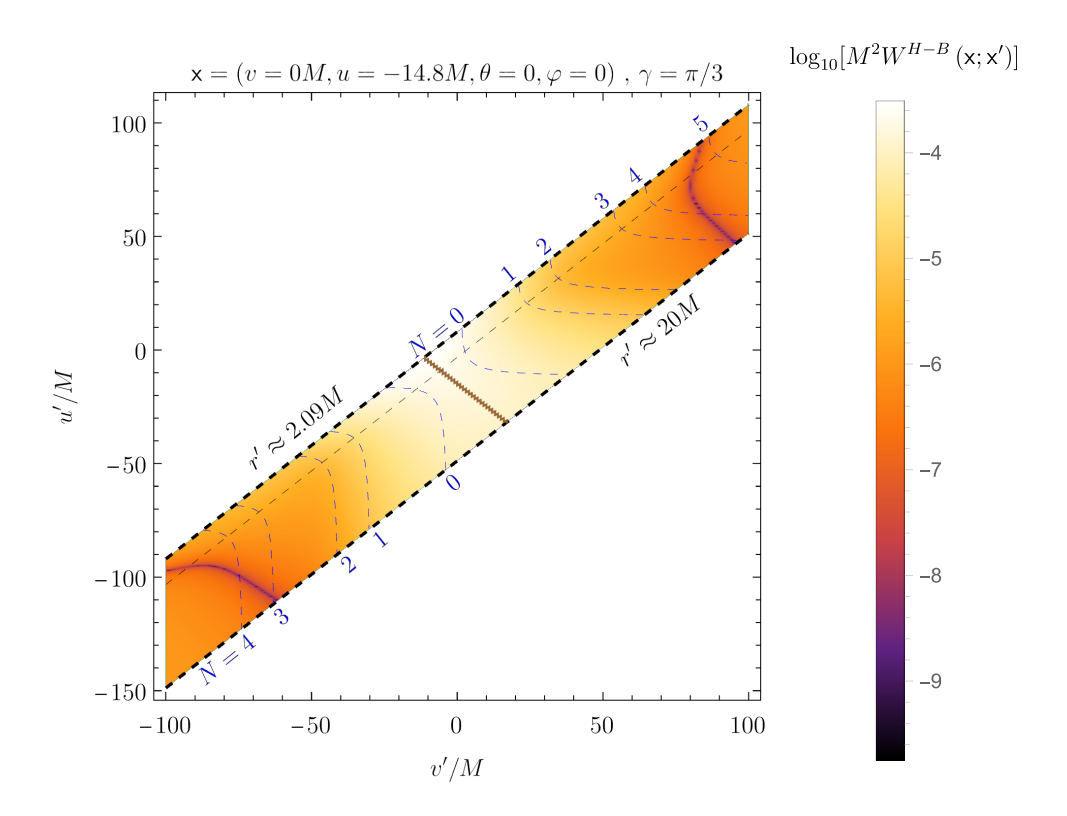


Figure 34 – The logarithm of the absolute value of the quantum relative contribution $W^{H-B}(\mathbf{x};\mathbf{x}')$ is presented as a function of v'/M and u'/M. Here we fixed $\mathbf{x}=(v=0M,\,r\approx6.009M,\,\theta=0,\,\varphi=0)$ and varied $\mathbf{x}'=(v',\,u'\approx,\,\theta=0,\,\varphi=\pi/3)$ across all points of the mesh in Figure 26. The thin black-dashed line is r'=3M, the photonsphere. The thin blue-dashed lines are the points \mathbf{x}' connected to \mathbf{x} by a null geodesic that completes N half-orbits around the black hole. The brown line tracks the local maxima and is obtained by joining the points where it happens for each r' in our data. Here, it was numerically verified to be tracking $\Delta t/M=0$.

and

$$W^{H}(\mathsf{x};\mathsf{x}') = \frac{1}{(4\pi)^{2}rr'} \sum_{\ell=0}^{\infty} (2\ell+1) P_{\ell}(\cos(\gamma)) \int_{0}^{\infty} \frac{\mathrm{d}\omega}{\omega} \frac{1}{2\sinh(2\pi r_{s}\omega)}$$

$$\times \left[\left(e^{-\mathrm{i}\omega\Delta t} e^{2\pi r_{s}\omega} \frac{\psi_{\omega\ell}^{\mathrm{ins}}(r)\bar{\psi}_{\omega\ell}^{\mathrm{in},\mathrm{R}*}(r')}{\left|\bar{I}_{\omega\ell}\right|^{2}} + e^{\mathrm{i}\omega\Delta t} e^{-2\pi r_{s}\omega} \frac{\psi_{\omega\ell}^{\mathrm{ins}*}(r)\bar{\psi}_{\omega\ell}^{\mathrm{in},\mathrm{R}}(r')}{\left|\bar{I}_{\omega\ell}\right|^{2}} \right) + \left(e^{-\mathrm{i}\omega\Delta t} e^{2\pi r_{s}\omega} \bar{\rho}_{\omega\ell}^{\mathrm{up}} \frac{\psi_{\omega\ell}^{\mathrm{ins}}(r)\bar{\psi}_{\omega\ell}^{\mathrm{up},\mathrm{R}*}(r')}{\left|\bar{I}_{\omega\ell}\right|^{2}} + e^{\mathrm{i}\omega\Delta t} e^{-2\pi r_{s}\omega} \bar{\rho}_{\omega\ell}^{\mathrm{up}*} \frac{\psi_{\omega\ell}^{\mathrm{ins}*}(r)\bar{\psi}_{\omega\ell}^{\mathrm{up},\mathrm{R}}(r')}{\left|\bar{I}_{\omega\ell}\right|^{2}} \right) + 2\mathrm{Re} \left[e^{\mathrm{i}\omega\Delta t} \frac{\psi_{\omega\ell}^{\mathrm{ins}}(r)\bar{\psi}_{\omega\ell}^{\mathrm{up},\mathrm{R}}(r')}{\bar{I}_{\omega\ell}} \right] \right], \quad \mathsf{x} \in II, \mathsf{x}' \in I.$$

$$(5.22)$$

Except at the light-crossing singularities, the convergence of these integrals in the high-frequency limit is guaranteed by the smoothing scheme as in the analysis in Section 5.1.2. In the low-frequency regime, convergence follows from the behavior of the ℓ -summed integrands

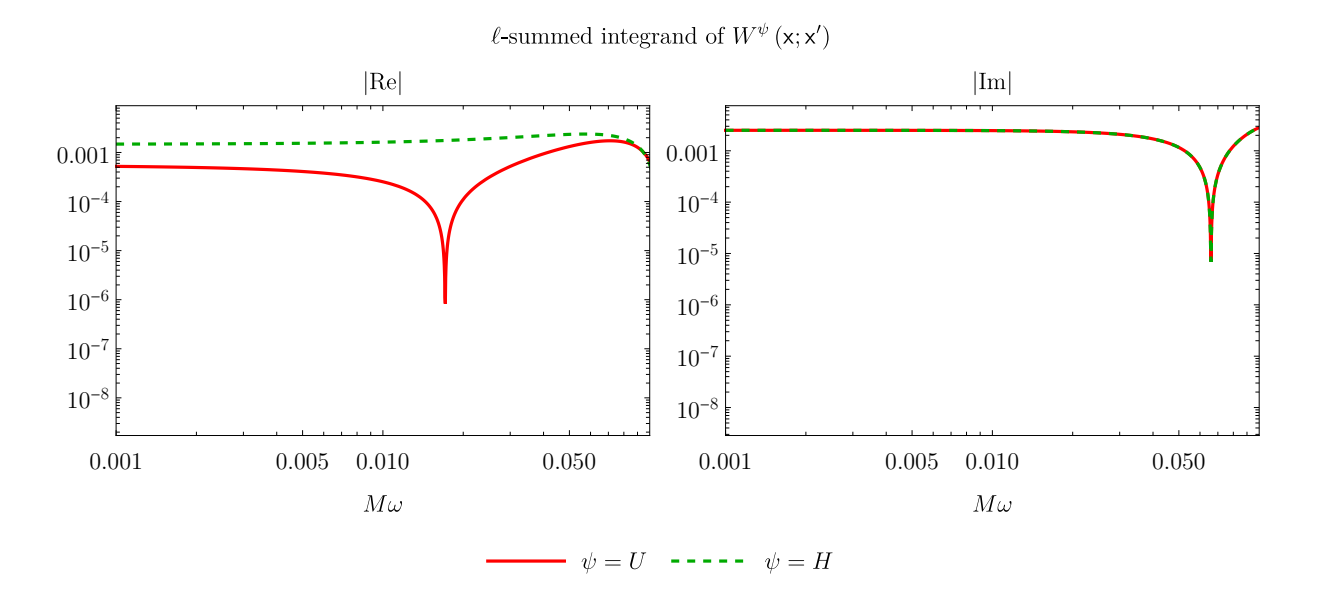


Figure 35 – Log-plots of the absolute values of the real (left) and imaginary (right) parts of the ℓ -summed integrand of W^{ψ} (x; x') as a function of $M\omega$ are presented for the Unruh ($\psi = U$, Equation (5.21)) and Hartle-Hawking ($\psi = H$, Equation (5.22)) states. Here, $\mathbf{x} = (v = 0M, r \approx 0.766M, \theta = 0, \varphi = 0)$, and $\mathbf{x}' = (v' = 25M, r \approx 6.009M, \theta = 0, \varphi = \pi/3)$. As $\omega \to 0$ the real and imaginary parts approach finite values. Notably, the imaginary parts of the plots overlap across all states, which is consistent with the state-independence of the imaginary component of the Wightman function for Hadamard states (including $|U\rangle$, and $|H\rangle$). The relative difference between the imaginary parts of the integrands peaks at $\sim 10^{-13}$ over the plotted frequency range.

of $W^{\psi}(\mathsf{x};\mathsf{x}')$, $\psi \in \{U,H\}$, which tends to finite values as $\omega \to 0$, as demonstrated in Figure 35. We remark that the coincidence limit is, by construction, excluded from this analysis because x is a point inside the horizon and x' is a point outside the horizon.

With convergence established, we compute the Wightman function for the $|U\rangle$ and $|H\rangle$ states across surfaces of constant v' (the outgoing EF-coordinate outside the horizon). This allows us to map correlations between a fixed interior point and multiple exterior points. We fix the base point $\mathbf{x} \in II$ at $(V=1,\,r\approx 0.766M,\,\theta=0,\,\varphi=0)$, and select exterior points $\mathbf{x}'\in I$ with an angular separation $\gamma=\pi/3$ from it. The EF-coordinates u' and v' of \mathbf{x}' are varied as follows: v' spans from -100M to 100M in increments of $\Delta v'=1M$. For each v', u' is determined through $u'=v'-2r'_*$, where r'_* iterates over all values in our dataset. This procedure generates a mesh of 28,743 points, shown as orange dots in Figure 36. The purple dot is the interior point \mathbf{x} .

The magnitude of the imaginary part of the Wightman function for the Unruh state is presented in Figure 37. The corresponding result for the Hartle-Hawking is visually identical and is omitted for this reason. This figure shows two expected features: The first is the decay (w.r.t. v') in $\left| \operatorname{Im} \left[W^U(\mathsf{x},\mathsf{x}') \right] \right|$ as x' moves into the region where it is not causally connected to x . The second is are the singularities tracing the past-directed null

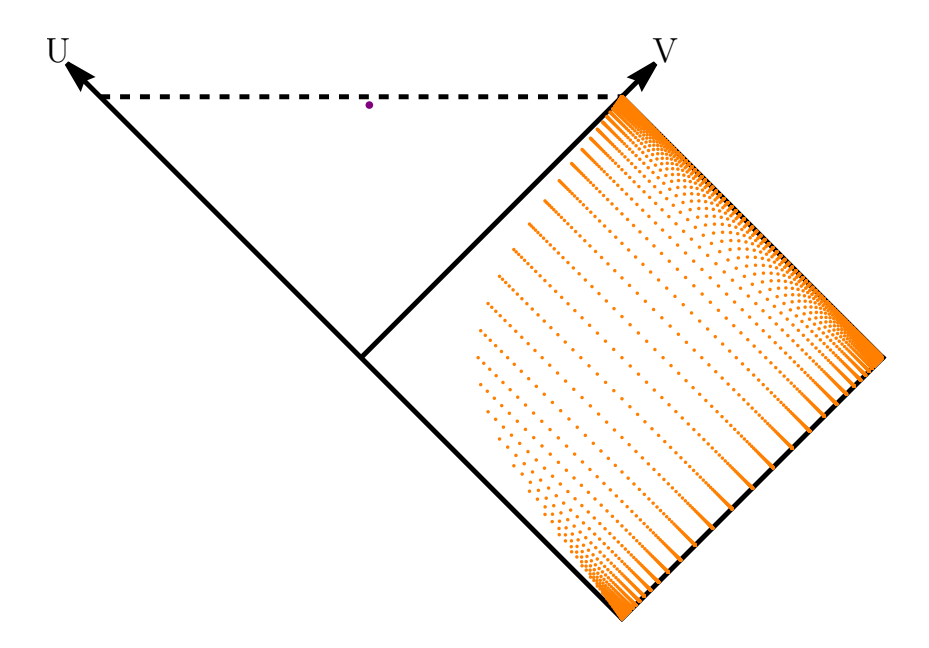


Figure 36 – Penrose diagram showing the mesh of points where $W^{\psi}(\mathbf{x};\mathbf{x}')$, $\psi \in \{B,U,H\}$ will be computed. The fixed interior point \mathbf{x} (purple dot) is located at $(V=1, r \approx 0.766M, \theta=0, \varphi=0)$. The exterior points \mathbf{x}' (orange dots) are parameterized by EF-coordinates v' and $u'=v'-2r'_*$, with v' ranging from -100M to 100M and r'_* spanning all values in our dataset. All \mathbf{x}' points maintain an angular separation of $\gamma=\pi/3$ from \mathbf{x} , hence, no radial null geodesic connects them.

geodesics connecting x and x' after N half-orbits around the horizon (we can see up to N=6).

A more detailed view of the aforementioned features can be seen in Figure 38, where we plot the r' = 6.009M slice of Figure 37, which was produced using a step of $\Delta v' = 0.1M$ to obtain a smoother curve. In that figure we see that for $v' \gtrsim -0.54M$, where x and x' become causally disconnected, $\left|\operatorname{Im}\left[W^{U}\left(\mathsf{x},\mathsf{x}'\right)\right]\right|$ exhibits a sharp exponential decay, stabilizing at $\approx 10^{-6}$. This is in contrast to the well-known property that $\text{Im}\left[W^{U}\left(\mathsf{x},\mathsf{x}'\right)\right]=0$ on noncausally connected points (as can be inferred from its relation with the Retarded and Advanced Green Functions). Such contradiction is expected because we are dealing with a numerical computation that uses cutoff and smoothing techniques. In this context, the $\approx 10^{-6}$ residual value is to be understood as the numerical noise floor of our method. This implies that any signal below $\approx 10^{-6}$ in the $v' \gtrsim -0.54 M$ region is indistinguishable from numerical noise. Adjusting the numerical parameters — such as increasing the cutoff frequency or employing weaker smoothing functions — could sharpen the exponential decay and suppress the noise floor further (albeit with trade-offs detailed in Section 5.1.1). However, these adjustments would not alter the qualitative behavior observed in Figure 38. Nevertheless, this issue does not affect the validity of our results, as no physical signal is theoretically expected in this causally disconnected regime.

Beyond the noise floor issue, this plot also shows an exponential decay in $\left|\operatorname{Im}\left[W^{U}\left(\mathsf{x},\mathsf{x}'\right)\right]\right|$

as x' moves (w.r.t v') deeper into the region where it is causally connected to x. This decay is similar to the one we observe in Figure 30 (which was produced considering both points outside the horizon) and is noticeable slower than the one we observe when x' becomes causally disconnected from x. Such decay in the region of causal connection is a known property of the Retarded Green Function (RGF) of a scalar field in a Schwarzschild spacetime, as presented in [57, Section III.B].

Finally, the singularities we see in Figures 38 and 37 are compatible (in magnitude) with the known singularity structure presented in Equation (3.56). To verify if there is complete compatibility, we repeated the plot from Figure 38 but in a linear scale and using suitable ranges to highlight the form of the singularities. The result is presented in Figure 39 and shows that the predicted singularity structure (Equation (3.56)) is reproduced. We remark that all these conclusions are also valid for the Hartle-Hawking state because the imaginary part of the Wightman function is state independent. We verified that, numerically, the corresponding plots from Figure 39 for the Hartle-Hawking state differs from the ones for the Unruh state by a relative difference of at most 10^{-10} .

The magnitudes of the real part of the Wightman function for $|U\rangle$ and $|H\rangle$ are presented in Figures 40 and 41, respectively. This figures shows the light-crossing tracing the past-directed null geodesics connecting x and x' after N half-orbits around the horizon (as for the imaginary part, we see up to the N=6 singularity). At least as importantly, it also shows that the magnitude of the real part decays symmetrically with increasing |v'/M| from the N=0 singularity. In particular, it does not vanishing (or decay to some noise floor) when x and x' are not causally connected, in contrast to the imaginary part. This is expected since the real part of the Wightman function is related to the field anti-commutator (Equation (3.48)) which need not to vanish on non causally-connected points. What comes as an intriguing surprise (for both $|U\rangle$ and $|H\rangle$) is the sharply localized zero surrounded by two local maxima in the magnitude of the imaginary part of the Wightman function. Before further exploring the regime where x and x' are not causally connected, we will analyze the singularity structure to confirm if it follows the expected 4-fold pattern (Equation (3.55)).

For this task, we plotted the $r' \approx 6.009 M$ slice of Figures 40 and 41, as presented in Figure 42, to show an overall visualization of the singularity structure. In this plot the N=0 singularity has an ambiguous shape that makes it very difficult to tell if it is a P.V.(1/ σ) or a $\delta(\sigma)$. The other singularities in this Figure are compatible with the 4-fold structure from Equation (3.55). What is left to do is verifying if each singularity has the correct sign and resolving the ambiguity in the shape of the N=0 singularity. This task is accomplished by repeating the plots from Figures 40 and 41 on a linear scale, using suitable ranges to highlight each singularity. The result is presented in Figure 43 and confirms that the 4-fold singularity structure is correctly reproduced.

We now begin to explore the regime where where x and x' are not causally connected.

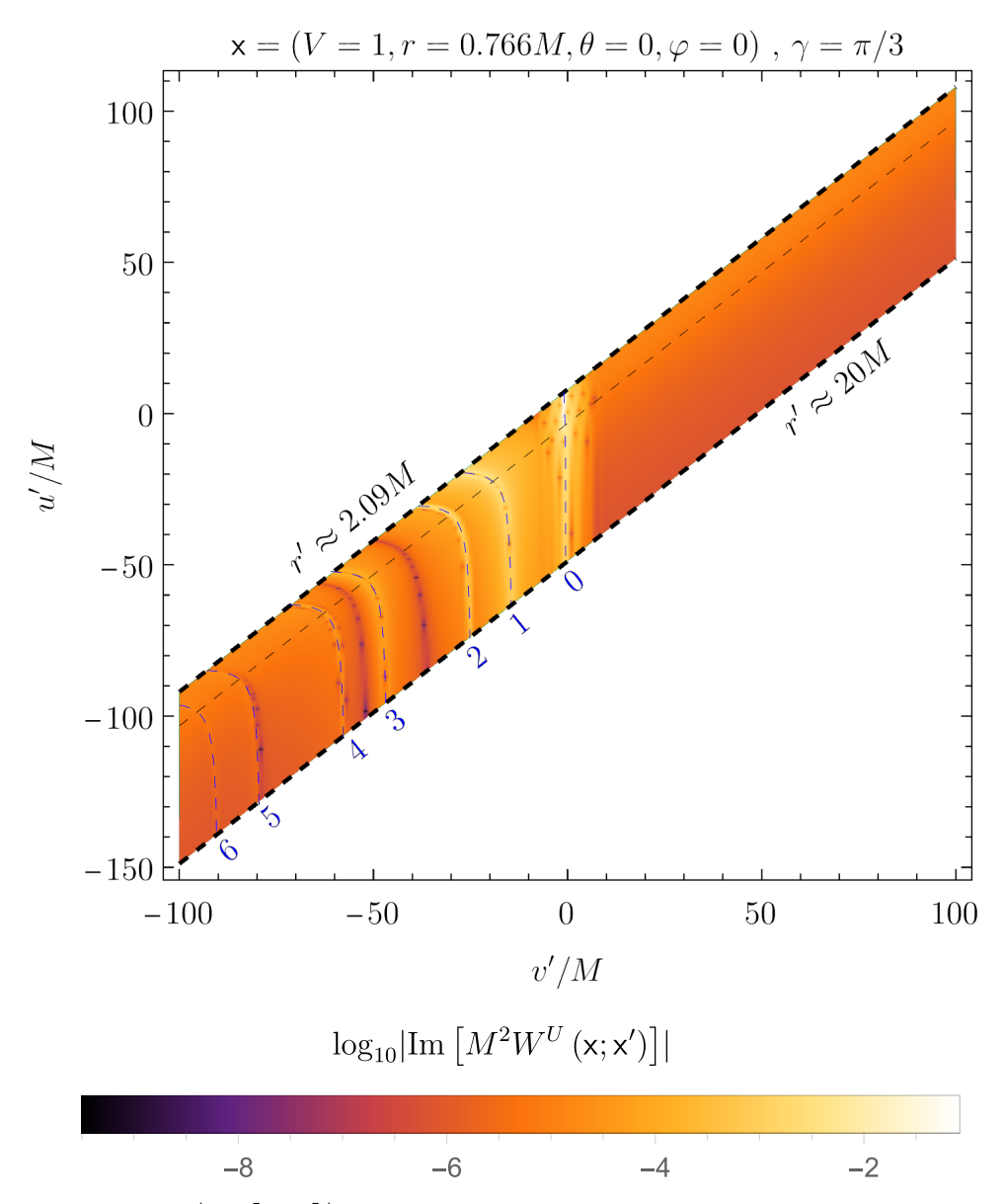


Figure 37 – Plot of $\left|\operatorname{Im}\left[W^U\right]\right|$ with $\mathsf{x}=(V=1,r\approx0.766M,\theta=0,\varphi=0)$ and $\mathsf{x}'=(v',u',\theta=0,\varphi=\pi/3)$ on the points of the mesh represented in Figure 36. The thin black-dashed line is r'=3M, the photonsphere. The thin blue-dashed lines are the points x' connected to x by a (past-directed) null geodesic that completes N (blue numbers) half-orbits around the black hole. The sharp darker curves for v'<0 are the zeroes of the Wightman function. The localized peaks (sharp whiter curves) are manifestations of the singularities that appear when x and x' are light-like connected, i.e., on the thin blue-dashed lines. Note that as v' increases to the right of the N=0 singularity, the magnitude of the imaginary part of the Wightman function decays exponentially (see Figure 38), reflecting the lack of causal connection between these points and x inside the horizon.

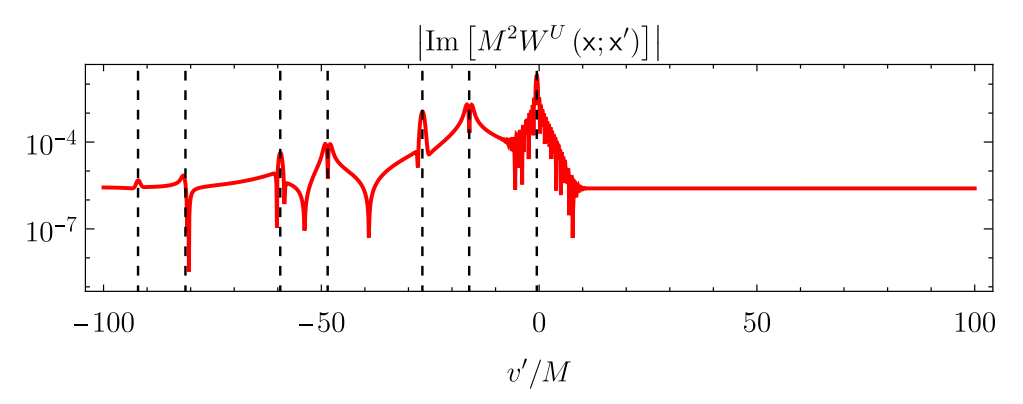


Figure 38 – Log-plot of $\left|\operatorname{Im}\left[W^{U}\right]\right|$ on $\mathbf{x}=(V=1,\,r\approx0.766M,\,\theta=0,\,\varphi=0);\,\mathbf{x}'=0$ $(v', r' \approx 6.009M, \, \theta' = 0, \, \varphi' = \pi/3)$ as a function of v'. For this plot we used a step of $\Delta v' = 0.1M$ for a smoother presentation. The dashed lines represent the values of v' such that x and x' are connected by a null geodesic after finishing N half-orbits around the horizon: The N=0 singularity happens at $v' \approx -0.54M$ and the N = 6 near $v' \approx -92M$. The noticeable decay with increasing |v'/M| is exponential and presents two distinct regimes: For $v' \lesssim 0$ it is slower and reflects diminishing classical correlations with increasing spacetime separation. For $v' \geq 0$ it is much faster (the fact that it is not a sharp, step-like, decay is due to the smoothing scheme and the cut-offs we used, which remove the infinitely large-frequencies and ℓ -modes that would produce such discontinuity) and reflects the fact that for these values of v', x and x' are not causally connected. The N=0 singularity is surrounded by fast oscillations that are likely due to its proximity to the v-coordinate coincidence (v=v'), which increases the difficulty in the convergence of the numerical integral and ℓ -sum. The sharp peaks align with light-like connections between x and x', as discussed in Section 3.4.1.

Our first observation was that in such case, the real part of the Wightman function does not decay to a noise floor (i.e., at a numerical level, it is non-zero), implying that there are correlations in this regime. This is interesting because correlations in the field on causally disconnected points cannot be reproduced in a classical system, meaning that these can be understood as genuinely quantum correlations.

To obtain insights about the overall behavior of these correlations, we plot the real part of the Wightman function for the Unruh and Hartle-Hawking states in several slices of constant r' to analyze the local maxima and the zero in its magnitude (see Figures 41 and 40). The result is presented in Figure 44, where we see a curious behavior for both states: Near the horizon only a local minima is visible but as r' increases, that minima moves towards larger v' and a step-like structure is revealed. The center of such a step-like structure is the sharply localized zero we see in Figures 41 and 40. We are then led to suspect that this zero might have an actual physical interpretation because it consistently follows the step-like structure that was just unveiled.

Continuing the investigation to understand the step-like behavior, we compared the expressions of the Wightman function for the Unruh (Equation (5.21)) and Hartle-Haking

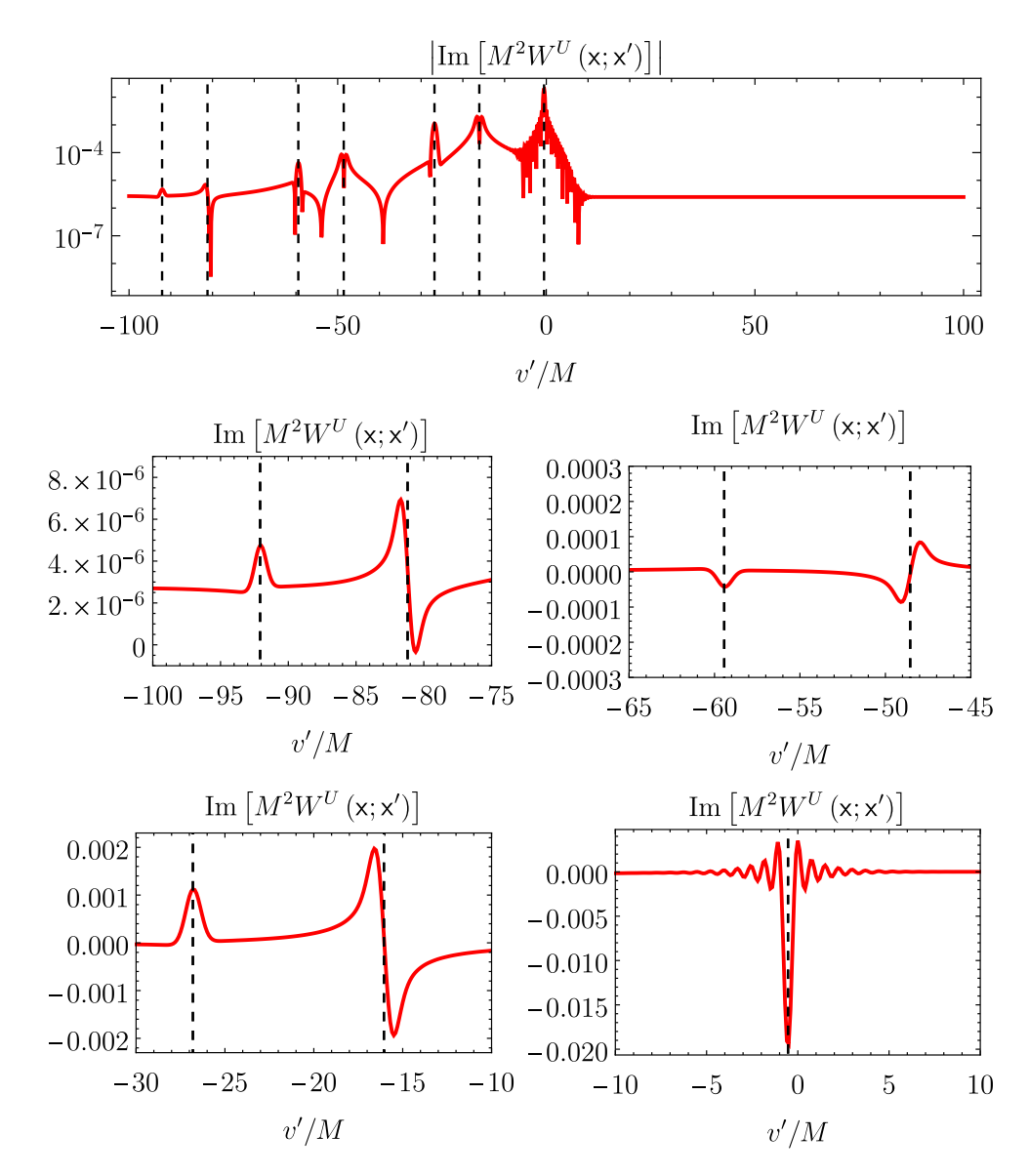


Figure 39 – The imaginary part of the Wightman function on $\mathbf{x}=(V=1,r\approx 0.766M,\,\theta=0,\,\varphi=0)\in II,\,\mathbf{x}'=(v',\,r'\approx 6.009M,\,\theta'=0,\,\varphi'=\pi/3)\in I$ is presented as a function of v'/M. For these plots we used a step of $\Delta v'=0.1M$. First row: The plot from Figure 38 is repeated for reference. Second row: The N=6 and N=5 singularities (left); the N=4 and N=3 singularities (right). Third row: The N=2 and N=1 singularities (left); the N=0 singularity (right). The singularities follow the 4-fold structure from equation (3.56). The small plots showing the singularities are smoother because they were produced using a step-size of $\Delta v=0.1M$ for this purpose.

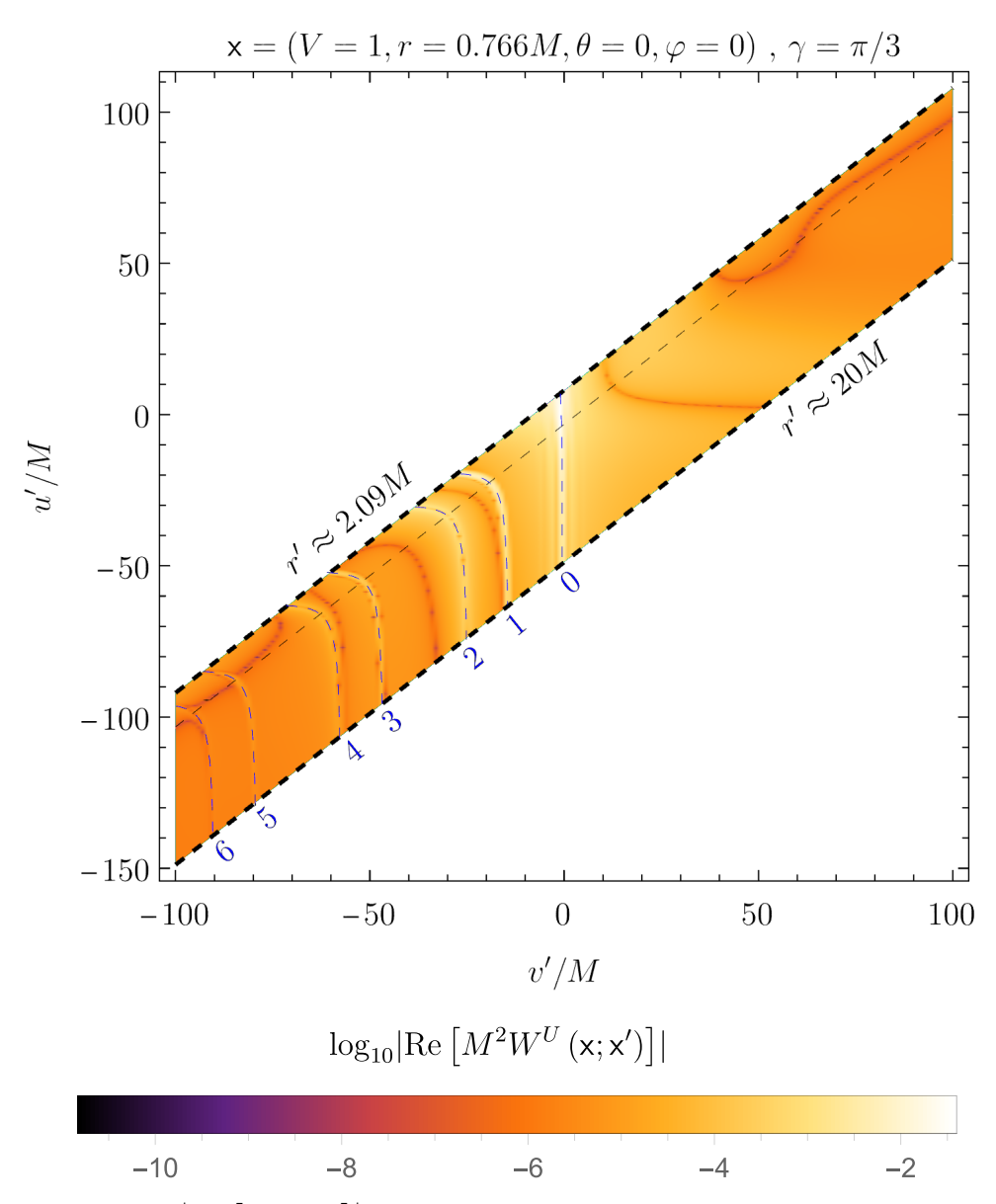


Figure 40 – Plot of $\left| \text{Re} \left[M^2 W^U \right] \right|$ on $\mathsf{x} = (V=1,\,r \approx 0.766M,\,\theta=0,\,\varphi=0)$ separated by an angle of $\gamma=\pi/3$ from all points x' of Figure 36. The thin black-dashed line is r'=3M, the photonsphere. The sharp darker curves are the zeroes of the Wightman function and the sharp whiter curves are peaks in the magnitude of the Wightman function. The thin blue-dashed lines are the points x' connected to x by a (past-directed) null geodesic that completes N (blue numbers) half-orbits around the black hole. Here we see all the features that are also present in the Boulware state (See Figure) with the addition of the N=5 and N=6 singularities. However the behavior in the $v'\gtrsim 0$ region, where x and x' are not causally connected is visually richer when compared to the Boulware state.

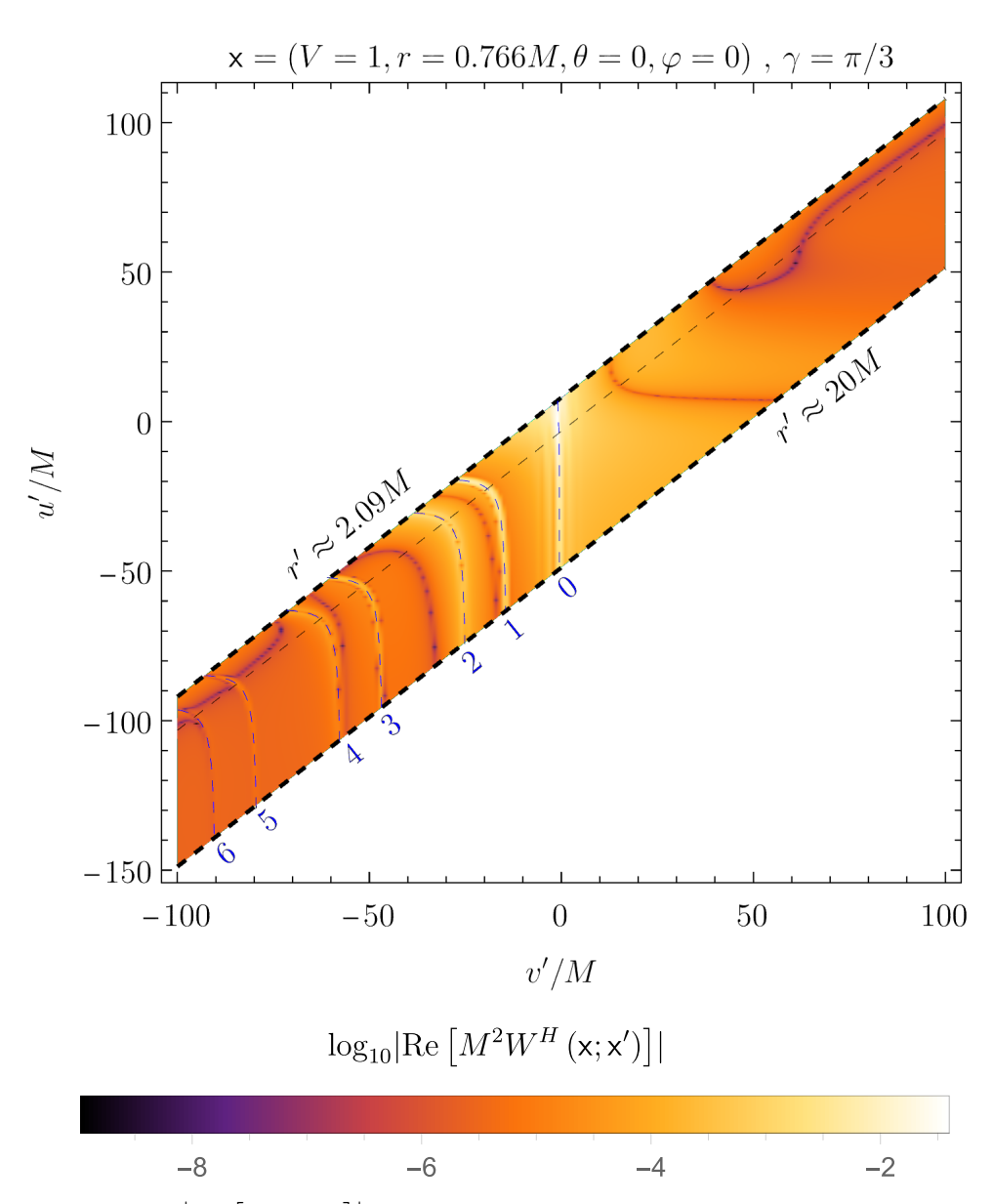


Figure 41 – Plot of $\left|\operatorname{Re}\left[M^2W^H\right]\right|$ on $\mathsf{x}=(V=1,\,r\approx0.766M,\,\theta=0,\,\varphi=0)$ separated by an angle of $\gamma=\pi/3$ from all points x' of Figure 36. The thin black-dashed line is r'=3M, the photonsphere. The sharp darker curves are the zeroes of the Wightman function and the sharp whiter curves are peaks in the magnitude of the Wightman function. The thin blue-dashed lines are the points x' connected to x by a (past-directed) null geodesic that completes N (blue numbers) half-orbits around the black hole. Here we see the same features that are also present in the Unruh state (See Figure 40).

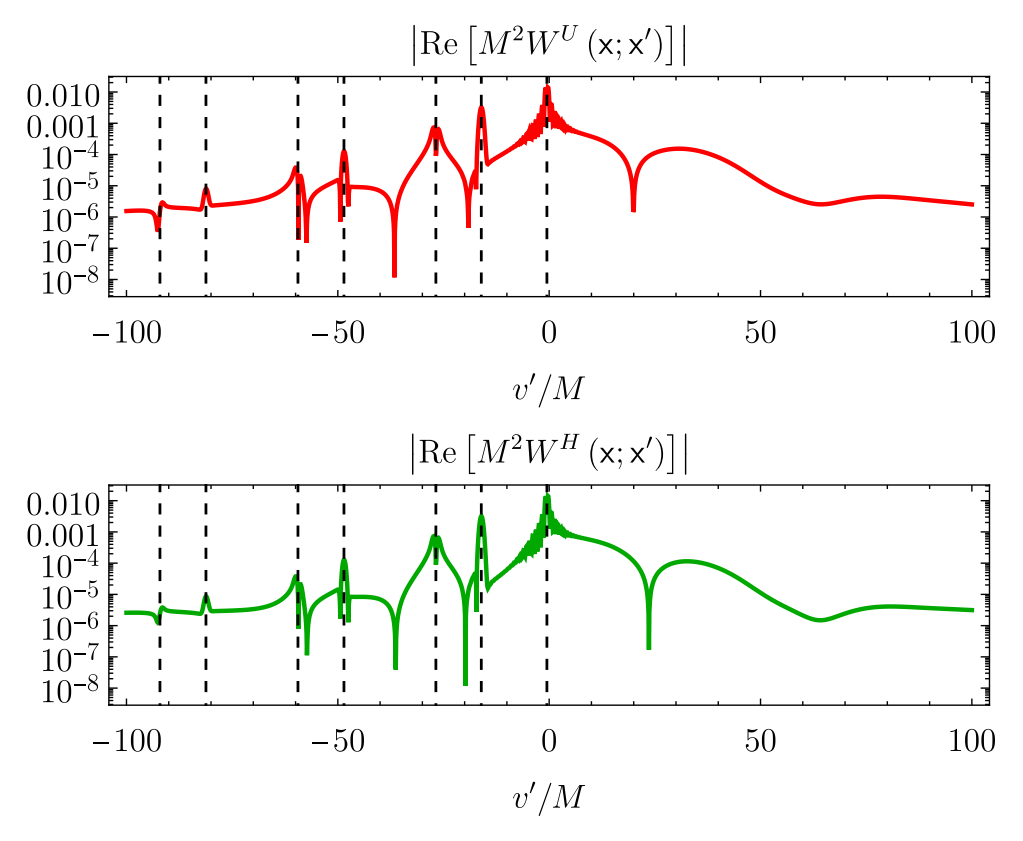


Figure 42 – Log-plot of $\left|\operatorname{Re}\left[W^U\right]\right|$ (top) and $\left|\operatorname{Re}\left[W^H\right]\right|$ (bottom) on $\mathbf{x}=(V=1,\,r\approx0.766M,\,\theta=0,\,\varphi=0);\,\mathbf{x}'=(v',\,r'\approx6.009M,\,\theta'=0,\,\varphi'=\pi/3)$ as a function of v'. For this plot we used a step of $\Delta v'=0.1M$ for a smoother presentation. The dashed lines represent the values of v' such that \mathbf{x} and \mathbf{x}' are connected by a null geodesic after finishing N half-orbits around the horizon: The N=0 singularity happens at $v'\approx-0.54M$ and the N=6 near $v'\approx-92M$. Here the decay with increasing |v'/M| is visually symmetric. The N=0 singularity is surrounded by fast oscillations that are likely due to its proximity to the v-coordinate coincidence (v=v'), which increases the difficulty in the convergence of the numerical integral and ℓ -sum. The sharp peaks align with light-like connections between \mathbf{x} and \mathbf{x}' , as discussed in Section 3.4.1.

(Equation (5.22)) states and noticed that they share a common term:

$$W_{\Delta}(\mathbf{x}, \mathbf{x}') = \frac{1}{(4\pi)^{2}rr'} \sum_{\ell=0}^{\infty} (2\ell+1) P_{\ell}(\cos(\gamma)) \int_{0}^{\infty} \frac{d\omega}{\omega} \frac{1}{\sinh(2\pi r_{s}\omega)} \operatorname{Re}\left[e^{i\omega\Delta t} \frac{\psi_{\omega\ell}^{ins}(r)\bar{\psi}_{\omega\ell}^{up,R}(r')}{\bar{I}_{\omega\ell}}\right]\right],$$

$$\mathbf{x} \in II, \mathbf{x}' \in I.$$
(5.23)

To understand its contrition to the Wightman function, we repeat the plots from Figure 44 but subtracting $W_{\Delta}(x,x')$ from each of them. The result is presented in Figure 45. It shows that the step-like behavior does not appear. More specifically, the result for the Hartle-Hawking state only shows a decaying behavior that stabilizes on a small constant value that varies with r'. The corresponding result for the Unruh state shows a local minimum that spreads across a wider range of v' with increasing r' for then decaying to a

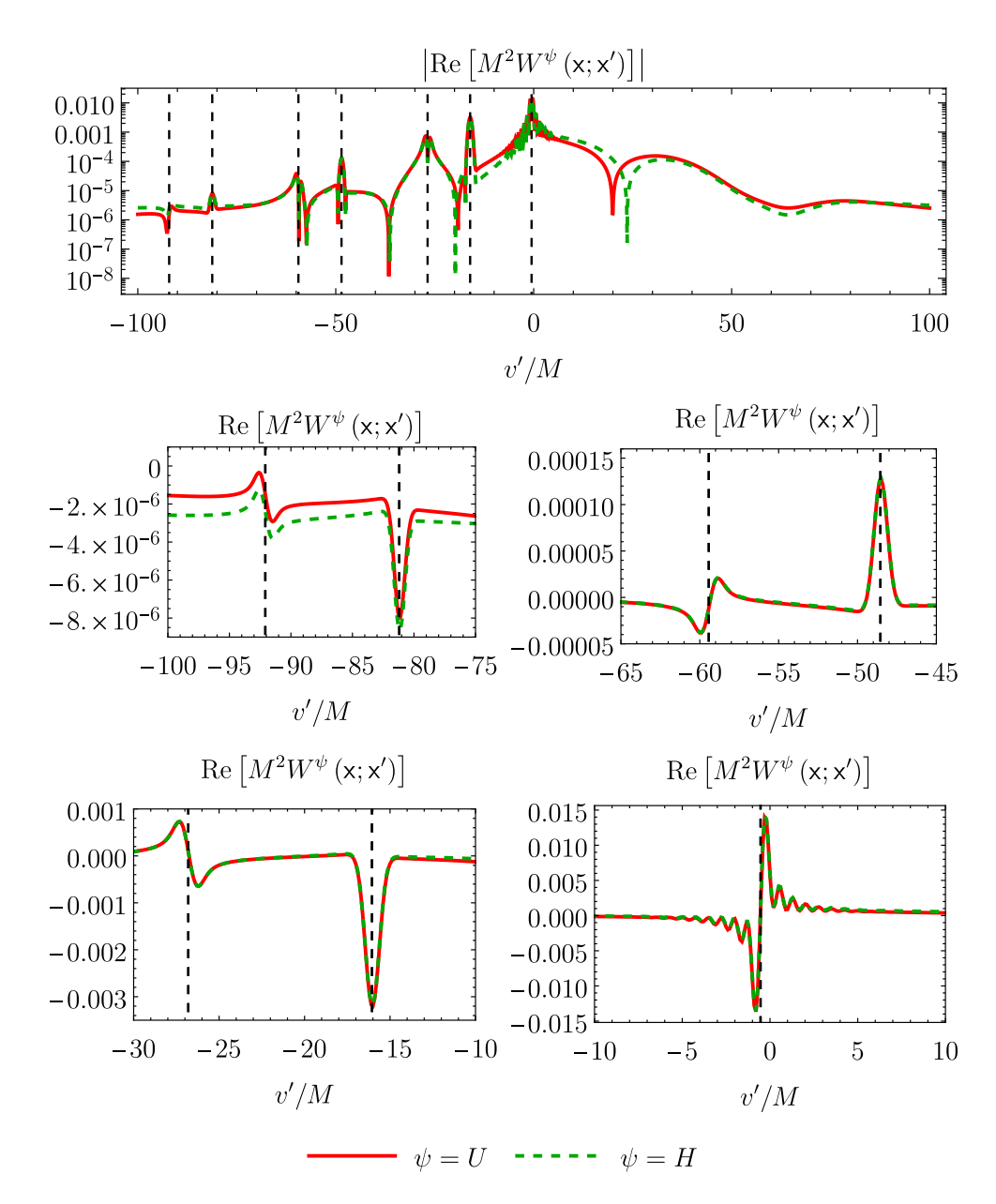


Figure 43 – The real part of the Wightman function for the Unruh (red) and Hartle-Hawking (green dashed) states on $\mathbf{x} = (V = 1, \, r \approx 0.766M, \, \theta = 0, \, \varphi = 0) \in II, \, \mathbf{x}' = (v', \, r' \approx 6.009M, \, \theta' = 0, \, \varphi' = \pi/3) \in I$ is presented as a function of v'/M. For these plots, we used a step of $\Delta v' = 0.1M$. First row: The plots from Figures 40 and 41 are replicated and overleaped for reference. Second row: The N=6 and N=5 singularities (left); the N=4 and N=3 singularities (right). Third row: The N=2 and N=1 singularities (left); the N=0 singularity (right). Here it is clear that the N=0 singularity is the expected P.V. $(1/\sigma)$, hence, the singularities follow the 4-fold structure from equation (3.56).

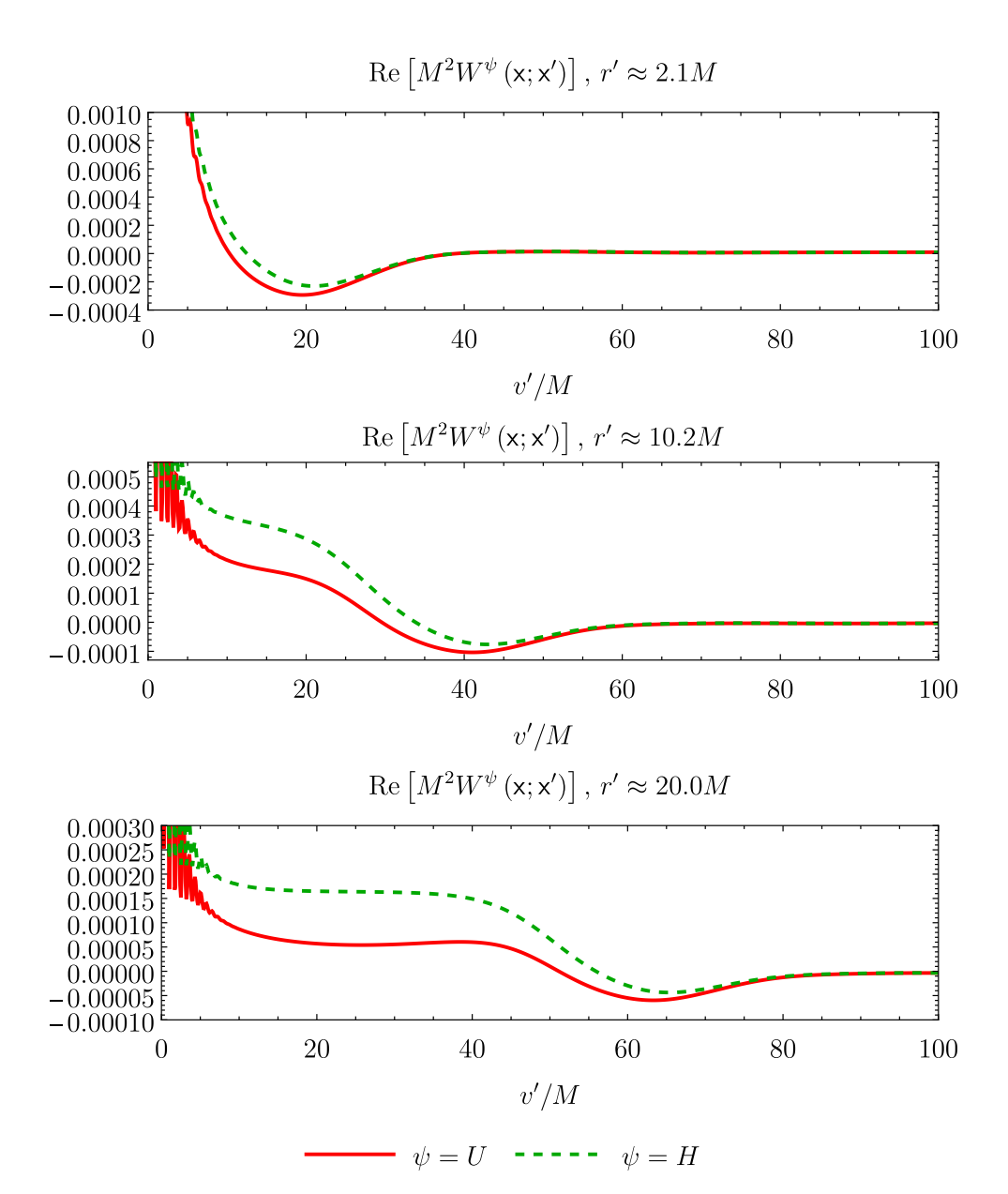


Figure 44 – Plots of Re $\left[M^2W^U\left(\mathbf{x};\mathbf{x}'\right)\right]$ (red) and Re $\left[M^2\left(W^U\left(\mathbf{x};\mathbf{x}'\right)-W_\Delta\left(\mathbf{x},\mathbf{x}'\right)\right)\right]$ (dashed green) as a function of v' on three different slices of constant r': 2.1M (top), 10.2M (middle) and 20.0M (bottom). Here $\mathbf{x}=(V=1,\,r\approx0.766M,\,\theta=0,\,\varphi=0)$ is separated by an angle of $\gamma=\pi/3$ from all points $\mathbf{x}'=(u',\,r',\,\theta=0,\,\varphi=0)$. For this plot we used a step-size of $\Delta v'=0.1M$. For clarity, the plot ranges are adjusted so that only the N=0 singularity is partially visible. Only a shallow local minimum is visible when r' is close to the horizon. On the other hand, as r' increases, the local maxima and minima that we see in Figures 41 and 40 become clearly visible. The combined shape of the local maximum and minima resemble a step-like behavior neighboring a subtle local maximum and a shallow, yet visible, local minimum. In summary, this figures show a stable step-like behavior (surrounded by a local maximum and a minimum) moving towards larger values of r' that only becomes visible once r' is large enough.

small, constant, r'-dependent value. Numerically, that r'-dependent value is the same for both states to a relative difference of 10^{-3} (for the values of r' used in Figure 45). The local minimum in the result for the Unruh state can be attributed to the asymmetric way with which the ingoing and upgoing modes contribute to $W^U(x;x')$.

Before proceeding with the exploration on W_{Δ} (x,x'), we find it important to give a heuristic understanding of the local minimum that appeared in the results for the Unruh state in Figure 45. While being a manifestation of correlations across the horizon, they are the product of the interference between the $\tilde{f}_{\omega\ell}^{\text{up,R}}$, $\tilde{f}_{\omega\ell}^{\text{in,R}}$ and $\tilde{f}_{\omega\ell}^{\text{R}}$ modes as can be seen in Equation (3.84). The initial data defining $\tilde{f}_{\omega\ell}^{\text{up,R}}$ and $\tilde{f}_{\omega\ell}^{\text{in,R}}$ has support on $\mathcal{H}_R^- \cup \mathscr{I}_R^-$ (see Equations (3.28) and (3.29)). On the other hand, the initial data defining $\tilde{f}_{\omega\ell}^{\text{R}}$ has support on \mathcal{H}_R^+ but one can trace it back to $\mathcal{H}_R^- \cup \mathscr{I}_R^-$. Therefore, the information encoded in the correlations that produced the local minimum can be traced back to $\mathcal{H}_R^- \cup \mathscr{I}_R^-$. Hence, in this case, the correlations we see between the field on x and x' have its origin in dynamical effects (such as the scattering by the effective potential from Equation (4.2)) during the propagation of the modes from $\mathcal{H}_R^- \cup \mathscr{I}_R^-$ towards the singularity at r=0 and \mathscr{I}_R^+ . In summary, these correlations are not encoded in the initial conditions and are dynamically generated.

We now return to the exploration of $W_{\Delta}(\mathsf{x},\mathsf{x}')$. By comparing Figures 44 and 45 we can conclude that the step-like behavior is produced by $W_{\Delta}(\mathsf{x},\mathsf{x}')$. This term encodes intrinsically quantum features that are independent of the classical spacetime geometry. Specifically, no information about $W_{\Delta}(\mathsf{x},\mathsf{x}')$ is captured by the Retarded (RGF) or Advanced (AGF) Green Functions — quantities fully determined by the classical spacetime geometry. This distinction arises because the RGF and AGF are encoded in the imaginary part of the Wightman function (via the field commutator), while $W_{\Delta}(\mathsf{x},\mathsf{x}')$ contributes exclusively to the real part.

To obtain additional insight about $W_{\Delta}(x,x')$, we work backwards from equation (5.21) to write it as

$$W_{\Delta}(\mathbf{x}, \mathbf{x}') = \frac{1}{(4\pi)^2 r r'} \sum_{\ell=0}^{\infty} (2\ell+1) P_{\ell}(\cos(\gamma)) \int_{0}^{\infty} \frac{\mathrm{d}\omega}{\omega} \frac{1}{\sinh(2\pi r_s \omega)} \mathrm{Re} \Big[\tilde{\mathbf{f}}_{\omega\ell}^{\mathrm{L}}(\mathbf{x}) \tilde{\mathbf{f}}_{\omega\ell}^{\mathrm{up,R}}(\mathbf{x}') \Big] \Big],$$

$$\mathbf{x} \in II, \mathbf{x}' \in I.$$
(5.24)

This expression reveals that this term carries correlations between two modes: $\tilde{\mathbf{f}}_{\omega\ell}^{\mathbf{L}}$, which is defined by initial conditions on \mathcal{H}_L^+ (see Equation (3.33)) that cannot be traced back to region I; and $\tilde{\mathbf{f}}_{\omega\ell}^{\mathrm{up},\mathrm{R}}$ which is defined by initial conditions on \mathcal{H}_R^- (see Equation (3.29)). Hence, $W_{\Delta}(\mathbf{x},\mathbf{x}')$ carries correlations between a field mode that originates inside the horizon (and cannot be traced outside because it never crosses the horizon) and another that originates outside the horizon. Moreover, the prescription (Equation (3.34)) used to defined the modes on region III implies the existence of correlations. In summary, the correlations

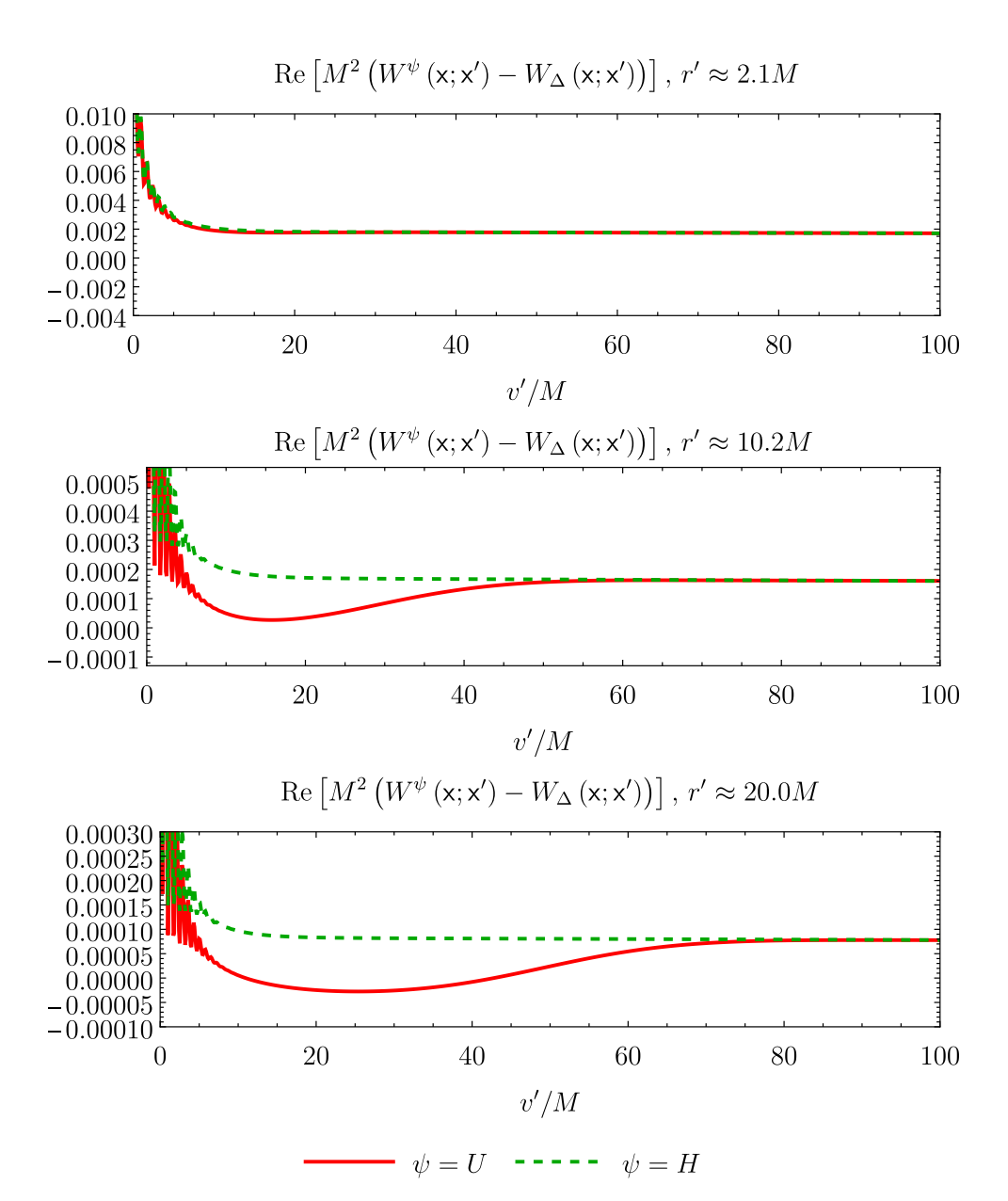


Figure 45 – Re $\left[M^2\left(W^\psi\left(\mathbf{x};\mathbf{x}'\right)-W_\Delta\left(\mathbf{x},\mathbf{x}'\right)\right)\right]$ for the Unruh (red) Hartle-Hawking (dashed green) states is plotted as a function of v' on three different slices of constant \mathbf{r}' : 2.1M (top), 10.2M (middle) and 20.0M (bottom). Here $\mathbf{x}=(V=1,\,r\approx0.766M,\,\theta=0,\,\varphi=0)$ is separated by an angle of $\gamma=\pi/3$ from all points $\mathbf{x}'=(u',\,r',\,\theta=0,\,\varphi=0)$. For this plot we used a step-size of $\Delta v'=0.1M$. For clarity, the plot ranges are adjusted so that only the N=0 singularity is partially visible. The step-like structure from Figure 44 does not appear. The plot for the Hartle-Hawking state shows no visible structure other than a decaying behavior that stabilizes at a small constant value that varies with r'. The corresponding plot for the Unruh state shows a local minimum that spreads across a wider range of v' with increasing r'. This local minimum can be attributed to the asymmetric way with which the ingoing and upgoing modes contribute to $W^U\left(\mathbf{x};\mathbf{x}'\right)$.

encoded in $W_{\Delta}(\mathsf{x},\mathsf{x}')$ are, at least partially, encoded in the boundary conditions defining $\tilde{\mathbf{f}}_{\omega\ell}^{\mathrm{L}}$ and $\tilde{\mathbf{f}}_{\omega\ell}^{\mathrm{up},\mathrm{R}}$.

Furthermore, the $\sinh{(2\pi r_s \omega)}^{-1}$ factor in Equation (5.24) exponentially dampens the large-frequency modes which are just oscillations with unit amplitude in that regime since the effective potential from equation (4.2) can be neglected for large-frequencies. Therefore, the main contributions to $W_{\Delta}(\mathbf{x}, \mathbf{x}')$ come from low-frequency modes. This is significant because the mode $\tilde{\mathbf{f}}_{\omega\ell}^{\mathrm{up},R}$, which propagates from the horizon \mathcal{H}_R^- towards \mathscr{I}_R^+ , undergoes partial scattering towards \mathcal{H}_R^+ . This scattering is governed by the effective potential from Equation (4.3), which vanishes at the horizon and peaks near the photonsphere (r=3M).

Consequently, low-frequency $\tilde{\mathbf{f}}_{\omega\ell}^{\mathrm{up,R}}$ modes outside the horizon are predominantly confined in the region $r_s < r < 3M$. This confinement implies that the correlations encoded in $W_{\Delta}(\mathbf{x}, \mathbf{x}')$ should be stronger in this region and should decay with increasing r.

As a final observation before computing this term, we note that it can be expressed as

$$W_{\Delta}(\mathsf{x},\mathsf{x}') = \frac{1}{(4\pi)^{2}rr'} \sum_{\ell=0}^{\infty} (2\ell+1) P_{\ell}(\cos(\gamma)) \int_{0}^{\infty} \frac{\mathrm{d}\omega}{\omega} \frac{1}{2\sinh(2\pi r_{s}\omega)}$$

$$\times \left(\tilde{\mathsf{f}}_{\omega\ell}^{\mathrm{up},\mathrm{L}*}(\mathsf{x})\tilde{\mathsf{f}}_{\omega\ell}^{\mathrm{up},\mathrm{R}*}(\mathsf{x}') + \tilde{\mathsf{f}}_{\omega\ell}^{\mathrm{up},\mathrm{L}}(\mathsf{x})\tilde{\mathsf{f}}_{\omega\ell}^{\mathrm{up},\mathrm{R}}(\mathsf{x}')\right), \, \mathsf{x} \in II, \, \mathsf{x}' \in I.$$

$$(5.25)$$

The first term in the summation originates from $\tilde{\mathbf{f}}_{\omega\ell}^{\mathrm{UP}}(\mathsf{x})\tilde{\mathbf{f}}_{\omega\ell}^{\mathrm{UP}}(\mathsf{x}')$, while the second term arises from $\tilde{\mathbf{f}}_{\omega\ell}^{\mathrm{UP}}(\mathsf{x})\tilde{\mathbf{f}}_{\omega\ell}^{\mathrm{UP}}(\mathsf{x}')$. Hence, these correlations are inherent to $\tilde{\mathbf{f}}_{\omega\ell}^{\mathrm{UP}}$ and $\tilde{\mathbf{f}}_{\omega\ell}^{\mathrm{UP}}$, as dictated by the prescription from Equation (3.34) for defining Boulware modes in region *III*. Thus, $W_{\Delta}(\mathsf{x},\mathsf{x}')$ encodes correlations between the $\tilde{\mathbf{f}}_{\omega\ell}^{\mathrm{UP}}$ and $\tilde{\mathbf{f}}_{\omega\ell}^{\mathrm{UP}}$ modes. Summarizing, $W_{\Delta}(\mathsf{x},\mathsf{x}')$ encodes correlations across the horizon between the $\tilde{\mathbf{f}}_{\omega\ell}^{\mathrm{UP}}$ and $\tilde{\mathbf{f}}_{\omega\ell}^{\mathrm{UP}}$ modes that are expected to decay with increasing r' from the horizon.

We now analyze $W_{\Delta}(\mathbf{x}, \mathbf{x}')$ numerically. First, we compute $\log_{10} |W_{\Delta}(\mathbf{x}, \mathbf{x}')|$ as a function of \mathbf{x}' , as shown in Figure 46. There we see the expected decay with increasing r' and a sharply localized zero contour that visually tracks a line of constant u'. It is also important to note that on surfaces of constant r', $W_{\Delta}(\mathbf{x}, \mathbf{x}')$ has roughly the same order of magnitude, except around the zero. In Figure 47 we plot the u' coordinate of the zero as a function of its v' coordinate. It shows that its locus seems to move towards some constant u' with increasing v' but we are not able to conclusively tell if it is moving towards $u' = -\bar{u} = 0.4M$, $u' = \bar{u} = -0.4M$ or u' = 0M. To resolve this ambiguity, we evaluated $W_{\Delta}(\mathbf{x}, \mathbf{x}')$ but with $\mathbf{x} = (V = 3, \, r \approx 0.766M, \, \theta = 0, \, \varphi = 0)$, i.e., we changed the V coordinate of \mathbf{x} from V = 1 to V = 3, which changed \bar{u} from -0.4M to $\approx -4.8M$. This allowed us to observe, although inconclusively, that the zero moves towards some some constant u' which is arguably close to $\bar{u} = -\bar{u} = 4.8M$ as shown in Figure 48.

To investigate further, we computed $W_{\Delta}(\mathsf{x},\mathsf{x}')$ as a function of x' , as shown in Figure 49. This shows that the zero of $W_{\Delta}(\mathsf{x},\mathsf{x}')$ traces the center of a smooth, step-like transition from positive values (below the zero) to negative values (above the zero). To obtain a closer view of this behavior we plotted $W_{\Delta}(\mathsf{x},\mathsf{x}')$ as a function of x' on different surfaces

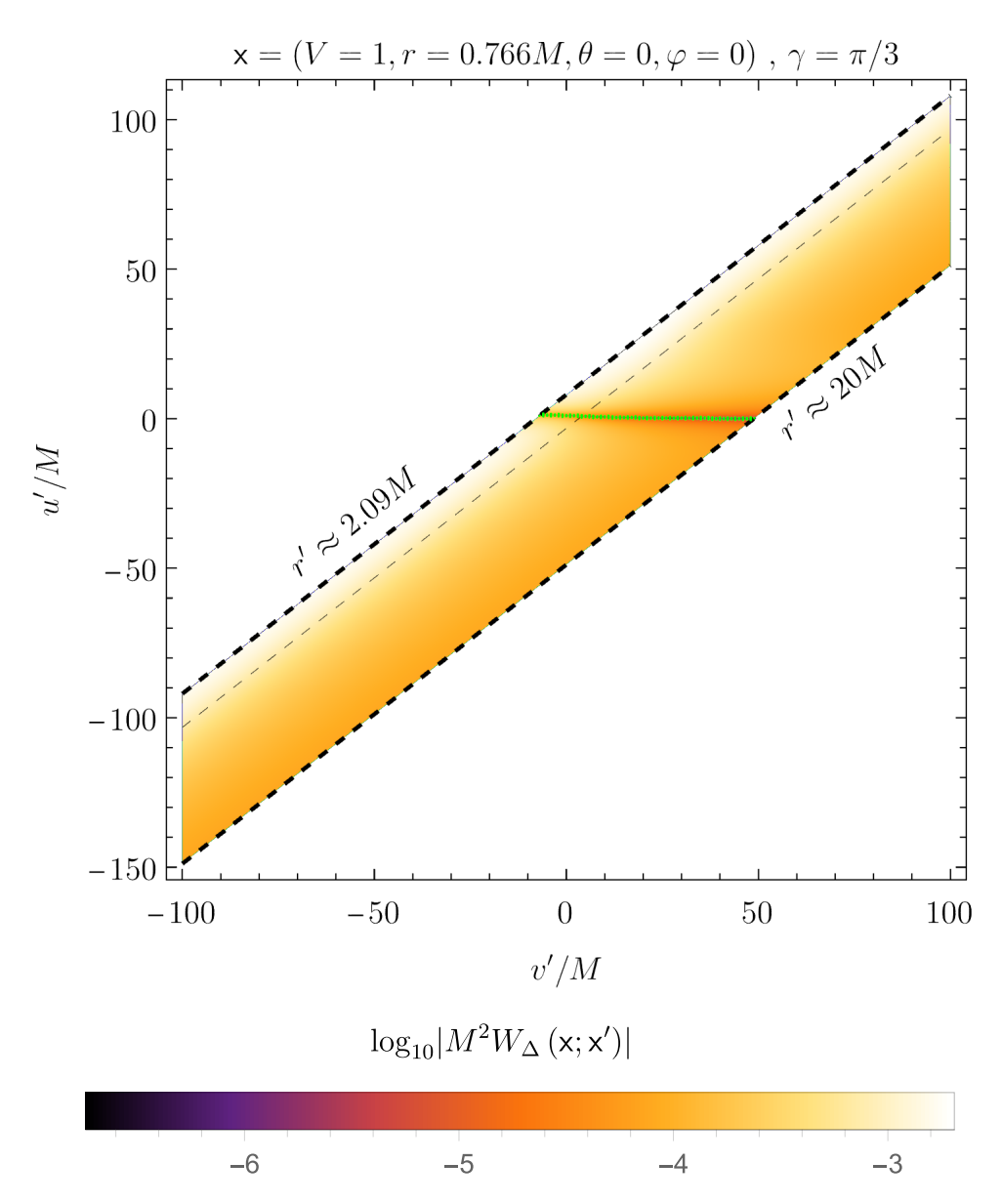


Figure 46 – Plot of $|W_{\Delta}(\mathsf{x},\mathsf{x}')|$ on $\mathsf{x} = (V = 1,\, r \approx 0.766M,\, \theta = 0,\, \varphi = 0)$ separated by an angle of $\gamma = \pi/3$ from all points x' of Figure 36. The thin black-dashed line is r' = 3M, the photonsphere. The green dots mark the points x' where $|W_{\Delta}(\mathsf{x},\mathsf{x}')| = 0$ (and the logarithm becomes a large negative number). These points were numerically checked to track a curve that travels from $u' > \bar{u} = 0.4M$ towards some constant value of u'. Unfortunately, as can be seen in Figure 47, here it is unclear if the zero is moving towards $u' = -\bar{u} = 0.4M$, $u' = \bar{u} = -0.4M$ or u' = 0M. Other than the zero, there is a clear decaying behavior with increasing r'.

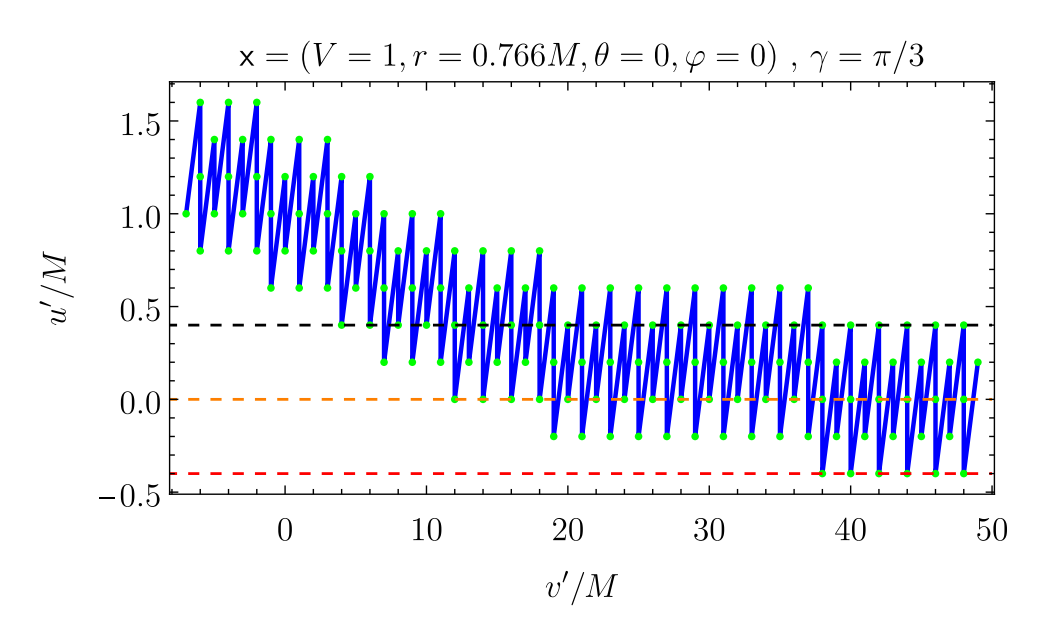


Figure 47 – The track of the zero in the magnitude of $W_{\Delta}(\mathsf{x},\mathsf{x}')$ at V=0. The green dots are the points where the zero appears. For clarity, they are joined by straight blue lines. It is unclear if the zeroes are moving towards $u'=-\bar{u}=0.4M$ (black dashed line), $u'=\bar{u}=-0.4M$ (red dashed line) or u'=0M (orange dashed line), since it is oscillating around these values.

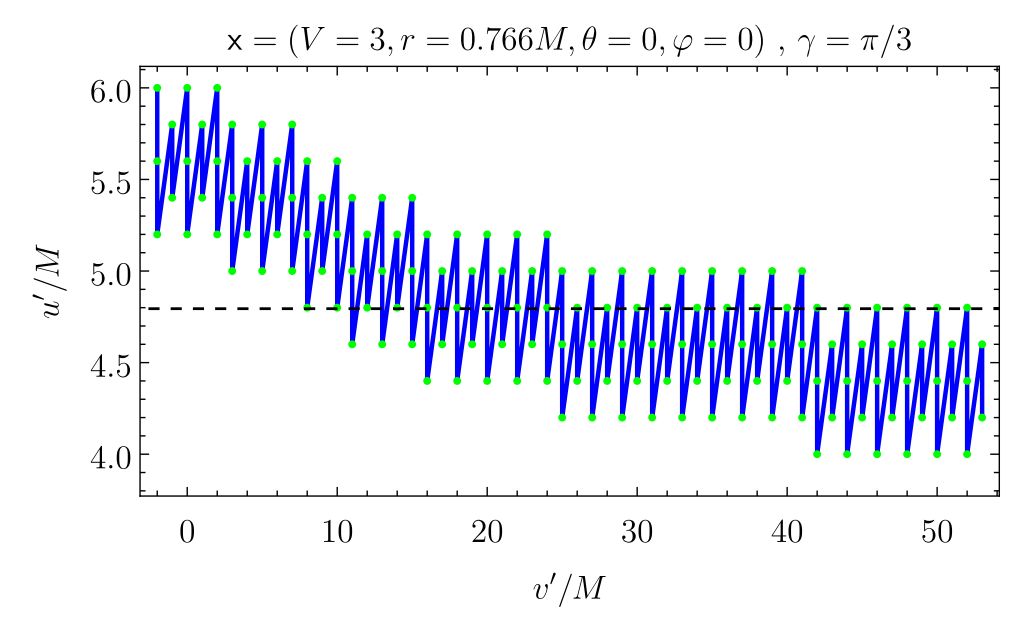


Figure 48 – The track of the zero in the magnitude (the middle of the step-like structure) of $W_{\Delta}(\mathsf{x},\mathsf{x}')$ with x at V=3. The green dots are the points where the zero appears. For clarity, they are joined by straight blue lines. Their behavior suggest, although inconclusively, that the zero moves towards some constant u', which, as far as the domain of this plot is considered, oscillates around $u' \approx 4.4 M$, arguably close to $u' = -\bar{u} = 4.8 M$ (black dashed line).

of constant r', as shown in Figure 50. This figure shows that this term presents a step-like behavior surround by a subtle local maximum and a pronounced local minimum. The height of such step as well as the amplitude of the local minimum decay with increasing r'. We also verified, as seen in the same figure, that the r'-dependence is not completely encoded in the $(rr')^{-1}$ factor Equation (5.23). In Figure 51 we repeated these plots but as a function of v' instead of u'. While complementing Figure 50 by presenting a different point of view, it shows no new effects.

In summary, $W_{\Delta}(\mathbf{x}, \mathbf{x}')$ encodes non-local correlations between modes originating on opposite sides of the event horizon. These correlations decay with increasing r' (the r-coordinate of the outside point) from r_s , being stronger near the horizon and diminishing outwards. Overall, they present a step-like transition near $u' = -\bar{u}$ (\bar{u} is the EF-coordinate of the inside point) as well as the subtle local minimum and visible local maximum. That local minimum becomes more pronounced with respect to the step-like behavior as r' increases. This hints that such a local minimum can be associated to scattering by the effective potential (Equation (4.3)): It is zero at the horizon and peaks near the photonsphere, therefore, scattering effects become increasingly stronger as r' increases from the horizon up to 3M, near its peak. For larger r', these effects become less important as the effective potential asymptotes to zero. Therefore, we can understand that as r' increases, the effect of the effective potential accumulates and becomes close to its peak as soon as $r' \gtrsim 3M$. This is in line with the local minima becoming increasingly visible as r' increases from 2.1M to 2.5M and roughly stabilizing for the larger values of r' in the bottom plot of Figure 50.

The sharp localization of this transition near $u' = -\bar{u}$ implies that $\partial_{u'}W_{\Delta}(x,x')$ and $\partial_u W_{\Delta}(x,x')$ will exhibit localized correlations propagating near $u' = -\bar{u}$. This mirrors results reported in Refs. [10] and [58] for (1+1)D Schwarzschild black holes, where analogous derivative structures were tied to outgoing null trajectories. On the other hand, the local minimum is a new structure that we conjectured to be associated to the effective potential. This hypothesis would also explain why we do not see such effect in (1+1)D: In that case, the field modes propagate as free waves.

In the full Wightman function $W^{\psi}(\mathbf{x}; \mathbf{x}')$, the contribution of $W_{\Delta}(\mathbf{x}, \mathbf{x}')$ to the Hartle-Hawking and Unruh states is subtle due to its small magnitude relative to the N=0 singularity. When r' is near the horizon, $W_{\Delta}(\mathbf{x}, \mathbf{x}')$ manifests itselfs as a shallow local minimum at u'-values slightly larger than the one where the N=0 singularity appears. In this regime, the intensity of the singularity obscures the step-like transition of $W_{\Delta}(\mathbf{x}, \mathbf{x}')$.

However, for larger r', the N=0 singularity decays significantly earlier as a function of u'. This allows the step-like transition of $W_{\Delta}(\mathbf{x}, \mathbf{x}')$ to emerge distinctly, as the singularity no longer dominates the local structure of the Wightman function. These contrasting behaviors are illustrated for the Unruh state in Figure 52 and for the Hartle-Hawking state in Figure 53.

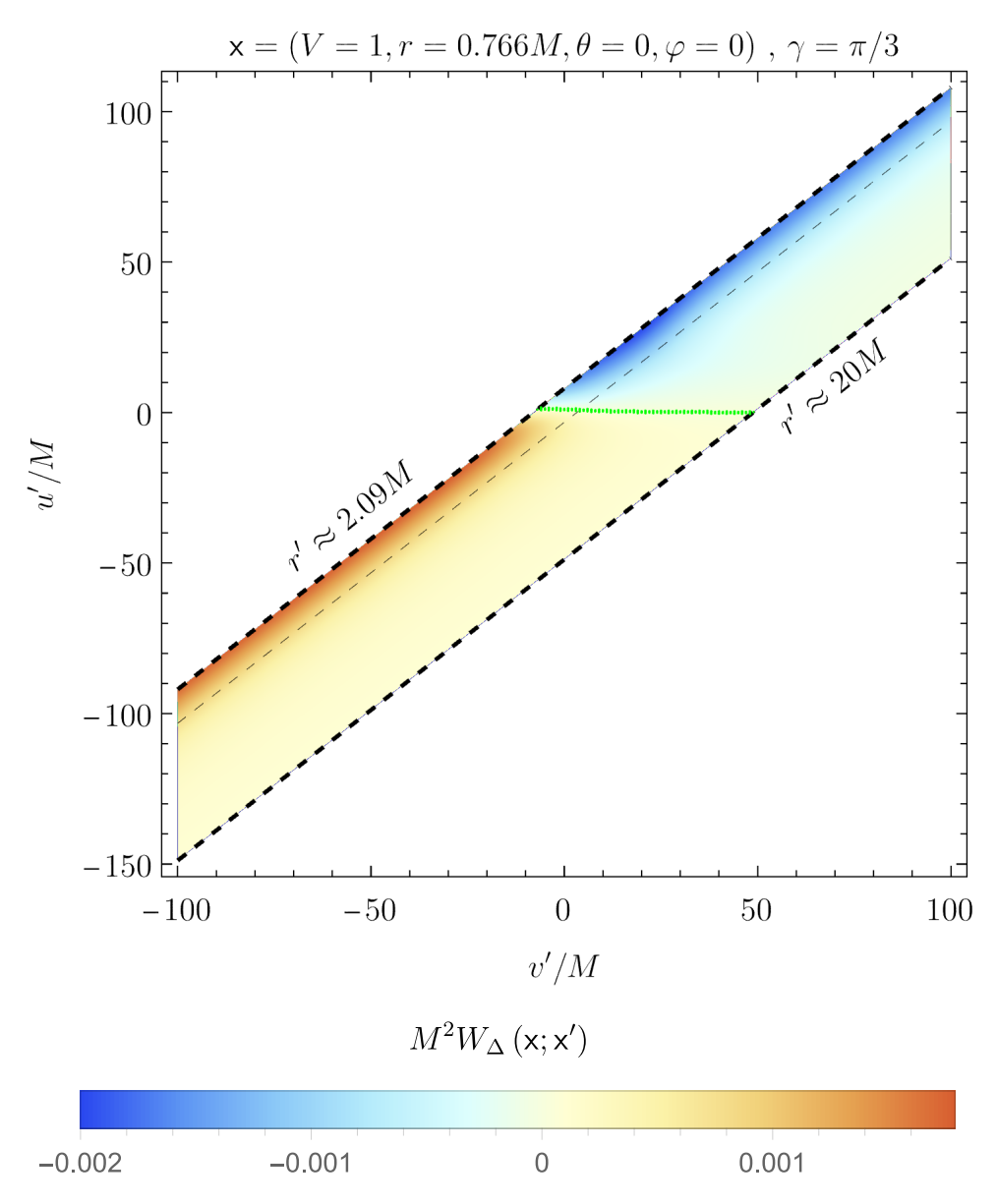


Figure 49 – Plot of $W_{\Delta}(\mathbf{x}, \mathbf{x}')$ as a function of v'/M and u'/M. Here we fixed $\mathbf{x} = (V = 1, r \approx 0.766M, \theta = 0, \varphi = 0)$ and varied $\mathbf{x} = (v', r'\theta = 0, \varphi = \pi/3)$ across all points of the mesh in Figure 36. The thin black-dashed line is r' = 3M, the photonsphere. The green dots mark the points \mathbf{x}' where $W_{\Delta}(\mathbf{x}, \mathbf{x}') = 0$. Here it is clear that this zero marks the transition between positive and negative values of $W_{\Delta}(\mathbf{x}, \mathbf{x}')$: For u' above the zero, it is negative while for u' below the zero, it is positive. The center of such transition (the zero) seems to travel from $u' > \bar{u}$ towards a constant value of $u' \approx -\bar{u} = -0.4M$ with increasing v' (as inferred from Figure 48).

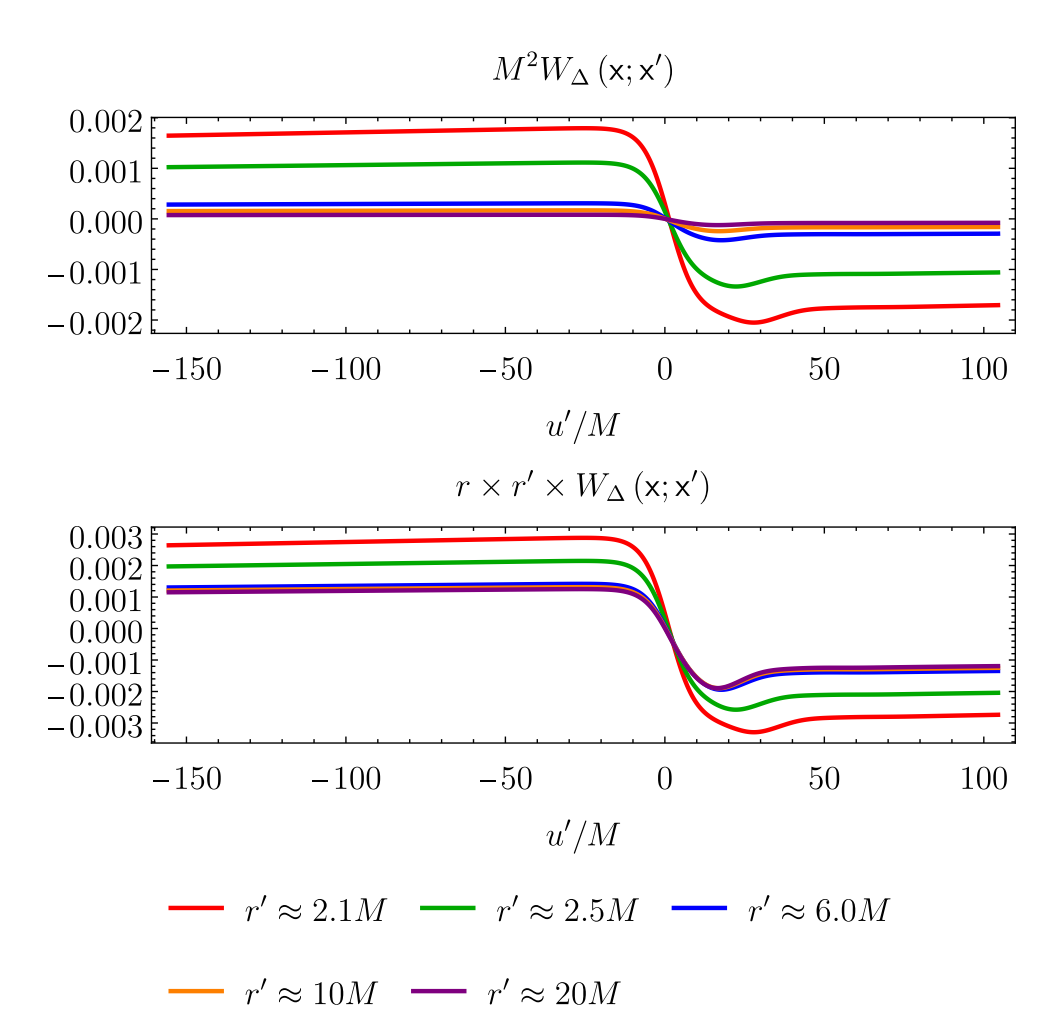


Figure 50 – $W_{\Delta}(\mathbf{x},\mathbf{x}')$ with $\mathbf{x}=(V=1,r\approx0.766M,\theta=0,\varphi=0)$ separated by an angle of $\gamma=\pi/3$ from all points $\mathbf{x}'=(v',r',\theta=0,\varphi=0)$ is plotted as a function of u' (top) plot for $r'\approx2.1M$ (red), $r'\approx2.52M$ (green), $r'\approx6.009M$ (blue), $r'\approx10M$ (blue) and $r'\approx20M$ (purple). The bottom plot shows $rr'\times W_{\Delta}(\mathbf{x},\mathbf{x}')$ for the same setup. The zeroes seem to approach $u'\approx-\bar{u}=-0.4M$ (as inferred from Figure 48) with increasing r' (Figures 47 and 48). In all cases we see a step-like behavior which is surrounded by a subtle local maxima and a visible local minima. The height of the step as well as the amplitude of the local minimum diminish with increasing r'. The bottom plot shows that there is r-dependence beyond the $(rr')^{-1}$ factor from Equation (5.23) and that such r'-dependence makes these curves asymptote towards a possible $r'\to\infty$ limit.

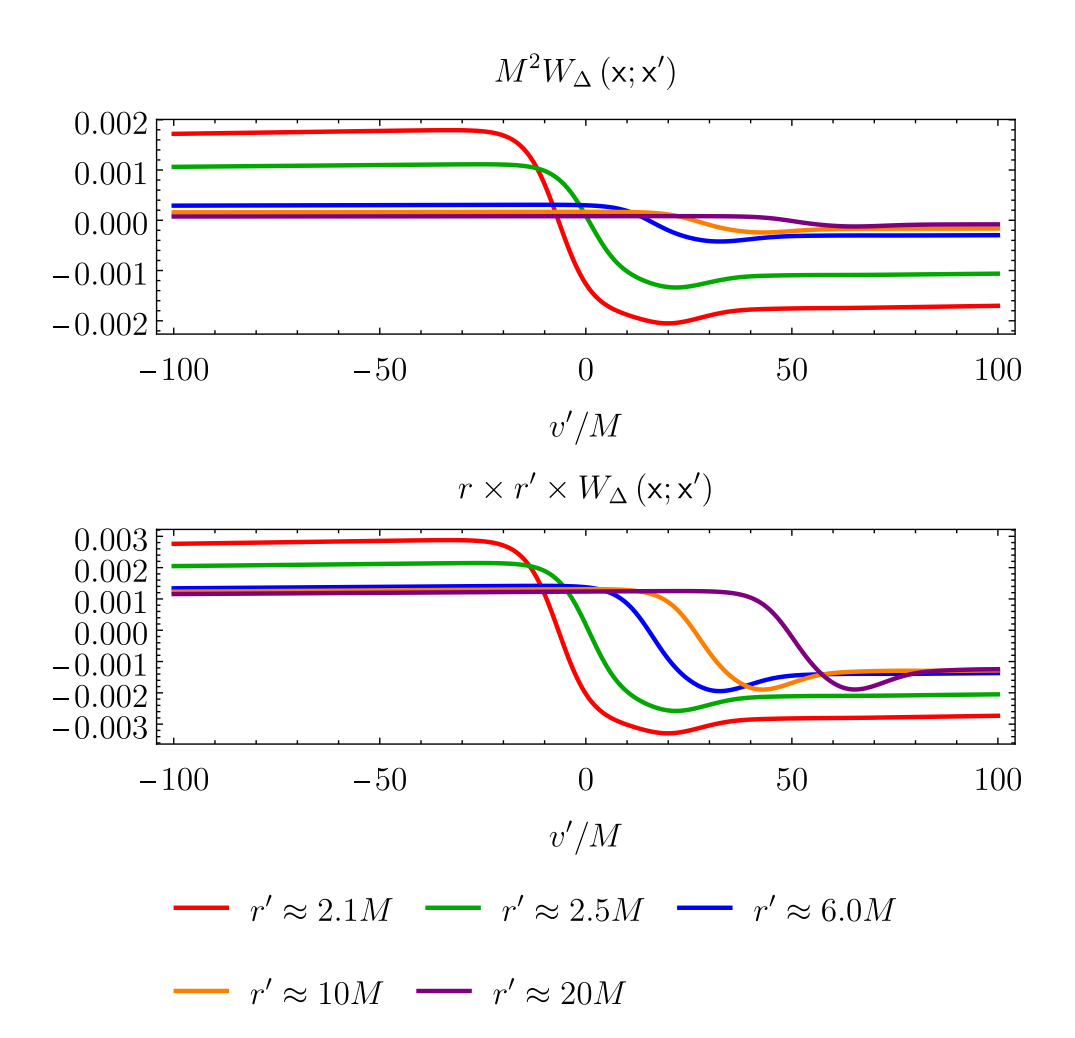


Figure 51 – $W_{\Delta}(\mathsf{x},\mathsf{x}')$ with $\mathsf{x} = (V = 1, r \approx 0.766M, \theta = 0, \varphi = 0)$ separated by an angle of $\gamma = \pi/3$ from all points $\mathsf{x}' = (v', r', \theta = 0, \varphi = 0)$ is plotted as a function of v' (top) plot for $r' \approx 2.1M$ (red), $r' \approx 2.52M$ (green), $r' \approx 6.009M$ (blue), $r' \approx 10M$ (blue) and $r' \approx 20M$ (purple). The bottom plot shows $rr' \times W_{\Delta}(\mathsf{x},\mathsf{x}')$ for the same setup. Overall, the qualitative behavior of the step-like transition, r'-dependence and local minima is identical to what we see in Figure 50. The difference is that the zeroes are not approaching some constant v', as expected, since we already seen that they are moving towards a constant u'.

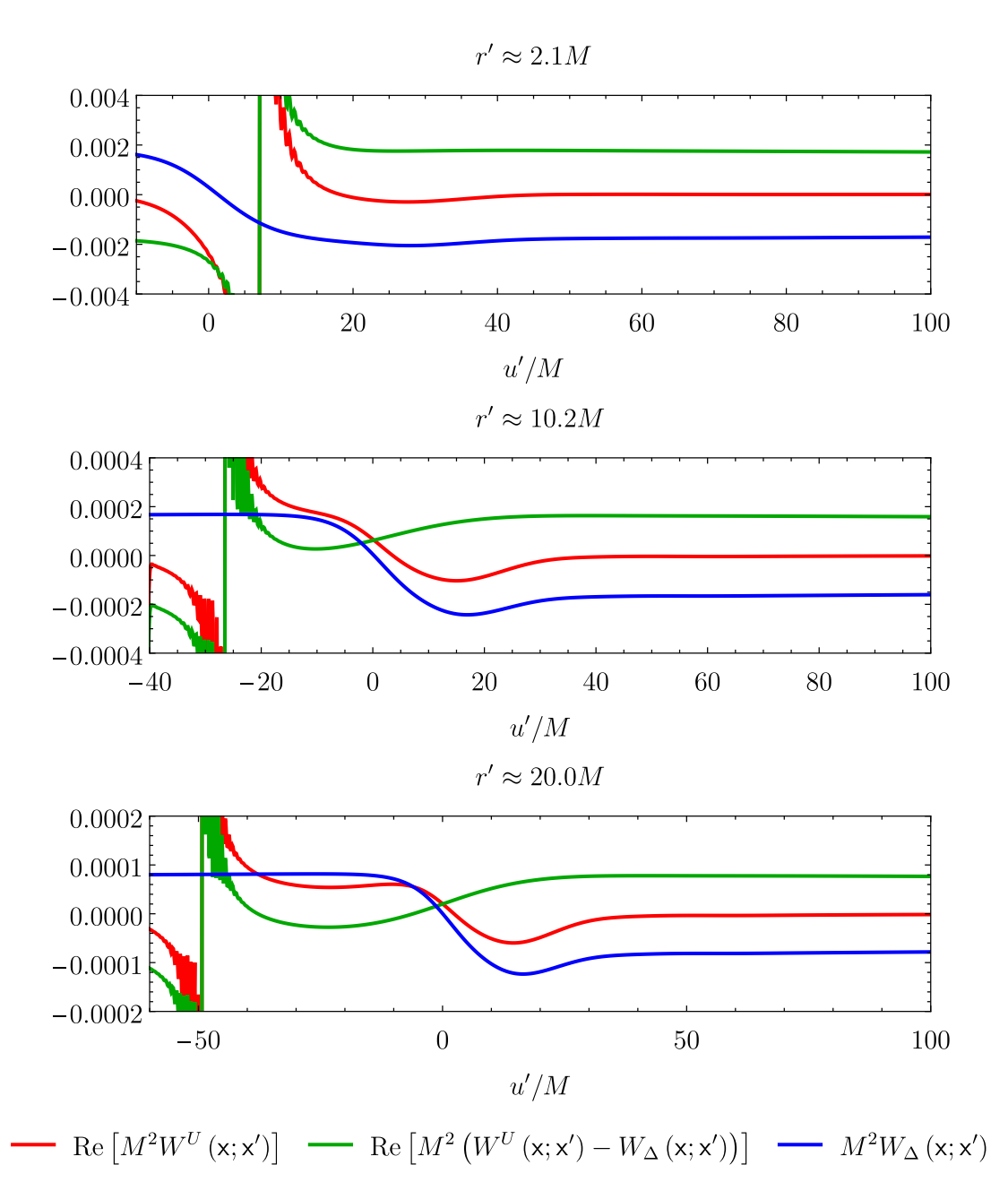


Figure 52 – Plots of Re $\left[M^2W^U\left(\mathbf{x};\mathbf{x}'\right)\right]$ (red), Re $\left[M^2\left(W^U\left(\mathbf{x};\mathbf{x}'\right)-W_\Delta\left(\mathbf{x},\mathbf{x}'\right)\right)\right]$ (green), and $W_\Delta\left(\mathbf{x},\mathbf{x}'\right)$ (blue) as a function of u' on three different slices of constant r': 2.1M (top), 10.2M (middle) and 20M (bottom). Here $\mathbf{x}=(V=1,\,r\approx0.766M,\,\theta=0,\,\varphi=0)$ is separated by an angle of $\gamma=\pi/3$ from all points $\mathbf{x}'=(u',\,r',\,\theta=0,\,\varphi=0)$. For clarity, the plot ranges are adjusted so that only the N=0 singularity is visible. Notice that when r' is too close to the horizon, the step-like behavior from $W_\Delta\left(\mathbf{x},\mathbf{x}'\right)$ is overwhelmed by the N=0 singularity. As a consequence, the localized zero that marks the center of the step is lost and all that remains from this term is a subtle local minima at u' larger than that where the N=0 singularity happens. With increasing r', the N=0 singularity moves towards smaller values of u' while the step remains centered close to $u'\approx -\bar{u}=0.4M$. This leads to a visible manifestation of the step behavior introduced by $W_\Delta\left(\mathbf{x},\mathbf{x}'\right)$ in the Wightman function.

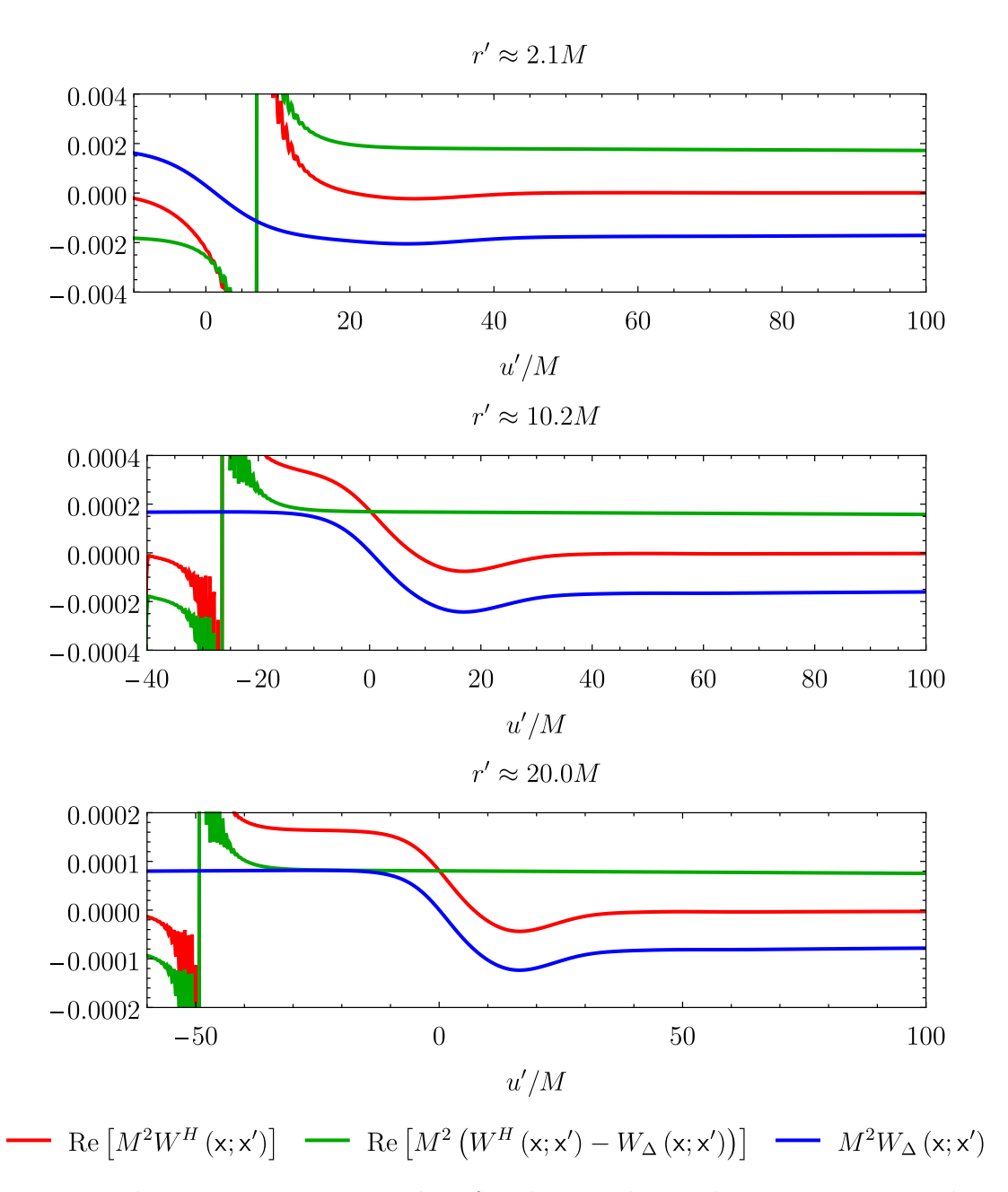


Figure 53 – The same as Figure 52 but for the Hartle-Hawking state. No qualitative differences emerge when compared to the results for the Unruh state.

The existence of a structure that behaves as a signature of correlations across the horizon carried by Hawking radiation is known in (1+1)D Schwarzschild: It shows as a local maximum in the field-field (Wightman function) and momentum-momentum correlations [10] and [58]. Such a structure also seem to be present in (3+1)D Schwarzschild. However, a key distinction emerges in this case: The correlations across the horizon encoded in the Wightman function are significantly stronger, enabling their direct resolution without recourse to momentum correlators (derivatives of the Wightman function). These are manifest in the form of the step-like behavior followed by a local minimum. Our analysis further suggests that momentum correlators — while not required here — would exhibit a sharper spatial localization than the field correlator itself.

Notably, when both points reside outside the horizon, field correlators (Wightman functions) display sharply localized correlations. Conversely, when one point lies inside the horizon, the field correlator becomes less localized, while momentum correlators — as inferred from our results — should retain strong spatial localization. This dichotomy underscores how causal separation across the horizon reshapes correlation structures in quantum fields.

5.3 Singularities in the ingoing and upgoing sectors of the Wightman function

During the explorations in Sections 5.1 and 5.2, we wondered how each family of field modes contributed to the Wightman function. This was motivated by [10, 58, 12, 11], where the Wightman function for the Boulware, Unruh and Hartle-Hawking states in (1+1)D Schwarzschild was written as a sum of two terms: one that depends only on Δu for the Boulware state (ΔU for the Unruh and Hartle-Hawking states) and another that depends only on Δv for the Boulware and Unruh states (ΔV for the Hartle-Hawking state). These can be read from Equations (3.67) for the Boulware state, (3.71) for the Unruh state and (3.72) for the Hartle-Hawking state. From these expressions, it is straightforward to see that each of the Δu -, Δv -, ΔU - and ΔV -dependent parts of the Wightman function present the known light-crossing singularities (Equations (3.55) and (3.56)) of the Wightman function.

The Δv - and ΔV -dependent parts of the Wightman functions for the Boulware, Unruh and Hartle-Hawking states arise from the ingoing modes while the Δu - and ΔU -dependent parts of the Wightman function arise from the upgoing modes. Therefore, these Wightman functions can always be understood as a sum of two terms: One arising from ingoing modes and another from upgoing modes. We will refer to these as the ingoing and upgoing sectors of these Wightman function.

In this section we construct an analogous decomposition of the Wightman functions for the Boulware, Unruh and Hartle-Hawking states in (3+1)D Schwarzschild in terms of

its ingoing and upgoing sectors and analyze how each of these contribute to each of these Wightman functions. For that purpose, we consider a fixed point $\mathbf{x}=(v=0M,r,\theta=0,\varphi=0)$ and \mathbf{x}' at the same r-coordinate outside the horizon $(r'=r>r_s)$ separated by an angle $\gamma=\pi/3$ and vary its v' coordinate.

Despite the simple setup, we found unanticipated behaviors that seem to depend on wether r' = r is above, on or below the photonsphere (r = 3M): When below or above the photonsphere, we found that not all sectors of the decomposition of the Wightman function present light-crossing singularities. On the other hand, we verified that all components of that decomposition present weaker non-light-crossing singularities, which to the best of our knowledge have not been reported before. When x and x' are on the photonsphere (r' = r = 3M), we found that both sectors of the Wightman functio present the light-crossing singularities but none of the weaker non-light-crossing singularities.

While we figured out a heuristic explanation for the behavior of the light-crossing singularities in the aforementioned situations, the nature of the non-light-crossing singularities is still not completely understood.

With these considerations we proceed to the exposition of our results, which is structured as follows: In Subsection 5.3.1, we construct the decomposition of the Wightman function for a given state in its so-called ingoing and upgoing sectors. In Subsection 5.3.2 we present plots of the ingoing and upgoing sectors of the Wightman function for the Boulware state in EF-coordinates. In Subsection 5.3.3 we use a slice of these maps on a surface of constant r' = r to characterize the functional form and the repeating pattern of non-light-crossing singularities in the ingoing and upgoing sectors of the Wightman function for the Boulware state. Finally, in Subsection 5.3.4 we show how the value of r' = r influences the magnitudes and singularities of the ingoing and upgoing sectors of the Wightman function for the Boulware state.

5.3.1 The ingoing and upgoing sectors of the Wightman function

To construct the (3+1)D analog of the (1+1)D Δv -dependent part of the Wightman function for the Boulware and Unruh states, we note that the latter arises from the (1+1)D $\tilde{f}_{\omega}^{\text{in,R}}$ modes (see Equation (3.62)). Therefore, we define its (3+1)D analog as

$$W_{\text{in,R}}(\mathbf{x};\mathbf{x}') = \frac{1}{(4\pi)^2 r r'} \sum_{\ell=0}^{\infty} (2\ell+1) P_{\ell}(\cos(\gamma)) \int_{0}^{\infty} \frac{d\omega}{\omega} \tilde{f}_{\omega\ell}^{\text{in,R}}(\mathbf{x}_{\perp}) \tilde{f}_{\omega\ell}^{\text{in,R}*}(\mathbf{x}'_{\perp}), \, \mathbf{x}, \mathbf{x}' \in I, \quad (5.26)$$

where x_{\perp} represents the non-angular coordinates of x. Following the same logic, the (3+1)D analog of the Δu -dependent part of the (1+1)D Wightman function for the Boulware state is defined as

$$W_{\text{up,R}}(\mathbf{x};\mathbf{x}') = \frac{1}{(4\pi)^2 r r'} \sum_{\ell=0}^{\infty} (2\ell+1) P_{\ell}(\cos(\gamma)) \int_{0}^{\infty} \frac{d\omega}{\omega} \tilde{f}_{\omega\ell}^{\text{up,R}}(\mathbf{x}_{\perp}) \tilde{f}_{\omega\ell}^{\text{up,R}*}(\mathbf{x}'_{\perp}), \, \mathbf{x}, \mathbf{x}' \in I. \quad (5.27)$$

The ΔU -dependent term of the (1+1)D Wightman function for the Unruh and Hartle-Hawking states arises from the $\tilde{f}_{\omega}^{\text{UP}}$ and $\tilde{f}_{\omega}^{\text{UP}}$ modes. Therefore, we define its (3+1)D analog as

$$W_{\text{UP},\bar{\text{UP}}}(\mathbf{x};\mathbf{x}') = \frac{1}{(4\pi)^2 r r'} \sum_{\ell=0}^{\infty} (2\ell+1) P_{\ell}(\cos(\gamma)) \int_{0}^{\infty} \frac{d\omega}{\omega} \left(\tilde{f}_{\omega\ell}^{\text{UP}}(\mathbf{x}_{\perp}) \tilde{f}_{\omega\ell}^{\text{UP}*}(\mathbf{x}'_{\perp}) + \tilde{f}_{\omega\ell}^{\bar{\text{UP}}*}(\mathbf{x}'_{\perp}) \tilde{f}_{\omega\ell}^{\bar{\text{UP}}*}(\mathbf{x}'_{\perp}) \right), \, \mathbf{x}, \mathbf{x}' \in I$$

$$= \frac{1}{(4\pi)^2 r r'} \sum_{\ell=0}^{\infty} (2\ell+1) P_{\ell}(\cos(\gamma)) \int_{0}^{\infty} \frac{d\omega}{\omega} \frac{1}{2 \sinh(2\pi r_s \omega)} \left(e^{2\pi r_s \omega} \tilde{f}_{\omega\ell}^{\text{up},R}(\mathbf{x}_{\perp}) \tilde{f}_{\omega\ell}^{\text{up},R*}(\mathbf{x}'_{\perp}) + e^{-2\pi r_s \omega} \tilde{f}_{\omega\ell}^{\text{up},R*}(\mathbf{x}_{\perp}) \tilde{f}_{\omega\ell}^{\text{up},R}(\mathbf{x}'_{\perp}) \right), \, \mathbf{x}, \mathbf{x}' \in I.$$

$$(5.28)$$

Finally, we note that the ΔV -dependent term of the (1+1)D Wightman function for the Hartle-Hawking state arises from the $\tilde{f}_{\omega}^{\rm IN}$ and $\tilde{f}_{\omega}^{\rm I\bar{N}}$ modes. Hence, we define its (3+1)D analog as

$$W_{\text{IN},\bar{\text{IN}}}(\mathsf{x};\mathsf{x}') = \frac{1}{(4\pi)^2 r r'} \sum_{\ell=0}^{\infty} (2\ell+1) P_{\ell}(\cos(\gamma)) \int_{0}^{\infty} \frac{\mathrm{d}\omega}{\omega} \left(\tilde{f}_{\omega\ell}^{\text{IN}}(\mathsf{x}_{\perp}) \tilde{f}_{\omega\ell}^{\text{IN}*}(\mathsf{x}'_{\perp}) \right) + \tilde{f}_{\omega\ell}^{\bar{\text{I}}\bar{\text{N}}*}(\mathsf{x}'_{\perp}) \hat{f}_{\omega\ell}^{\bar{\text{I}}\bar{\text{N}}*}(\mathsf{x}'_{\perp}) \right), \, \mathsf{x}, \mathsf{x}' \in I$$

$$= \frac{1}{(4\pi)^2 r r'} \sum_{\ell=0}^{\infty} (2\ell+1) P_{\ell}(\cos(\gamma)) \int_{0}^{\infty} \frac{\mathrm{d}\omega}{\omega} \frac{1}{2 \sinh(2\pi r_s \omega)} \left(e^{2\pi r_s \omega} \tilde{f}_{\omega\ell}^{\text{in},R}(\mathsf{x}_{\perp}) \tilde{f}_{\omega\ell}^{\text{in},R*}(\mathsf{x}'_{\perp}) + e^{-2\pi r_s \omega} \tilde{f}_{\omega\ell}^{\text{in},R*}(\mathsf{x}_{\perp}) \tilde{f}_{\omega\ell}^{\text{in},R}(\mathsf{x}'_{\perp}) \right), \, \mathsf{x}, \mathsf{x}' \in I.$$

$$(5.29)$$

In terms of these quantities, the Wightman function for the Boulware (Equation (3.74)), Unruh (Equation (3.75)) and Hartle-Hawking states (Equation (3.86)) can be written as:

$$W^{B}(\mathbf{x}; \mathbf{x}') = W_{\text{in,R}}(\mathbf{x}; \mathbf{x}') + W_{\text{up,R}}(\mathbf{x}; \mathbf{x}'), \, \mathbf{x}, \mathbf{x}' \in I,$$
(5.30)

$$W^{U}(x; x') = W_{\text{in,R}}(x; x') + W_{\text{UP,UP}}(x; x'), x, x' \in I$$
 (5.31)

and

$$W^{H}(\mathbf{x}; \mathbf{x}') = W_{\text{IN},\bar{\text{IN}}}(\mathbf{x}; \mathbf{x}') + W_{\text{UP},\bar{\text{UP}}}(\mathbf{x}; \mathbf{x}'), \, \mathbf{x}, \mathbf{x}' \in I,$$
 (5.32)

respectively.

In these equations, the Wightman function for a given state can always be understood as a sum of two terms: one that is defined by ingoing modes and another one by upgoing modes. We will refer to them, respectively, as the ingoing and upgoing sectors of that Wightman function. For instance, the ingoing sector of the Wightman function for the Unruh state is $W_{\text{in},R}(x;x')$ and its upgoing sector is $W_{\text{UP},\bar{\text{UP}}}(x;x')$.

5.3.2 Overview of the ingoing and upgoing sectors of the Wightman function

To produce a map of the ingoing and upgoing sectors of the Wightman function, we proceed as in Section 5.1.2: Let $\mathbf{x} = (v = 0M, r \approx 6.009M, \theta = 0, \varphi = 0)$ and \mathbf{x}' be at an angular separation of $\gamma = \pi/3$ with respect to it. Then vary the EF-coordinates v' and v' of \mathbf{x}' from v' = -100M up to v' = 100M in steps of $\Delta v' = 1M$ and for each v', vary $v' = v' - 2r'_*$ using all values of v'_* in our dataset. The corresponding mesh of points is presented in an EF-diagram and a Penrose diagram in Figure 26. The numerical computations are performed using the method described in Section 5.1.1.

In Figures 54 and 55 we plot the magnitudes of Re $[W_{\rm in,R}(x;x')]$ and Im $[W_{\rm in,R}(x;x')]$, respectively, as a function of u' and v'. These figures reveal bright curves indicating local maxima and darker curves marking zero crossings. In this context, the zero crossings correspond to ordinary zeroes of the Wightman function, lacking a particular physical interpretation. The local maxima, however, carry physical significance.

To interpret these maxima, we include blue-dashed curves in those figures, representing the points x' connected to x by a null geodesic that completes N half-orbits around the black hole. For $v' \gtrsim 0M$, there is a local maximum aligned with each of the blue-dashed curves. For $v' \lesssim 0M$, however, these curves only track the local maxima located above the photonsphere (r' > 3M).

Beyond the maxima traced by the blue-dashed curves, we also observe the greenencircled local maxima. Despite not being tracked by these curves, the shape traced by these local maxima is similar to that of the blue-dashed curves from the $v' \gtrsim 0M$ region.

The local maxima following the blue-dashed curves are smoothed versions of the Wightman function's light-crossing singularities (see Figures 58 and 59). The local maxima encircled in green are generally smaller than those associated with these smoothed singularities. It is for this reason that in Figures 54 and 55 they do not visibly extend from $r \approx 2.09M$ up to $r \approx 20M$ for $v' \lesssim 0M$.

However their magnitudes are still large enough to manifest in these figures alongside the smoothed light-crossing singularities. Thus, we assume that they are smoothed versions of an as-yet-unidentified singularity in $W_{\text{in,R}}(\mathbf{x};\mathbf{x}')$, weaker than P.V. $(1/\sigma)$ and $\delta(\sigma)$. Because these singularities do not coincide with light-crossings, we refer to them as non-light-crossing singularities.

In Figures 56 and 57 we plot the magnitudes of Re $[W_{\rm up,R}(x;x')]$ and Im $[W_{\rm up,R}(x;x')]$ as a function of u' and v'. The features revealed are similar to those observed in the magnitudes of the real and imaginary parts of $W_{\rm in,R}(x;x')$: bright curves indicating local maxima and darker curves marking zero crossings. The differences lie in the location of these features.

To facilitate analysis, we also include the aforementioned blue-dashed curves in these figures and verify that they align with local maxima only below the photonsphere (r' < 3M) for $v' \lesssim 0M$. This behavior is complementary to that we observed in the real and imaginary

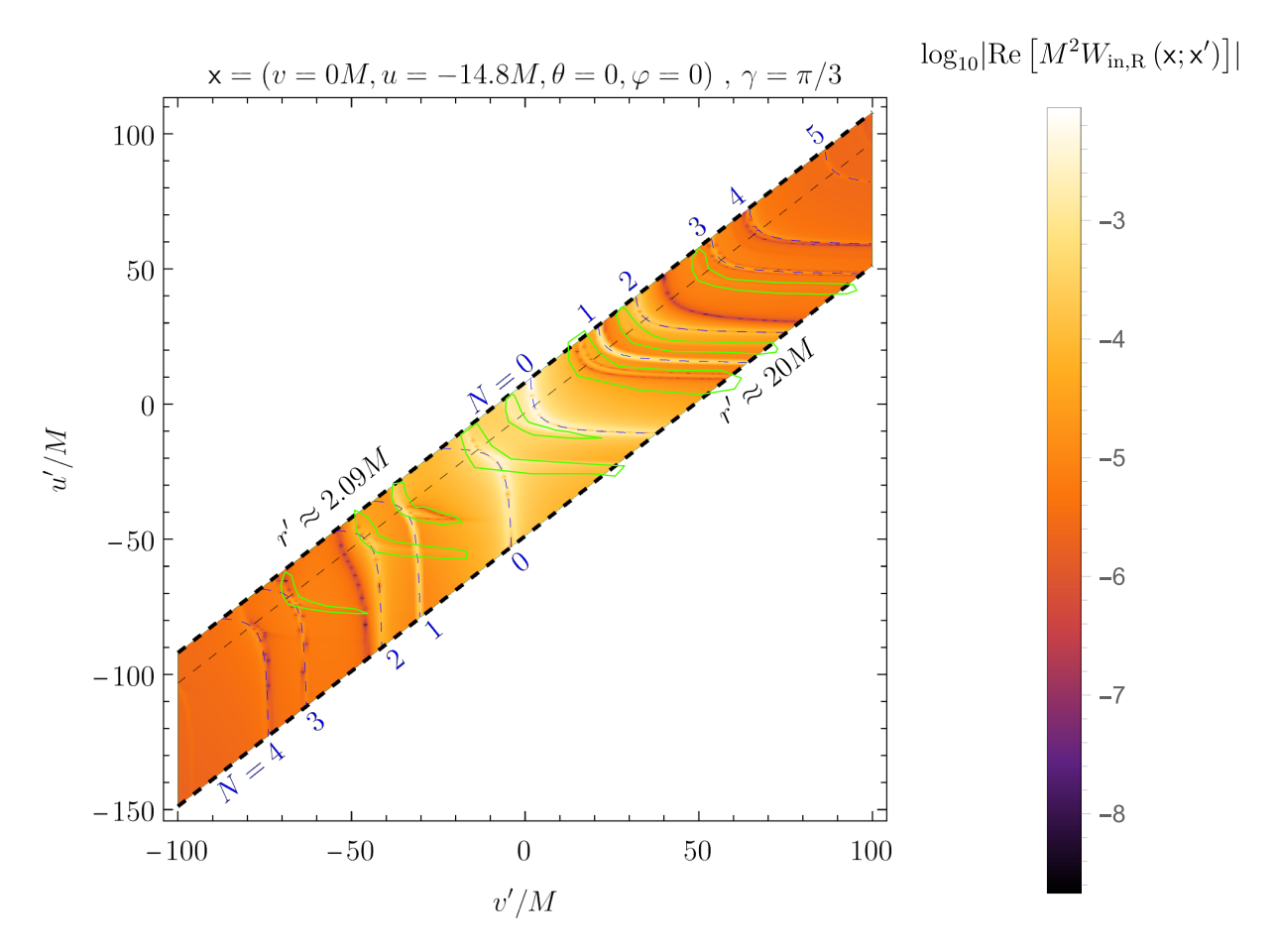


Figure 54 – Plot of $|\text{Re}\,[M^2W_{\text{in,R}}]|$ on $\mathsf{x}=(v=0M,\,r\approx6.009M,\,\theta=0,\,\varphi=0)$ separated by an angle of $\gamma=\pi/3$ from all points x' of Figure 26. The thin black-dashed line is r'=3M, the photonsphere. The sharp darker curves are zeroes of the Wightman function and the sharp whiter curves are peaks in its magnitude. The thin blue-dashed lines are the points x' connected to x by a null geodesic that completes N (blue numbers) half-orbits around the black hole. In this plot we see several local maxima. The ones tracked by the blue-dashed lines coincide with the location of the Wightman function light-crossing singularities. The rest of them (circled in green) are not tracked by the blue-dashed lines. We will refer to them as non-light-crossing singularities. These are more pronounced in the region $v'\lesssim 0M$ and seem to stem from the blue-dashed line near the photonsphere (r=3M).

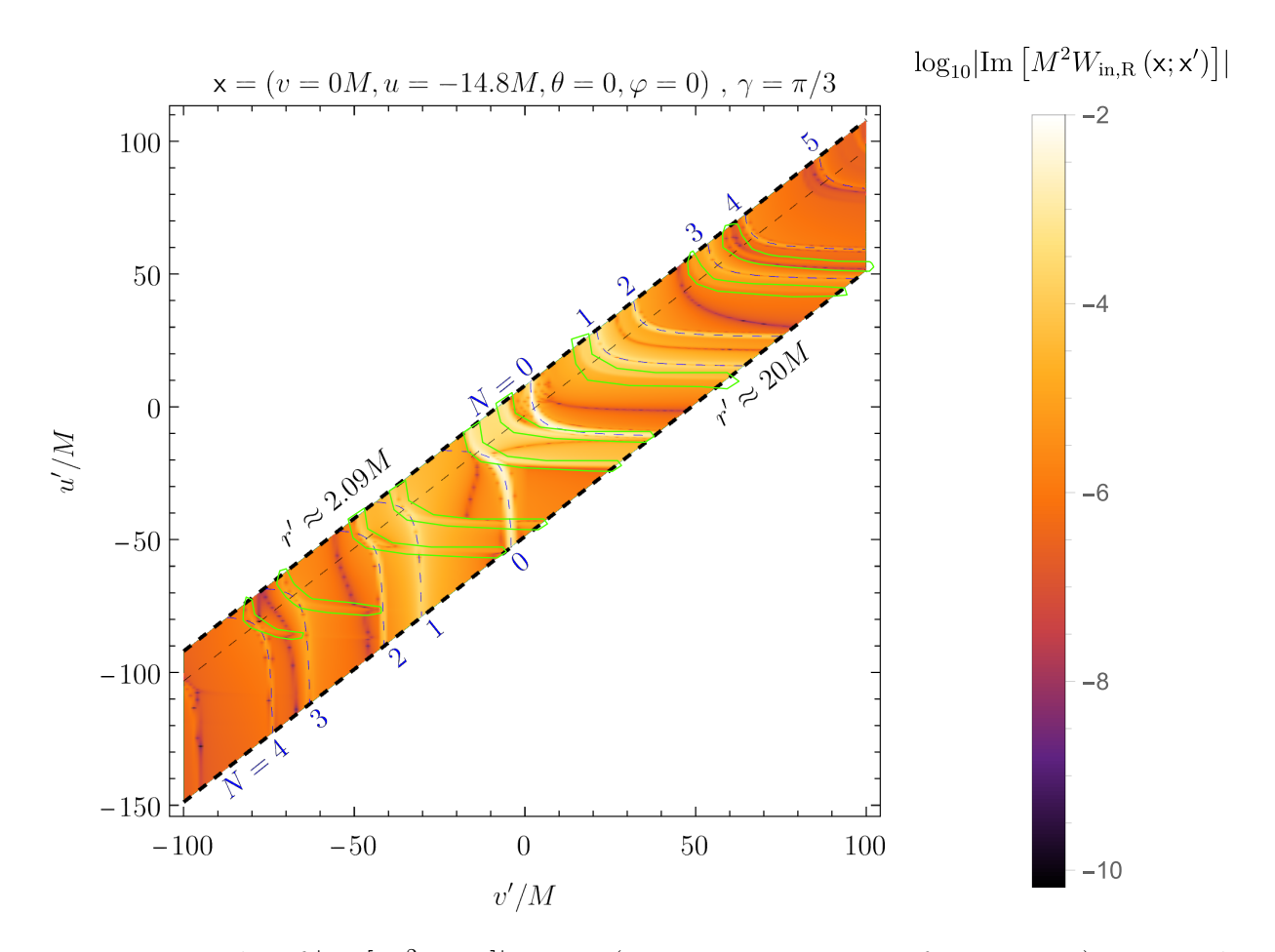


Figure 55 – Plot of $|\text{Im}[M^2W_{\text{in,R}}]|$ on $x = (v = 0M, r \approx 6.009M, \theta = 0, \varphi = 0)$ separated by an angle of $\gamma = \pi/3$ from all points x' of Figure 26. The thin black-dashed line is r' = 3M, the photonsphere. The sharp darker curves are zeroes of the Wightman function and the sharp whiter curves are peaks in its magnitude. The thin blue-dashed lines are the points x' connected to x by a null geodesic that completes N (blue numbers) half-orbits around the black hole. The green circles highlight the local maxima that are not tracked by the blue-dashed lines. Here we see that $|\text{Im}[M^2W_{\text{in,R}}]|$ presents the same qualitative behavior as $|\text{Re}[M^2W_{\text{in,R}}]|$ (Figure 54).

parts of $W_{\rm in,R}$ (x;x'), where the blue-dashed curves for $v' \lesssim 0M$ align exclusively with local maxima above the photonsphere (r' > 3M). For $v' \gtrsim 0M$ these curves do not track any local maxima in the magnitudes of Re $[W_{\rm up,R}$ (x;x')] and Im $[W_{\rm up,R}$ (x;x')]. This is in contrast to what we observed in the real and imaginary parts of $W_{\rm in,R}$ (x;x'), where they tracked local maxima for $v' \gtrsim 0$.

Similarly to the behavior observed in Figures 54 and 55 for the real and imaginary parts of $W_{\rm in,R}$ (x; x'), here we also see local maxima that are not tracked by the blue-dashed curves. However, in this case, they are more clearly visible across the full range of v', extending from $r \approx 2.09 M$ up to $r \approx 20 M$. Once again, the shape traced by these local maxima resembles that of the blue-dashed curves from the $v' \gtrsim 0 M$ region.

As was the case in those figures, the local maxima following the blue-dashed curves

in Figures 56 and 57 for $|\text{Re}[W_{\text{up,R}}(\mathbf{x};\mathbf{x}')]|$ and $|\text{Im}[W_{\text{up,R}}(\mathbf{x};\mathbf{x}')]|$, respectively, also are smoothed versions of the Wightman function's light-crossing singularities. Moreover, the local maxima in the magnitudes of $\text{Re}[W_{\text{up,R}}(\mathbf{x};\mathbf{x}')]$ and $\text{Im}[W_{\text{up,R}}(\mathbf{x};\mathbf{x}')]$ that are not tracked by the blue-dashed curves are also assumed to be smoothed versions of an asyet-unidentified singularity in $W_{\text{up,R}}(\mathbf{x};\mathbf{x}')$, weaker than a P.V. $(1/\sigma)$ and $\delta(\sigma)$. Here, this assumption finds its justification in the fact that by summing $W_{\text{in,R}}(\mathbf{x};\mathbf{x}')$ and $W_{\text{up,R}}(\mathbf{x};\mathbf{x}')$ we recover $W^B(\mathbf{x};\mathbf{x}')$ (Equation (5.30)), which has no non-light-crossing singularities (see Figures 27 and 28). Therefore, $W_{\text{up,R}}(\mathbf{x};\mathbf{x}')$ must also contain non-light-crossing singularities (with opposite behavior) in order to cancel those in $W_{\text{in,R}}(\mathbf{x};\mathbf{x}')$. This also implies that the non-light-crossing singularities in $W_{\text{in,R}}(\mathbf{x};\mathbf{x}')$ and $W_{\text{up,R}}(\mathbf{x};\mathbf{x}')$ occur at the same locations.

For brevity, we choose to omit the equivalent plots for $W_{\text{IN},\bar{\text{IN}}}(\mathsf{x};\mathsf{x}')$ and $W_{\text{UP},\bar{\text{UP}}}(\mathsf{x};\mathsf{x}')$ because in our setup no extra insights come from them: $W_{\text{IN},\bar{\text{IN}}}(\mathsf{x};\mathsf{x}')$ is qualitatively similar to $W_{\text{in},R}(\mathsf{x};\mathsf{x}')$, and visible differences only appear in the subtraction of these terms. An analogous conclusion holds for the comparison between $W_{\text{UP},\bar{\text{UP}}}(\mathsf{x};\mathsf{x}')$ and $W_{\text{up},R}(\mathsf{x};\mathsf{x}')$. For now we concentrate in the analysis of the non-light-crossing singularities and relegate that of the differences for future work.

At this stage the reader might be wondering what is the functional form of the non-light-crossing singularities and whether the light-crossing ones present the same form as those of the Wightman function or just happen to appear at the same location but have a different functional form. Both of these points are addressed in the next subsection.

5.3.3 The structure of the light-crossing and non-light-crossing singularities

To study the properties of the singularities in the magnitudes of the real and imaginary parts of $W_{\text{in,R}}(\mathbf{x};\mathbf{x}')$ (Figures 54 and 55) and $W_{\text{up,R}}(\mathbf{x};\mathbf{x}')$ (Figures 56 and 57), we use the slice of $r' = r \approx 6.009 M$ from these plots². It provides a suitable tool to assess the functional form of these singularities. We begin our analysis with log-plots that highlight the symmetry properties of these quantities.

In Figures 58 and 59 we plot the magnitudes of the real and imaginary parts, respectively, of $W_{\text{in,R}}(\mathbf{x};\mathbf{x}')$, $W_{\text{up,R}}(\mathbf{x};\mathbf{x}')$ and $W^B(\mathbf{x};\mathbf{x}')$ on $r'=r\approx 6.009M$ as a function of v'/M. As expected, the magnitude of both parts of the Wightman function for the Boulware state is symmetric about $\Delta t = t' - t = 0$, which is equivalent to $\Delta v = v' - v = 0$ because here $r = r'^3$. These figures also reveal that the magnitudes of the real and imaginary parts of the ingoing and upgoing sectors of $W^B(\mathbf{x};\mathbf{x}')$ are symmetric about $\Delta t = 0$ (equivalent to $\Delta v = 0$).

Any other slice with r' = r > 3M would provide the same conclusions that will be drawn in this subsection. This assertion is justified by the analysis presented in Subsection 5.3.4. On the other hand, the case where $r' \neq r$ demands a more careful treatment as many of the symmetries presented in the course of this subsection are broken in this case. We relegate this investigation for future work.

For $r' \neq r$, the relation is $\Delta v = \Delta t + \Delta r_*$, where $\Delta r_* = r'_* - r_*$.

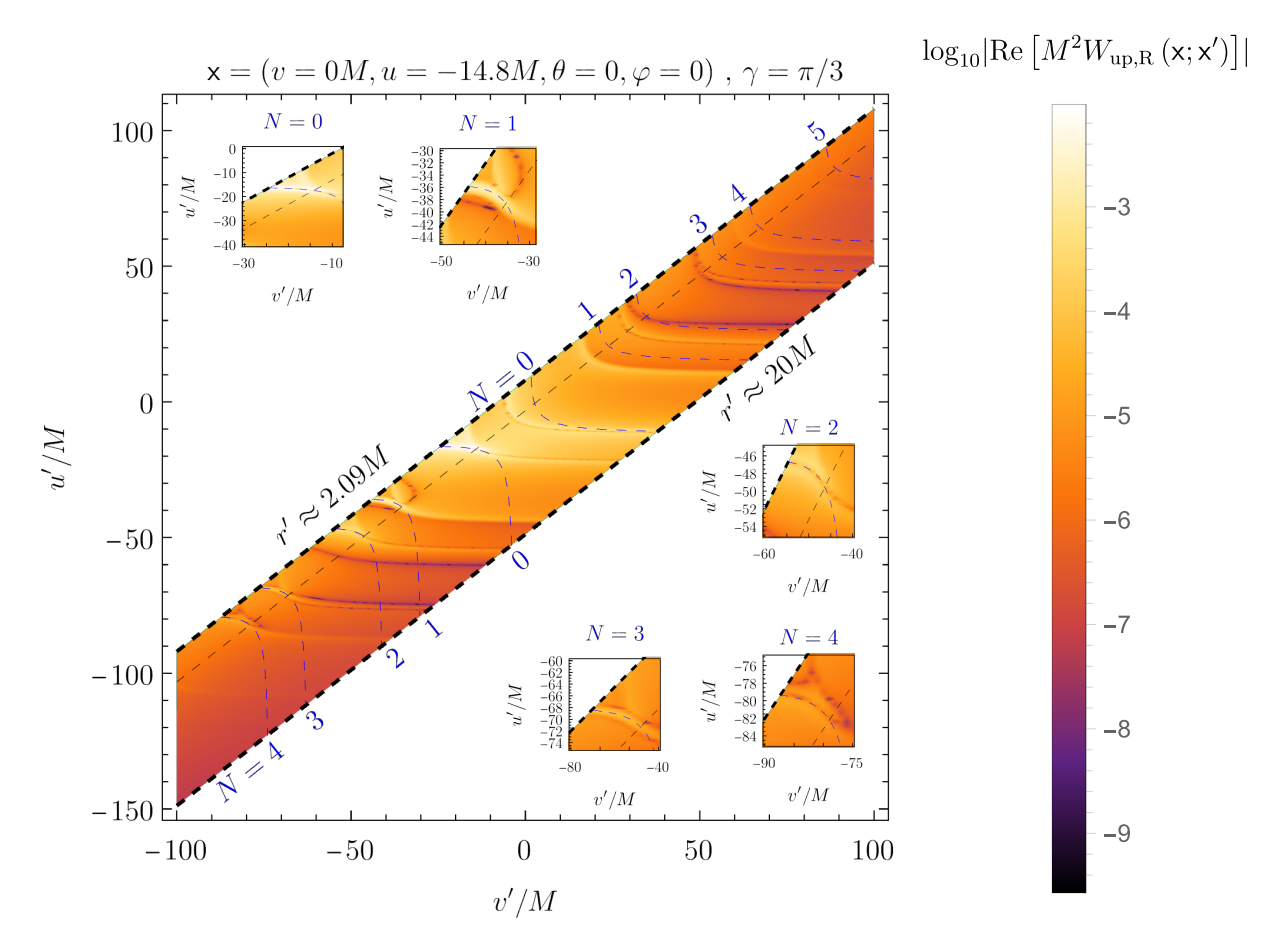


Figure 56 – Plot of $|\text{Re}\,[M^2W_{\text{up,R}}]|$ on $\mathsf{x}=(v=0M,\,r\approx6.009M,\,\theta=0,\,\varphi=0)$ separated by an angle of $\gamma=\pi/3$ from all points x' of Figure 26. The thin black-dashed line is r'=3M, the photonsphere. The sharp darker curves are zeroes of the Wightman function and the sharp whiter curves are peaks in its magnitude. The thin blue-dashed lines are the points x' connected to x by a null geodesic that completes N (blue numbers) half-orbits around the black hole. In this figure we see several local maxima. The ones that happen at $v'\lesssim 0M$ and below the photonsphere are tracked by the blue-dashed line (see the insets for a zoomed in view) and coincide in location with the Wightman function light-crossing singularities. The rest of the local maxima are not tracked by the blue-dashed lines and will be referred to as non-light-crossing singularities. They are evident for both positive and negative values of v' and seem to stem from the blue-dashed line near the photonsphere for $v'\lesssim 0M$.

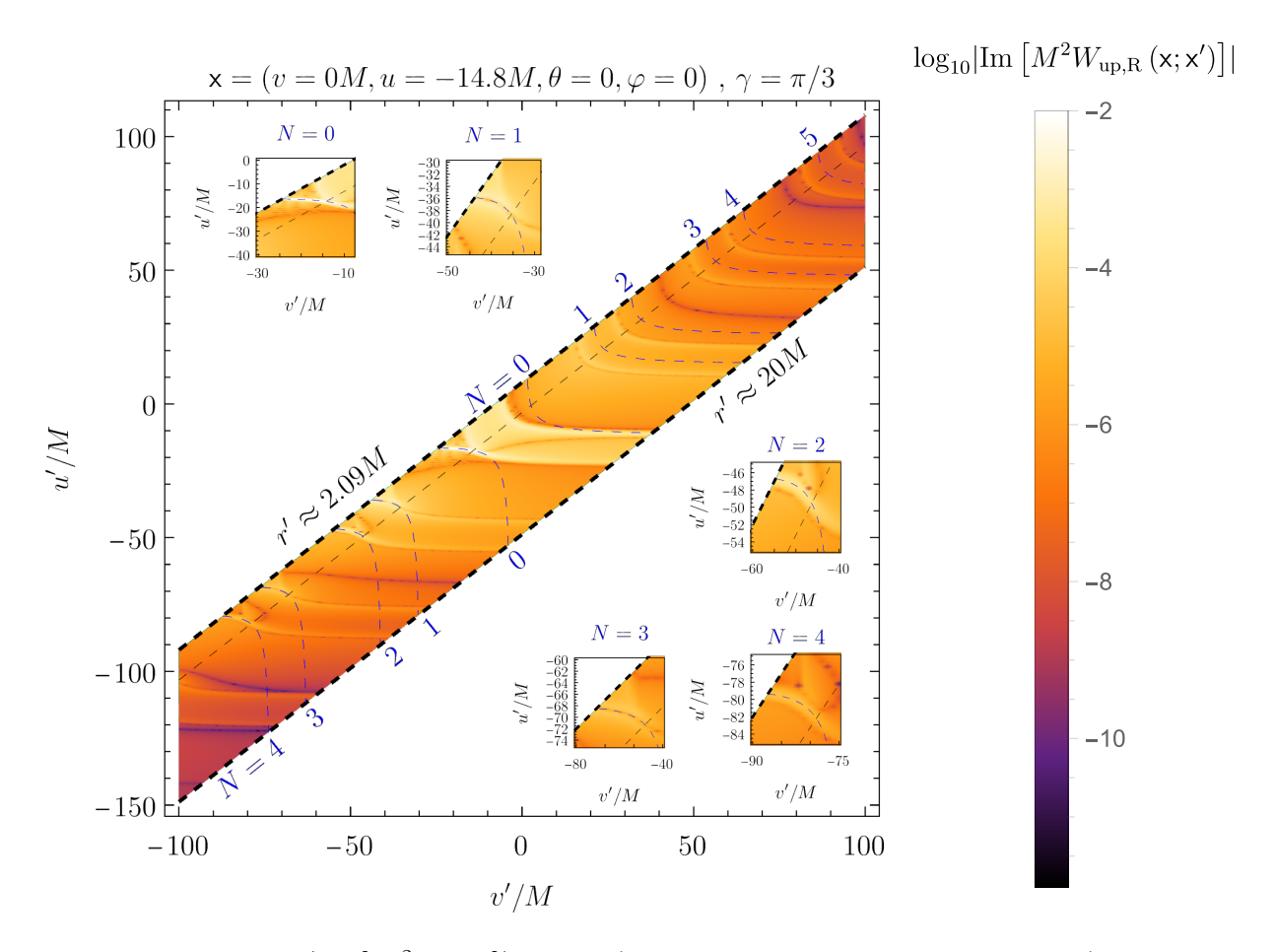


Figure 57 – Plot of $|\text{Im}[M^2W_{\text{up,R}}]|$ on $\mathbf{x} = (v = 0M, \, r \approx 6.009M, \, \theta = 0, \, \varphi = 0)$ separated by an angle of $\gamma = \pi/3$ from all points \mathbf{x}' of Figure 26. The thin black-dashed line is r' = 3M, the photonsphere. The sharp darker curves are zeroes of the Wightman function and the sharp whiter curves are peaks in its magnitude. The thin blue-dashed lines are the points \mathbf{x}' connected to \mathbf{x} by a null geodesic that completes N (blue numbers) half-orbits around the black hole. This plot shows that $|\text{Im}[M^2W_{\text{up,R}}]|$ presents the same qualitative behavior as $|\text{Re}[M^2W_{\text{up,R}}]|$ (Figure 56).

In addition to these symmetry properties, Figures 58 and 59 show that the Wightman function for the Boulware state is overall dominated by its ingoing sector. This dominance is stronger near the light-crossing singularities because these do not appear in the upgoing sector of that Wightman function. On the other hand the non-light-crossing singularities manifest in both sectors of $W^B(\mathbf{x};\mathbf{x}')$, as can be seen in these figures. The non-light-crossing singularities are more visible in the upgoing sector due to its absence of light-crossing singularities for $r' = r \approx 6.009M$. On the other hand, in the ingoing sector of $W^B(\mathbf{x};\mathbf{x}')$, the non-light-crossing singularities are obfuscated by the surrounding light-crossing-singularities. In this sector, the non-light-crossing singularities manifest as small peaks near the light-crossing singularities.

We now proceed to the linear plots that exhibit the functional form of the light-crossing singularities and reveal that of the non-light-crossing singularities. Given the symmetry

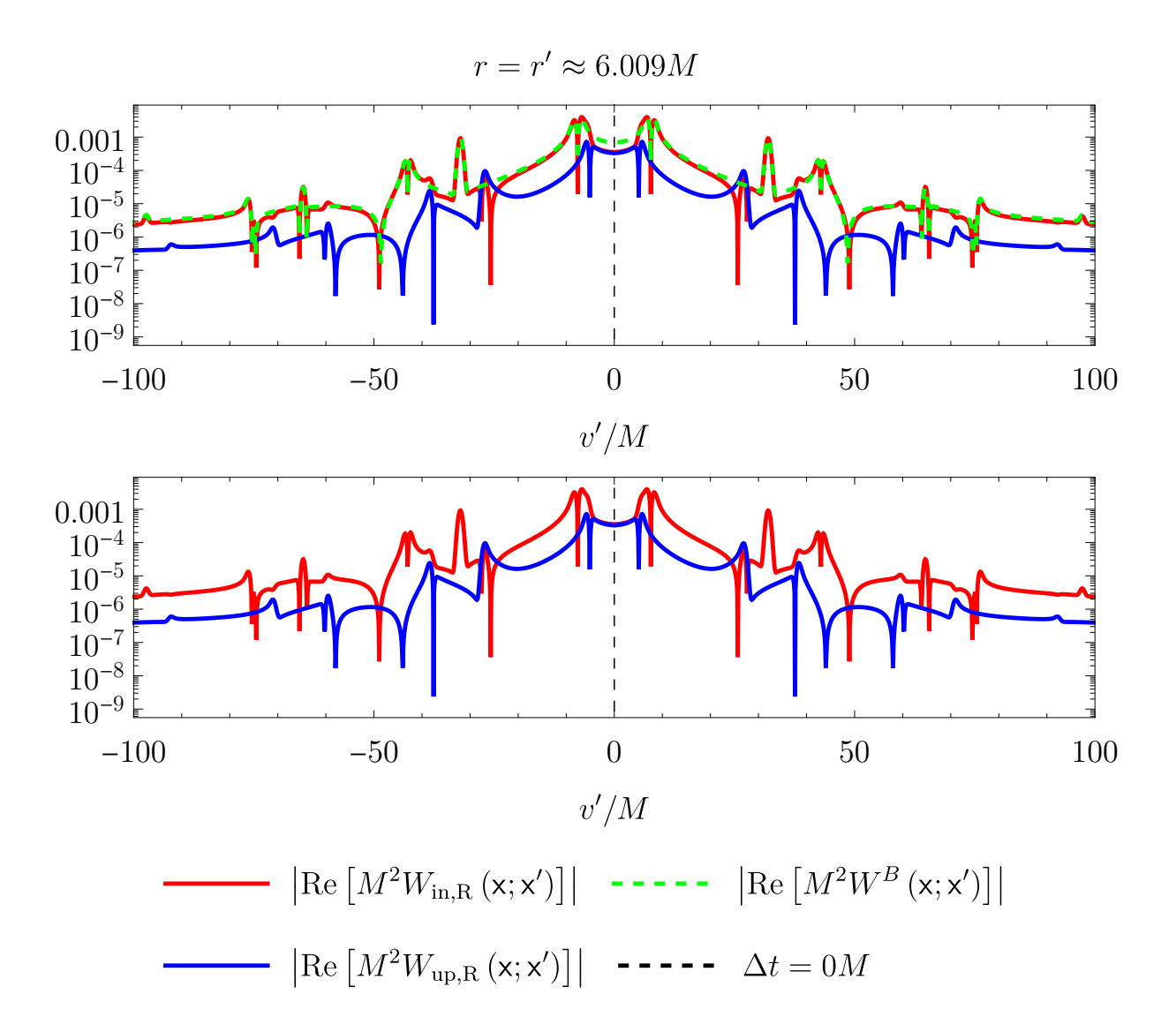


Figure 58 – Log-plots of the magnitudes of Re $[M^2W_{\text{in,R}}(\mathbf{x};\mathbf{x}')]$ (red), Re $[M^2W_{\text{up,R}}(\mathbf{x};\mathbf{x}')]$ (blue) and Re $[M^2W^B(\mathbf{x};\mathbf{x}')]$ (green-dashed) as a function of v'. Here $\mathbf{x}=(v=0M,\,r\approx6.009M,\,\theta=0,\,\varphi=0)$ is separated by an angle of $\gamma=\pi/3$ from all points \mathbf{x}' on $r'\approx6.009M$. The top plot shows Re $[M^2W_{\text{in,R}}(\mathbf{x};\mathbf{x}')]$, Re $[M^2W_{\text{up,R}}(\mathbf{x};\mathbf{x}')]$ and Re $[M^2W^B(\mathbf{x};\mathbf{x}')]$. The bottom plot shows only Re $[M^2W_{\text{in,R}}(\mathbf{x};\mathbf{x}')]$ and Re $[M^2W_{\text{up,R}}(\mathbf{x};\mathbf{x}')]$ for a cleaner visualization. The black-dashed line is $\Delta t=0M$, here equivalent to v'=0M. These plots show that Re $[M^2W_{\text{in,R}}(\mathbf{x};\mathbf{x}')]$ and Re $[M^2W_{\text{up,R}}(\mathbf{x};\mathbf{x}')]$ are symmetric about $\Delta t=0$ and present non-light-crossing singularities across the whole span of v'. However only Re $[M^2W_{\text{in,R}}(\mathbf{x};\mathbf{x}')]$ presents light-crossing singularities, which are compatible in magnitude and location with the singularities in the real part of the Wightman function.

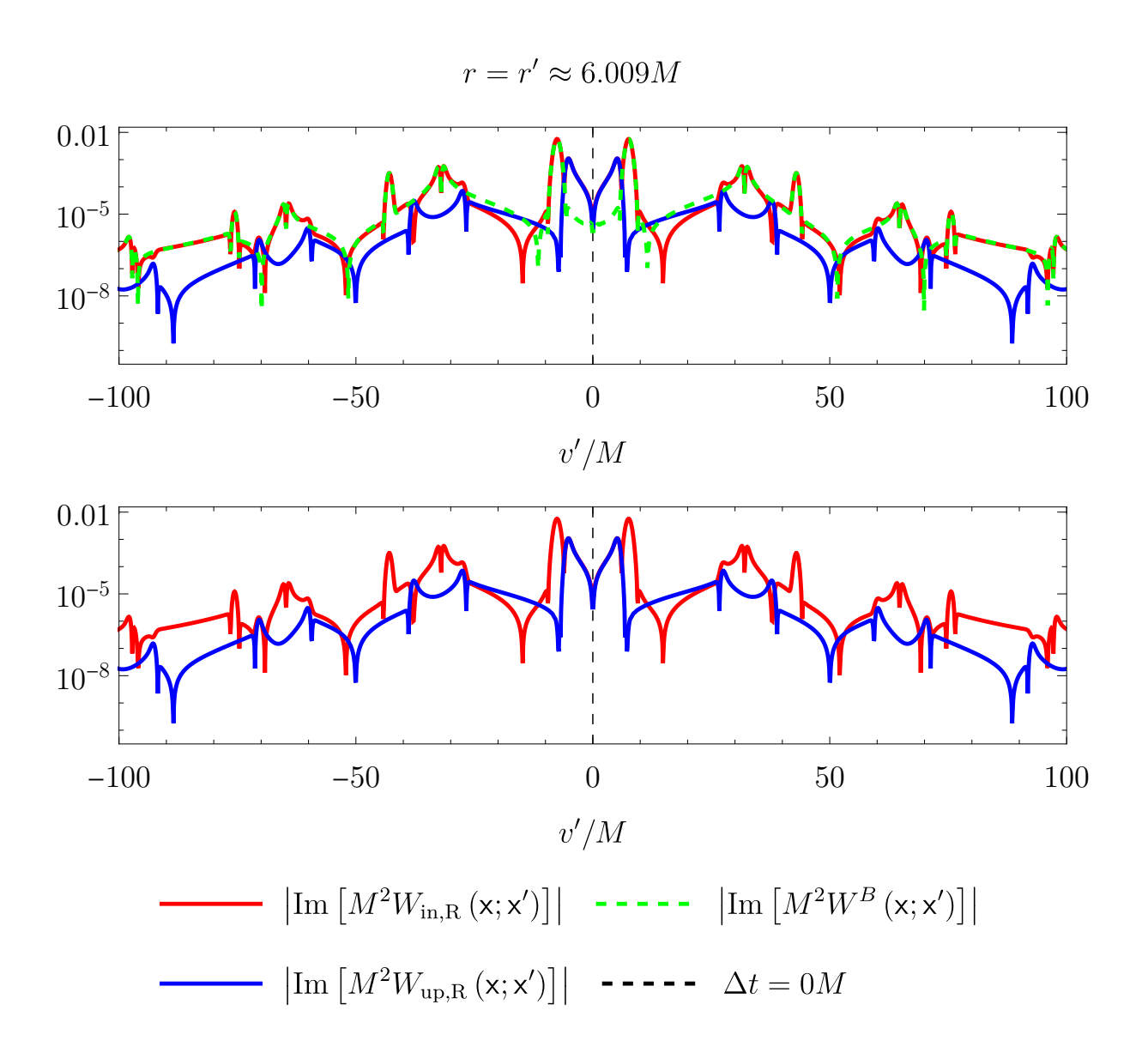


Figure 59 – Log-plots of the magnitudes of $\operatorname{Im} [M^2W_{\operatorname{in},R} (\mathsf{x};\mathsf{x}')]$ (red), $\operatorname{Im} [M^2W_{\operatorname{up},R} (\mathsf{x};\mathsf{x}')]$ (blue) and $\operatorname{Im} [M^2W^B (\mathsf{x};\mathsf{x}')]$ (green-dashed) as a function of v'. Here $\mathsf{x} = (v = 0M, \, r \approx 6.009M, \, \theta = 0, \, \varphi = 0)$ is separated by an angle of $\gamma = \pi/3$ from all points x' on $r' \approx 6.009M$. The top plot shows the magnitude of the imaginary parts of $W_{\operatorname{in},R} (\mathsf{x};\mathsf{x}')$, $W_{\operatorname{up},R} (\mathsf{x};\mathsf{x}')$ and $W^B (\mathsf{x};\mathsf{x}')$. In the bottom plot we omit $W^B (\mathsf{x};\mathsf{x}')$ for a cleaner visualization. The black-dashed line is $\Delta t = 0M$, here equivalent to v' = 0M. Both $\operatorname{Im} [M^2W_{\operatorname{in},R} (\mathsf{x};\mathsf{x}')]$ and $\operatorname{Im} [M^2W_{\operatorname{up},R} (\mathsf{x};\mathsf{x}')]$ are symmetric around $\Delta t = 0M$ and present non-light-crossing singularities throughout all values of v'. However only the ingoing sector presents light-crossing singularities. These are compatible in magnitude with the singularities of the imaginary part of the Wightman function.

of $W_{\text{in,R}}(\mathbf{x};\mathbf{x}')$, $W_{\text{up,R}}(\mathbf{x};\mathbf{x}')$ and $W^B(\mathbf{x};\mathbf{x}')$ about $\Delta v = 0$, we will only include an explicit analysis for $\Delta v > 0$.

Figure 60 shows the real parts of $W_{\rm in,R}$ (x; x'), $W_{\rm up,R}$ (x; x') and W^B (x; x'). From it, we immediately conclude that the light-crossing singularities in Re $\left[W^B({\sf x}; {\sf x}')\right]$ agree in both functional form and location with the ones in the real part of its ingoing sector. It also shows that both of its sectors present non-light-crossing singularities with opposite behaviors at the same values of Δv : when the non-light-crossing singularity in Re $\left[W_{\rm in,R}({\sf x}; {\sf x}')\right]$ is a local maximum (minimum), the one in Re $\left[W_{\rm up,R}({\sf x}; {\sf x}')\right]$ is a local minimum (maximum). This illustrates how they cancel out when combined.

When it comes to predicting the locations of the non-light-crossing singularities, Figure 60 also provides a clue. To state it, we label the non-light-crossing singularities by N_u (in the same way we labeled the light-crossing ones by N). In this figure N_u and N range from 0 (the singularity closest to $\Delta v = 0$) to 5 (the singularity furthest from $\Delta v = 0$). We observe that each N_u singularity always happens slightly before (w.r.t. Δv) the corresponding N singularity (at least up to $\Delta v = 100M$). More precisely, the v-coordinate distance between the visible extreme value⁴ of a given N_u singularity and the following extreme value of the corresponding N singularity are such that: the $N_u = 0$ singularity appears 1M before the N = 0 singularity; the odd $N_u > 0$ singularity manifests 5M before the corresponding odd N > 0 singularity and the even $N_u > 0$ singularity happens 4M before from the corresponding even N > 0 singularity.

The observation that the Δv interval between two successive even (or odd) N_u singularities is well approximated⁵ by the coordinate-time period of a null geodesic around the horizon on the photonsphere, $T_{\text{orbit}} = 6\pi\sqrt{3}M \approx 32.7M$ (which is equivalent to $\Delta v_{\text{orbit}} = 32.7M$ because r' = r) suggests that the non-light-crossing singularities are caused by signals orbiting the horizon on null geodesics, just like the light-crossing singularities. This is further corroborated by the fact that shape traced by the non-light-crossing singularities is the same as the one traced by orbiting null geodesics from the v' > 0M region in Figures 54, 55, 56 and 57.

Figure 60 also reveals a pattern in the functional form of the non-light-crossing singularities (which will be further complemented by the analysis of Figure 62). In Re $[W_{\text{in,R}}(\mathbf{x};\mathbf{x}')]$ (Re $[W_{\text{up,R}}(\mathbf{x};\mathbf{x}')]$), the $N_u=0$ singularity contains an increase (decay) into a local maximum (minimum) followed by a subtly slower decay (increase)⁶. The next

⁴ Figure 62 shows that each non-light-crossing singularity actually contains two local extrema.

From $N_u = 0$ to $N_u = 1$ this approximation becomes progressively worse as r and/or r' move away from the photonsphere at r = 3M. This happens for the light-crossing because the null geodesic that traces N = 0 travels from x to x' increasingly far away from the photonsphere, where that approximation is performed. The explanation is likely similar for the non-light-crossing singularities, although we do not yet understand their nature.

For Re $[W_{\text{in,R}}(\mathsf{x};\mathsf{x}')]$ this is arguably not visible in Figure 60, however we can infer that from the complementary behavior between it and Re $[W_{\text{up,R}}(\mathsf{x};\mathsf{x}')]$ that is observed for all other N_u . Further evidence is provided by the $N_u = 0$ non-light-crossing singularity in 61. There it is not obfuscated by the more localized N = 0, which is a $\delta(\sigma)$.

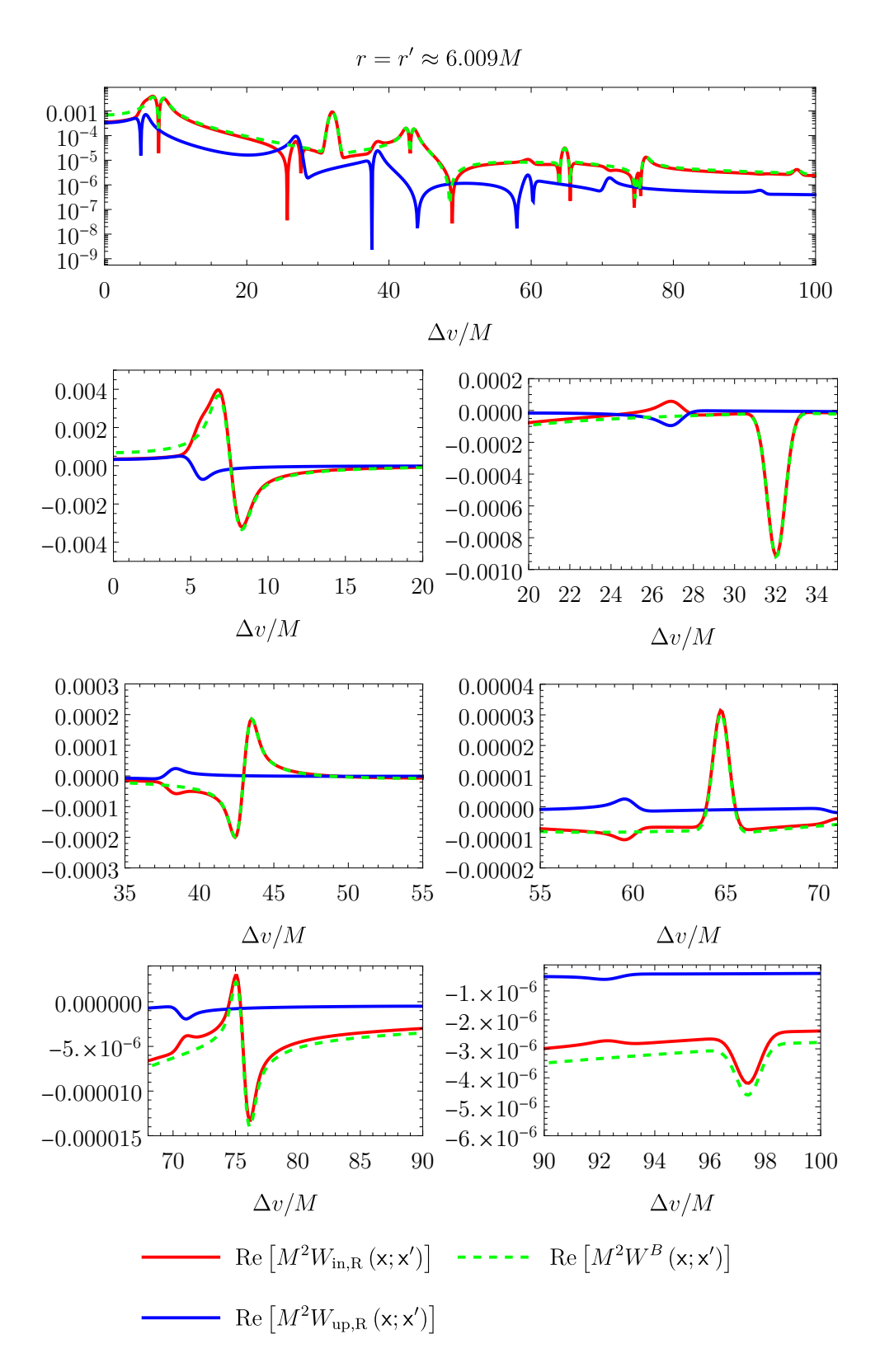


Figure 60 – Log-plot (top) of the magnitudes of $\operatorname{Re}\left[M^2W_{\operatorname{in,R}}\left(\mathbf{x};\mathbf{x}'\right)\right]$ (red), $\operatorname{Re}\left[M^2W_{\operatorname{up,R}}\left(\mathbf{x};\mathbf{x}'\right)\right]$ (blue) and $\operatorname{Re}\left[M^2W^B\left(\mathbf{x};\mathbf{x}'\right)\right]$ (green-dashed) as a function of $\Delta v = v' - v$ with $\Delta v > 0$. Here $\mathbf{x} = (v = 0M, \, r \approx 6.009M, \, \theta = 0, \, \varphi = 0)$ is separated by an angle of $\gamma = \pi/3$ from all points \mathbf{x}' on $r' \approx 6.009M$. The smaller plots highlight the singularities in a linear scale. They show that the light-crossing singularities in $\operatorname{Re}\left[M^2W_{\operatorname{in,R}}\left(\mathbf{x};\mathbf{x}'\right)\right]$ and $\operatorname{Re}\left[M^2W_{\operatorname{up,R}}\left(\mathbf{x};\mathbf{x}'\right)\right]$ agree in functional form with the light-crossing singularities of the Wightman function. The non-light-crossing singularities in those terms are always close w.r.t. Δv to the light-crossing ones.

singularity, $N_u = 1$, has the same shape but its rate of change is mirrored w.r.t. Δv : it presents a subtle increase (decay) into a local maximum (minimum) followed by a faster decay (increase). The $N_u = 2$ has qualitatively the same behavior as the $N_u = 0$ multiplied by -1, that is, it presents a decay (increase) into a local minimum (maximum) followed by a subtly slower increase (decay). The $N_u = 3$ has qualitatively the same behavior as the $N_u = 1$ multiplied by -1: It presents a decay (increase) into a local minimum (maximum) followed by a faster increase (decay). The $N_u = 4$ and $N_u = 5$ are qualitatively similar to the N = 0 and the $N_u = 1$ singularities, respectively. This establishes, on a qualitative level, a 4-fold pattern for the non-light-crossing singularities in the real parts of the ingoing and upgoing sectors, which we synthesize as

$$N_u = 0 \rightarrow \text{mirror} \Rightarrow N_u = 1 \rightarrow \text{mirror} \times (-1) \Rightarrow N_u = 2 \rightarrow \text{mirror} \Rightarrow N_u = 3$$

 $\rightarrow \text{mirror} \times (-1) \Rightarrow N_u = 4 \sim N_u = 0 \rightarrow \text{mirror} \Rightarrow N_u = 5 \sim N_\mu = 1 \rightarrow \dots,$ (5.33)

where \sim denotes equivalence in the sense that, for instance, the $N_u = 4$ singularity presents the same qualitative behavior as the $N_u = 0$ singularity.

Analogous considerations follow for $\Delta v < 0$ based on the symmetry of Re $[W_{\text{in,R}}(\mathsf{x};\mathsf{x}')]$, Re $[W_{\text{up,R}}(\mathsf{x};\mathsf{x}')]$ and Re $[W^B(\mathsf{x};\mathsf{x}')]$ about $\Delta v = 0$.

As a brief summary, this analysis establishes that for $r'=r\approx 6.009M$, the light-crossing singularities of the Wightman function for the Boulware state agree with the ones of its ingoing sector in functional form and location. Additionally, we observe that the non-light-crossing singularities in the real parts of the ingoing and upgoing sectors of that Wightman function obey a 4-fold singularity structure. Finally, we note that two successive odd (or even) non-light-crossing singularities are separated by an interval $\Delta t \approx 32.7M$ which is the coordinate time interval a null geodesic takes to complete an orbit around the horizon on the photonsphere.

These conclusions also apply to the imaginary parts of $W_{\text{in,R}}(x;x')$ and $W_{\text{up,R}}(x;x')$ as can be verified by a similar analysis of Figure 61. We remark that, in a similar way to what happens in the singularity structure of the Wightman function (Equations (3.55) and (3.56)), the non-light-crossing singularities in Im $[W_{\text{in,R}}(x;x')]$ and Im $[W_{\text{up,R}}(x;x')]$ are one fold ahead of the corresponding singularities in the real parts of these terms. For instance, the $N_u = 1$ non-light-crossing singularity in the imaginary part of $W_{\text{in,R/up,R}}(x;x')$ presents the same behavior as the $N_u = 0$ non-light-crossing singularity in the real part of $W_{\text{in,R/up,R}}(x;x')$.

We close this subsection with a more thorough analysis comparing the non-light-crossing singularities in the real and imaginary parts of $W_{\rm up,R}$ (x;x'). We choose it because in this case ($r' = r \approx 6.009M$) it presents no light-crossing singularities to obfuscate the non-light-crossing ones we are trying to understand. In Figure 62 we plotted the real and imaginary parts of $W_{\rm up,R}$ (x;x') as a function of $\Delta v/M$. There we see a confirmation of the singularity structure for the non-light-crossing singularities, summarized in Equation (5.33). Additionally, this plot offers a better visualization of the shape of these singularities when

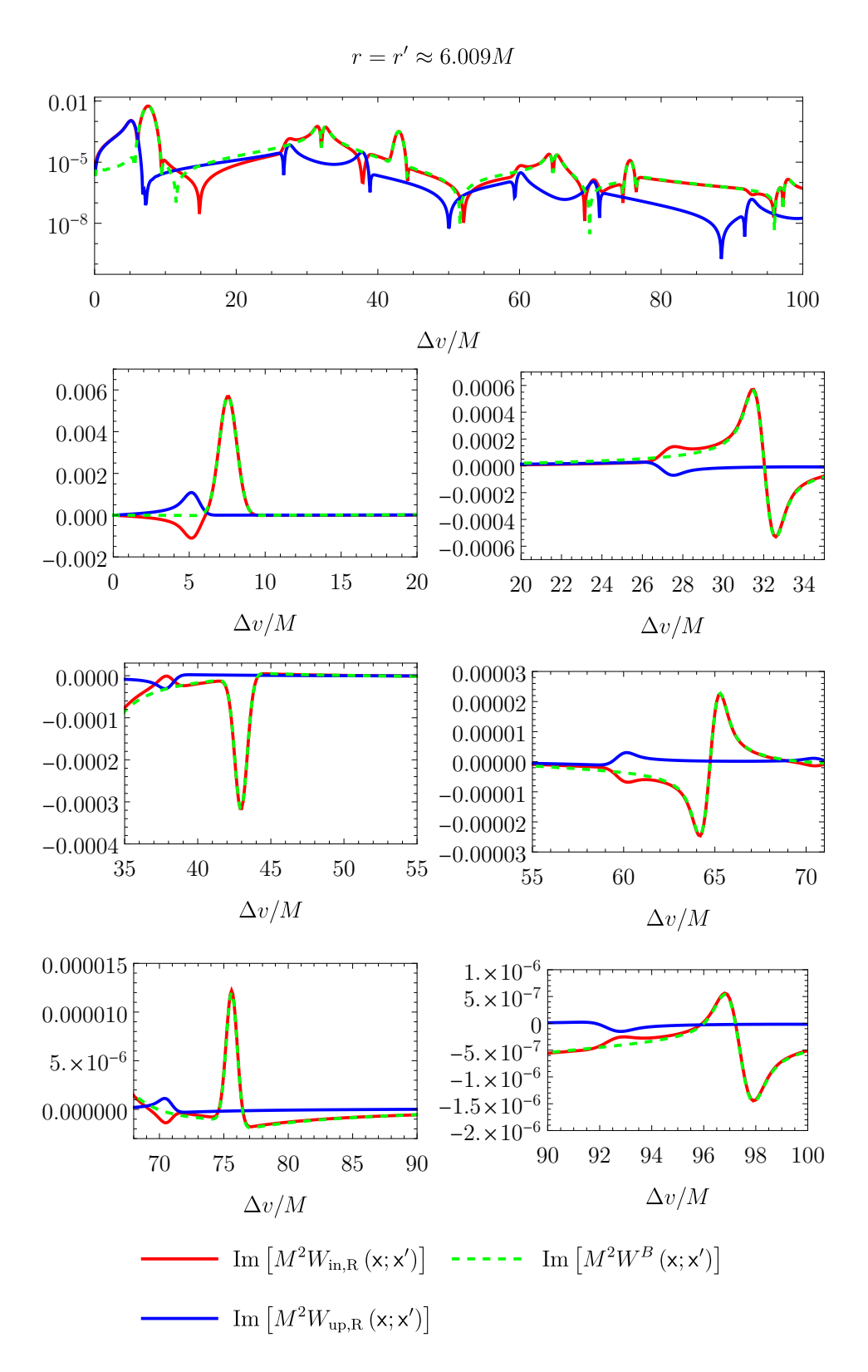


Figure 61 – Log-plot (top) of the magnitudes of $\operatorname{Im}[M^2W_{\operatorname{in,R}}(\mathsf{x};\mathsf{x}')]$ (red), $\operatorname{Im}[M^2W_{\operatorname{up,R}}(\mathsf{x};\mathsf{x}')]$ (blue) and $\operatorname{Im}[M^2W^B(\mathsf{x};\mathsf{x}')]$ (green-dashed) as a function of $\Delta v = v' - v$ with $\Delta v > 0$. Here $\mathsf{x} = (v = 0M, \, r \approx 6.009M, \, \theta = 0, \, \varphi = 0)$ is separated by an angle of $\gamma = \pi/3$ from all points x' on $r' \approx 6.009M$. The smaller plots highlight the singularities in a linear scale. They show that the light-crossing singularities in $\operatorname{Im}[M^2W_{\operatorname{in,R}}(\mathsf{x};\mathsf{x}')]$ and $\operatorname{Im}[M^2W_{\operatorname{up,R}}(\mathsf{x};\mathsf{x}')]$ agree in functional form with the singularities of $\operatorname{Im}[M^2W^B(\mathsf{x};\mathsf{x}')]$. The non-light-crossing singularities in those terms are always close w.r.t. Δv to the light-crossing ones.

compared to the previous plots (Figures 60 and 61) where we were only able to see the larger maximum (or minimum) in each of the non-light-crossing singularities. Here we see that each of them actually contains two extrema: a larger one, that we already spotted, and a smaller one, that we can only see here — Even in this case, we needed an inset that zoomed in the shallow minimum of the $N_u = 0$ singularity in Re $[W_{up,R}(x;x')]$.

As can be seen in Figure 62, the functional form of the non-light-crossing singularities is not a P.V. $(1/\sigma)$ or a $\delta(\sigma)$. However, its qualitative behavior can be modeled by

$$\Xi(\Delta v, \sigma_{std}, \alpha) = \frac{1}{\sigma_{std}\sqrt{2\pi}} e^{-\frac{\Delta v^2}{2\sigma_{std}^2}} \left(\frac{\Delta v + \alpha}{\alpha}\right), \tag{5.34}$$

where σ_{std} is the standard deviation of the Gaussian (and should not be confused with Synge's world function) and $\alpha, \sigma_{std} \in \mathbb{R}_{>0}$. The midpoint between its extrema is $\Delta v = -\alpha/2$ and its behavior is illustrated in Figure 63.

Using that model, the 4-fold structure of the non-light-crossing singularities in Re $[W_{\text{up,R}}(\mathsf{x};\mathsf{x}')]$ and Im $[W_{\text{up,R}}(\mathsf{x};\mathsf{x}')]$ is more precisely (but still qualitatively) described by:

Re
$$[W_{\text{up,R}}(\mathsf{x};\mathsf{x}')]$$
: $\Xi(\Delta v, -\sigma_{std}, \alpha) \to \Xi(\Delta v, -\sigma_{std}, -\alpha) \to \Xi(\Delta v, \sigma_{std}, \alpha) \to \Xi(\Delta v, \sigma_{std}, -\alpha) \to \Xi(\Delta v, -\sigma_{std}, \alpha) \to \dots$ (5.35)

and

Im
$$[W_{\text{up,R}}(\mathbf{x};\mathbf{x}')]$$
: $\Xi(\Delta v, \sigma_{std}, -\alpha) \to \Xi(\Delta v, -\sigma_{std}, \alpha) \to \Xi(\Delta v, -\sigma_{std}, -\alpha) \to \Xi(\Delta v, \sigma_{std}, \alpha) \to \Xi(\Delta v, \sigma_{std}, -\alpha) \to \ldots,$

$$(5.36)$$

where each singularity is assumed to be suitably displaced so that it is correctly centered. From the observation that the non-light-crossing singularities in Re $[M^2W_{\rm in,R}(\mathbf{x};\mathbf{x}')]$ and Im $[M^2W_{\rm in,R}(\mathbf{x};\mathbf{x}')]$ must cancel the ones in the upgoing sector, we can infer their singularity structures as well:

Re
$$[W_{\text{in,R}}(\mathsf{x};\mathsf{x}')]$$
: $\Xi(\Delta v, \sigma_{std}, \alpha) \to \Xi(\Delta v, \sigma_{std}, -\alpha) \to \Xi(\Delta v, -\sigma_{std}, \alpha) \to \Xi(\Delta v, -\sigma_{std}, -\alpha) \to \Xi(\Delta v, \sigma_{std}, \alpha) \to \dots,$ (5.37)

and

Im
$$[W_{\text{in,R}}(\mathsf{x};\mathsf{x}')]$$
: $\Xi(\Delta v, -\sigma_{std}, -\alpha) \to \Xi(\Delta v, \sigma_{std}, \alpha) \to \Xi(\Delta v, \sigma_{std}, -\alpha) \to \Xi(\Delta v, -\sigma_{std}, \alpha) \to \Xi(\Delta v, -\sigma_{std}, -\alpha) \to \dots$

$$(5.38)$$

In the following subsection, we analyze how the r-coordinate affects the relation between $W_{\text{in,R}}(\mathsf{x};\mathsf{x}')$, $W_{\text{up,R}}(\mathsf{x};\mathsf{x}')$ and $W^B(\mathsf{x};\mathsf{x}')$.

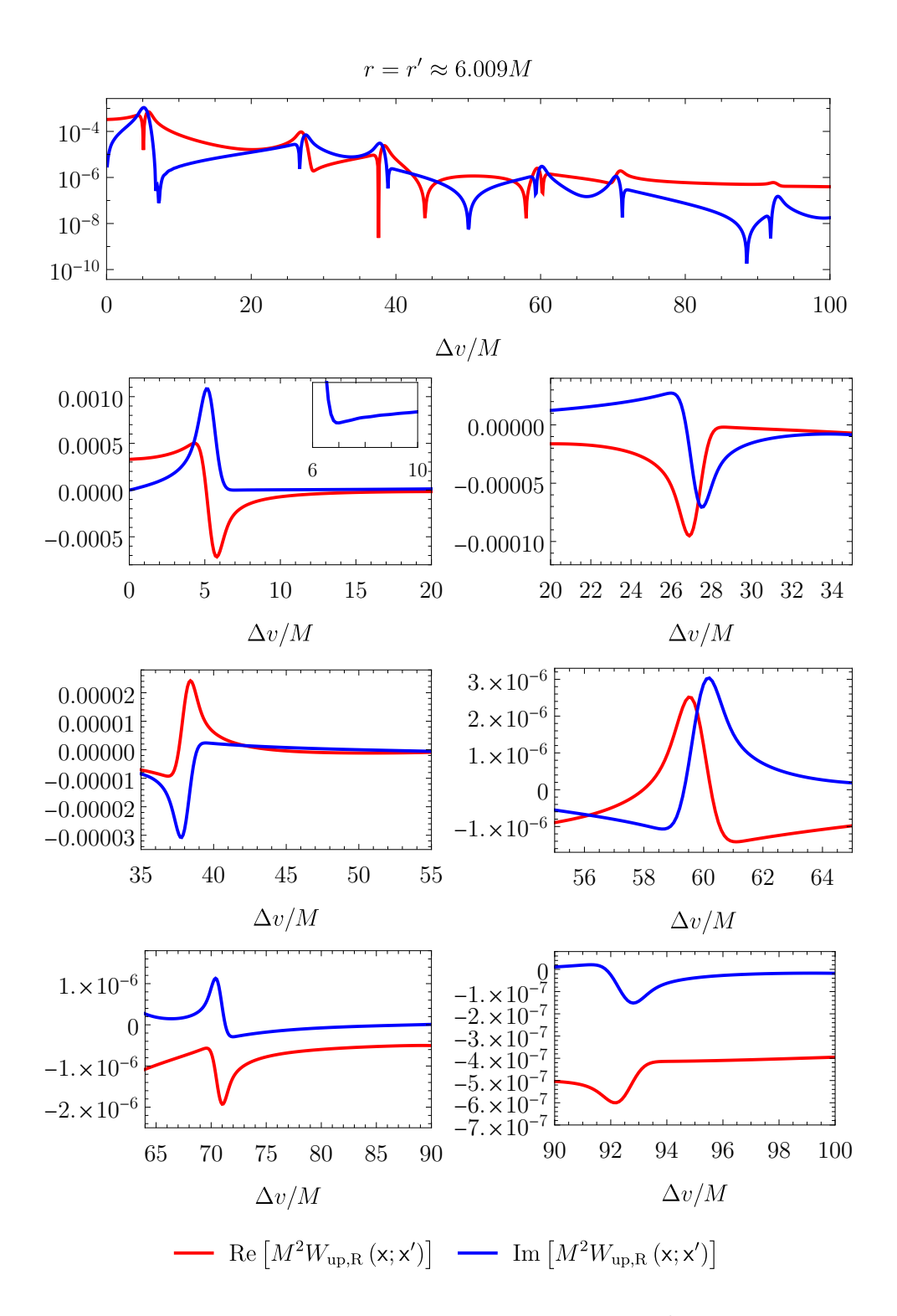


Figure 62 – Log-plot (top) of the magnitudes of $\operatorname{Re}\left[M^2W_{\operatorname{in,R}}\left(\mathbf{x};\mathbf{x}'\right)\right]$ (red) and $\operatorname{Im}\left[M^2W_{\operatorname{up,R}}\left(\mathbf{x};\mathbf{x}'\right)\right]$ (blue) as a function of $\Delta v=v'-v$ with $\Delta v>0$. Here $\mathbf{x}=(v=0M,\,r\approx 6.009M,\,\theta=0,\,\varphi=0)$ is separated by an angle of $\gamma=\pi/3$ from all points \mathbf{x}' on $r'\approx 6.009M$. The smaller plots highlight the singularities in a linear scale. These plots show that the non-light-crossing singularities are always composed by two extrema: a local maxima and a local minima and follow a 4-fold pattern.

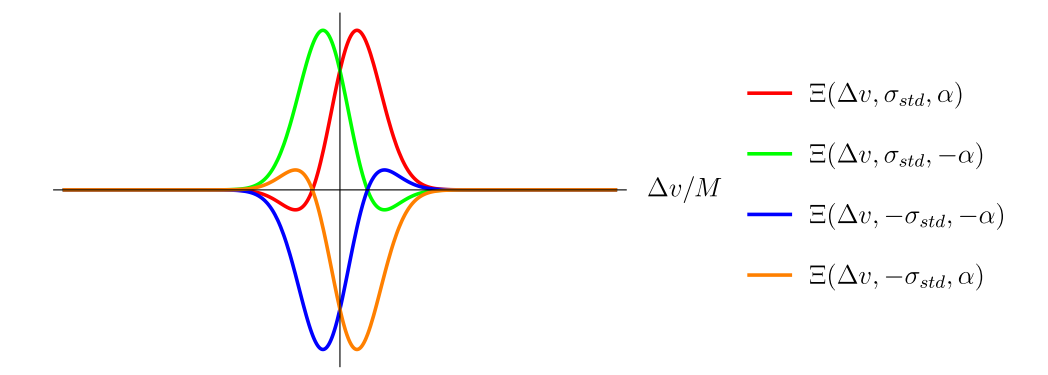


Figure 63 – Plots of $\Xi(\Delta v, \sigma_{std}, \alpha) = \frac{1}{\sigma_{std}\sqrt{2\pi}} \mathrm{e}^{-\frac{\Delta v^2}{2\sigma_{std}^2}} \left(\frac{\Delta v + \alpha}{\alpha}\right)$ (Equation (5.34)) for different choices of sign for σ_{std} and α . Here we used $\alpha = 1$ and $\sigma_{std} = 1$, which is sufficient to depict its behavior.

5.3.4 The dependence on the r-coordinate

In Figures 58 and 59 we saw that when $r = r' \approx 6.009M$, the Wightman function for the Boulware state and its singularities are dominated by $W_{\rm in,R}$ (x;x') while $W_{\rm up,R}$ (x;x') is generally of smaller magnitude and contained only non-light-crossing singularities. Here we present evidences that this behavior depends on wether x and x' are taken to be above (r' = r > 3M) or below (r' = r < 3M) the photonsphere. For that end, we repeated the plots from the aforementioned figures but using $r' = r \approx 2.1M$ and $r' = r \approx 2.995M$.

The results for $r' = r \approx 2.1 M$ are presented in Figures 64 and 65. There we see that $W_{\rm up,R}$ (x;x') dominates the Wightman function for the Boulware state for almost all v'/M, specially near its light-crossing singularities, while $W_{\rm in,R}$ (x;x') contains only non-light-crossing singularities and is overall of smaller magnitude. This is the opposite of what we observed for $r' = r \approx 6.009 M$. Given that, we conjecture that whenever r' = r > 3M (r' = r < 3M), the light-crossing singularities of the Wightman function for a given state are dominated by its ingoing (upgoing) sector while its upgoing (ingoing) sector contains only non-light-crossing singularities and is of overall smaller magnitude. This hypothesis suggests that the photonsphere is a privileged place, in the sense that when r' = r = 3M the ingoing and upgoing sectors of the Wightman function for the Boulware, Unruh and Hartle-Hawking states should provide equal contributions to its light-crossing singularities.

This is almost what is observed in the Wightman function for the Boulware state in our results for $r' = r \approx 2.995M$, which is the closest to the photonsphere we have data for, presented in Figures 66 and 67. Moreover, as an intriguing surprise, we see no trace of non-light-crossing singularities in this situation, making the photonsphere an even more special place while also suggesting that the nature of these singularities is related to it.

The conjecture we presented can be heuristically understood through a simple analysis of the propagation of the ingoing and upgoing field modes. To understand how, remember

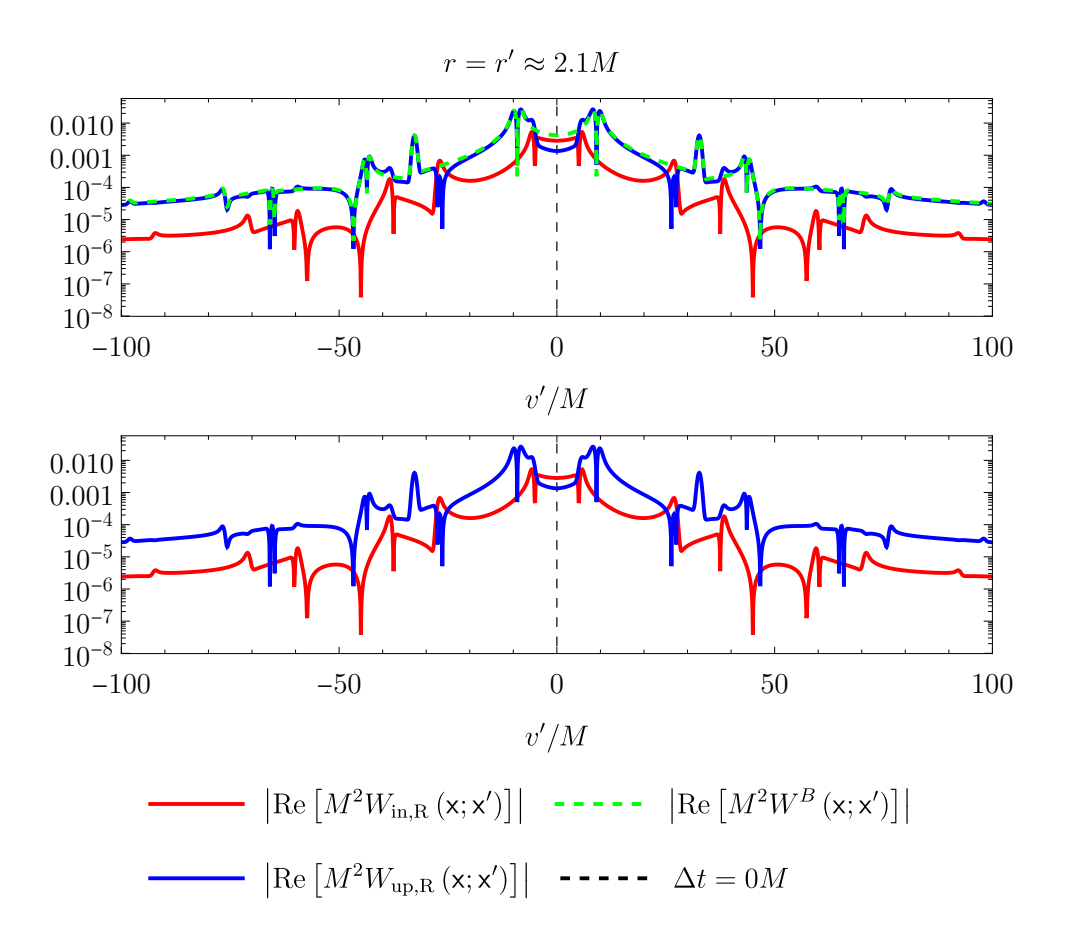


Figure 64 – Log-plot (top) of the magnitudes of $\operatorname{Re}\left[M^2W_{\operatorname{in,R}}\left(\mathbf{x};\mathbf{x}'\right)\right]$ (red), $\operatorname{Re}\left[M^2W_{\operatorname{up,R}}\left(\mathbf{x};\mathbf{x}'\right)\right]$ (blue) and $\operatorname{Re}\left[M^2W^B\left(\mathbf{x};\mathbf{x}'\right)\right]$ (green-dashed) as a function of $\Delta v = v' - v$ with $\Delta v > 0$. Here $\mathbf{x} = (v = 0M, \, r \approx 2.1M, \, \theta = 0, \, \varphi = 0)$ is separated by an angle of $\gamma = \pi/3$ from all points \mathbf{x}' on $r' \approx 2.1M$. Here we see that for r = r' < 3M, the real part of the Wightman function for the Boulware state is dominated by its upgoing sector, in contrast to the case r = r' > 3M where it was dominated by its ingoing sector.

that the upgoing sector of the Wightman function for the Boulware, Unruh and Hartle-Hawking states is composed by field modes launched from the horizon $r = r_s$ towards $r \to \infty$ and the ingoing sector is composed by field modes launched from $r \to \infty$ towards $r \to r_s$. Out of these modes, the ones that have a large enough frequency (so that the effective potential from Equation (4.3) can be neglected) propagate along null geodesics [59]. We will consider only these modes here. This simplification should be innocuous due to the fact that the light-crossing singularities are produced by modes propagating along null geodesics, hence, by large-frequency modes. Using this simplification, in the next paragraph we assume that the ingoing and upgoing modes propagate along future-directed ingoing and outgoing null geodesics, respectively.

For the first analysis, let x and x' be causally connected points at some r' = r < 3M. Then consider a future-directed ingoing null geodesic that is launched from $r \to \infty$ and reaches x (or x') at r < 3M. There is no turning point for such a geodesic, as can be

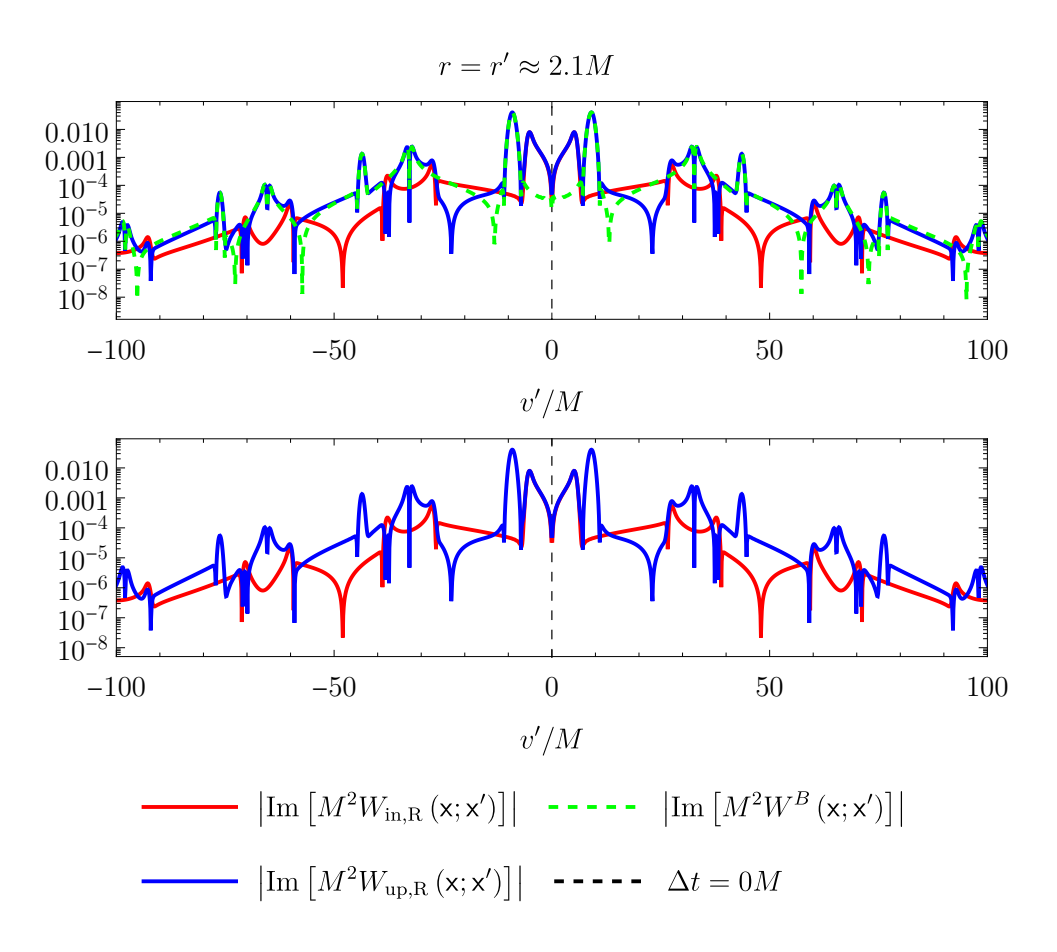


Figure 65 – Log-plot (top) of the magnitudes of $\operatorname{Im}\left[M^2W_{\operatorname{in,R}}\left(\mathbf{x};\mathbf{x}'\right)\right]$ (red), $\operatorname{Im}\left[M^2W_{\operatorname{up,R}}\left(\mathbf{x};\mathbf{x}'\right)\right]$ (blue) and $\operatorname{Im}\left[M^2W^B\left(\mathbf{x};\mathbf{x}'\right)\right]$ (green-dashed) as a function of $\Delta v = v' - v$ with $\Delta v > 0$. Here $\mathbf{x} = (v = 0M, \, r \approx 2.1M, \, \theta = 0, \, \varphi = 0)$ is separated by an angle of $\gamma = \pi/3$ from all points \mathbf{x}' on $r' \approx 2.1M$. Here we see that for r = r' < 3M, the imaginary part of the Wightman function for the Boulware is dominated by its upgoing sector, in contrast to the case r = r' > 3M where it was dominated by its ingoing sector.

seen in the effective potential for the null geodesics (Equation (2.30) and Figure 4). Then, that geodesic is bound to spiral down towards the singularity. As a side effect, it will never be able to reach \mathbf{x}' (or \mathbf{x}). Hence, we conclude that no future-directed ingoing null geodesic launched from $r \to \infty$ can connect two points \mathbf{x} and \mathbf{x}' at some r' = r < 3M. This explains the absence of light-crossing singularities in $W_{\text{in,R}}(\mathbf{x};\mathbf{x}')$ for $r' = r \approx 2.1M$ (Figures 64 and 65): The (large-frequency) ingoing modes travel on null geodesics that cannot connect \mathbf{x} and \mathbf{x}' . The caveat here is that despite not being able to connect \mathbf{x} to \mathbf{x}' , these null geodesics can connect \mathbf{x} to points that are increasingly close to \mathbf{x}' as r = r' approaches 3M. Since we are using smoothing functions in our calculations, the light-crossing singularities are smeared across a region of the spacetime. This enables them to be captured by the ingoing sector of the Wightman function if r' = r < 3M is close enough to the photonsphere. An example of this behavior is observed in Figures 66 and 67 where we considered $r = r' \approx 2.995M$.

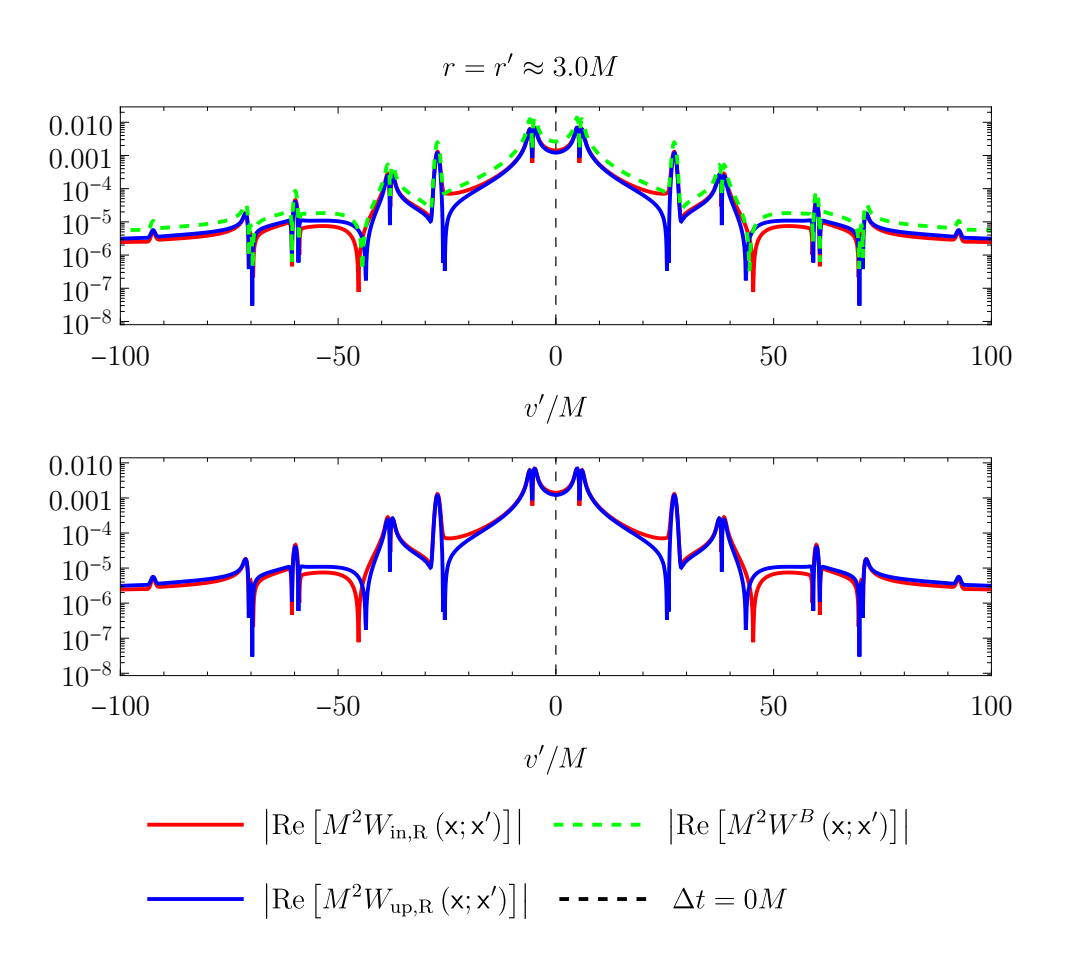


Figure 66 – Log-plot (top) of the magnitudes of $\operatorname{Re}\left[M^2W_{\operatorname{in,R}}\left(\mathbf{x};\mathbf{x}'\right)\right]$ (red), $\operatorname{Re}\left[M^2W_{\operatorname{up,R}}\left(\mathbf{x};\mathbf{x}'\right)\right]$ (blue) and $\operatorname{Re}\left[M^2W^B\left(\mathbf{x};\mathbf{x}'\right)\right]$ (green-dashed) as a function of $\Delta v = v' - v$ with $\Delta v > 0$. Here $\mathbf{x} = (v = 0M, \, r \approx 3M, \, \theta = 0, \, \varphi = 0)$ is separated by an angle of $\gamma = \pi/3$ from all points \mathbf{x}' on $r' \approx 3M$. Here we see that for $r = r' \approx 3M$ both the ingoing and upgoing sectors provide similar contributions to the real part of the Wightman function. We also note that in this case no non-light-crossing singularities appear.

To finish the analysis of this case, consider a future-directed outgoing null geodesic that is launched from $r=r_s$ towards $r\to\infty$ and reaches x (or x') at r<3M. Since it has not yet traveled past the photonsphere, that null geodesic can still meet a turning point and travel back towards the singularity. For that turning process, the geodesic can be fine-tuned to travel as close as needed to the photonsphere, so that it finishes as many orbits as necessary to reach x' (or x) on its way back to the singularity. Hence, the light-crossing singularities in this situation should always figure in the upgoing sector of the Wightman function for the Boulware, Unruh and Hartle-Hawking states. This is what we see for the Boulware state in Figures 64, 65, 66 and 67.

Now consider x and x' on r=r'=3M. In this case there exists both, ingoing and outgoing future-direct null geodesics connecting x and x'. This is because any ingoing or outgoing null geodesic launched with a critical impact parameter ($\varepsilon=\pm 3\sqrt{3}r_s/2$) will end up orbiting forever around the photonsphere, allowing them to freely connect points on

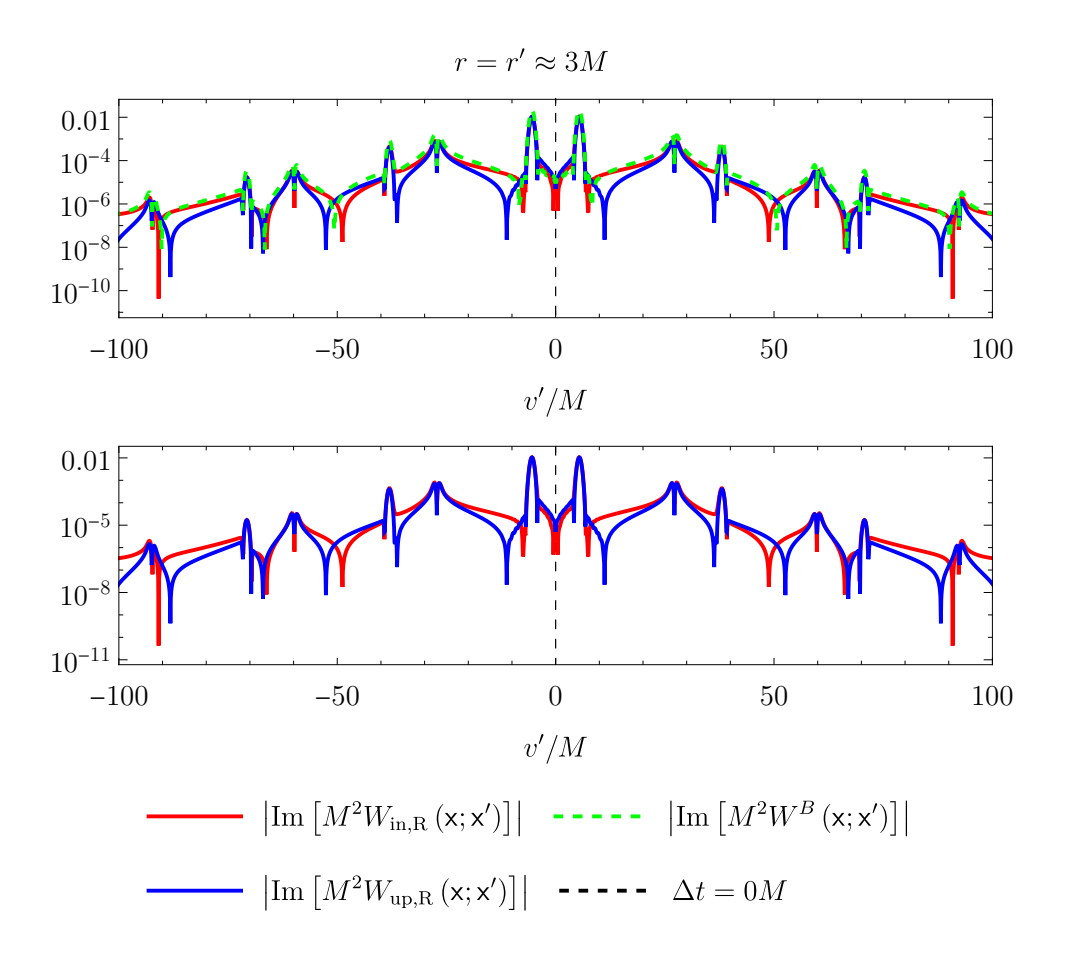


Figure 67 – Log-plot (top) of the magnitudes of $\operatorname{Im} [M^2W_{\operatorname{in,R}}(\mathsf{x};\mathsf{x}')]$ (red), $\operatorname{Im} [M^2W_{\operatorname{up,R}}(\mathsf{x};\mathsf{x}')]$ (blue) and $\operatorname{Im} [M^2W^B(\mathsf{x};\mathsf{x}')]$ (green-dashed) as a function of $\Delta v = v' - v$ with $\Delta v > 0$. Here $\mathsf{x} = (v = 0M, \, r \approx 3M, \, \theta = 0, \, \varphi = 0)$ is separated by an angle of $\gamma = \pi/3$ from all points x' on $r' \approx 3M$. Here we see that for $r = r' \approx 3M$ both the ingoing and upgoing sectors provide similar contributions to the imaginary part of the Wightman function. We also note that in this case no non-light-crossing singularities appear.

the photonsphere. Therefore, in this situation light-crossing singularities should appear in both the ingoing and upgoing sectors of the Wightman function for the Boulware, Unruh and Hartle-Hawking states, which is what Figures 66 and 67 illustrate.

Then consider x and x' on r' = r > 3M. Let a future-directed ingoing null geodesic be launched from $r \to \infty$ towards $r = r_s$, such that it reaches x at r > 3M. Since this null geodesic has not yet crossed the photonsphere, it can still meet a turning point and escape back to $r \to \infty$. In that process, that geodesic can be fine-tuned to travel as close as needed to the photonsphere, so that it completes as many orbits as necessary in order to reach x' in its way back to $r \to \infty$. Therefore, the ingoing sector of the Wightman function for the Boulware, Unruh and Hartle-Hawking states should always display the light-crossing singularities, which is in line with Figures 58 and 59.

To complete the analysis of that case, consider a future-direct outgoing null geodesic that is launched from $r = r_s$ towards $r \to \infty$ and reaches x at r > 3M. Since it has

already traveled past the photonsphere, it will not meet a turning point and is bound to travel towards $r \to \infty$, never meeting x' at r' = r on its way. Therefore, there are no future-directed outgoing null geodesic that connect x and x' at r = r' > 3M. This explains the absence of light-crossing singularities in $W_{\rm up,R}$ (x; x') for $r = r' \approx 6.009M$ (Figures 58 and 59). A caveat similar to that of the ingoing sector below the photonsphere also applies here: If r = r' > 3M becomes close enough to the photonsphere, the upgoing sector will be able to capture the smeared light-crossing singularities.

6 Lensing of entanglement harvesting near Schwarzschild Black Holes

In this chapter we adapted our published work [1] to the structure of this thesis, making partial use of its content (including figures) in the process.

In chapter 4 we constructed a method to analyze correlations in a quantum scalar field $\hat{\phi}$ (as constructed in Section ??) by directly evaluating its Wightman function which encodes all two-point correlations in a given state of the field. With this method we studied correlations in $\hat{\phi}$ on a (3+1)D Schwarzschild spacetime, as presented in Chapter 5. We now turn to another method, that is based on a simple particle detector model known as the Unruh-DeWitt (UdW) detector. With these detectors, we will explore entanglement in $\hat{\phi}$ via the effect of entanglement harvesting on a (3+1)D Schwarzschild spacetime.

This chapter is structured as follows: In Section 6.1 we introduce the formalism of Unruh-DeWitt detectors. In Section 6.2 we present the phenomenon of entanglement harvesting. In Section 6.3 we construct the setup with which we will treat the problem. In Section 6.4 we make a few considerations regarding how to differentiate harvested entanglement from the entanglement that is generated by communication through the field. Finally, in Section 6.5 we present our results.

6.1 Unruh-DeWitt detectors

In a general curved spacetime, a global timelike Killing vector is not guaranteed to exist. The lack of such vector leads to an issue when constructing a quantum field theory on a curved spacetime: It implies that there is no preferred choice of time direction, therefore, the very definition of vacuum is ambiguous in the sense that there are many physically reasonable vacuum states that are not related by a unitary transformation. This is discussed in Chapter 3. As a consequence, there are several non-equivalent notions of particle.

One approach to provide an operational meaning to the concept of particle in this context was given by Unruh and DeWitt [39, 60] in the form of simple particle detector model: A non-relativistic quantum system locally coupled to a quantum field. Such detector interacts with field modes that are of positive frequency with respect to the detector's proper time. A comprehensive account of this particle detector model is presented in [34, Chapter 3.3].

Despite its simplicity and non-relativistic nature, this detector model is covariant¹, causal [63, 62, 64, 61] and when angular momentum exchanges between its internal degrees

For non-pointlike detectors, this is not strictly true. For details see Refs. [61, 62]

of freedom and the field are negligible, it reproduces the main features of the light-matter interaction [65].

In this work we make use of a perturbative approach that will follow the same notation and conventions as those of [66]. For that end, we model a UdW detector D as a two-level system with a ground state $|g\rangle_{\rm D}$ and an excited state $|e\rangle_{\rm D}$ separated by an energy gap $\Omega_{\rm D}$. The interaction between the detector D and the quantum scalar field $\hat{\phi}$ along the detector's worldline $\mathbf{x}_{\rm D}(t)$ is given by the Hamiltonian ²

$$\hat{H}_{\text{int,D}}^t = \lambda_{\text{D}} \eta_{\text{D}}(t) \frac{\mathrm{d}\tau_{\text{D}}}{\mathrm{d}t} \hat{\mu}_{\text{D}}(t) \otimes \hat{\phi}(\mathsf{x}_{\text{D}}(t)), \tag{6.1}$$

where λ_D is a dimensionless — in (3+1)D — coupling constant, $\eta(t) \in [0, 1]$ is a real-valued switching function, τ_D is the detector's proper time and

$$\hat{\mu}_{D}(t) = e^{i\Omega_{D}\tau_{D}(t)} |e\rangle\langle g|_{D} + e^{-i\Omega_{D}\tau_{D}(t)} |g\rangle\langle e|_{D}$$
(6.2)

is the monopole operator. We remark that this Hamiltonian generates time-translations with respect to the t-coordinate but not with respect to the detector's proper time (see [66, 64] for a detailed discussion).

6.2 A brief introduction to entanglement harvesting

That quantum scalar fields typically present entanglement is a well-known fact [67, 68, 69, 70]. In general, the structure of this entanglement is determined by both the geometry of the underlying spacetime and the state of the quantum field. The influence of the state on entanglement is heuristically straightforward to understand. What might be slightly opaque is how a classical structure, such as the geometry of the underlying spacetime (in the semiclassical framework) can contribute to the entanglement — which is an inherently quantum feature — in a quantum field. At least for the Hadamard states, one can shed light on this issue by observing the singularity structure of the real part of the Wightman function (Equations 3.55), which contains information about quantum correlations (including entanglement) in the quantum field: For the Hadamard states, we can understand that geometry leaves its fingerprint in the entanglement structure of the quantum field through these singularities and that this fingerprint is state independent and as strong as these singularities. Examples of works exploring this issue are [71, 72, 73].

That entanglement structure plays a major role when studying phenomena that ranges from holography to Hawking radiation, including the information loss problem [6, 74, 75, 76, 77, 42, 2, 78, 79, 80, 81, 82]. To probe the spacetime distribution of entanglement, a possible method is to couple initially unentangled localized quantum systems (such as

In the context of the fully covariant formulation of [64], we can understand this as the result of integrating the Hamiltonian density [64, Equation 16] with $\delta(\mathsf{x}_d D)/\sqrt{-g}$ smearing over a spacelike hypersurface of constant t-coordinate.

UdW detectors) to the field at different spacetime regions. The entanglement acquired by these local systems in this process can be quantified by standard methods [20, 21].

Such experiment is tightly connected to entanglement harvesting which is an effect where the entanglement acquired by the localized quantum systems is extracted from preexisting entanglement in the field. This was first hinted at in [83, 84], in both flat and curved spacetimes. As the reader might have anticipated, this effect can capture the geometry [85] and topology [86] of the underlying spacetime. These properties suggest that entanglement harvesting is a promising tool to study entanglement in quantum fields. However, entanglement harvesting in black hole spacetimes has only been studied in very idealized scenarios such as (2+1)D Bañados-Teitelboim-Zanelli (BTZ) black holes [87] and (1+1)D spacetimes with horizons [23]. Exploring harvesting in (3+1)D black holes remained an open issue until we published the work that is being described in this chapter. The (3+1)D Schwarzschild spacetime is interesting because it provides a realistic description of electrically uncharged non-spinning spherically symmetrical black holes and introduces new phenomena due to the possibility of lensing [88] (due to orbiting null geodesics), the presence of caustics and the existence of an effective potential (4.3) near the horizon.

The issue of communication through quantum fields close to a Schwarzschild black hole has already been explored in [89]. The work described throughout this chapter investigates entanglement harvesting outside a Schwarzschild black hole for the quantum field $\hat{\phi}$ in the Boulware ($|B\rangle$), Unruh ($|U\rangle$) and Hartle-Hawking states ($|H\rangle$).

6.3 Setting up the theoretical experiment

As a remark before beginning the description of the setup, we note that in [1] we use a slightly different form of the mode-sum expression of the Wightman function for the Boulware, Unruh and Hartle-Hawking states in region I (Equations (3.74), (3.77) and (3.89), respectively). More precisely, in [1] we write these expressions in terms of integrals from $-\infty$ to ∞ in the frequencies, as in [41]:

$$W^{\psi}(\mathbf{x}; \mathbf{x}') = \frac{1}{(4\pi)^2} \sum_{\ell=0}^{\infty} (2\ell+1) P_{\ell}(\cos\gamma) \int_{-\infty}^{\infty} \frac{d\omega}{\omega} e^{-i\omega\Delta t} G_{\ell\omega}^{\psi}(r, r'; \Delta t), \tag{6.3}$$

where γ is the angular separation between x and x' and $\Delta t = t - t'$. The integrand kernel depends on the state of the quantum field. For the $|B\rangle$, $|U\rangle$ and $|H\rangle$ states, it takes the forms

$$G_{\ell\omega}^{B}(r,r') = \theta(\omega) \left(\frac{\psi_{\omega\ell}^{\text{in,R}}(r)\psi_{\omega\ell}^{\text{in,R}*}(r') + \psi_{\omega\ell}^{\text{up,R}}(r)\psi_{\omega\ell}^{\text{up,R}*}(r')}{rr'} \right), \tag{6.4}$$

$$G_{\ell\omega}^{U}(r,r') = \theta(\omega) \frac{\psi_{\omega\ell}^{\text{in,R}}(r)\psi_{\omega\ell}^{\text{in,R}*}(r')}{rr'} + \frac{1}{1 - e^{-4\pi\omega r_s}} \frac{\psi_{\omega\ell}^{\text{up,R}}(r)\psi_{\omega\ell}^{\text{up,R}*}(r')}{rr'}, \tag{6.5}$$

$$G_{\ell\omega}^{H}(r,r') = \frac{1}{1 - e^{-4\pi\omega r_s}} \frac{\psi_{\omega\ell}^{\text{in,R}}(r)\psi_{\omega\ell}^{\text{in,R}*}(r') + \psi_{\omega\ell}^{\text{up,R}}(r)\psi_{\omega\ell}^{\text{up,R}*}(r')}{rr'}.$$
(6.6)

We remark that the $\psi_{\omega\ell}^{\text{in,R/up,R}}$ modes defined in this thesis (Equations (4.5) and (4.13)) are related to the $\bar{R}_{\ell\omega}^{\text{in/up}}$ modes in [1] by

$$\bar{R}_{\ell\omega}^{\text{in/up}}(r) = \frac{\psi_{\omega\ell}^{\text{in,R/up,R}}(r)}{r}.$$
(6.7)

To investigate entanglement harvesting in the Schwarzschild spacetime we make use of two UdW detectors labeled by $D \in \{A, B\}$. As usual in the literature, we refer to detector A as Alice and B as Bob. Both are considered to be static, following world-lines $x_D(t)$ given by

$$\mathbf{x}_{\mathrm{D}}(t) = (t, r_{\mathrm{D}}, \theta_{\mathrm{D}}, \varphi_{\mathrm{D}}) \tag{6.8}$$

in SD-coordinates of region I (See table 5). The relation between the proper time of detector D and the coordinate time (t-coordinate) is given by

$$\frac{\mathrm{d}\tau_{\mathrm{D}}}{\mathrm{d}t} = \sqrt{f(r_{\mathrm{D}})},\tag{6.9}$$

where $f(r) = (1 - r_s/r)^{-1}$ is defined in Equation (2.4) (repeated here for the convenience of the reader) and $r_s = 2M$ is the Schwarzschild radius. We choose the integration constant to be zero (i.e., $\tau_D(0) = 0$), so that

$$\tau_{\rm D}(t) = \sqrt{f(r_{\rm D})}t. \tag{6.10}$$

The switching functions $\eta_{\rm D}(t)$ are chosen as the Gaussians

$$\eta_{\rm D}(t) = e^{-((t - t_{\rm 0D})/T_{\rm D})^2},$$
(6.11)

where t_{0D} denotes the center of the switching function (the coordinate time when the detector is completely turned on) and T_{D} is the switching width (the coordinate time interval within which the detector is considered to be turned on).

These detectors will interact with $\hat{\phi}$ through the Hamiltonian $\hat{H}_{\text{int,D}}^t$ (Equation (6.1)). We assume that initially $(t \to -\infty)$ the state of the system is a product state between the detectors in their ground state, represented by $\hat{\rho}_{AB} = |g\rangle\langle g|_{A} \otimes |g\rangle\langle g|_{B}$ and the field in a vacuum state $\hat{\rho}_{\psi} = |\psi\rangle\langle\psi|$ with $(\psi \in \{B, U, H\})$:

$$\hat{\rho}_0 = \hat{\rho}_{AB,0} \otimes \hat{\rho}_{\psi}. \tag{6.12}$$

This means that initially there is no entanglement between the detectors A and B or between each of them detectors and the field $\hat{\phi}$.

The time evolved version up to $t \to \infty$ of this state is given by

$$\hat{\rho}_{\infty} = \hat{U}\hat{\rho}_0 \hat{U}^{\dagger}, \tag{6.13}$$

where \hat{U} is the time evolution operator generated by $\hat{H}_{\text{int}}^t = \hat{H}_{\text{int,A}}^t + \hat{H}_{\text{int,B}}^t$. We can obtain a perturbative expression for that operator by using the so-called Dyson series:

$$\hat{U} = \mathbb{1} - i \int_{-\infty}^{\infty} dt \, \hat{H}_{\text{int}}^t - \int_{-\infty}^{\infty} dt \int_{-\infty}^t dt' \, \hat{H}_{\text{int}}^t \hat{H}_{\text{int}}^{t'} + \dots$$
 (6.14)

To simplify the notation, we define

$$\hat{U}^{(1)} = -i \int_{-\infty}^{\infty} dt \, \hat{H}_{\text{int}}^t \quad \text{and} \quad \hat{U}^{(2)} = -\int_{-\infty}^{\infty} dt \int_{-\infty}^t dt' \, \hat{H}_{\text{int}}^t \hat{H}_{\text{int}}^{t'}. \tag{6.15}$$

Using this convention, the perturbative expansion of $\hat{\rho}_{\infty}$ is written as

$$\hat{\rho}_{\infty} = \hat{\rho}_0 + \hat{\rho}_0 \hat{U}^{(1)\dagger} + \hat{\rho}_0 \hat{U}^{(2)\dagger} + \hat{U}^{(1)} \hat{\rho}_0 + \hat{U}^{(1)} \hat{\rho}_0 \hat{U}^{(1)\dagger} + \hat{U}^{(1)} \hat{\rho}_0 \hat{U}^{(2)\dagger} + \dots$$
(6.16)

The state of the detectors after such a time evolution is given by the reduced density matrix $\hat{\rho}_{AB,\infty}$ obtained by tracing over the field degrees of freedom:

$$\hat{\rho}_{AB,\infty} = \text{Tr}_{\phi} \left[\hat{\rho}_{\infty} \right]. \tag{6.17}$$

In terms of the perturbative expansion,

$$\hat{\rho}_{AB,\infty} = \hat{\rho}_{AB,\infty}^{(0,0)} + \hat{\rho}_{AB,\infty}^{(0,1)} + \hat{\rho}_{AB,\infty}^{(0,2)} + \hat{\rho}_{AB,\infty}^{(1,0)} + \hat{\rho}_{AB,\infty}^{(1,1)} + \dots, \tag{6.18}$$

where

$$\hat{\rho}_{AB,\infty}^{(i,j)} = \text{Tr}_{\phi} \left[\hat{U}^{(i)} \hat{\rho}_0 \hat{U}^{(j)\dagger} \right], \tag{6.19}$$

with $\hat{U}^{(0)} = \mathbb{1}$. In this expansion, the odd terms $(i + j = 2n + 1 \text{ with } n \in \mathbb{N}_{\geq 0})$ vanish and only the even terms contribute. To illustrate how, we compute $\hat{\rho}_{AB,\infty}^{(0,1)}$:

$$\hat{\rho}_{AB,\infty}^{(0,1)} = \operatorname{Tr}_{\phi} \left[\hat{U}^{(0)} \hat{\rho}_{0} \hat{U}^{(1)\dagger} \right]
= \operatorname{Tr}_{\phi} \left[\hat{\rho}_{0} \left(-i \int_{-\infty}^{\infty} dt \, \hat{H}_{int}^{t\dagger} \right) \right]
= -i \int_{-\infty}^{\infty} dt \, \operatorname{Tr}_{\phi} \left[\hat{\rho}_{0} \hat{H}_{int}^{t\dagger} \right]
= -i \int_{-\infty}^{\infty} dt \, \operatorname{Tr}_{\phi} \left[\hat{\rho}_{0} \left(\hat{H}_{int,A}^{t\dagger} + \hat{H}_{int,B}^{t\dagger} \right) \right]
= -i \int_{-\infty}^{\infty} dt \left(\operatorname{Tr}_{\phi} \left[\hat{\rho}_{0} \hat{H}_{int,A}^{t\dagger} \right] + \operatorname{Tr}_{\phi} \left[\hat{\rho}_{0} \hat{H}_{int,B}^{t\dagger} \right] \right)
= -i \int_{-\infty}^{\infty} dt \left(\lambda_{A} \eta_{A}(t) \frac{d\tau_{A}}{dt} \hat{\rho}_{AB} \hat{\mu}_{A}^{\dagger}(t) \operatorname{Tr}_{\phi} \left[\hat{\rho}_{\psi} \hat{\phi}(\mathbf{x}_{A}(t)) \right] \right)
+ \lambda_{B} \eta_{B}(t) \frac{d\tau_{B}}{dt} \hat{\rho}_{AB} \hat{\mu}_{B}(t) \operatorname{Tr}_{\phi} \left[\hat{\rho}_{0} \hat{\phi}(\mathbf{x}_{B}(t)) \right] \right)
= -i \int_{-\infty}^{\infty} dt \left(\lambda_{A} \eta_{A}(t) \frac{d\tau_{A}}{dt} \hat{\rho}_{AB} \hat{\mu}_{A}^{\dagger}(t) \langle \psi | \hat{\phi}(\mathbf{x}_{A}(t)) | \psi \rangle
+ \lambda_{B} \eta_{B}(t) \frac{d\tau_{B}}{dt} \hat{\rho}_{AB} \hat{\mu}_{B}(t) \langle \psi | \hat{\phi}^{\dagger}(\mathbf{x}_{B}(t)) | \psi \rangle \right)
\hat{\rho}_{AB,\infty}^{(0,1)} = 0,$$
(6.20)

since the field one-point function is zero for the $|B\rangle$, $|U\rangle$ and $|H\rangle$ vacuum states. By a similar calculation it is straightforward to show that $\hat{\rho}_{{}^{AB},\infty}^{(1,0)}=0$.

Therefore, the final perturbative expansion for $\rho_{AB,\infty}$ is

$$\hat{\rho}_{AB,\infty} = \hat{\rho}_{AB,\infty}^{(0,0)} + \hat{\rho}_{AB,\infty}^{(1,1)} + \hat{\rho}_{AB,\infty}^{(0,2)} + \hat{\rho}_{AB,\infty}^{(2,0)} + \mathcal{O}(\lambda^4), \tag{6.21}$$

where λ^n is a short notation for λ^{i+j} . Using the straightforward result $\hat{\rho}_{AB,\infty}^{(0,0)} = |g\rangle\langle g|_A \otimes |g\rangle\langle g|_B$, we finally obtain

$$\hat{\rho}_{AB,\infty} = \hat{\rho}_{AB} + \hat{\rho}_{AB,\infty}^{(1,1)} + \hat{\rho}_{AB,\infty}^{(0,2)} + \hat{\rho}_{AB,\infty}^{(2,0)} + \mathcal{O}(\lambda^4). \tag{6.22}$$

Using the basis order $|g\rangle_{\rm A}|g\rangle_{\rm B}$, $|e\rangle_{\rm A}|g\rangle_{\rm B}$, $|g\rangle_{\rm A}|e\rangle_{\rm B}$, $|e\rangle_{\rm A}|e\rangle_{\rm B}$, this state is represented by the density matrix

$$\hat{\rho}_{AB,\infty} = \begin{pmatrix} 1 - L_{AA}^{\psi} - L_{BB}^{\psi} & 0 & 0 & (M^{\psi})^* \\ 0 & L_{AA}^{\psi} & L_{AB}^{\psi} & 0 \\ 0 & L_{BA}^{\psi} & L_{BB}^{\psi} & 0 \\ M^{\psi} & 0 & 0 & 0 \end{pmatrix} + \mathcal{O}(\lambda^4), \tag{6.23}$$

where

$$M^{\psi} = -\lambda_{A}\lambda_{B} \int_{-\infty}^{\infty} dt \int_{-\infty}^{t} dt' \left(\eta_{A}(t) \frac{d\tau_{A}}{dt} e^{i\Omega_{A}\tau_{A}(t)} \frac{d\tau_{B}}{dt'} \eta_{B}(t') e^{i\Omega_{B}\tau_{B}(t')} W^{\psi} \left(\mathsf{x}_{A}(t); \mathsf{x}_{B}(t') \right) + \eta_{A}(t') \frac{d\tau_{A}}{dt'} e^{i\Omega_{A}\tau_{A}(t')} \frac{d\tau_{B}}{dt} \eta_{B}(t) e^{i\Omega_{B}\tau_{B}(t)} W^{\psi} \left(\mathsf{x}_{B}(t); \mathsf{x}_{A}(t') \right) \right)$$

$$(6.24)$$

and

$$L_{\rm DD'}^{\psi} = \lambda_{\rm D} \lambda_{\rm D'} \int_{-\infty}^{\infty} dt \int_{-\infty}^{\infty} dt' \, \eta_{\rm D}(t) \frac{d\tau_{\rm D}}{dt} \eta_{\rm D'}(t') \frac{d\tau_{\rm D'}}{dt'} e^{-i\Omega_{\rm D}\tau_{\rm D}(t) + i\Omega_{\rm D'}\tau_{\rm D'}(t')} W^{\psi} \left(\mathsf{x}_{\rm D}(t); \mathsf{x}_{\rm D'}(t') \right), \quad (6.25)$$

where $M^{\psi} \in \mathbb{C}$ while $L_{\mathrm{DD'}}^{\psi} \in \mathbb{R}_{\geq 0}$ when $\mathrm{D} = \mathrm{D'}$. For our case, where the detectors are static and their switching functions are Gaussian, we can use the mode-sum expression of the Wightman function for the Boulware, Unruh and Hartle-Hawking states in region I (Equation (6.3)) to manipulate M^{ψ} and $L_{\mathrm{DD'}}^{\psi}$ into forms that are more amenable to numerical evaluation due to demanding only a single numerical integration. The resulting expressions are Equations (A.9) and (A.10), repeated here for the convenience of the reader:

$$L_{\rm DD'}^{\psi} = \frac{\lambda_{\rm D} \lambda_{\rm D'} N_{\rm D} N_{\rm D'} T_{\rm D} T_{\rm D'}}{16\pi} \sum_{\ell=0}^{\infty} (2\ell+1) P_{\ell}(\cos\gamma)$$

$$\times \int_{-\infty}^{\infty} \! \mathrm{d}\omega \, \frac{G_{\ell\omega}^{\psi}(r_{\rm D}, r_{\rm D'})}{\omega} \mathrm{e}^{\mathrm{i}(\Omega_{\rm D'} N_{\rm D'} + \omega) t_{\rm 0D'} - \mathrm{i}(\Omega_{\rm D} N_{\rm D} + \omega) t_{\rm 0D} - \frac{1}{4}(\Omega_{\rm D} N_{\rm D} + \omega)^2 T_{\rm D}^2 - \frac{1}{4}(\Omega_{\rm D'} N_{\rm D'} + \omega)^2 T_{\rm D'}^2}$$
(6.26)

and

$$M^{\psi} = \frac{-\lambda_{A}\lambda_{B}f_{A}f_{B}T_{A}T_{B}}{32\pi} \sum_{\ell=0}^{\infty} (2\ell+1)P_{\ell}(\cos\gamma) \int_{-\infty}^{\infty} d\omega \frac{1}{\omega} \times \left(e^{-\frac{\mu_{A}^{2}T_{A}^{2} + \nu_{B}^{2}T_{B}^{2}}{4}} e^{i(\nu_{B}t_{0B} + \mu_{A}t_{0A})} \left(1 - i \operatorname{erfi} \left[\frac{\nu_{B}T_{B} - \mu_{A}T_{A}}{2\sqrt{2}} + \frac{i}{\sqrt{2}} \left(\frac{t_{0A}}{T_{A}} - \frac{t_{0B}}{T_{B}} \right) \right] \right) G_{\ell\omega}^{\psi}(r_{A}, r_{B}) + e^{-\frac{\mu_{B}^{2}T_{B}^{2} + \nu_{A}^{2}T_{A}^{2}}{4}} e^{i(\nu_{A}t_{0A} + \mu_{B}t_{0B})} \left(1 - i \operatorname{erfi} \left[\frac{\nu_{A}T_{A} - \mu_{B}T_{B}}{2\sqrt{2}} + \frac{i}{\sqrt{2}} \left(\frac{t_{0B}}{T_{B}} - \frac{t_{0A}}{T_{A}} \right) \right] \right) G_{\ell\omega}^{\psi}(r_{B}, r_{A}) \right),$$

$$(6.27)$$

where $f_{\rm D}=f(r_{\rm D}),\,N_{\rm D}=\sqrt{f_{\rm D}},\,\nu_{\rm D}=\omega+\Omega_{\rm D}N_{\rm D},\,\mu_{\rm D}=\Omega_{\rm D}N_{\rm D}-\omega,\,{\rm erfi}(z)=-{\rm i}\,{\rm erf}(z)$ and ${\rm erf}(z)$ is the error function ([48, Chapter 7.2(i)]). Details of the derivation of these expressions are presented in Appendix A. To perform the numerical evaluations, we fold these integrals so that they run from 0 to ∞ .

As can be noticed, these integrals are of the same form as the ones we solved in Chapter 5, hence, the same technique will be applied to solve them (but without ℓ -smoothing and here the ω -smoothing is given by the setup). We also take the opportunity to highlight that both M^{ψ} and $L_{\rm DD}^{\psi}$ are integrals of the Wightman function smeared against a smoothing function that is given by the setup — This is in contrast to the arbitrary choice of smoothing function in Chapter 5.

To quantify and study the entanglement between the two detectors in their final state $\rho_{AB,\infty}$ we use its negativity³ since we do not expect their joint-state to always be a pure state (if this was the case, we could have used the entanglement entropy, for instance).

The negativity of a given quantum state represented by a density matrix ρ is defined as the absolute value of the sum of the negative eigenvalues of its partial-transpose $\hat{\rho}^{\text{pt}}$ with respect to the first system. In our case, the partial transpose of $\hat{\rho}_{AB,\infty}$ with respect to the basis of A is

$$\hat{\rho}_{AB,T}^{pt} = \begin{pmatrix} 1 - L_{AA}^{\psi} - L_{BB}^{\psi} & 0 & 0 & L_{AB}^{\psi} \\ 0 & L_{AA}^{\psi} & (M^{\psi})^{*} & 0 \\ 0 & M^{\psi} & L_{BB}^{\psi} & 0 \\ L_{BA}^{\psi} & 0 & 0 & 0 \end{pmatrix} + \mathcal{O}(\lambda^{4})$$
(6.28)

and its only (possibly) negative eigenvalue (to $\mathcal{O}(\lambda^4)$) is

$$E_1 = \frac{1}{2} \left(L_{AA}^{\psi} + L_{BB}^{\psi} - \sqrt{(L_{AA}^{\psi} - L_{BB}^{\psi})^2 + 4|M^{\psi}|^2} \right) + \mathcal{O}(\lambda^4).$$
 (6.29)

The negativity of a quantum state is an example of an entanglement monotone. Entanglement monotones are functions of state capable of quantifying entanglement. Another popular example is the entanglement entropy. For a complete view on this topic, the reader is referred to [90, Section 16.8].

For simplicity, we define $\mathcal{N}^{\psi,(2)} = -E_1$. Therefore, the negativity of $\hat{\rho}_{AB,T}$ is

$$\mathcal{N}^{\psi} = \max \left[\mathcal{N}^{\psi,(2)}, 0 \right] + \mathcal{O}(\lambda^{4})
= \max \left[\frac{1}{2} \left(\sqrt{(L_{AA}^{\psi} - L_{BB}^{\psi})^{2} + 4|M^{\psi}|^{2}} - L_{AA}^{\psi} - L_{BB}^{\psi} \right), 0 \right] + \mathcal{O}(\lambda^{4}).$$
(6.30)

This expression shows that there are three quantities involved in the quantification of entanglement: M^{ψ} , L_{AA} and L_{BB} . The first is a non-local term in the sense that it depends on the histories of both detectors. Due to this property, we can understand M^{ψ} as the term that produces the entanglement. On the other hand, L_{AA} and L_{BB} are local terms because each of them depend only on the history of a single detector. For this reason, these terms do not carry information about field correlations between the regions where the detectors interact with the field. In the end, we see in Equation (6.29) that what defines if $\mathcal{N}^{\psi} > 0$ is a competition between these local terms and M^{ψ} . In particular, it is clear that L_{AA} and L_{BB} spoil the entanglement we are trying to measure. For this reason, we refer to them as local noise terms.

For the case we are going to study in Section 6.5, the local noise term is equal for both detectors, $L_{\text{DD}}^{\psi} := L_{\text{AA}}^{\psi} = L_{\text{BB}}^{\psi}$. This will happen because we will assume identical detectors that follow the same world-line and differ only by the coordinate time where their switching-functions peak, i.e., $t_{0A} \neq t_{0B}$. In this case the negativity simplifies to

$$\mathcal{N}^{\psi} = \max\left[\left|M^{\psi}\right| - L_{\text{DD}}^{\psi}, 0\right] + \mathcal{O}(\lambda^{4}), \tag{6.31}$$

and intuitively shows that there will be entanglement between the detectors only if the non-local term overcomes the local noise.

6.4 When is the entanglement extracted versus generated?

The phenomenon of entanglement harvesting, presented in Section 6.2, is a handy tool to probe the entanglement structure of a quantum field in a given state as it can demonstrate the existence of entanglement in that field across different spacetime regions. However, it should be handled with care: Considering our setup, where a pair of initially uncorrelated particle detectors become entangled after interacting with a quantum scalar field, one cannot immediately conclude that this entanglement was harvested from the field. The reason is that there are two ways through which these particle detectors can acquire entanglement: By harvesting from the background field and/or by indirectly interacting with one another via the field — we will refer to the last one as entanglement generated by communication, since it is a byproduct of causal communication (through the field) between the detectors.

When the detectors are causally disconnected (spacelike separated) it is immediate to conclude that any entanglement they acquire is due to harvesting from the field (see [84, 21] for examples on flat spacetime) because in this case causal communication

between them is impossible. On the other hand, when the detectors are causally connected (timelike separated), distinguishing harvested entanglement from that produced through communication is a delicate task. For that end, we will anchor our arguments in the fact that the real part of the Wightman function carries information about quantum correlations (Equation (3.48)) while the imaginary part contains information about classical correlations and is state-independent (Equation (3.47)).

With that in mind, we note that to leading order in the perturbative correction to $\rho_{AB,\infty}$ (Equation (6.23)), the non-local term M^{ψ} (Equation (6.24)) can be written as a sum of a state-dependent and a state-independent quantity as in [19, Equation (31)],

$$M^{\psi} = M_{+}^{\psi} + iM_{-}^{\psi}, \tag{6.32}$$

where M_{+}^{ψ} is obtained by replacing W^{ψ} by its real part (which is symmetric) on the right-hand side of Equation (6.24), and M_{-}^{ψ} by replacing it with its imaginary part (which is antisymmetric). Note that, in general, M_{+}^{ψ} and M_{-}^{ψ} are complex-valued.

Considering this decomposition there are scenarios where the detectors become entangled while M^{ψ} is dominated by M^{ψ}_{-} with M^{ψ}_{+} (almost or exactly) vanishing. In this case, most of the entanglement acquired by the detectors is state-independent and should not to be attributed to preexisting entanglement in the field, that is, most of it was not harvested. To see why, notice that in this scenario the entanglement between the detectors, as measured by $\mathcal{N}^{\psi,(2)}$, remains (almost or exactly) unchanged if we replace the initial field state ρ_{ψ} by another state $\rho_{\psi'}$ such that L^{ψ}_{AA} and L^{ψ}_{BB} also remain unchanged — Since both L^{ψ}_{AA} and L^{ψ}_{BB} are local terms, this condition implies that the Wightman function for $\rho_{\psi'}$ is equal to that of ρ_{ψ} on the world-lines of A and B but can be different everywhere else. The value of $M^{\psi} \approx M^{\psi}_{-}$ would remain almost (or exactly, if M^{ψ}_{+} vanishes) unchanged due to the fact that M^{ψ}_{-} is state-independent.

Therefore, the entanglement acquired by the detectors in this situation is almost the same, independently of the initial state of the field. Hence, it is reasonable to assume that such entanglement is predominantly generated through causal communication instead of being harvested from the field. This line of reasoning is analogous to that presented in [19] to argue that in these cases where M_+^{ψ} is (almost or exactly) vanishing, the entanglement acquired by the detectors should not be attributed to "entanglement harvesting" from the field.

On the other hand, when the detectors are not causally connected $M^{\psi} = M_{+}^{\psi}$ because M_{-}^{ψ} depends on the field commutator, which is zero in this case. As pointed before, in this situation all of the entanglement between the detectors was harvested from the field. In this scenario we can understand that the entanglement was transferred from the field to the detectors via the (state-dependent) field anti-commutator.

In addition, as pointed in [19], for causally connected (timelike-separated) detectors, M_+^{ψ} encodes contributions to the resulting entanglement (between the detectors) that

can be attributed to both, harvesting — due to its state-dependent nature — and causal communication. This happens because the same process that allow causally connected detectors to harvest entanglement also allows causal communication between them. In the causal communication process, the field carries information between the detectors an can get them entangled independently of any preexisting entanglement in the field. However, to leading order in perturbation theory (which we are considering), the causal influence that one detector has on the other is determined solely by the field's commutator(see [63, Equation 24]). Hence, as argued in [19], we find it reasonable to conclude that the detectors are harvesting preexisting entanglement from the field if M^{ψ} is dominated by contributions arising from the anticommutator, that is, if $M^{\psi} \approx M_{+}^{\psi}$.

6.5 Harvesting of gravitationally lensed vacuum entanglement

(Disclaimer: In what follows, we reproduce the corresponding section from [1] in full.)

This section contains the main results which demonstrate the impact of gravitational lensing — which at caustics refocuses null geodesics emanating from a common source — on entanglement harvesting. To this end, we consider two static UdW detectors placed close to the black hole horizon and compare their behavior with the well-studied case of static detectors in flat spacetime.

As one would expect, an important parameter that decides if and to what extent two detectors become entangled is their distance. The distance between (the static worldlines of) the two detectors can be defined in terms of various meaningful measures (see [89]). In the present context (of static observers in Schwarzschild or Minkowski spacetime), the light propagation coordinate time is an intuitive choice of measure which we use henceforth when referring to the distance between detectors. This is the minimal amount of (Schwarzschild or Minkowski) coordinate time that it takes light to propagate from the spatial position of one detector to that of the other detector along a null geodesic.

Once the spatial positions of the two detectors are chosen and, thus, their distance is fixed, the interaction of the detectors with the field can still be made to happen at spacelike, lightlike or timelike separation by introducing a switching delay; this means that the switching function of the second detector is shifted with respect to the first one by a certain amount of coordinate time. For example, in the following we will assume that both detectors couple through the same switching function (6.11) and introduce the switching delay $\Delta_{\text{BA}} = t_{0\text{B}} - t_{0\text{A}}$ as the (coordinate time) difference between the centers of the switching functions. The switching delay can then be used to maximize the entanglement in the final state of the two detectors.

In Minkowski spacetime, as far as the impact of the switching delay is concerned, the entanglement in the final state between two detectors at a fixed distance is maximized when the switching functions are exactly null aligned [19], i.e., when the switching delay

equals the light propagation time.⁴ As far as the impact of the distance between the detectors is concerned, its impact on the final entanglement is straightforward: if the distance between the detectors is increased (while allowing the switching delay to be optimal and leaving other coupling parameters unchanged), the entanglement between the detectors in their final state decreases and goes to zero beyond a certain distance. This holds even if the switching delay is readjusted to uphold null alignment. Furthermore, in (3+1)D Minkowski spacetime, the entanglement between exactly null aligned detectors is dominated by correlations generated by communication rather than by harvesting, because the M^{ψ} term is dominated by M^{ψ}_{-} rather than M^{ψ}_{+} , as shown in [19].

This raises two questions regarding entanglement harvesting in Schwarzschild spacetime. First: does the presence of caustics enhance the ability of detectors to become entangled? What is more, can caustics make the harvested entanglement no longer decrease monotonically with distance?

Second: does the singularity structure of the Wightman function allow for the entanglement to be dominated by harvesting rather than signaling if the detectors' switching instead of being aligned along a direct null geodesic is aligned along a secondary null geodesic, i.e., a null geodesic that has passed through a caustic? As discussed in Section 3.4.1, in this case the singularity structures of the real and imaginary parts of the Wightman function are shifted, so that M_+^{ψ} could dominate over M_-^{ψ} because the real part now carries the $\delta(\sigma)$ singularity. This would then constitute entanglement harvesting between timelike-separated detectors, since the secondary null geodesics lie inside the causal cone which is bounded by the direct null geodesics between detectors.

The following results answer both questions in the affirmative.

Figure 68 shows the gravitational lensing effect on the harvesting of entanglement by two static detectors in Schwarzschild spacetime when the field is in the Boulware state. The scenario is as follows: Two identical detectors, with detector gap $\Omega_{AA} = \Omega_{BB} = 5M^{-1}$ and $\lambda = \lambda_A = \lambda_B^{5}$ are placed on static worldlines at the same radial coordinate $r \approx 6.009M$. The angular separation γ between the two detectors varies along the horizontal axes of each panel. Both detectors are coupled to the field through the Gaussian switching function (6.11), but the difference between the two centers of the switching functions is shifted by an amount of coordinate time $\Delta_{BA} = t_{0B} - t_{0A}$ which varies between the panels as indicated.

An inset in each panel visualizes how far null geodesics, emanating from detector A at time t_{0A} , propagate within the coordinate time interval Δ_{BA} : the black filled circle represents the interior of the black hole horizon at $r = r_s = 2M$, a black ring around it represents all points with radial coordinate $r \approx 6.009M$ and the red dot represents the

This statement is not entirely precise, as in Minkowski spacetime the maximum is located very close to
— but not exactly at — null alignment of the switching functions, see [19].

Note that because λ is dimensionless and all terms are of order $\mathcal{O}(\lambda^2)$ the numerical value of λ only affects the result by an overall factor. We choose $\lambda = 1$ for improved readability.

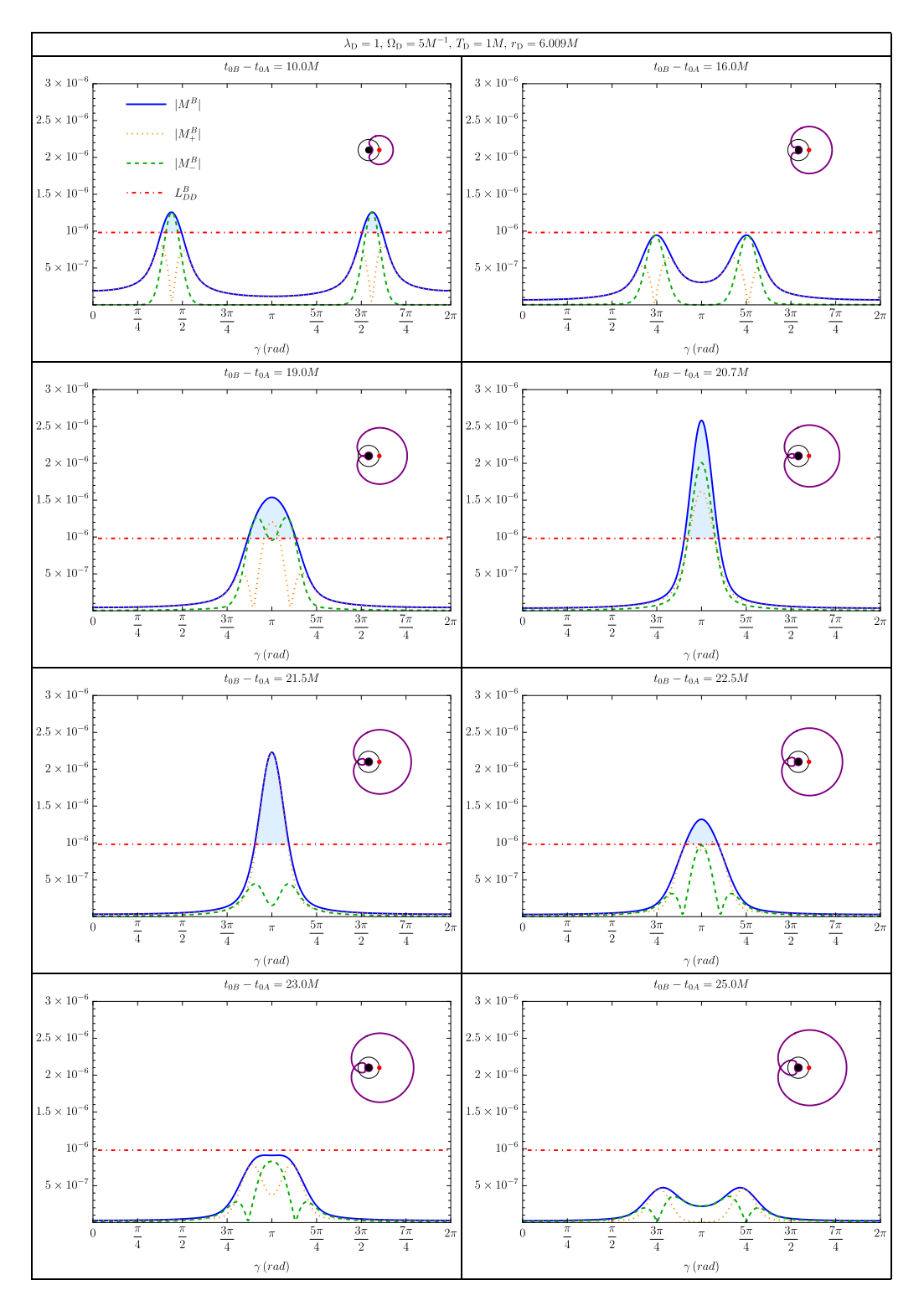


Figure 68 – Gravitational lensing of entanglement harvesting from the Boulware state: the plots show the entries $|M^B|$, $|M_{\pm}^B|$ and $|L_{\rm DD}^B|$ of the final detectors' state (6.23) for two static detectors placed at radial coordinate r=6.009M with varying angular separation γ . Blue shading indicates where $|M^B| > L_{\rm DD}^B$, i.e., the negativity (6.30) is positive and the detectors become entangled. All detector parameters are equal ($\lambda_{\rm D}=1,~\Omega_{\rm D}=5M^{-1},~T_{\rm D}=1M$); only the delay $\Delta_{\rm BA}=t_{\rm 0B}-t_{\rm 0A}$ between the switching functions (6.11) varies between plots. The insets indicate how far a null wave front propagates from the red point within a coordinate time interval $\Delta_{\rm BA}$. In particular, at $\Delta_{\rm BA}\approx 20.7386M$ at the antipodal point of the red point, i.e., at $\gamma=\pi$, the wave front intersects itself and the first caustic point forms.

spatial location of detector A. The violet curve then indicates the spatial position of the null wave front after propagation time $\Delta_{\rm BA}$. In particular, the different insets show the formation of caustics located at angular separation $\gamma = \pi$ from the point of origin (which is plotted in red) where the null wave front intersects itself. The caustic reaches $r \approx 6.009 M$ at $\Delta_{\rm BA} \approx 20.7386 M$.

The four different curves in each panel show the resulting contributions to the final density matrix of the two detectors (6.23), when the field is in the Boulware state. (Accordingly they are denoted with a superscript $\psi = B$.) The horizontal, red and dashed line shows the single detector noise term $L_{\text{\tiny DD}}^B:=L_{\text{\tiny AA}}^B=L_{\text{\tiny BB}}^B$. Because it only depends on the radial coordinate and the switching function's width T_D , it is equal for both detectors and constant for all positions of detectors considered here. The blue solid curve shows the absolute value $|M^B|$ resulting from the chosen value of the switching delay $\Delta_{\rm BA}$ in each panel, as a function of the angular separation between the detectors. The two remaining dashed curves show the absolute values $|M_{-}^{B}|$ in green and $|M_{+}^{B}|$ in orange which, as discussed in Section 6.4, are obtained by replacing the Wightman function by its imaginary and real parts, respectively. In particular, as discussed in Section 6.4, if $|M^B|$ is dominated by $|M_{-}^{B}|$ (obtained from the imaginary part), then the detectors' entanglement is predominantly generated in the sequential interaction of the detectors with the field. On the other hand, if $|M^B|$ is dominated by $|M_+^B|$ then final entanglement between the detectors is predominantly harvested from preexisting entanglement in the vacuum of the field.

Altogether the panels in Figure 68 illustrate the lensing effect which appears in proximity to the caustics. The first two panels show the settings with the shortest switching delay Δ_{BA} between the switching functions. In these two plots, we see that the correlations between the detectors, as captured by $|M^B|$, are largest when the centers of the intervals during which the detectors couple to the field are connected by (direct) null geodesics. In the first panel there is a certain interval of angular separations in which the blue line for $|M^B|$ exceeds the noise term L_{D}^B and the detectors end up entangled. However, in the second panel the detectors' final state remains separable, even for null separated detectors, because Δ_{BA} is increased. Note that here the contribution from M_{-}^B dominates the peaks of M^B ; hence entanglement between the detectors cannot be attributed to harvesting of preexisting entanglement from the field but to entanglement generation due to sequential interaction.

In flat spacetime no entanglement would be observed in the final detectors' state for larger switching delay between the detectors. Intuitively this is related to the growth of the light cone's surface area which dilutes the entanglement. In Schwarzschild spacetime, however, where the light cone refocuses at caustics the opposite can happen. As seen in the third through sixth panels (in order of increasing Δ_{BA}), the detectors can become entangled at larger switching delays Δ_{BA} again, at angular separations close to $\gamma = \pi$

in the proximity of caustics. This answers in the affirmative the first of the two guiding questions raised in the previous paragraphs.

The second of the two questions raised above pertains to the Wightman function's singularity structure described in Section 3.4.1. Its effect is easy to recognize when comparing the last (bottom right) panel to the first (top left) panel of Figure 68. In both panels the correlations between the two detectors, as captured by $|M^B|$, are maximal for null aligned detectors. However, in the first panel the detectors are connected by primary null geodesics, whereas in the last panel they are connected by secondary null geodesics. At secondary null geodesics, as discussed in Section 3.4.1, the singularity structure of the Wightman function is shifted from primary null geodesics so that now the real (anticommutator) part carries the $\delta(\sigma)$ singularity, which used to be carried instead by the imaginary (commutator) part in the case of primary null geodesics. Accordingly, the two contributions $|M_{+}^{B}|$ have a qualitatively similar overall shape in the first and the last panels, except that the M_{+}^{B} and M_{-}^{B} have swapped places. For detectors aligned along a secondary null geodesic, the real part contribution M_{+}^{B} dominates over the imaginary part contribution M_{-}^{B} . So if these correlations overcame the noise, $|M^{B}| > |L_{\text{DD}}|$, the detectors would become entangled by harvested entanglement. However, the correlations in the last panel are too weak for the detectors to end up entangled. To find detectors that get entangled by genuinely harvested correlations around secondary null geodesics, we need to position the detectors closer to caustics so as to make use of the overall enhancement of the Wightman function there. Such a setting is seen in the fifth panel (for $\Delta_{\text{BA}} = 21.5M$) of Figure 68. In this and the following panels of Figure 68, the switching delay Δ_{BA} is larger than the shortest light propagation (Schwarzschild coordinate) time between detectors with angular separation $\gamma = \pi$, and the detectors (at $r \approx 6.009M$) which are null aligned here are aligned along a secondary null geodesic and timelike separated. With this we have answered in the affirmative the second of the above questions, as we observe the genuine harvesting of preexisting entanglement from the field by timelike-separated detectors, aligned along secondary null geodesics. In the following, we will see further examples allowing for entanglement harvesting between timelike-separated detectors with angular separation $\gamma = \pi$.

Complementary to Figure 68, the same scenario and effects are seen in Figure 69 from a slightly different perspective. Here, the contributions to the detectors' final density matrix are plotted over the coordinate time switching delay $\Delta_{\rm BA}$, while the four different panels correspond to four different angular separations. (Figure 70 provides a logarithmic plot of the same data.) Note that these plots over $\Delta_{\rm BA}$ are directly comparable to the plots also found in [19] in (3+1)D Minkowski spacetime.

In the first panel of Figure 69, for angular separation $\gamma = \pi/5$, there are three peaks appearing in $|M^B|$ which correspond to an alignment of the switching functions along primary, secondary and tertiary null geodesics, respectively. The qualitative structure of

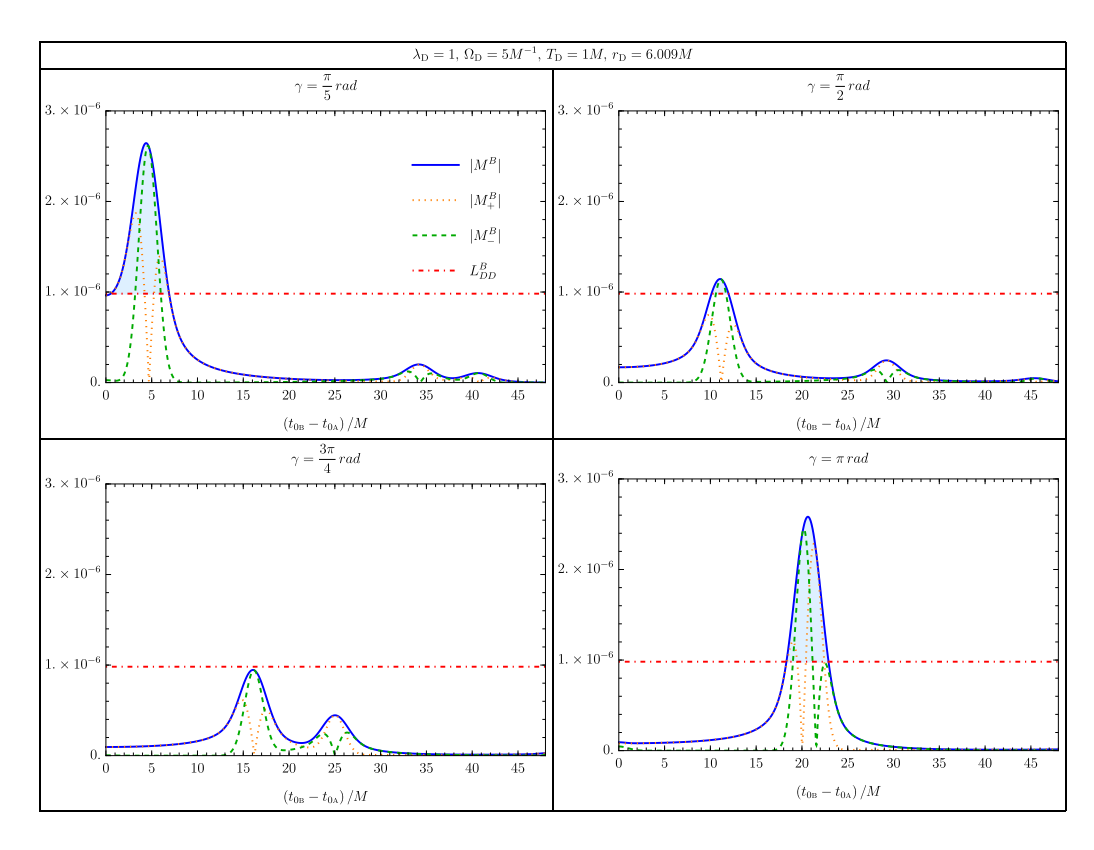


Figure 69 – Same data as Figure 68 from a different perspective: the switching delay $\Delta_{\text{BA}} = t_{0\text{B}} - t_{0\text{A}}$ is plotted on the horizontal axis, while the panels show detectors with four different angular separations. (See Figure 70 for a logarithmic plot.)

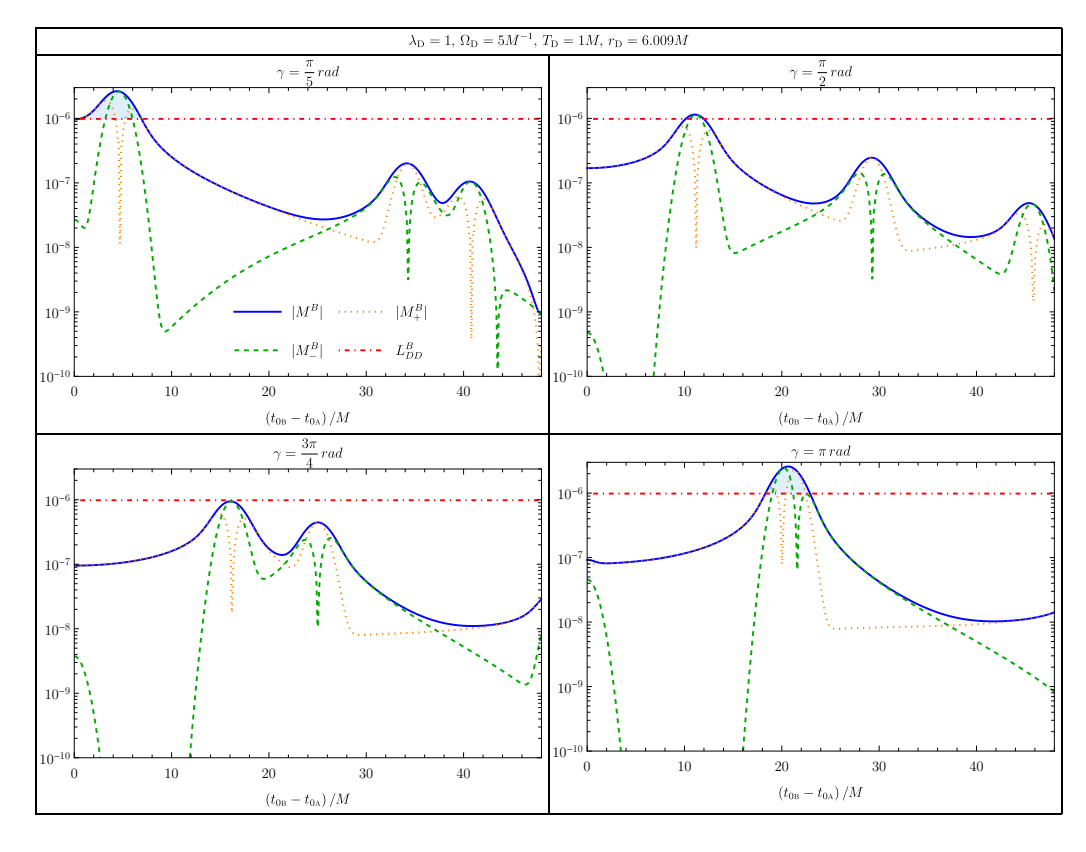


Figure 70 – Logarithmic plot version of Figure 69.

State	Local noise term
Boulware state	$L_{\scriptscriptstyle DD}^{B}/(\lambda_{\scriptscriptstyle \rm A}\lambda_{\scriptscriptstyle \rm B}) = 9.82\times 10^{-7}$
Unruh state	$L_{\scriptscriptstyle DD}^{\scriptscriptstyle U}/(\lambda_{\scriptscriptstyle \rm A}\lambda_{\scriptscriptstyle \rm B}) = 9.96\times 10^{-7}$
Hartle-Hawking state	$L_{\scriptscriptstyle DD}^{\scriptscriptstyle H}/(\lambda_{\scriptscriptstyle \rm A}\lambda_{\scriptscriptstyle \rm B}) = 1.08\times 10^{-6}$

Table 11 – Numerical values of the local noise terms in the three different states considered, for the scenarios in Figure 68, Figure 71 and Figure 72, respectively.

the first peak and its contributions from $|M_{+}^{B}|$ and $|M_{-}^{B}|$ correspond to the structure found in flat spacetime in [19]. However, in the secondary peak the qualitative roles of $|M_{+}^{B}|$ and $|M_{-}^{B}|$ are interchanged due to the shifted singularity structure of the Wightman function, as is easy to see in the logarithmic plot in Figure 70. For the tertiary peak, together with the singularity structure of the Wightman function, the qualitative structure of the peak also shifts back to its primary form.

Even if there are three peaks appearing at angular separation $\gamma = \pi/5$, only the first one corresponding to alignment along the direct, primary null geodesic exhibits entanglement in the detectors' final state. In an intermediate regime of angular separations, for $0.64\pi \lesssim \gamma \lesssim 0.81\pi$, not even the primary peak overcomes the noise and the detectors' final state remains separable for all switching delays $\Delta_{\rm BA}$. An example of this is seen in the third (bottom left) panel of Figure 69 for angular separation $\gamma = 3\pi/4$. However, as the angular separation approaches $\gamma = \pi$ both the primary and secondary peaks increase their size again and they overcome the noise, thus, leaving the detectors in an entangled state. Gradually, as $\gamma \to \pi$, the primary and secondary peaks superpose and finally create one joint peak aligned at the caustic for $\gamma = \pi$. Here we see that for switching delays that are somewhat larger than the direct null alignment, the extracted entanglement can be dominated by $|M_+^B|$ and thus can be attributed to entanglement harvesting from the field.

The results shown in Figure 68 are for the field in the Boulware state. As seen in the analogous Figure 71 for the Unruh state and Figure 72 for the Hartle-Hawking state, the same phenomena appear in these states as well. In fact, the quantitative differences between the states (which may be difficult to see with the naked eye) are mostly due to the difference in the noise term, which is given in Tab. 11. The correlation terms, in particular in the scenarios of detectors that harvest entanglement in the proximity of caustics, agree to many digits for all three states, as can be seen in Figure 73, which shows their relative differences.

We conclude this section with a study of entanglement harvesting from the Boulware state between detectors at antipodal locations with the black hole exactly in the middle between them, i.e., at identical radial coordinates $r = r_{\rm A} = r_{\rm A}$ and with an angular separation $\gamma = \pi$, for a range of detector locations reaching down very close to the horizon at radial positions $r \approx 2.095 M$.

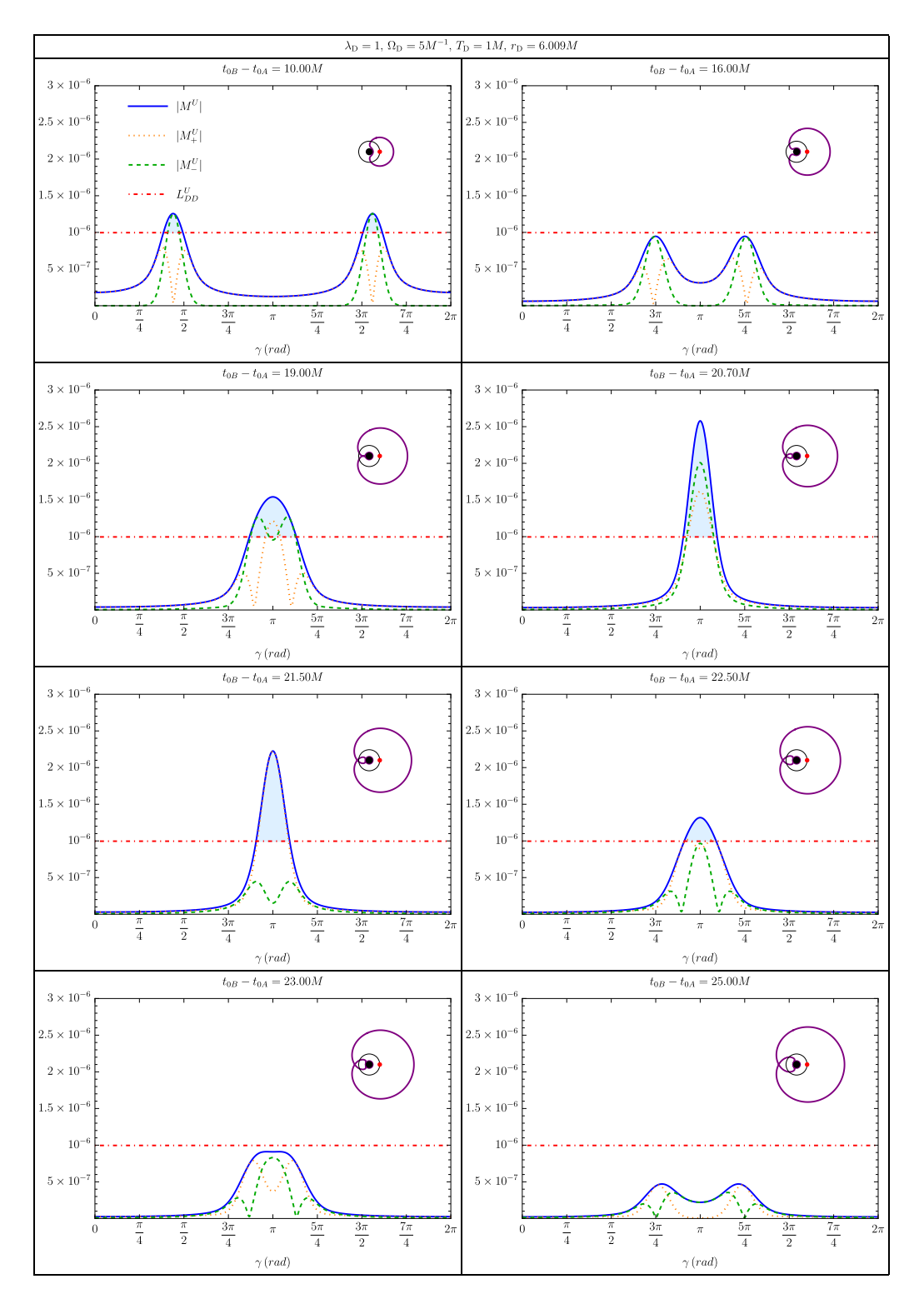


Figure 71 – Gravitational lensing of entanglement harvesting from the field in the Unruh state: the entire setup is identical to the setup of Figure 68, except that here the initial state for the field is the Unruh state. The plots show the absolute values of M^U , M_{\pm}^U and $L_{\rm DD}^U$ in Eq. (6.23) for two static detectors placed at radial coordinate r=6.009M with varying angular separation γ . All detector parameters are equal ($\lambda_{\rm D}=1$, $\Omega_{\rm D}=5M^{-1}$, $T_{\rm D}=1M$); only the offset $\Delta_{\rm BA}=t_{\rm 0B}-t_{\rm 0A}$ between the two switching functions (6.11) varies between the plots. The inset indicates how far a null wave front propagates from the red point within a coordinate time interval $\Delta_{\rm BA}$.

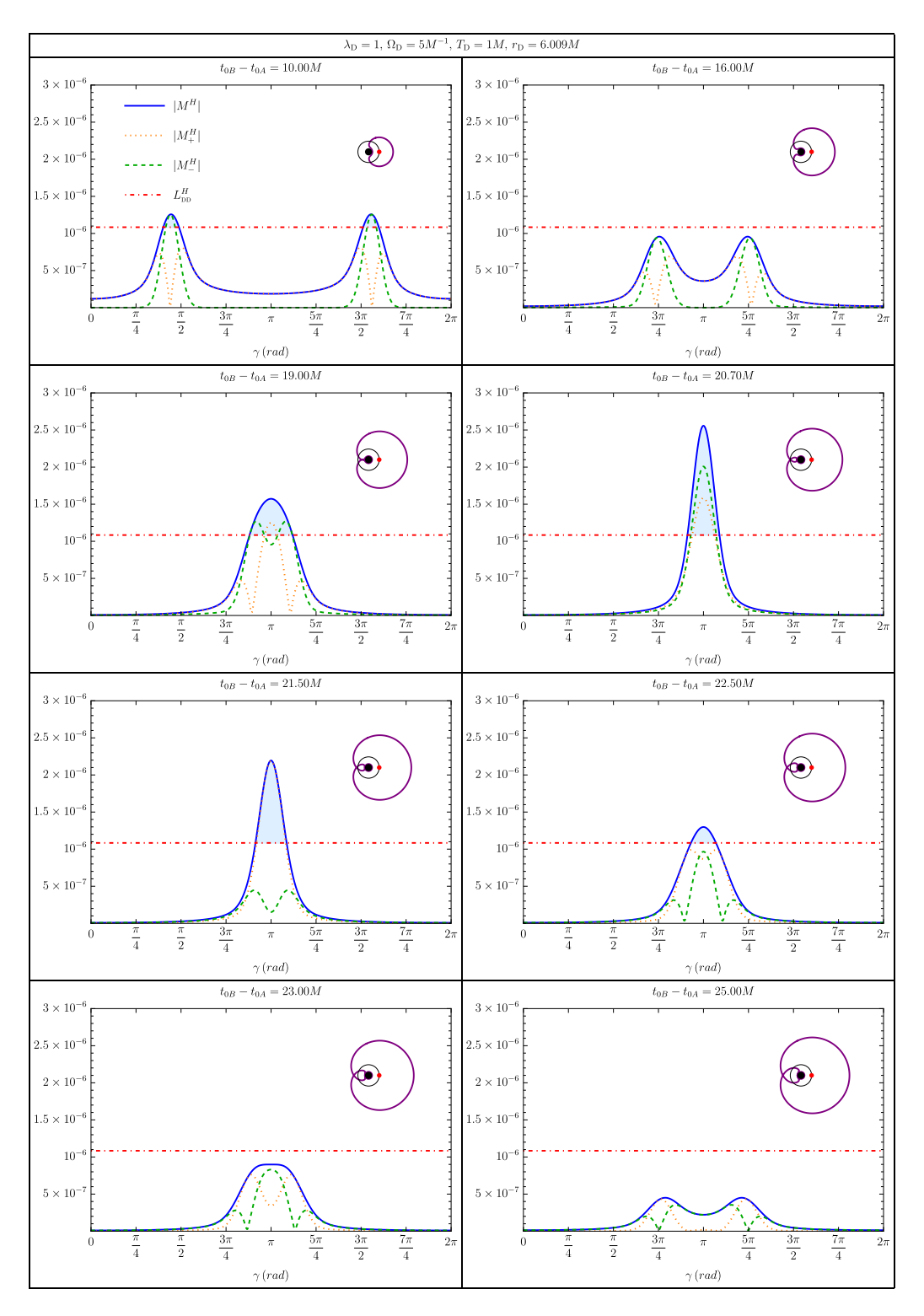


Figure 72 – Gravitational lensing of entanglement harvesting from the field in the Hartle-Hawking state: the entire setup is identical to the setup of Figure 68, except that here the initial state for the field is the Hartle-Hawking state. The plots show the absolute values of M^H , M_{\pm}^H and $L_{\rm DD}^H$ in Eq. (6.23) for two static detectors placed at radial coordinate r=6.009M with varying angular separation γ . All detector parameters are equal ($\lambda_{\rm D}=1,~\Omega_{\rm D}=5M^{-1},~T_{\rm D}=1M$); only the offset $\Delta_{\rm BA}=t_{0\rm B}-t_{0\rm A}$ between the two switching functions (6.11) varies between the plots. The inset indicates how far a null wave front propagates from the red point within a coordinate time interval $\Delta_{\rm BA}$.

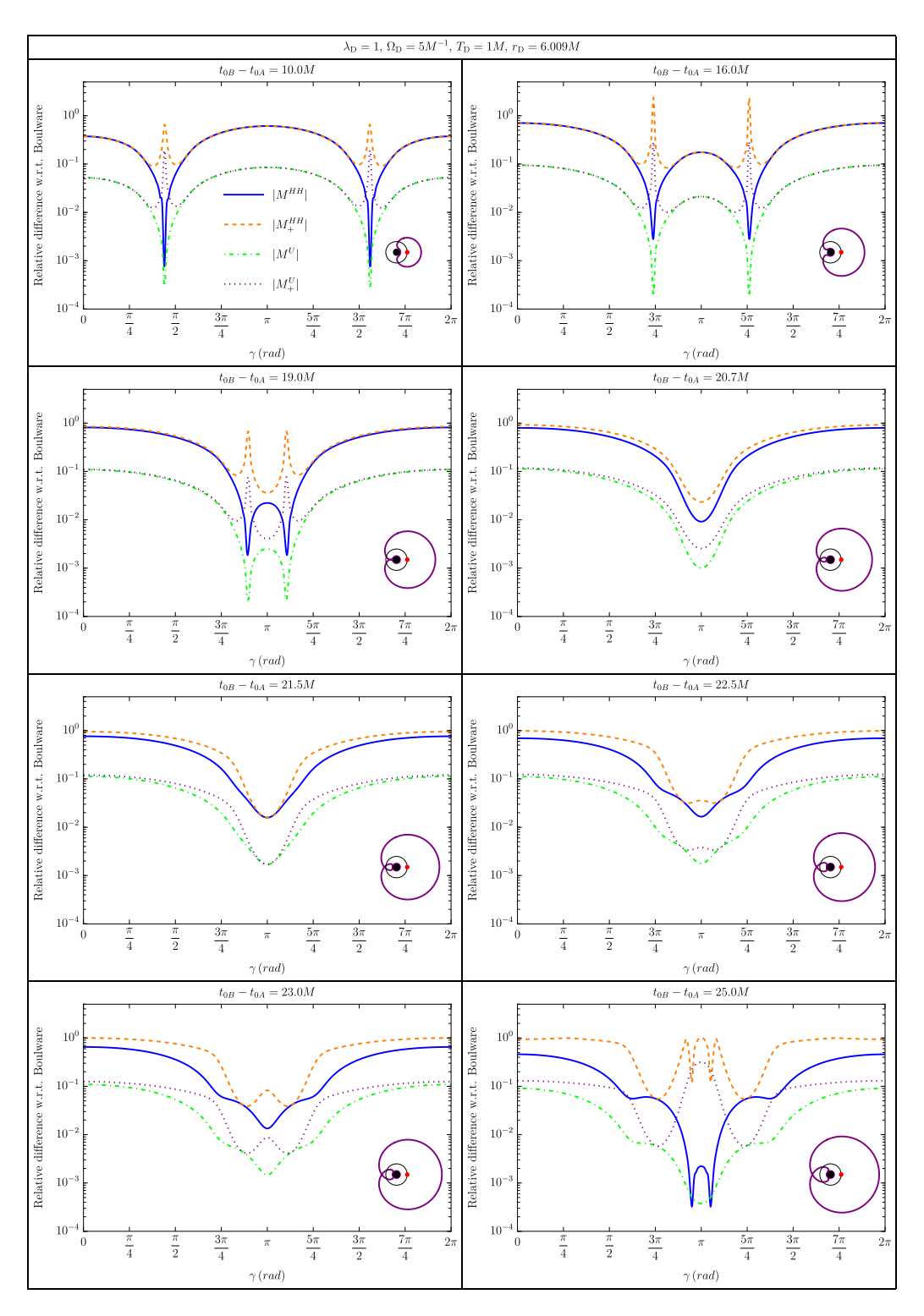


Figure 73 – Relative differences between correlation terms in the Boulware state, and the Hartle-Hawking and Unruh states, respectively, i.e., plotting $\frac{|M^H-M^B|}{|M^B|}$, $\frac{|M^H-M^B|}{|M^B|}$, $\frac{|M^H-M^B|}{|M^B|}$, and $\frac{|M^U-M^B|}{|M^B|}$, in analogy to Figure 68.

At the different radial coordinates the detectors experience different gravitational redshifts. To account for this, we adjust the width of the switching functions (6.11) to $T_{\rm D}(r) = T_{\infty}/\sqrt{f(r)} = T_{\infty}/\sqrt{1-2M/r}$, such that, at all radial coordinates $T_{\rm D}(r)$, corresponds to the same amount of proper time given by some value T_{∞} . Analogous to the plots above, Figure 74 shows the resulting contributions to the detectors' final state for $T_{\infty} = 1M$. It shows that at all radial coordinates considered, even close to the horizon, the two detectors can become entangled and the entanglement can be dominated by entanglement harvesting, when the switching delay $\Delta_{\rm BA} = t_{\rm 0B} - t_{\rm 0A}$ is chosen appropriately.

To understand the structure of the plots and its dependence on Δ_{BA} it is useful to consider the light propagation coordinate time Δt between the two detectors. This is the coordinate time that it takes for a null geodesic starting at spatial coordinates $(r, \theta = \pi/2, \phi)$ to reach the antipodal point $(r, \theta = \pi/2, \phi + \pi)$. Figure 75 shows this time for the range of radial coordinates we consider. It shows that Δt is minimal at r = 3M (the photonsphere). For this critical case, it takes the value $\Delta t_{\min} = 3\sqrt{3}\pi M$. Setting the switching delay equal to the light propagation time, i.e., setting $\Delta_{\text{BA}} = \Delta t$, yields exact null alignment of the detectors' switching functions.

Around exact null alignment between the detectors we expect a peak in the final detector entanglement, and this is, indeed, what we observe in Figure 74. At first, in the panels showing the lower values of Δ_{BA} , one peak forms around r = 3M since the detectors located at this radial coordinate are the first to be exactly null aligned. As Δ_{BA} is increased in the following panels, a double-peak structure forms since for $\Delta_{\text{BA}} > 3\sqrt{3\pi}M$ there are always two radial coordinate positions at which the detectors are exactly null aligned. Regarding the relative size of the contributions M_{+}^{B} and M_{-}^{B} , we observe again that both contributions are of comparable size when the detectors are exactly null aligned, as we already observed in the panel of Figure 69, for $\gamma = \pi$. This is in contrast to scenarios where the detectors are null aligned along primary null geodesics and sufficiently far away from any caustics. There, just as in flat Minkowski spacetime, the correlations are dominated by the M_{-} contribution when the detectors are exactly null aligned. However, at the caustics, where a whole envelope of null geodesics connects the detectors at once, the singularity structure of the two-point function is altered (see [91]). This results in the M_{+} contribution dominating before exact null alignment and the M_{-} contribution dominating after exact null alignment of the switching functions.

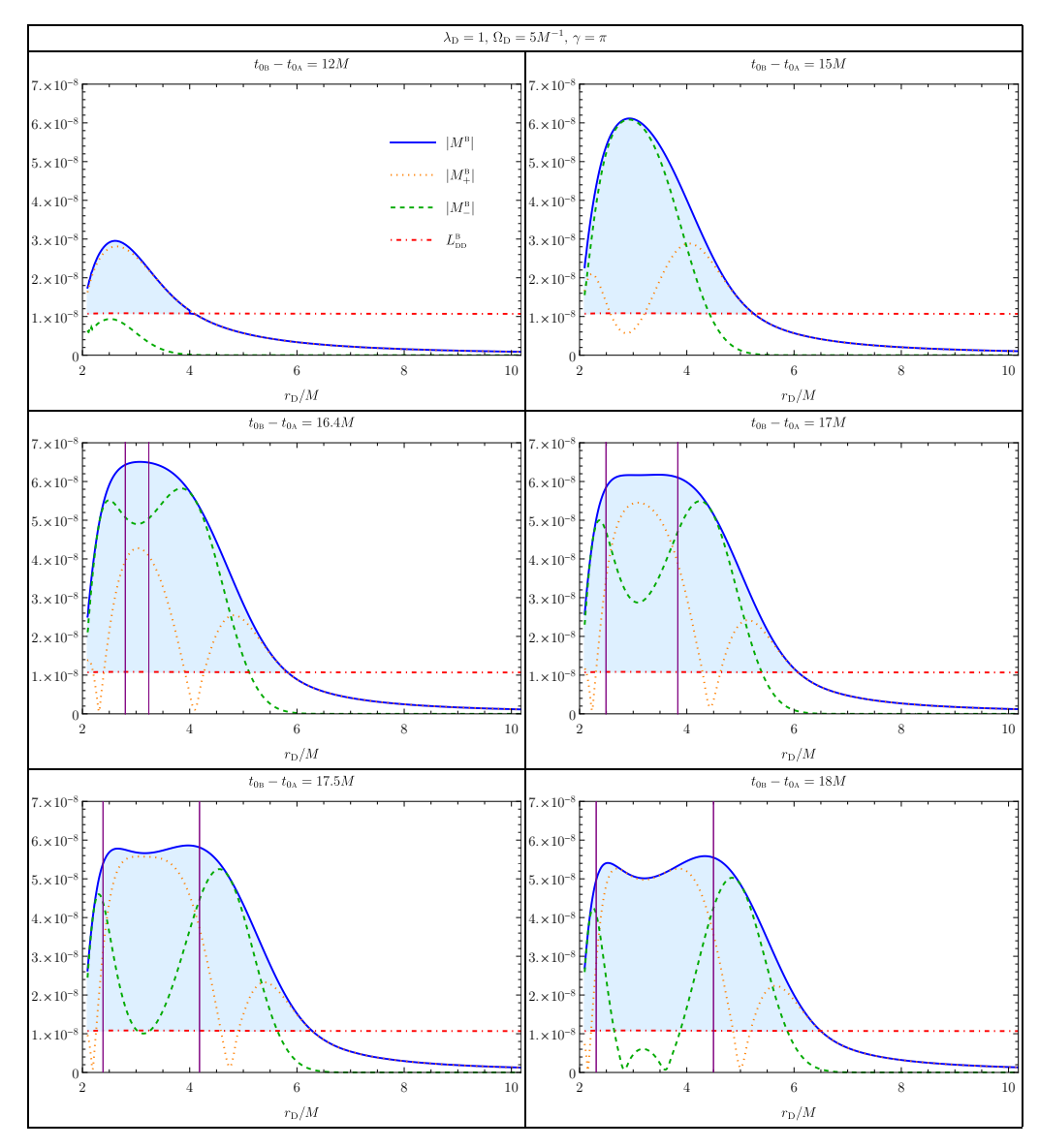


Figure 74 – Entanglement harvesting from the Boulware state by static detectors at antipodal positions close to a Schwarzschild black hole: the plots show the entries of the final detectors' state from Equation (6.23) for two identical detectors $(\lambda_D = 1, \Omega_D = 5/M)$ which are placed at equal radial coordinates r_D at angular separation $\gamma = \pi$, i.e., with the black hole exactly in the middle between them. To account for the different redshifts the width of the detector switching functions in Equation (6.11) is set to $T_D = M/\sqrt{1-2M/r}$, i.e., kept equal with respect to the detectors' proper time. The different panels show the results for different switching delays $\Delta_{\text{BA}} = t_{0\text{B}} - t_{0\text{A}}$. Detectors placed at r = 3M are the first for which the switching functions are exactly null aligned at $\Delta_{\rm BA} = 3\sqrt{3\pi}M \approx 16.32M$. Both for larger and lower radial coordinates the light propagation time is longer, and hence two peaks form in the later panels around the radial coordinates for which exact null alignment is achieved (see Figure 75). The vertical purple lines indicate the radial coordinates at which null alignment of the switching function is achieved, i.e., where $\Delta_{\text{BA}} = \Delta t$ (see Figure 75).

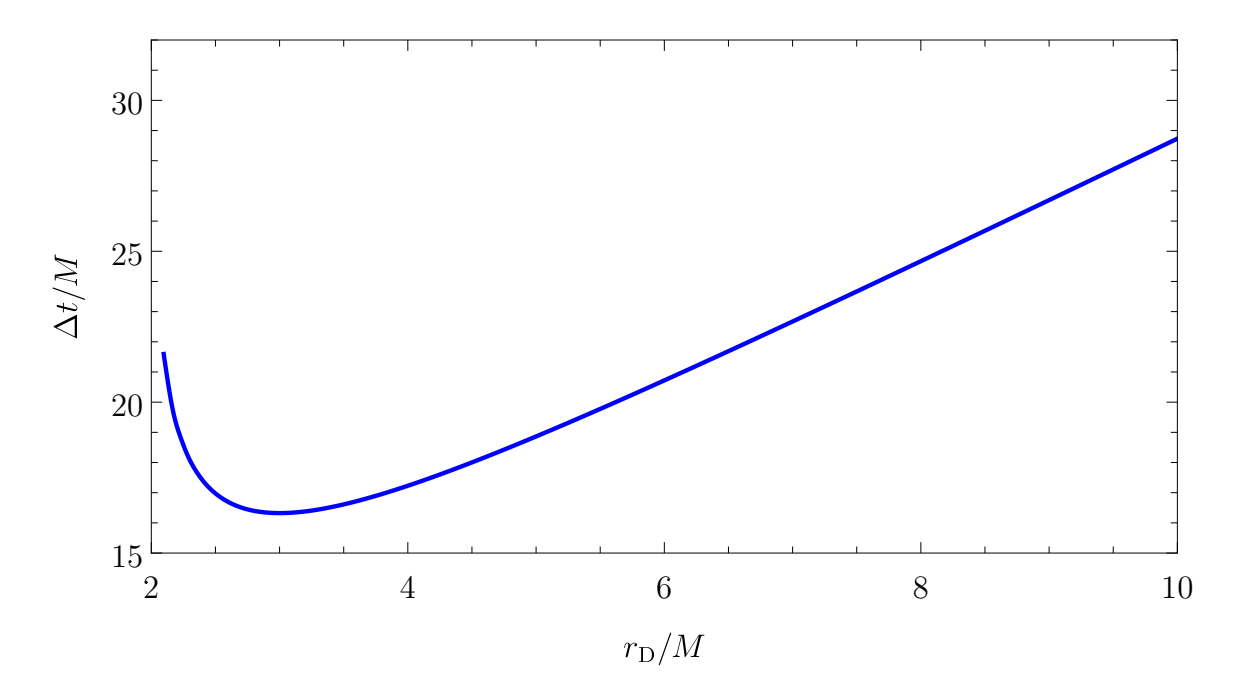


Figure 75 – Light propagation coordinate time between detectors in the scenario of Figure 74.

7 Conclusion

This work was motivated by the information loss puzzle, which the author considers an intriguing issue. However we do not attempt to solve it or attack it directly in this work. Instead, we choose to advance in the understanding of the distribution and propagation of correlations in a massless scalar field $\hat{\phi}$ on the (3+1)D Schwarzschild spacetime within the semi-classical framework. While by no means solving the puzzle, the methods developed in this thesis as well as the results obtained with it contribute to understanding what happens to the initial information encoded in a given state of $\hat{\phi}$ as it propagates through the spacetime. We attacked this problem — To the best of our knowledge, for the first time in this setup — by performing an analysis of the Wightman function of $\hat{\phi}$ for the Boulware $(|B\rangle)$, Unruh $(|U\rangle)$ and Hartle-Hawking $(|H\rangle)$ states (which we will refer to, respectively, as W^B , W^U and W^H) considering the case with both points outside the horizon and the one with one point inside and another outside it. As a positive outcome, the methods developed here also allow to study the phenomenon of entanglement harvesting from $\hat{\phi}$ on $|B\rangle$, $|U\rangle$ and $|H\rangle$ on the (3+1)D Schwarzschild spacetime, a setup that was never explored before our published paper [1] where we analyzed how angular separation between two identical Unruh-DeWitt (UdW) detectors placed at the same radial position around the horizon affects their capacity of harvesting entanglement from $|B\rangle$, $|U\rangle$ and $|H\rangle$. In what follows, we provide a recap of each chapter and summarize the results obtained in the course of this thesis. In the end, we present our perspective for future work.

Chapters 1 and 2 were written with the intent of presenting motivations, notations, conventions and the concepts of General Relativity that will be used throughout the text. Hence, no new results were introduced in these chapters.

Chapter 3 funnels towards the more specific prerequisites for this work. There we constructed the quantum field $\hat{\phi}$, as in [25], and defined $|B\rangle$ [40], $|U\rangle$ [39] and $|H\rangle$ [42] states in terms of the Eddington-Finkelstein (EF) and Unruh modes. Then we presented the Wightman function and its Hadamard form [44], together with its 4-fold singularity structure [54, 91]. In what follows, we presented the well-known expressions [34] for the Wightman function of $\hat{\phi}$ for $|B\rangle$, $|U\rangle$ and $|H\rangle$ on the (1+1)D Schwarzschild spacetime. Then this exercise is repeated on the (3+1)D Schwarzschild spacetime. In this case, the expressions of W^B , W^U and W^H when both points are outside [54] the horizon and inside [32] the horizon are already known. However, to the best of our knowledge, the one for the case where one point is inside the horizon and another outside it have not been presented before. We consider this as our first novel result.

Before using the expressions of these Wightman functions, we needed to compute the ingoing, upgoing and inside EF-modes (and their derivatives) defined in Section 3.3.1. This is done in Chapter 4. We applied the Jaffé-series [53] to compute the ingoing EF-modes, the

integrator implemented in the Black Hole Perturbation Toolkit [26] to compute the upgoing EF-modes and the Frobenius series to compute the inside EF-modes. With this approach, we obtained a precision of 16 significant digits in all inside EF-modes, 20 digits in all ingoing EF-modes and 9 digits in the upgoing modes within $\ell \in [0, 29]$ and $M\omega \in [0, 10]$.

The incidence amplitudes for the ingoing and upgoing EF-modes were obtained directly from the data of [54]. The reflection amplitudes for these modes were evaluated using our data via the Wronskian relations in terms of the EF-modes. Then we used the Wronskian relations in terms of the scattering amplitudes to conclude that all incidence amplitudes were self-consistent to 9 significant digits while the reflection amplitudes were verified to be self-consistent to 9 significant digits for $\ell \in [0, \approx 75]$ and $M\omega \in [0, \approx 9.3]$.

The set of these modes and amplitudes compose the dataset that was used throughout the computations in the next chapters. We estimate that this data-production step demanded a total of 1,5 months of uninterrupted computational work, spread across several Mathematica kernels, making it the most computer-intensive part of this work. We consider the time invested in this task to be worth it due to the multitude of potential use-cases for the produced data, which is, to the best of our knowledge, not available elsewhere.

Chapter 5 contains our new results regarding W^B , W^U and W^H . We begin it by constructing the method used to produce numerical results for these quantities from the dataset generated in Chapter 4. We managed to engineer it to allow us to go from raw data to a map of these Wightman functions in a matter of hours. Moreover, we verified that this method produces data, under a conservative estimate, correct to at least two significant digits. This can be improved by including modes with larger frequencies in the integrals. However the necessity of results with refined precision in any future work must be carefully considered since this would demand another round of time-consuming data generation.

To test the developed method, we conduced two tests with both points outside the horizon: In the first one the these points were positioned out of caustics and we verified that the computed W^B , W^U and W^H reproduce the expected 4-fold singularity structure. In the second one, we successfully reproduced known results [57] for the retarded Green Function on caustics. This batch of tests finishes with a new result: The real part of W^B on caustics (two points separated by an angle of $\gamma = \pi$), which show a 2-fold structure analogous to the one described by [57] for the retarded Green Function in this setup.

In the second part of Chapter 5, we showcase the capabilities of the method we developed by presenting maps of the real and imaginary parts of W^B , W^U and W^H with both points outside the horizon. These allow one to obtain, for the first time, a birds-eye view of the Wightman function in this setup. From them we concluded that the imaginary part of the Wightman function is visually indistinguishable across all of them — as expected, since it is state-independent. By analyzing a strip of constant r-coordinate

from these maps, which we consider to be representative for this purpose, we verified that even numerically, the imaginary part of W^B , W^U and W^H agree to a relative error of 10^{-3} when both points lie on the same surface of constant coordinate time and 10^{-8} everywhere else. The real maps of the real parts of W^B are also visually indistinguishable W^U , however that of W^H presented minor, yet visible, differences. These results represent a major advance in the capacity of working with the Wightman function in this setup, which was, in fact, not possible before this work. From these maps we managed to calculate the difference between the real parts of these Wightman functions to extract important differences between them.

This leads to the next section of that chapter, where we compare the correlations in $|U\rangle$ and $|H\rangle$ using $|B\rangle$ as a reference. That is, we compute the difference $W^{\psi-B}(\mathbf{x},\mathbf{x}')$ between the Wightman function W^{ψ} with $\psi \in \{U, H\}$ and W^B . We observed that W^{U-B} presents a local maxima that seem to travel from u' > u (the u-coordinate of the moving x' and fixed x points) towards $u' \approx u$ with increasing v'. We interpret this as an out-flux of quantum correlations between x and x' that is carried by Hawking radiation from the horizon towards infinity $(r \to \infty)$. Unfortunately, we were not able to figure what curve is tracking this local maxima. On the other hand W^{H-B} presents a local maxima that tracks $\Delta t = 0M$, where Δt is the coordinate time separation between x and x'. We associate it to a combination of an influx of correlations between x and a point x' that moves from infinity towards the horizon and an the out-flux of correlations carried by Hawking radiation from the horizon towards infinity. Finally, we note that on slices of constant r-coordinate, the local maxima that manifested in W^{U-B} and W^{H-B} decay exponentially as we move x' away from x, up to around the arrival of the first null geodesic that connects x and x' after a complete orbit. Beyond this point, that decay transitions into a polynomial regime. We then conjecture that the transition from the exponential to polynomial decay in these correlations happen around the boundary of the normal neighborhood of x.

In the following section of Chapter 5, we produced maps of W^U and W^H with one point x fixed inside the horizon and another, x', varying outside. As expected, the 4-fold singularity structure of the Wightman function was manifest. Moreover, we also note that the imaginary parts of W^U and W^H decay exponentially towards a residual value once x' moves out of causal connection from x. This is nothing but the manifestation of the lack of support of the advanced and retarded Green functions on spacelike connected points. As a novel result, we noticed that the real parts of W^U and W^H , which carries quantum correlations, manifest a structure composed by step-like behavior followed by a local minimum when x' is sufficiently far from the horizon. Both structures decay as x' moves away from the horizon in such a way that the local minimum becomes more evident compared to the step-like behavior. If x' is too close to the horizon, that structure merges with the light-crossing singularity on the direct null geodesic connecting x and x'. We shown that the aforementioned structure is produced by correlations across the

horizon encoded in the initial data that defines W^U and W^H . In particular, we noted that the most relevant contributions to that structure raises from low-frequency modes. Finally, by isolating that structure we noticed that the center of the step-like behavior travels from some value of EF-coordinates u' > u towards $u' \approx -u$ with increasing EF-coordinate v'. This behavior is similar to the characteristic signature of Hawking radiation in (1+1)D Schwarzschild [11, 10, 12], however in (3+1)D it is already evident in the Wightman functions while in (1+1)D it is only evident in the momentum-momentum and energy density correlators, which are constructed from derivatives of the Wightman function. We believe that such step-like behavior is the (3+1)D version of that signature.

In the final section of that chapter, we decomposed W^B , W^U and W^H in two sectors, one that depends only on ingoing EF-modes and another that depends only on upgoing EF-modes. Then we considered two points outside the horizon, at the same radial coordinate, separated by an angle of $\gamma = \pi/3$. We observe that for all states both sectors present non-light-crossing singularities which are different in both shape a location from the standard, light-crossing singularities of the Wightman function. Then we showed that these non-light-crossing singularities also follow a 4-fold structure, however we were not able to determine the functional form of these singularities. On top of that, we noted that the standard light-crossing singularities appear exclusively in the ingoing sector of the Wightman function when both points are above the photonsphere and exclusively in its upgoing sector when they are below it. Additionally, on the photonsphere no non-light-crossing singularities appear. We concluded that the light-crossing singularities in each sector do happen on null geodesics connecting x and x' but with a tweak: These of the ingoing sector appear on ingoing null geodesics connecting x and x' while these of the upgoing sector appear on outgoing null geodesics connecting these points.

In Chapter 6 we presented our published work [1]. We used two Unruh-DeWitt detectors outside the horizon to study entanglement harvesting from a massless quantum scalar field on the (3+1)D Schwarzschild spacetime. We placed these detectors at the same radial coordinate and varied the angular separation between them to assess their ability to harvest entanglement from the Boulware, Unruh and Hartle-Hawking vacua. We used the method developed in Chapter 5 throughout the calculations, with the difference that here the frequency smoothing naturally arises from the setup. Then we concluded that the capacity of harvesting entanglement is amplified near caustic points. This effect is intense enough to allow the entanglement acquired by the detectors to be dominated by the harvested entanglement even when they are causally timelike connected. This effect arises as a consequence of the change in the singularity of the Wightman function as the field waves cross caustic points.

We finish by stating that there are a number of possible extensions of the work presented in this thesis. An immediate one would be to study the correlations with both points inside the horizon through maps of the Wightman function. Another one would be to evaluate the momentum-momentum correlator and compare it directly with [10, 11, 12] to complement our findings on correlations across the horizon. Another possibility is to use our method to compare the results obtained by [51] and [92] since they disagree about the existence of a peak in the response function of a freely-falling Unruh-DeWitt detector slightly after it crosses the horizon. We could use our data and knowledge to explore that issue. Other than that, we could, for instance, evolve the Wightman function backwards from \mathscr{I}_R^+ while neglecting all modes from \mathscr{H}_R^+ , to study how well an observer that could collect all information that have not fallen through the horizon can reconstruct the initial data on $\mathcal{H}_R^- \cup \mathscr{I}_R^-$. A bolder proposal would be to use our method to obtain maps of the Wightman function for the Vaidya spacetime, which would allow us to follow the history of correlations during (and after) the formation of the horizon. When it comes to entanglement harvesting, we are in a unique position because we can effectively extend all of the existing literature on (1+1)D Schwarzschild to (3+1)D Schwarzschild, analyzing, for instance, if it is still possible to harvest entanglement across the horizon from the Boulware, Unruh and Hartle-Hawking vacua in this spacetime.

A Density matrix contributions

In this appendix, we give a detailed derivation of the expressions used for the calculation of the perturbative contributions to the final density state of the two detectors in Equation (6.23). To evaluate the leading-order contributions to the detectors' final density matrix, we need certain Fourier-type integrals of the switching function (6.11),

$$\eta_{\rm D}(t) = e^{-((t-t_{\rm 0D})/T_{\rm D})^2}.$$
 (A.1)

First, we have

$$\int_{-\infty}^{s} dt \, e^{i\nu t} \eta_{\rm D}(t) = \frac{\sqrt{\pi} T_{\rm D}}{2} e^{-\frac{\nu^2 T_{\rm D}^2}{4}} e^{i\nu t_{\rm 0D}} \left(1 + \operatorname{erf} \left(-\frac{i\nu T_{\rm D}}{2} + \frac{s - t_{\rm 0D}}{T_{\rm D}} \right) \right), \tag{A.2}$$

$$\int_{-\infty}^{\infty} dt \, e^{i\nu t} \eta_{D}(t) = \sqrt{\pi} T_{D} e^{-\frac{1}{4}\nu^{2} T_{D}^{2}} e^{i\nu t_{0D}}, \tag{A.3}$$

where $\operatorname{erf}(z) = \frac{2}{\sqrt{\pi}} \int_0^z dt \, e^{-t^2}$ is the error function [48, Section 7.1 (i)]. Furthermore, we need the integral

$$\int_{-\infty}^{\infty} dt' \, \mathrm{e}^{\mathrm{i}\mu t'} \eta_{\mathrm{D}'}(t') \int_{-\infty}^{t'} dt \, \mathrm{e}^{\mathrm{i}\nu t} \eta_{\mathrm{D}}(t). \tag{A.4}$$

To this end, consider

$$\frac{\sqrt{\pi}T_{\rm D}}{2} e^{-\frac{\nu^{2}T_{\rm D}^{2}}{4}} e^{i\nu t_{\rm 0}D} \int_{-\infty}^{\infty} dt' e^{i\mu t'} e^{-\frac{(t'-t_{\rm 0D'})^{2}}{T_{\rm D}^{\prime 2}}} \left(1 + \operatorname{erf}\left(-\frac{i\nu T_{\rm D}}{2} + \frac{t'-t_{\rm 0D}}{T_{\rm D}}\right)\right) \\
= \frac{\sqrt{\pi}T_{\rm D}}{2} e^{-\frac{\nu^{2}T_{\rm D}^{2}}{4}} e^{i\nu t_{\rm 0}D} e^{-\frac{t_{\rm 0D'}^{2}}{T_{\rm D}^{\prime 2}}} \int_{-\infty}^{\infty} dt' \left[e^{-\frac{t'^{2}}{T_{\rm D}^{2}} + t'\left(2\frac{t_{\rm 0D'}}{T_{\rm D}^{2}} + i\mu\right)} \operatorname{erf}\left(-\frac{i\nu T_{\rm D}}{2} + \frac{t'-t_{\rm 0D}}{T_{\rm D}}\right) \right] \\
+ \frac{\pi T_{\rm D}T_{\rm D'}}{2} e^{-\frac{\mu^{2}T_{\rm D'}^{2} + \nu^{2}T_{\rm D}^{2}}{4}} e^{i(\mu t_{\rm 0D'} + \nu t_{\rm 0D})}.$$
(A.5)

For the t'-integral, we use [21, Equations (A3) and (A7)] to write

$$I(a,b) = \int_{-\infty}^{\infty} dy \, e^{-a^2 - iby - y^2} \operatorname{erf}(y - ia) = -i\sqrt{\pi} e^{-a^2 - b^2/4} \operatorname{erfi}\left(\frac{a + b/2}{\sqrt{2}}\right), \quad (A.6)$$

where ${\rm erfi}(z) = -{\rm i}\,{\rm erf}({\rm i}z)$, with $y=t'/T_{\rm D'}$, $a=\frac{\nu T_{\rm D}}{2}-{\rm i}\frac{t_{\rm 0D}}{T_{\rm D}}$ and $b=2{\rm i}\frac{t_{\rm 0D'}}{T_{\rm D'}}-\mu T_{\rm D'}$, then

$$\int_{-\infty}^{\infty} dt' e^{-\frac{t'^2}{T_{D'}^2} + t' \left(2\frac{t_{0D'}}{T_{D'}^2} + i\mu\right)} \operatorname{erf}\left(-\frac{i\nu T_{D}}{2} + \frac{t' - t_{0D}}{T_{D}}\right)
= -i\sqrt{\pi}T_{D'}e^{-\frac{-\mu^2 T_{D'}^2}{4} + \frac{t_{0D'}^2}{T_{D'}^2} + i\mu t_{0D'}} \operatorname{erfi}\left(\frac{1}{\sqrt{2}}\left(\frac{\nu T_{D} - \mu T_{D'}}{2} - i\frac{t_{0D}}{T_{D}} + i\frac{t_{0D'}}{T_{D'}}\right)\right).$$
(A.7)

Inserting this above yields

$$\int_{-\infty}^{\infty} dt' \, e^{i\mu t'} \eta_{D'}(t') \int_{-\infty}^{t'} dt \, e^{i\nu t} \eta_{D}(t) = \frac{T_{D} T_{D'} \pi}{2} e^{-\frac{\mu^{2} T_{D'}^{2} + \nu^{2} T_{D}^{2}}{4}} e^{i(\nu t_{0}D + \mu t_{0}D')} \times \left(1 - i \operatorname{erfi}\left[\frac{\nu T_{D} - \mu T_{D'}}{2\sqrt{2}} + \frac{i}{\sqrt{2}} \left(\frac{t_{0}D'}{T_{D'}} - \frac{t_{0}D}{T_{D}}\right)\right]\right). \tag{A.8}$$

For stationary detectors we use $\tau_{\rm D}(t) = \sqrt{f(r_{\rm D})}t$ as the relation between proper time and coordinate time (see Equation (6.9)). With this, and Equations (6.3) and (A.3), the single detector noise term $L_{\rm DD'}^{\psi}$ in Equation (6.25) takes the following form (denoting $r = r_{\rm D}, r' = r_{\rm D'}, f_{\rm D} = f(r_{\rm D})$ and $N_{\rm D} = \sqrt{f_{\rm D}}$):

$$\begin{split} L_{\mathrm{DD}'}^{\psi} &= \lambda_{\mathrm{D}} \lambda_{\mathrm{D}'} f_{\mathrm{A}} f_{\mathrm{B}} \int_{-\infty}^{\infty} \mathrm{d}t \int_{-\infty}^{\infty} \mathrm{d}t' \, \eta_{\mathrm{D}}(t) \eta_{\mathrm{D}'}(t') \mathrm{e}^{-\mathrm{i}\Omega_{\mathrm{D}} N_{\mathrm{D}} t + \mathrm{i}\Omega_{\mathrm{D}'} N_{\mathrm{D}'} t'} W^{\psi} \left(\mathsf{x}_{\mathrm{D}}(t) ; \mathsf{x}_{\mathrm{D}'}(t') \right) \\ &= \frac{\lambda_{\mathrm{D}} \lambda_{\mathrm{D}'} f_{\mathrm{A}} f_{\mathrm{B}}}{(4\pi)^{2}} \sum_{\ell=0}^{\infty} (2\ell+1) P_{\ell}(\cos \gamma) \int_{-\infty}^{\infty} \mathrm{d}\omega \left[\frac{G_{\ell\omega}^{\psi}(r_{\mathrm{D}}, r_{\mathrm{D}'})}{\omega} \left(\int_{-\infty}^{\infty} \mathrm{d}t \, \eta_{\mathrm{D}}(t) \mathrm{e}^{-\mathrm{i}(\Omega_{\mathrm{D}} N_{\mathrm{D}} + \omega) t} \right) \right] \\ &\times \left(\int_{-\infty}^{\infty} \mathrm{d}t' \, \eta_{\mathrm{D}'}(t') \mathrm{e}^{\mathrm{i}(\Omega_{\mathrm{D}'} N_{\mathrm{D}'} + \omega) t'} \right) \right] \\ &= \frac{\lambda_{\mathrm{D}} \lambda_{\mathrm{D}'} N_{\mathrm{D}} N_{\mathrm{D}'} T_{\mathrm{D}} T_{\mathrm{D}'}}{16\pi} \sum_{\ell=0}^{\infty} (2\ell+1) P_{\ell}(\cos \gamma) \int_{-\infty}^{\infty} \mathrm{d}\omega \left[\frac{G_{\ell\omega}^{\psi}(r_{\mathrm{D}}, r_{\mathrm{D}'})}{\omega} \right. \\ &\times \mathrm{e}^{\mathrm{i}(\Omega_{\mathrm{D}'} N_{\mathrm{D}'} + \omega) t_{0\mathrm{D}'} - \mathrm{i}(\Omega_{\mathrm{D}} N_{\mathrm{D}} + \omega) t_{0\mathrm{D}} - \frac{1}{4} (\Omega_{\mathrm{D}} N_{\mathrm{D}} + \omega)^{2} T_{\mathrm{D}}^{2} - \frac{1}{4} (\Omega_{\mathrm{D}'} N_{\mathrm{D}'} + \omega)^{2} T_{\mathrm{D}'}^{2}}{\right]. \end{split} \tag{A.9}$$

Analogously, for M^{ψ} in Equation (6.24) we obtain using Equation (A.8),

$$M^{\psi} = \frac{-\lambda_{A}\lambda_{B}f_{A}f_{B}}{(4\pi)^{2}} \sum_{\ell=0}^{\infty} (2\ell+1)P_{\ell}(\cos\gamma) \int_{-\infty}^{\infty} d\omega \frac{1}{\omega} \left[G_{\ell\omega}^{\psi}(r_{A}, r_{B}) \int_{-\infty}^{\infty} dt \, e^{i(\Omega_{A}f_{A}-\omega)t} \eta_{A}(t) \int_{-\infty}^{t} dt' \, \left(e^{i(\omega+\Omega_{B}f_{B})t'} + \eta_{B}(t') \right) + G_{\ell\omega}^{\psi}(r_{B}, r_{A}) \int_{-\infty}^{\infty} dt \, \eta_{B}(t) e^{i(\Omega_{B}f_{B}-\omega)t} \int_{-\infty}^{t} dt' \, e^{i(\omega+\Omega_{A}f_{A})t'} \eta_{A}(t') \right]$$

$$= \frac{-\lambda_{A}\lambda_{B}f_{A}f_{B}T_{A}T_{B}}{32\pi} \sum_{\ell=0}^{\infty} (2\ell+1)P_{\ell}(\cos\gamma) \int_{-\infty}^{\infty} d\omega \frac{1}{\omega}$$

$$\times \left[e^{-\frac{\mu_{A}^{2}T_{A}^{2}+\nu_{B}^{2}T_{B}^{2}}{4}} e^{i(\nu_{B}t_{OB}+\mu_{A}t_{OA})} \left(1 - i \, erfi \left[\frac{\nu_{B}T_{B}-\mu_{A}T_{A}}{2\sqrt{2}} + \frac{i}{\sqrt{2}} \left(\frac{t_{OA}}{T_{A}} - \frac{t_{OB}}{T_{B}} \right) \right] \right) G_{\ell\omega}^{\psi}(r_{A}, r_{B})$$

$$+ e^{-\frac{\mu_{B}^{2}T_{B}^{2}+\nu_{A}^{2}T_{A}^{2}}{4}} e^{i(\nu_{A}t_{OA}+\mu_{B}t_{OB})} \left(1 - i \, erfi \left[\frac{\nu_{A}T_{A}-\mu_{B}T_{B}}{2\sqrt{2}} + \frac{i}{\sqrt{2}} \left(\frac{t_{OB}}{T_{B}} - \frac{t_{OA}}{T_{A}} \right) \right] \right) G_{\ell\omega}^{\psi}(r_{B}, r_{A}) \right], \tag{A.10}$$

with $\nu_{\rm D} = \omega + \Omega_{\rm D} N_{\rm D}$, $\mu_{\rm D} = \Omega_{\rm D} N_{\rm D} - \omega$. For practical evaluation purposes, one can manipulate the integrals in Equations (A.10) and (A.9) further so that the integration over ω only runs over $0 < \omega < \infty$.

B Numerical techniques for the Wightman function

In order to evaluate the Wightman function in the situations presented in this work, integrals over $\psi_{\omega\ell}^{\text{in,R/up,R}}(r)$ with respect to r are needed. However, there is no known closed-form expression for $\psi_{\omega\ell}^{\text{in,R/up,R}}(r)$. Hence, one has to use numerical techniques. For evaluating these modes and their respective scattering amplitudes we used the methods delineated in Chapter 4.

In the following subsections, we provide the analysis of the convergence of the integrals defining M^{ψ} and $L_{\text{DD}'}^{\psi}$, as well as specific details regarding the precision of their numerical evaluation.

B.1 $L_{ m DD}^{\psi}$ -terms

By setting D = D' in Equation (A.9) and manipulating the integration range from $-\infty < \omega < \infty$ to $0 < \omega < \infty$, we obtain the following expression for the L_{DD}^{ψ} -terms:

$$L_{\rm DD}^{\psi}(r_{\rm D}) = \frac{(N_{\rm D}\lambda_{\rm D}T_{\rm D})^2}{16\pi} \sum_{\ell=0}^{\infty} (2\ell+1) \int_0^{\infty} d\omega \, \frac{1}{\omega} \left(G_{\ell\omega}^{\psi}(r_{\rm D}, r_{\rm D}) e^{-\frac{1}{2}(\Omega_{\rm D}N_{\rm D}+\omega)^2 T_D^2}\right)$$
(B.1)

$$- G_{\ell,-\omega}^{\psi}(r_{\rm D}, r_{\rm D}) e^{-\frac{1}{2}(\Omega_{\rm D} N_{\rm D} - \omega)^2 T_D^2}).$$
 (B.2)

To verify the convergence of such an integral, one should analyze the large- $|\omega|$ behavior of the $G_{\ell\omega}^{\psi}(r_{\rm D}, r_{\rm D})$, which varies among the quantum states as in Equations (6.4), (6.5) and (6.6):

$$G_{\ell\omega}^{B}(r_{\mathrm{D}}, r_{\mathrm{D}}) \sim \theta(\omega) \left(\left| \frac{\psi_{\omega\ell}^{\mathrm{in,R}}(r_{\mathrm{D}})}{r_{\mathrm{D}}} \right|^{2} + \left| \frac{\psi_{\omega\ell}^{\mathrm{up,R}}(r_{\mathrm{D}})}{r_{\mathrm{D}}} \right|^{2} \right), \tag{B.3}$$

$$G_{\ell\omega}^{U}(r_{\mathrm{D}}, r_{\mathrm{D}}) \sim \theta(\omega) \left| \frac{\psi_{\omega\ell}^{\mathrm{in,R}}(r_{\mathrm{D}})}{r_{\mathrm{D}}} \right|^{2} + \left(\theta(\omega) - \theta(-\omega) \mathrm{e}^{4\pi\omega r_{s}} \right) \left| \frac{\psi_{\omega\ell}^{\mathrm{up,R}}(r_{\mathrm{D}})}{r_{\mathrm{D}}} \right|^{2}, \tag{B.3}$$

$$G_{\ell\omega}^{H}(r_{\mathrm{D}}, r_{\mathrm{D}}) \sim \left(\theta(\omega) \mathrm{e}^{-4\pi\omega r_{s}} - \theta(-\omega) \right) \left| \frac{\psi_{\omega\ell}^{\mathrm{in,R}}(r_{\mathrm{D}})}{r_{\mathrm{D}}} \right|^{2} + \left(\theta(\omega) - \theta(-\omega) \mathrm{e}^{4\pi\omega r_{s}} \right) \left| \frac{\psi_{\omega\ell}^{\mathrm{up,R}}(r_{\mathrm{D}})}{r_{\mathrm{D}}} \right|^{2}.$$

The leading asymptotic behavior of $\left|\psi_{\omega\ell}^{\text{in,R/up,R}}(r_{\text{D}})\right|^2$ as $|\omega| \to \infty$ is [93, Appendix D.2]¹

$$\left|\psi_{\omega\ell}^{\text{in,R/up,R}}(r_{\text{D}})\right|^{2} \sim 1.$$
 (B.4)

Hence, to leading order for large $|\omega|$, $G_{\ell\omega}^{\psi}(r_{\rm D}, r_{\rm D}) \sim 1$.

Such asymptotics are nonuniform and valid only when $\omega \gg V_{\ell}(r)$, as illustrated in Fig. 76

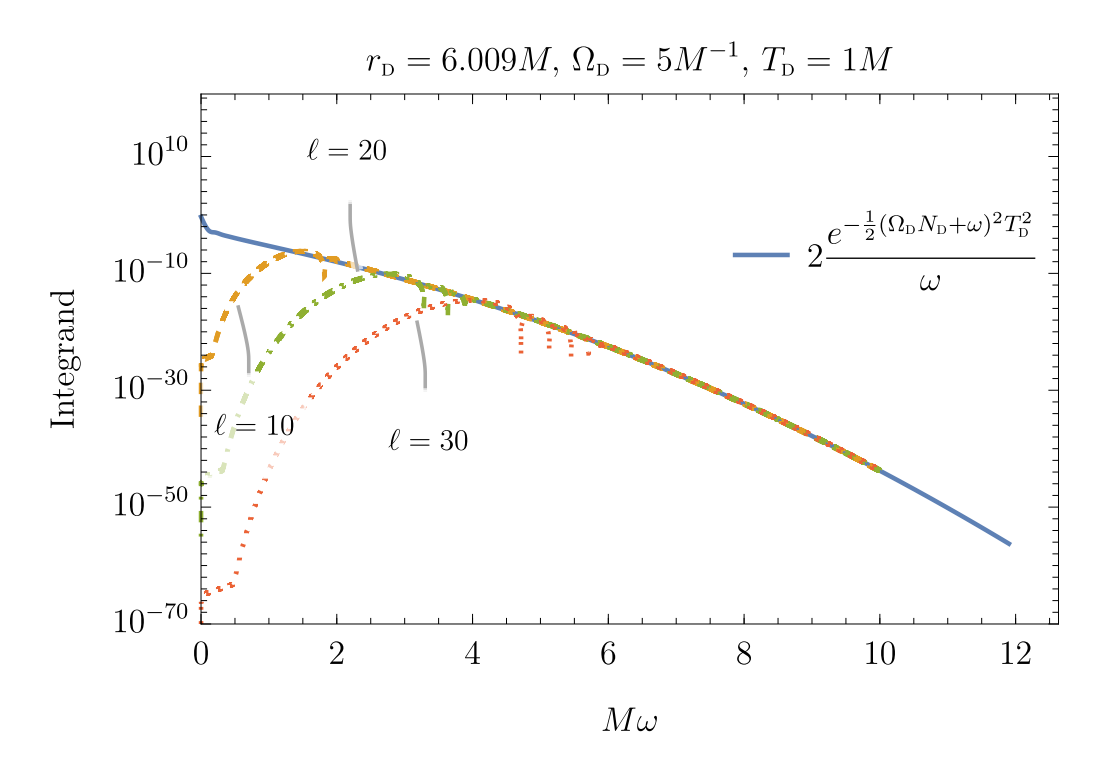


Figure 76 – Integrand in Equation (B.1) as a function of $M\omega$ and ℓ for the Boulware state. The value of $M\omega$ where the asymptotic regime begins grows with ℓ . More precisely, the transition to the asymptotic regime begins around $\omega r \sim \sqrt{\ell (\ell+1)}$ (for $\ell > 0$ and radii not too close to the horizon). Notice that thanks to the $\theta(\omega)$ in Equation (6.4), the slowest decaying term in Equation (B.1) for the Boulware state is proportional to $\sim 2 \frac{\mathrm{e}^{-\frac{1}{2}(\Omega_{\mathrm{D}}\mathrm{D}N_{\mathrm{D}}\mathrm{D}+\omega)^{2}T_{D}^{2}}}{\omega}$.

By substituting such a result into the integrand in Equation (B.1), one concludes that the slowest-decaying term of the integrand falls off as

$$\sim 2 \frac{e^{-\frac{1}{2}(\Omega_{\rm D} N_{\rm D} - \omega)^2 T_D^2}}{\omega}$$
 (B.5)

Therefore, the integral in Equation (B.1) is fast-converging — Indeed, it converges much faster than the integrals involved in the evaluation of the Wightman function in Chapter 5. Given that, we are able to numerically evaluate it accurately enough with a frequency cutoff $M\omega_{cut} = 10$. The asymptotic regime of the integrand and the convergence of the integral are illustrated in Figs. 76 and 77.

In order to verify the convergence of the ℓ -sum, we begin by evaluating the integrals in Equation (B.1), multiplying by $2\ell+1$ and plotting the result against ℓ . The outcome is shown in Fig. 78, where we can see that such a quantity decays superexponentially. Given this numerical evidence, the ℓ -sum in that equation is expected to converge with a good accuracy even with a cutoff lower than the $\ell_{\rm cut}=100$ we use. In fact, as presented in Fig. 79, $\ell_{\rm cut}=30$ is enough to converge to all ten significant digits used when evaluating the Boulware integrals. Remarkably, this is achieved without using an ℓ -smoothing, as was necessary in the evaluations from Chapter 5. This is due to the strong ω -smoothing

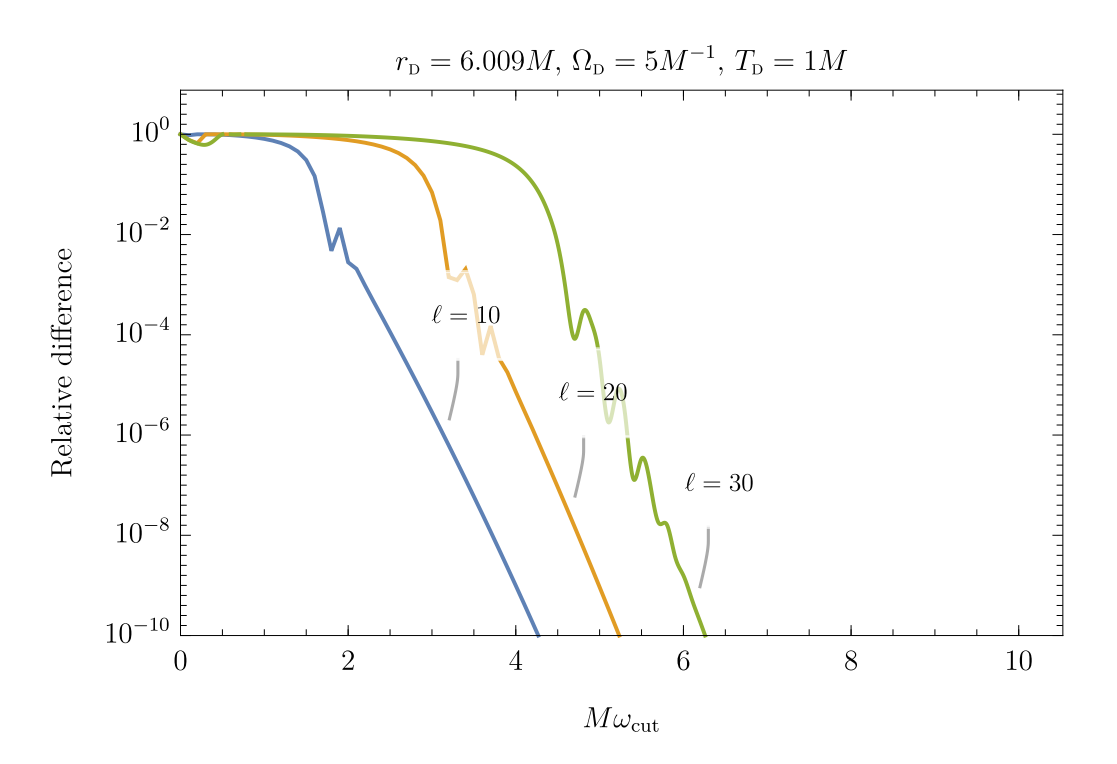


Figure 77 – Relative difference between the integral in Equation (B.1) for the Boulware state when integrated up to $\omega_{\rm cut}$ and up to $\omega_{\rm cut} + \delta$, with $\delta = 1/10$. The reason to limit this plot to 10^{-10} is that those integrals where evaluated to ten significant digits; hence, a relative difference of 10^{-10} means that the integral converged completely to all significant digits. Comparing with Fig. 76, we see that exponentially fast convergence happens after $M\omega_{\rm cut}$ becomes slightly larger than the $M\omega$ where the asymptotic regime begins.

that is imposed by the setup.

B.2 M^{ψ} -terms

Since we already know the large- $|\omega|$ asymptotics of $G_{\ell\omega}^{\psi}(r_{\rm D}, r_{\rm D})$, to analyze the behavior of the integrand in Equation (A.10) in that regime we have to study the factors that multiply each of its terms. These factors are very similar and it suffices to analyze only one of them:

$$e^{-\frac{\mu_{\rm A}^2 T_{\rm A}^2 + \nu_{\rm B}^2 T_{\rm B}^2}{4}} e^{i(\nu_{\rm B} t_{0\rm B} + \mu_{\rm A} t_{0\rm A})} \operatorname{erfc} \left[\frac{i(\nu_{\rm B} T_{\rm B} - \mu_{\rm A} T_{\rm A})}{2\sqrt{2}} - \frac{1}{\sqrt{2}} \left(\frac{t_{0\rm A}}{T_{\rm A}} - \frac{t_{0\rm B}}{T_{\rm B}} \right) \right], \tag{B.6}$$

where $\operatorname{erfc}(z) = 1 - \operatorname{erf}(z)$ is the complementary error function [48, Section 7.2(i)]. Expanding the exponential functions, we obtain

$$\alpha_{\rm AB} {\rm e}^{-\frac{1}{4}(T_{\rm A}^2 + T_{\rm B}^2)\omega^2} {\rm e}^{-\frac{1}{2}\left(N_{\rm B}T_{\rm B}^2\Omega_{\rm B} - N_{\rm A}T_{\rm A}^2\Omega_{\rm A}\right)\omega} {\rm e}^{{\rm i}\omega(t_{0\rm B} - t_{0\rm A})} {\rm erfc} \left[\frac{{\rm i}(\nu_{\rm B}T_{\rm B} - \mu_{\rm A}T_{\rm A})}{2\sqrt{2}} - \frac{1}{\sqrt{2}}\left(\frac{t_{0\rm A}}{T_{\rm A}} - \frac{t_{0\rm B}}{T_{\rm B}}\right)\right], \tag{B.7}$$

where

$$\alpha_{AB} = e^{-\frac{1}{4} \left(N_B^2 T_B^2 \Omega_B^2 + N_A^2 T_A^2 \Omega_A^2 \right)} e^{i(\Omega_B N_B t_{0B} + \Omega_A N_A t_{0A})}.$$
(B.8)

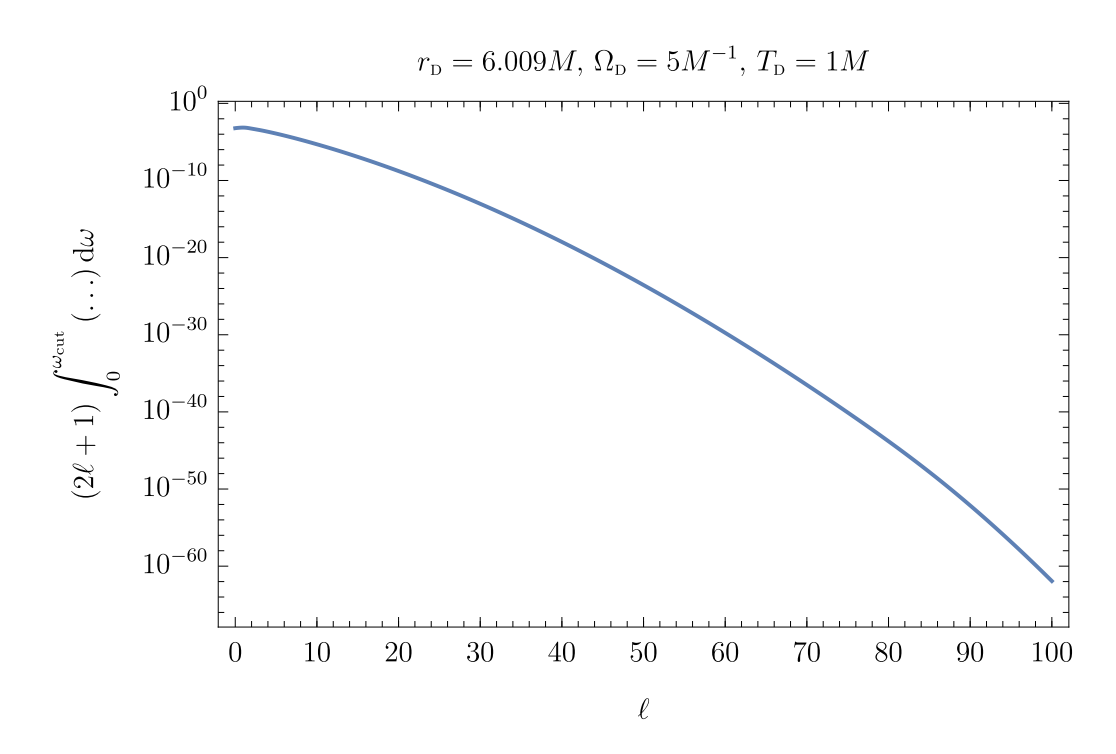


Figure 78 – Summand in Equation (B.1) as a function of ℓ for the Boulware state. One can notice from this figure that the summand decays superexponentially with increasing ℓ . In fact, for $\ell > 30$, it has already converged to all 10 significant digits that we got when evaluating the integrals.

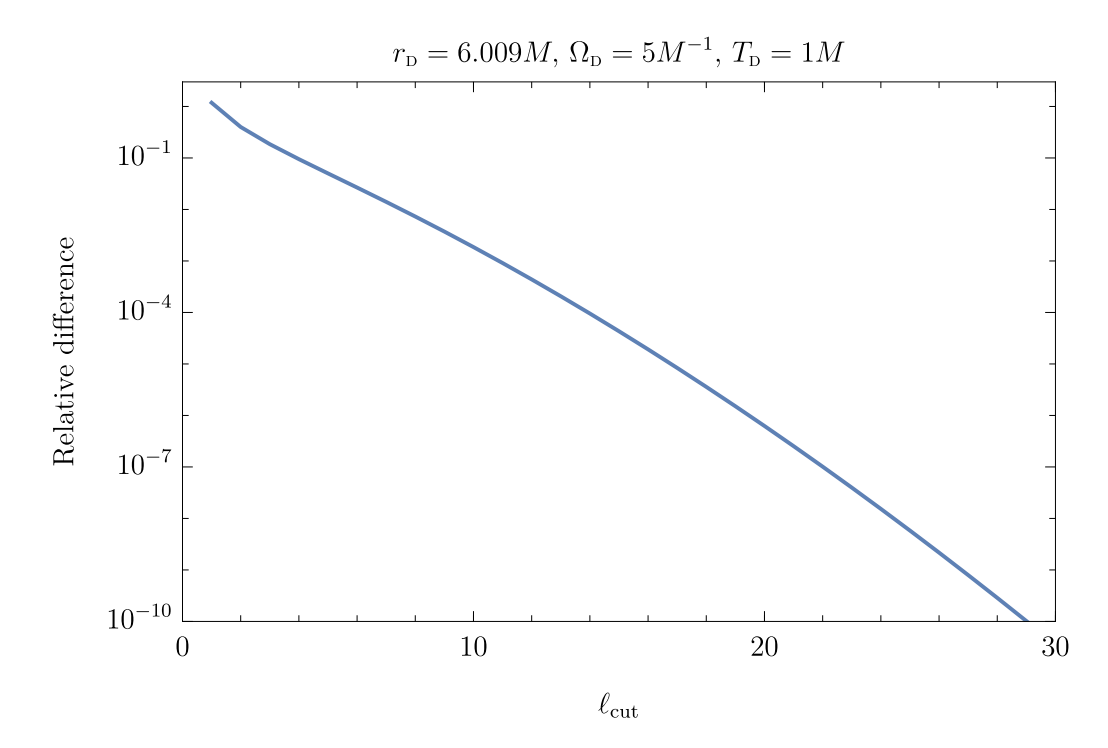


Figure 79 – Relative difference between the ℓ -sum in Equation (B.1) for the Boulware state when summed up to $\ell_{\rm cut}$ and $\ell_{\rm cut} - 1$. The reason to limit this plot to 10^{-10} is that the integrals in the sums were to 10 digits of precision. Hence, a relative difference that is smaller than 10^{-10} should represent numerical noise and not actual significant digits.

Now we use an asymptotic approximation for the $\operatorname{erfc}(z)$ [48, Section 7.12(i)],

$$\operatorname{erfc}(z) \sim \frac{e^{-z^2}}{z\sqrt{\pi}}, \quad z \to \infty, \quad |\operatorname{ph}(z)| < 3\pi/4,$$
 (B.9)

to conclude that as $\omega \to \infty$,

$$\operatorname{erfc} \left[\frac{i(\nu_{\rm B} T_{\rm B} - \mu_{\rm A} T_{\rm A})}{2\sqrt{2}} - \frac{1}{\sqrt{2}} \left(\frac{t_{0\rm A}}{T_{\rm A}} - \frac{t_{0\rm B}}{T_{\rm B}} \right) \right] \sim \tag{B.10}$$

$$\beta_{AB} \frac{e^{\frac{1}{8}(T_A + T_B)^2 \omega^2} e^{\frac{1}{4}(T_A + T_B)(N_B T_B \Omega_B - N_A T_A \Omega_A) \omega} e^{-i\omega \frac{1}{2}(T_A + T_B)\left(\frac{t_{0B}}{T_B} - \frac{t_{0A}}{T_A}\right)}}{\frac{i((N_B \Omega_B + \omega) T_B - (N_A \Omega_A - \omega) T_A)}{2\sqrt{2}} - \frac{1}{\sqrt{2}} \left(\frac{t_{0A}}{T_A} - \frac{t_{0B}}{T_B}\right)}, \quad (B.11)$$

where

$$\beta_{AB} = (\pi \alpha_{AB})^{-1/2} e^{-\frac{1}{2} (\frac{t_{0B}}{T_B} - \frac{t_{0A}}{T_A})^2} e^{\frac{i}{2} (N_A T_A \Omega_A \frac{t_{0B}}{T_B} + N_B T_B \Omega_B \frac{t_{0A}}{T_A})} e^{-\frac{1}{4} (N_A T_A \Omega_A N_B T_B \Omega_B)}.$$
(B.12)

Putting everything together we conclude that

$$e^{-\frac{\mu_{\rm A}^{2}T_{\rm A}^{2} + \nu_{\rm B}^{2}T_{\rm B}^{2}}{4}} e^{i(\nu_{\rm B}t_{\rm 0B} + \mu_{\rm A}t_{\rm 0A})} \operatorname{erfc} \left[\frac{i(\nu_{\rm B}T_{\rm B} - \mu_{\rm A}T_{\rm A})}{2\sqrt{2}} - \frac{1}{\sqrt{2}} \left(\frac{t_{\rm 0A}}{T_{\rm A}} - \frac{t_{\rm 0B}}{T_{\rm B}} \right) \right] \sim \\ \alpha_{\rm AB}\beta_{\rm AB} \frac{e^{-\frac{1}{8}(T_{\rm A} - T_{\rm B})\omega^{2}} e^{\frac{1}{4}(T_{\rm A} - T_{\rm B})(N_{\rm B}T_{\rm B}\Omega_{\rm B} + N_{\rm A}T_{\rm A}\Omega_{\rm A})\omega} e^{\frac{i}{2}\omega(T_{\rm B} - T_{\rm A})\left(\frac{t_{\rm 0A}}{T_{\rm A}} + \frac{t_{\rm 0B}}{T_{\rm B}}\right)}{i((N_{\rm B}\Omega_{\rm B} + \omega)T_{\rm B} - (N_{\rm A}\Omega_{\rm A} - \omega)T_{\rm A})} - \frac{1}{\sqrt{2}} \left(\frac{t_{\rm 0A}}{T_{\rm A}} - \frac{t_{\rm 0B}}{T_{\rm B}} \right)}{i(T_{\rm A} - t_{\rm 0B})}, \quad \omega \to \infty,$$
(B.13)

which leads to the conclusion that, whenever $T_A \neq T_B$, the whole term decays superexponentially as $e^{-\frac{1}{8}(T_B-T_A)^2\omega^2}$. On the other hand, if $T_A = T_B = T$, which is the case we study in this work, (B.13) simplifies to

$$e^{-\frac{(\mu_{A}^{2} + \nu_{B}^{2})T^{2}}{4}} e^{i(\nu_{B}t_{0B} + \mu_{A}t_{0A})} \operatorname{erfc} \left[\frac{i(\nu_{B} - \mu_{A})T}{2\sqrt{2}} + \frac{1}{T\sqrt{2}} (t_{0B} - t_{0A}) \right] \sim \frac{\alpha_{AB}\beta_{AB}}{\frac{i(N_{B}\Omega_{B} - N_{A}\Omega_{A} + 2\omega)T}{2\sqrt{2}} - \frac{(t_{0A} - t_{0B})}{T\sqrt{2}}}, \quad \omega \to \infty.$$
(B.14)

Then both, the real and imaginary parts of this quantity decay linearly with ω , since the absolute value of the denominator grows linearly with the frequency. Given that, by considering the extra ω^{-1} in the integrand in Equation (A.10), we conclude that it decays as ω^{-2} . Hence, the integrals defining the M^{ψ} -terms are convergent.

We remark that such leading asymptotic behavior in Equation (B.14) is, in general, not achieved by $M\omega=10$, but one can still perform the numerical integration to a good accuracy because, before this leading asymptotic regime, there is an intermediary regime where the integrand is exponentially decaying, as can be seen in Fig. 80. We can further confirm that convergence by looking at the integral in Equation (A.10) as a function of ω_{cut} : as can be seen in Fig. 81, up to $\ell=20$ we have convergence up to four significant digits, while for larger values of ℓ , the convergence becomes worse, resulting in no significant digits at all. Yet, since the resulting integral decays superexponentially with ℓ , as presented in Fig. 82, one can still obtain up to four significant digits, as can be seen in Fig. 83.

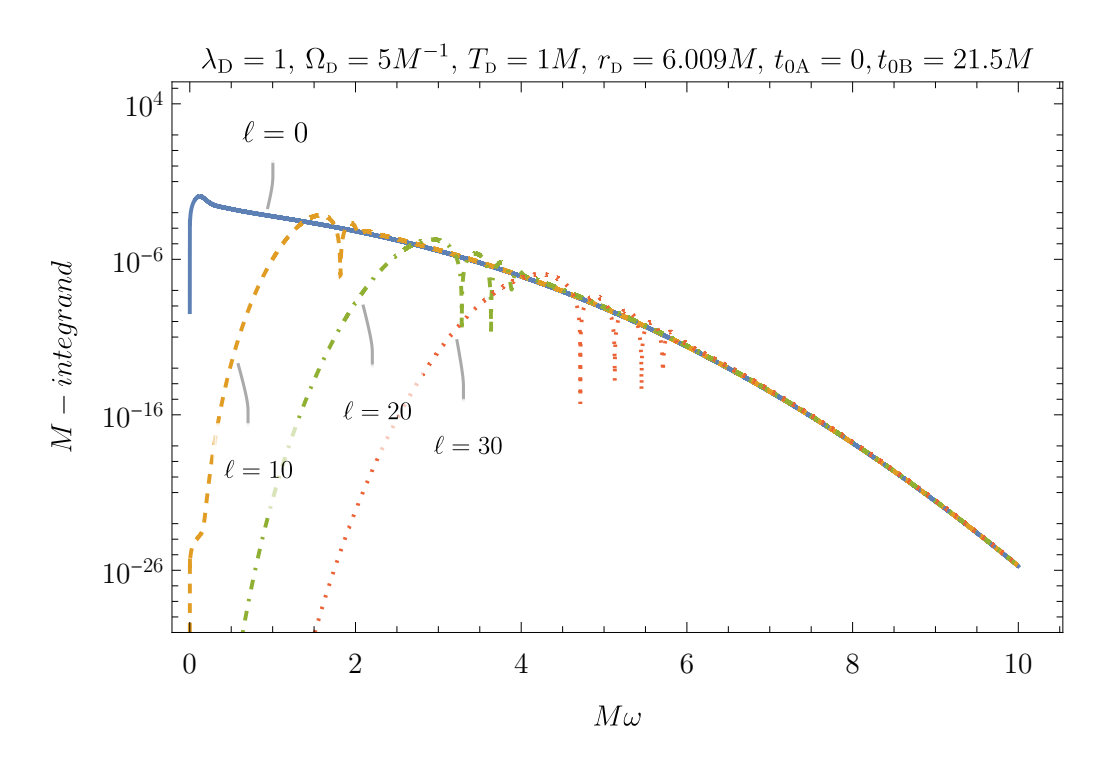


Figure 80 – Boulware state integrand in Equation (A.10) after rewriting the integral so that it ranges from $\omega = 0$ to $M\omega = 10$, as a function of $M\omega$, for several different $\ell = 0, 10, 20, 30$.

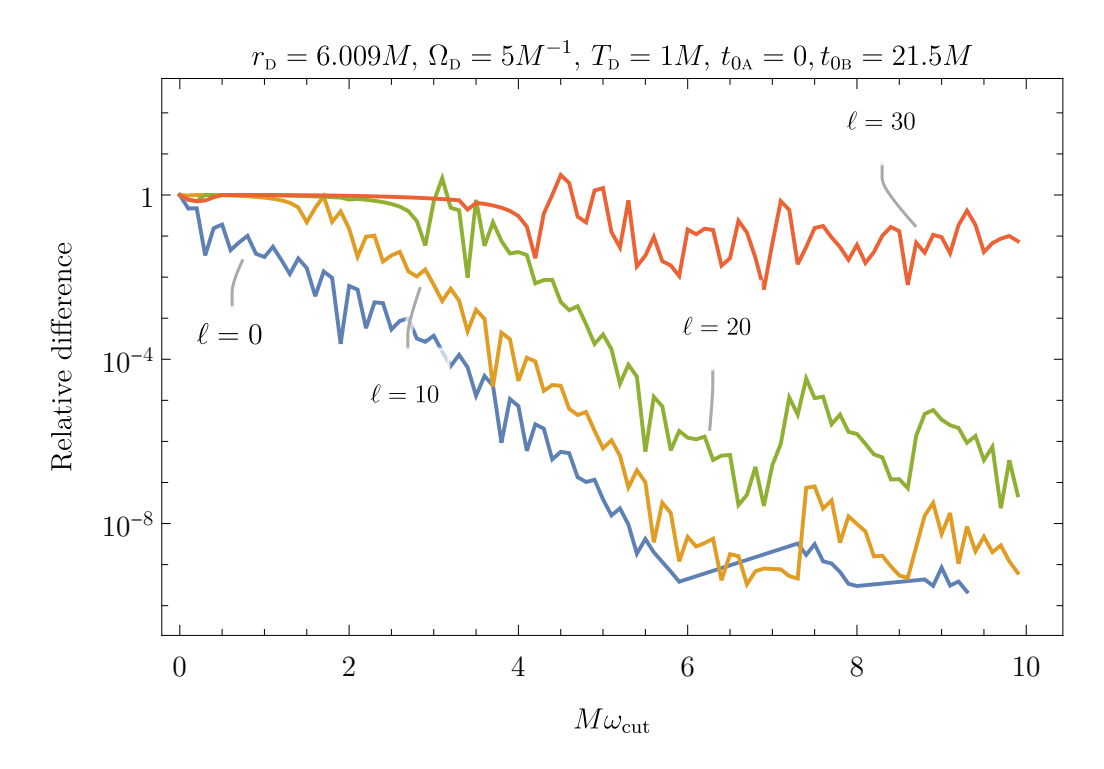


Figure 81 – Relative difference in the Boulware state integral in Eq. (A.10) after rewriting the integral so that it ranges from $\omega = 0$ to $\omega = \omega_{cut}$ for several different $\ell = 0, 10, 20, 30$. To evaluate the relative difference, we integrate up to ω_{cut} and then to $\omega_{cut} + \delta$, with $\delta = 1/10$.

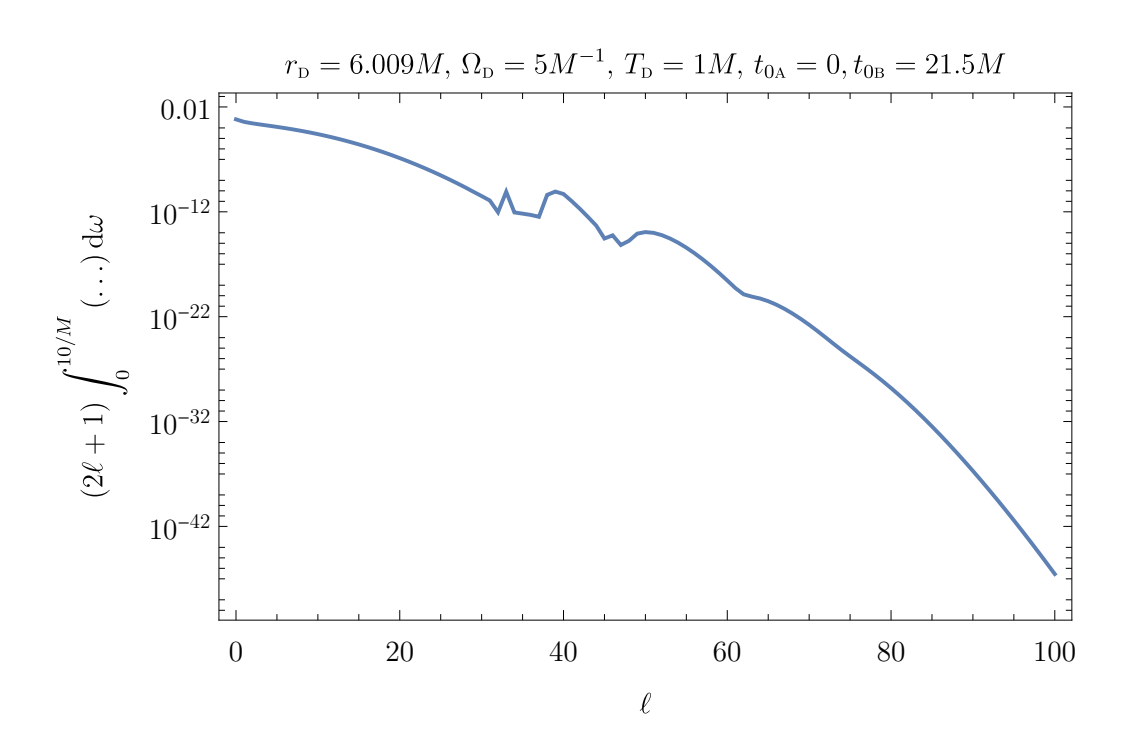


Figure 82 – Boulware state integral in Equation (A.10), after rewriting the integral so that it ranges from $\omega = 0$ to $\omega = \omega_{cut}$ for several different $\ell = 0, 10, 20, 30$, here integrated up to $M\omega_{cut} = 10$.

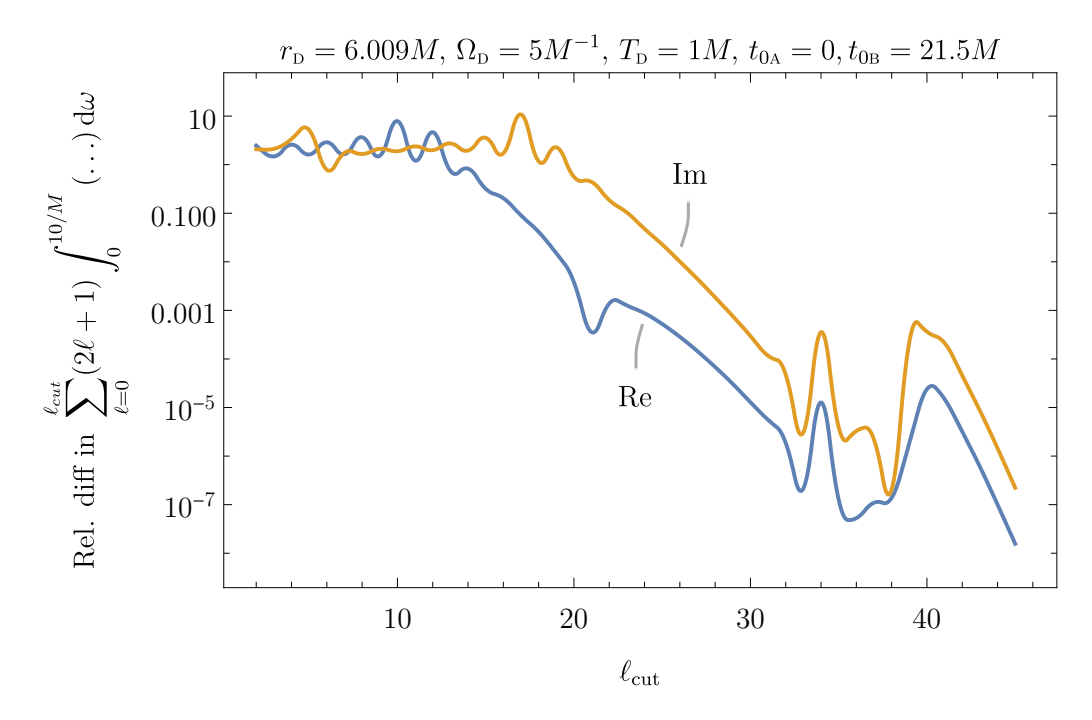


Figure 83 – Relative difference in the Boulware state integral from Equation (A.10), after rewriting the integral so that it ranges from $\omega = 0$ to $\omega = \omega_{cut}$ for several different $\ell = 0, 10, 20, 30$. To evaluate the relative difference, we sum up to ℓ_{cut} and then to $\ell_{cut} + 1$, ranging form $\ell_{cut} = 1$ up to $\ell_{cut} = 100$. For $\ell_{cut} > 45$ all significant digits exactly cancel out when evaluating the relative difference.

- [1] J. G. Caribé, R. H. Jonsson, M. Casals, A. Kempf, and E. Martín-Martínez, Physical Review D 108, 025016 (2023).
- [2] S. W. Hawking, Nature **248**, 30 (1974).
- [3] D. J. Fixsen, The Astrophysical Journal 707, 916 (2009).
- [4] C. J. Shallue, J. B. Muñoz, and G. Z. Krnjaic, Journal of Cosmology and Astroparticle Physics 2025, 026 (2025).
- [5] C. Yang, S. Wang, M.-L. Zhao, and X. Zhang, Journal of Cosmology and Astroparticle Physics **2024**, 083 (2024).
- [6] J. D. Bekenstein, Physical Review D 7, 2333 (1973).
- [7] S. W. Hawking, Phys. Rev. D 14, 2460 (1976).
- [8] S. Raju, Physics Reports **943**, 1 (2022).
- [9] W. G. Unruh and R. M. Wald, Reports on Progress in Physics 80, 092002 (2017).
- [10] R. Schützhold and W. G. Unruh, Physical Review D 81, 124033 (2010).
- [11] R. Parentani, Phys. Rev. D 82, 025008 (2010).
- [12] R. Balbinot and A. Fabbri, Physical Review D 105, 1 (2022).
- [13] R. Balbinot, A. Fabbri, S. Fagnocchi, A. Recati, and I. Carusotto, Phys. Rev. A 78, 021603 (2008).
- [14] I. Carusotto, S. Fagnocchi, A. Recati, R. Balbinot, and A. Fabbri, New Journal of Physics 10, 103001 (2008).
- [15] J. Macher and R. Parentani, Phys. Rev. A 80, 043601 (2009).
- [16] J. Steinhauer, Nature Physics **12**, 959 (2016).
- [17] J. R. Muñoz de Nova, K. Golubkov, V. I. Kolobov, and J. Steinhauer, Nature 569, 688 (2019).
- [18] V. I. Kolobov, K. Golubkov, J. R. M. de Nova, and J. Steinhauer, Nature Physics 17, 362 (2021).
- [19] E. Tjoa and E. Martín-Martínez, Physical Review D 104, 125005 (2021).

- [20] B. Reznik, A. Retzker, and J. Silman, Phys. Rev. A 71, 042104 (2005).
- [21] A. Pozas-Kerstjens and E. Martín-Martínez, Phys. Rev. D 92, 064042 (2015).
- [22] E. Tjoa and R. B. Mann, Journal of High Energy Physics 2020 (2020), 10.1007/JHEP08(2020)155.
- [23] K. Gallock-Yoshimura, E. Tjoa, and R. B. Mann, Phys. Rev. D 104, 025001 (2021).
- [24] S. Barman, D. Barman, and B. R. Majhi, Journal of High Energy Physics **2022**, 106 (2022).
- [25] R. M. Wald, General Relativity (University of Chicago Press, 1984) p. 507.
- [26] "Black Hole Perturbation Toolkit," (bhptoolkit.org).
- [27] C. Buss and M. Casals, Physics Letters B 776, 168 (2018).
- [28] E. Poisson, A Relativist's Toolkit (Cambridge University Press, 2004) p. 190.
- [29] V. P. Frolov and I. D. Novikov, Black Hole Physics, Vol. 96 (Springer Netherlands, 1998).
- [30] S. W. Hawking and G. F. R. Ellis, *The Large Scale Structure of Space-Time* (Cambridge University Press, 1973).
- [31] C. W. Misner, K. S. Thorne, J. A. Wheeler, and D. Kaiser, Gravitation (Princeton University Press, 2017) p. 1279.
- [32] A. Lanir, A. Levi, A. Ori, and O. Sela, Physical Review D 97, 024033 (2018).
- [33] E. Honig, K. Lake, and R. C. Roeder, Physical Review D 10, 3155 (1974).
- [34] N. D. Birrell and P. C. W. Davies, *Quantum Fields in Curved Space* (Cambridge University Press, 1982).
- [35] S. A. Fulling, Aspects of Quantum Field Theory in Curved Space-Time (Cambridge University Press, 1989).
- [36] A. Fabbri and J. Navarro-Salas, Modeling Black Hole Evaporation (PUBLISHED BY IMPERIAL COLLEGE PRESS AND DISTRIBUTED BY WORLD SCIENTIFIC PUBLISHING CO., 2005) pp. 1–335.
- [37] M. Casals, A. Fabbri, C. Martínez, and J. Zanelli, Physics Letters B 760, 244 (2016).
- [38] S. Hollands, R. M. Wald, and J. Zahn, Classical and Quantum Gravity 37, 115009 (2020).

- [39] W. G. Unruh, Physical Review D 14, 870 (1976).
- [40] D. G. Boulware, Physical Review D 11, 1404 (1975).
- [41] P. Candelas, Physical Review D 21, 2185 (1980).
- [42] J. B. Hartle and S. W. Hawking, Physical Review D 13, 2188 (1976).
- [43] S. M. Christensen and S. A. Fulling, Physical Review D 15, 2088 (1977).
- [44] S. Hollands and R. M. Wald, Physics Reports 574, 1 (2015).
- [45] M. Ikawa, Hyperbolic Partial Differential Equations and Wave Phenomena, Vol. 189 (American Mathematical Society, 2000).
- [46] P. R. Garabedian, Partial Differential Equations (Chelsea Pub Co, New York, 1998).
- [47] M. Casals and B. C. Nolan, Physical Review D 108, 044033 (2023).
- [48] DLMF, "NIST Digital Library of Mathematical Functions," https://dlmf.nist.gov/, Release 1.2.1 of 2024-06-15, f. W. J. Olver, A. B. Olde Daalhuis, D. W. Lozier, B. I. Schneider, R. F. Boisvert, C. W. Clark, B. R. Miller, B. V. Saunders, H. S. Cohl, and M. A. McClain, eds.
- [49] M. Abramowitz and I. A. Stegun, Handbook of Mathematical Functions: With Formulas, Graphs, and Mathematical Tables Applied mathematics series (Dover Publications, 1970).
- [50] G. B. Arfken, H. J. Weber, and F. E. Harris, Mathematical Methods for Physicists (Elsevier, 2013).
- [51] K. K. Ng, C. Zhang, J. Louko, and R. B. Mann, New Journal of Physics 24, 103018 (2022).
- [52] K. D. Kokkotas and B. G. Schmidt, Living Reviews in Relativity 2, 2 (1999).
- [53] E. W. Leaver, Journal of Mathematical Physics 27, 1238 (1986).
- [54] C. S. Buss, Two-point correlation function for a scalar field on a Schwarzschild background, Master's thesis, Brazilian Center for Research in Physics (2016).
- [55] W. E. Boyce, R. C. DiPrima, and D. B. Meade, Elementary Differential Equations and Boundary Value Problems, 11th ed. (John Wiley & Sons, 2018).
- [56] M. Sasaki and H. Tagoshi, Living Reviews in Relativity 6, 6 (2003).
- [57] A. Zenginoğlu and C. R. Galley, Physical Review D 86, 064030 (2012).

- [58] R. Balbinot and A. Fabbri, Physics 5, 968 (2023).
- [59] S. R. Dolan, International Journal of Modern Physics D 27, 1843010 (2018), https://doi.org/10.1142/S0218271818430101.
- [60] B. DeWitt, General Relativity; an Einstein Centenary Survey (Cambridge University Press, Cambridge, UK, 1980).
- [61] E. Martín-Martínez, T. R. Perche, and B. d. S. L. Torres, Phys. Rev. D 103, 025007 (2021).
- [62] J. de Ramón, M. Papageorgiou, and E. Martín-Martínez, Phys. Rev. D 103, 085002 (2021).
- [63] E. Martín-Martínez, Physical Review D 92, 104019 (2015).
- [64] E. Martín-Martínez, T. R. Perche, and B. de S. L. Torres, Phys. Rev. D 101, 045017 (2020).
- [65] R. Lopp and E. Martín-Martínez, Phys. Rev. A 103, 013703 (2021).
- [66] E. Martin-Martinez and P. Rodriguez-Lopez, Physical Review D 97, 105026 (2018).
- [67] S. J. Summers (1990) pp. 393–413.
- [68] S. J. Summers and R. Werner, Physics Letters A 110 (1985), 10.1016/0375-9601(85)90093-3.
- [69] I. Agullo, B. Bonga, P. Ribes-Metidieri, D. Kranas, and S. Nadal-Gisbert, Physical Review D 108, 085005 (2023).
- [70] I. Agullo, B. Bonga, E. Martín-Martínez, S. Nadal-Gisbert, T. R. Perche, J. Polo-Gómez, P. Ribes-Metidieri, and B. d. S. L. Torres, Phys. Rev. D 111, 085013 (2025).
- [71] M. Saravani, S. Aslanbeigi, and A. Kempf, Physical Review D 93, 045026 (2016).
- [72] A. Kempf, Frontiers in Physics 9, 655857 (2021).
- [73] T. R. Perche and E. Martín-Martínez, Phys. Rev. D 105, 066011 (2022).
- [74] L. Bombelli, R. K. Koul, J. Lee, and R. D. Sorkin, Phys. Rev. D 34, 373 (1986).
- [75] M. Srednicki, Phys. Rev. Lett. **71**, 666 (1993).
- [76] J. Eisert, M. Cramer, and M. B. Plenio, Rev. Mod. Phys. 82, 277 (2010).
- [77] E. Witten, Rev. Mod. Phys. **90**, 045003 (2018).

[78] S. W. Hawking, Communications in Mathematical Physics 43, 199 (1975).

- [79] P. C. W. Davies, J. Phys. A 8, 609 (1975).
- [80] D. N. Page, Phys. Rev. Lett. **71**, 3743 (1993).
- [81] D. N. Page, J. Cosmol. Astropart. Phys. **2013**, 028 (2013).
- [82] G. Penington, J. High Energy Phys. **2020**, 2 (2020).
- [83] A. Valentini, Physics Letters A 153, 321 (1991).
- [84] B. Reznik, Foundations of Physics **33**, 167 (2003).
- [85] G. VerSteeg and N. C. Menicucci, Phys. Rev. D 79, 044027 (2009).
- [86] E. Martín-Martínez, A. R. H. Smith, and D. R. Terno, Phys. Rev. D 93, 044001 (2016).
- [87] L. J. Henderson, R. A. Hennigar, R. B. Mann, A. R. H. Smith, and J. Zhang, Classical and Quantum Gravity 35, 21LT02 (2018).
- [88] M. Cliche and A. Kempf, Physical Review D 83, 045019 (2011).
- [89] R. H. Jonsson, D. Q. Aruquipa, M. Casals, A. Kempf, and E. Martín-Martínez, Physical Review D 101, 125005 (2020).
- [90] I. Bengtsson and K. Życzkowski, Geometry of Quantum States (Cambridge University Press, 2017).
- [91] M. Casals and B. Nolan, Physical Review D (2016).
- [92] C. J. Shallue and S. M. Carroll, "What hawking radiation looks like as you fall into a black hole," (2025), arXiv:2501.06609 [gr-qc].
- [93] A. Levi and A. Ori, Phys. Rev. D **94**, 044054 (2016).